

CARBON ANODE PERFORMANCE AND SAFETY EVALUATION OF  
POTASSIUM-ION BATTERIES

A Dissertation

Submitted to the Faculty

of

Purdue University

by

Ryan A. Adams

In Partial Fulfillment of the

Requirements for the Degree

of

Doctor of Philosophy

May 2019

Purdue University

West Lafayette, Indiana

**THE PURDUE UNIVERSITY GRADUATE SCHOOL**  
**STATEMENT OF DISSERTATION APPROVAL**

Dr. Arvind Varma, Co-Chair

Davidson School of Chemical Engineering

Dr. Vilas G. Pol, Co-Chair

Davidson School of Chemical Engineering

Dr. James M. Caruthers

Davidson School of Chemical Engineering

Dr. Kejie Zhao

School of Mechanical Engineering

**Approved by:**

Dr. Sangtae Kim

Head of the Graduate Program

*In memory of Kerri A. Mowen and John N. Murrell,  
for initiating and inspiring my academic journey.*

## ACKNOWLEDGMENTS

Thank you to my advisors, Arvind Varma and Vilas Pol, for providing mentorship, encouragement, and countless opportunities.

Thank you to the members of my committee, Jim Caruthers and Kejie Zhao, for their invaluable insights, perspectives, and critiques.

Thank you to the Varma research group for the companionship in the office throughout the years, with special thanks to Wooram Kang, Yang Xiao, Greg Honda, Chunxiao Xu, and Rex Lagare.

Thank you to the ViPER research group for the research assistance and rapport, with special thanks to Patrick Kim, Kyungho Kim, Daw Gen Lim, Neal Cardoza, and Tommy Zhao.

Thank you to my collaborators for expanding my horizons, with special thanks to Bing Li, Michael Naguib, Jonathan Phillips, and Aashutosh Mistry.

Thank you to Arthur Dysart and Jimmy Tang for the continual camaraderie, guidance, and moral support.

Thank you to Lily the cat for providing me with an excuse to go home at a reasonable hour every day.

Most importantly, thank you to my wife and best friend Karen, who sacrificed her love of California weather to be with me in Indiana.

## TABLE OF CONTENTS

	Page
LIST OF TABLES . . . . .	viii
LIST OF FIGURES . . . . .	x
ABSTRACT . . . . .	xix
1 INTRODUCTION TO ENERGY STORAGE . . . . .	1
1.1 Energy Storage Technologies . . . . .	1
1.2 Lithium-ion Batteries . . . . .	1
1.3 Alternative Alkali Metal-ion Batteries . . . . .	5
1.4 Dissertation Overview . . . . .	6
1.5 References . . . . .	8
2 POTASSIUM-ION BATTERIES AND SAFETY . . . . .	10
2.1 Non-aqueous Potassium-ion Batteries . . . . .	10
2.2 Carbon Anodes . . . . .	13
2.3 Safety Concerns of Lithium-ion Batteries . . . . .	15
2.4 SEI Layer Relation to Thermal Runaway . . . . .	17
2.5 Research Objectives . . . . .	19
2.6 References . . . . .	20
3 FLEXIBLE, BINDER-FREE, N- AND O- RICH CARBON NANOFIBER ANODES FOR LONG CYCLE LIFE K-ION BATTERIES . . . . .	24
3.1 Summary . . . . .	24
3.2 Introduction . . . . .	25
3.3 Experimental Section . . . . .	27
3.4 Results and Discussion . . . . .	29
3.5 Conclusions . . . . .	41
3.6 Acknowledgements . . . . .	42
3.7 References . . . . .	42
4 MECHANISTIC ELUCIDATION OF THERMAL RUNAWAY IN POTASSIUM- ION BATTERIES . . . . .	45
4.1 Summary . . . . .	45
4.2 Introduction . . . . .	45
4.3 Experimental . . . . .	48
4.4 Results and Discussion . . . . .	49
4.5 Conclusions . . . . .	59

	Page
4.6	Acknowledgements . . . . . 60
4.7	References . . . . . 60
5	TEMPERATURE DEPENDENT ELECTROCHEMICAL PERFORMANCE OF GRAPHITE ANODES FOR K-ION AND LI-ION BATTERIES . . . . . 63
5.1	Summary . . . . . 63
5.2	Introduction . . . . . 64
5.3	Experimental . . . . . 66
5.4	Results and Discussion . . . . . 67
	5.4.1 Kinetics . . . . . 67
	5.4.2 Aging . . . . . 72
	5.4.3 Polarization . . . . . 75
	5.4.4 Full Cell . . . . . 80
5.5	Conclusions . . . . . 82
5.6	Acknowledgements . . . . . 83
5.7	References . . . . . 83
6	MATERIALS BY DESIGN: TAILORED MORPHOLOGY AND STRUC- TURES OF CARBON ANODES FOR ENHANCED BATTERY SAFETY . 86
6.1	Summary . . . . . 86
6.2	Introduction . . . . . 87
6.3	Results and Discussion . . . . . 89
	6.3.1 Materials Characterization . . . . . 89
	6.3.2 Electrochemical Implications . . . . . 90
	6.3.3 Inhomogeneity in Self-heating . . . . . 97
	6.3.4 Thermal Abuse Behavior . . . . . 100
6.4	Conclusions . . . . . 102
6.5	Acknowledgements . . . . . 103
6.6	References . . . . . 103
7	ELECTROCHEMICAL PERFORMANCE OF MXENES AS K-ION BAT- TERY ANODES . . . . . 106
7.1	Summary . . . . . 106
7.2	Introduction . . . . . 106
7.3	Experimental . . . . . 108
7.4	Results and Discussion . . . . . 108
7.5	Conclusions . . . . . 114
7.6	Acknowledgements . . . . . 114
7.7	References . . . . . 114
8	SUMMARY AND RECOMMENDATIONS . . . . . 116
8.1	Summary . . . . . 116
8.2	Recommendations . . . . . 117
	8.2.1 Accelerating Rate Calorimetry . . . . . 117

	Page
8.2.2 K-ion Battery SEI Layer . . . . .	118
8.2.3 Electrochemical Impedance Spectroscopy . . . . .	119
A CHAPTER 3 SUPPORTING INFORMATION . . . . .	120
B CHAPTER 4 SUPPORTING INFORMATION . . . . .	130
C CHAPTER 5 SUPPORTING INFORMATION . . . . .	139
D CHAPTER 6 SUPPORTING INFORMATION . . . . .	155
E CHAPTER 7 SUPPORTING INFORMATION . . . . .	166
VITA . . . . .	173
PUBLICATIONS . . . . .	174

## LIST OF TABLES

Table	Page
2.1 Comparison of Alkali Metal Properties . . . . .	12
3.1 Elemental composition of CNF samples via XPS analysis. . . . .	31
3.2 Material properties and porosity for CNF samples. . . . .	32
C.1 Freezing point range of liquid electrolyte used in Li-ion and K-ion batteries.	140
C.2 Fitting parameters for Li-ion battery electrochemical impedance spectra measured at each temperature. All measurements were performed at 200 mV, for cells conditioned at C/10 for 10 cycles at 22°C. . . . .	145
C.3 Fitting parameters for K-ion battery electrochemical impedance spectra measured at each temperature. All measurements were performed at 500 mV, for cells conditioned at C/10 for 10 cycles at 22°C. . . . .	145
C.4 Fitting parameters for Li-ion battery electrochemical impedance spectra after three slow conditioning cycles (5 mA g <sup>-1</sup> ) at various temperatures. All electrochemical impedance spectra were measured at 200 mV (vs. Li/Li <sup>+</sup> ) and 22°C, corresponding to the data in Figure C.7a . . . . .	146
C.5 Fitting parameters for K-ion battery electrochemical impedance spectra after three slow conditioning cycles (5 mA g <sup>-1</sup> ) at various temperatures. All electrochemical impedance spectra were measured at 500 mV (vs. K/K <sup>+</sup> ) and 22°C, corresponding to the data in Figure C.7b . . . . .	146
C.6 Fitting parameters for Li-ion battery electrochemical impedance spectra after 100 cycles (50 mA g <sup>-1</sup> ) at various temperatures. All electrochemical impedance spectra were measured at 200 mV (vs. Li/Li <sup>+</sup> ) and 22°C, corresponding to the data in Figure C.8a . . . . .	147
C.7 Fitting parameters for K-ion battery electrochemical impedance spectra after 100 cycles (50 mA g <sup>-1</sup> ) at various temperatures. All electrochemical impedance spectra were measured at 500 mV (vs. K/K <sup>+</sup> ) and 22°C, corresponding to the data in Figure C.8b . . . . .	147
D.1 Material properties of carbon anodes . . . . .	160
D.2 Elemental composition of carbon anodes (wt. %) . . . . .	160

Table	Page
D.3 Fitting parameters for electrochemical impedance spectroscopy modeling, conducted for carbon anodes before aging at 1C for 100 cycles at 50°C. . .	161
D.4 Fitting parameters for electrochemical impedance spectroscopy modeling, conducted for carbon anodes after aging at 1C for 100 cycles at 50°C. . .	161
E.1 Atomic percentage estimated from X-ray photoelectron spectroscopy for all the elements on the surface of the $\text{Ti}_3\text{CNT}_z$ electrodes before electrochemical cycling, after discharging to 5 mV, and recharging back to 3 V vs. K/K <sup>+</sup> . . . . .	167

## LIST OF FIGURES

Figure	Page
1.1 Schematic of a Lithium-ion Battery. . . . .	3
3.1 (a) SEM image of prepared electrospun CNF after carbonization at 800°C. Inset: Flexible CNF mat. (b) SEM image of electrospun CNF post oxygen plasma treatment (CNF-O). (c) TEM image of CNF. (d) TEM image of CNF-O. . . . .	30
3.2 (a) XRD pattern for CNF samples with graphitic Miller indices indicated. (b) Raman spectroscopy for CNF samples with disordered and graphitic peaks labeled. . . . .	31
3.3 (a) & (b) Differential capacity curves for the first five cycles of CNF (a) and CNF-O (b) at C/10 rate (current density = 27.9 mA g <sup>-1</sup> ). (c) & (d) Charge-discharge curves for the first, second, and fifth cycle of the CNF (c) and CNF-O (d) samples at C/10 rate. . . . .	34
3.4 (a) & (b) Cycling performance of CNF (a) and CNF-O (b) at 1C current density. (c) & (d) Cycling performance of CNF (c) and CNF-O (d) at various rates. (e) & (f) Charge-discharge curves of CNF (e) and CNF-O (f) for stable performance at various rates. 1C = 279 mA g <sup>-1</sup> . . . . .	36
3.5 Electrochemical characterization of CNF and CNF-O materials. (a) Electrochemical impedance spectroscopy for fresh cells at OCV (2.5 V vs. K/K <sup>+</sup> ). (b) Diffusional coefficient of K <sup>+</sup> in the carbon nanofiber materials, calculated by GITT. (c) Cyclic voltammetry (0.1 mV s <sup>-1</sup> ) for conditioned cells for CNF and CNF-O (inset), with red line showing total current. Charge storage contribution from pseudo-capacitance shown by shaded region. (d) Comparison of charge storage mechanism from intercalation and capacitance contributions for CNF and CNF-O at 0.1 and 1 mV s <sup>-1</sup> scan rates. . . . .	37
3.6 <i>Ex-situ</i> material characterization of CNF after 100 cycles at 1C rate (a) SEM image. (b) EDS analysis with (c) carbon, (d) phosphorous, and (e) potassium, shown in purple, orange, and blue respectively. The scale bar for all images is 10 m. (f) Post-cycling XRD patterns. (g) Post-cycling Raman spectra. . . . .	40

Figure	Page
4.1 (a) Typical charge-discharge voltage profile for graphite electrode in Li-ion and K-ion battery configuration at 20 mA g <sup>-1</sup> current density. (b) DSC profiles of fully charged graphite electrodes prepared by a Li-ion or K-ion battery configuration, with Li-ion degradation reactions labeled. (c) Total heat generation as a function of temperature of DSC profiles. . . . .	50
4.2 (a) DSC profiles for K-ion graphite anode prepared at various states of charge from 0% (depotassiated) to 100% (potassiated). (b) DSC profiles of washed graphite electrodes to remove electrolyte. (c) DSC profiles of chemically synthesized KC <sub>8</sub> with electrolyte. (d) Repeated DSC analysis of K-ion graphite electrode with incrementing temperature. . . . .	53
4.3 (a) DSC profiles of K-ion graphite electrodes after different numbers of cycles. (b) EIS of K-ion graphite electrodes after different numbers of cycles at 200 mV vs. K <sup>+</sup> /K. . . . .	55
4.4 (a) First cycle charge-discharge voltage profile for graphite ball milled for varying lengths of time. (b) DSC profiles for potassiated graphite electrodes after ball milling. . . . .	56
4.5 (a) Coulombic efficiency for the first five cycles of K-ion graphite electrodes using either PVDF, CMCNa, or Na alginate as binder. (b) DSC profiles of potassiated graphite electrodes prepared with different binders. . . . .	58
4.6 (a) XRD patterns of potassiated graphite quenched at 100°C, 150°C, or 250°C. (b) Raman spectra of potassiated graphite quenched at 100°C, 150°C, or 250°C. . . . .	59
5.1 Kinetic analysis of graphite across temperatures. (a) Charge capacity of Li at various specific currents. (b) Charge capacity of K at various specific currents. (c) Voltage profile for discharge at 22°C with subsequent charge at 0°C or 22°C, at 20 mA g <sup>-1</sup> and cycle 5. (d) Solid-state diffusion coefficients of Li <sup>+</sup> and K <sup>+</sup> in graphite from 0 - 40°C, with calculated diffusion activation energies determined by the Arrhenius equation. . . . .	68
5.2 Dependence of cell impedance with temperature. Nyquist plots of electrochemical impedance spectra conducted at various temperatures for (a) Li at 200 mV and (b) K at 500 mV. (c) Charge-transfer resistance and (d) SEI resistance, with corresponding activation energies determined by the Arrhenius equation. . . . .	71

Figure	Page
5.3 (a) Discharge capacity of LIB cycled at 50 mA g <sup>-1</sup> . (b) Discharge capacity of KIB cycled at 50 mA g <sup>-1</sup> . Aging of cells conditioned at various temperatures, with subsequent electrochemical impedance spectroscopy analysis conducted at 22°C. (c) SEI and charge-transfer resistances after 3 slow formation cycles conducted at 5 mA g <sup>-1</sup> . (d) SEI and charge-transfer resistances after 100 cycles at 50 mA g <sup>-1</sup> . . . . .	73
5.4 First cycle charge-discharge voltage profile variation with temperature. (a) Voltage profile for LIB at 0°C, 22°C, and 40°C at 5 mA g <sup>-1</sup> , and corresponding (b) differential capacity plot of LIB voltage profile. (c) Voltage profile for KIB at 0°C, 22°C, and 40°C at 5 mA g <sup>-1</sup> , and corresponding (d) differential capacity plot of KIB voltage profile. . . . .	76
5.5 Polarization of the alkali metal counter electrode. (a) Voltage profile of 3-electrode LIB cell at 20 mA g <sup>-1</sup> and 0°C. (b) Voltage profile of 3-electrode KIB cell at 20 mA g <sup>-1</sup> and 0°C. (c) Dependence of the average alkali metal counter electrode polarization with temperature. (d) Differential capacity plot of the graphite voltage profile across temperatures in a 3-electrode KIB cell. . . . .	77
5.6 Cell aging from high temperature storage. (a) Specific capacity before and after aging, at 50 mA g <sup>-1</sup> and 22°C. Aging was performed in the middle of cycle 6 at 50°C for 7 days for fully lithiated / potassiated (discharged) batteries under open circuit voltage. (b) Nyquist plots for electrochemical impedance spectra immediately before and after aging. . . . .	79
5.7 KIB full cell evaluation. (a) First cycle voltage profiles of Prussian blue cathode and graphite anode half-cells at 50 mA g <sup>-1</sup> . The capacities are normalized to show the positive to negative charge ratio of the full cell. (b) Full cell charge-discharge voltage profiles across various temperatures from 1.0 - 3.9 V at 50 mA g <sup>-1</sup> of graphite. (c) Charge capacities and Coulombic efficiencies for full cell cycling conducted from 1.0 - 3.9 V at 50 mA g <sup>-1</sup> of graphite and 22°C. Specific current and capacity values in (b) and (c) are normalized by the weight of active material in the graphite anode.	81
6.1 Different carbon-types studied here: (a) commercial graphite (b) spherical carbon and (c) spiky carbon. (a) and (c) are prepared in-house. Their (d) crystalline structure is examined by X-ray diffraction and (e) Raman spectroscopy. (f) Multimodal interactions related to particle morphology. . . . .	88

Figure	Page
6.2	Electrochemical trends upon cycling. Initial cycles refer to the formation of a stable SEI film and accordingly large capacity variations are seen across all carbon types (a) graphite (b) spherical and (c) spiky. These tests are carried out at C/10. (d) Constant current cycling quantifies the capacity decay due to SEI growth on repeated cycling. (e) Capacity retention trends differ as SEI formation and intercalation dynamics vary across different particle types Electrochemical impedance spectra of (f) graphite, (g) spherical carbon, and (h) spiky carbon. Cells were aged at 50°C for 100 cycles at 1C rate, and EIS was collected at 200 mV (vs. Li/Li <sup>+</sup> ).92
6.3	A spiky particle has two attributes (a) spike amplitude and (b) spike count. A spherical particle is a special instance of a spiky particle with vanishingly small spike amplitude. (c) Such geometrical features bring about complexities in the intercalation response which in turn affects side reaction rates. . . . . 93
6.4	Intercalation nonuniformity due to geometrical features. (a) Concentration and (b) intercalation flux distribution on particle surface at 20% lithiation. (c) Corresponding intercalation flux as a function of concentration and surface map (inset). (d) and (e) show the progression of flux concentration maps at higher lithiation extents, 40%, and 80%, respectively. (f) Potential evolution and contribution from side reaction. Concentration evolution upon lithiation in the interior of the particle (g) initial (h) 20% (i) 40% and (j) 80% lithiation. Vertical and horizontal sections are shown in (g) through (j). . . . . 95
6.5	Progression of (a) - (d) local overpotential (e) - (h) kinetic and (i) - (l) reversible heat generation rates as lithiation takes place. The inhomogeneity translates to all the different fields and is observable during intermediate stages of lithiation. For comparison, states of an equivalent spherical particle are also shown. A spherical particle has a uniform surface state. . . . 98
6.6	(a) Differential scanning calorimetry (DSC) captures the thermally activated reactions (endothermic and exothermic) of active material. This reaction information is further useful in estimating thermal abuse response of cells composed of the same active material. (b) DSC responses of the three carbon materials and corresponding (c) oven test trends. Note that a larger spike in the heat flow does not necessarily mean poorer thermal stability as reaction rate constant can change the rate of heat generation. 101

Figure	Page
7.1 The electrochemical performance of the $\text{Ti}_3\text{CNT}_z$ electrode. (a) Galvanostatic voltage profiles for cycles 1, 2, 50 and 100 at $20 \text{ mA g}^{-1}$ between 5.0 mV and 3.0 V. (b) The corresponding $dQ/dV$ for the results presented in 1a. The inset shows a higher magnification for the potassiation part of the plot in b. (c) Capacity vs. cycle number at $20 \text{ mA g}^{-1}$ . (d) Capacity vs. cycle number at rates of 10 - $500 \text{ mA g}^{-1}$ . . . . .	110
7.2 Nitrogen adsorption-desorption isotherms for $\text{Ti}_3\text{CNT}_z$ measured at 77 K. The inset shows a typical SEM image for the as synthesized $\text{Ti}_3\text{CNT}_z$ particle. (b) XRD patterns for $\text{Ti}_3\text{CNT}_z$ electrodes that were as-synthesized (black), fully discharged from OCV to 5 mV (orange), re-charged to 3 V (purple), and cycled for 100 cycles (lime green). The vertical broken lines are for guiding the eye to show the changes in the peak position. The * sign represents the peak position of the $\text{Ti}_4\text{Al}(\text{C}_x\text{N}_{1-x})_3$ secondary phase. . . . .	112
7.3 Schematic for the structure of $\text{Ti}_3\text{CNO}_2$ before and after electrochemical potassiation and de-potassiation. $\text{O}_2$ was used instead of $\text{T}_z$ for simplicity (c-LP stands for the c-lattice parameter). . . . .	113
A.1 Schematic of flexible carbon nanofiber mat electrospinning synthesis, thermal treatment, and application as K-ion anode material. . . . .	120
A.2 Nitrogen adsorption isotherms taken at 77K for CNF and CNF-O. . . . .	121
A.3 <i>Ex-situ</i> XRD analysis of CNF and CNF-O materials after the first discharge (0.005 V) and charge (back to 3.0 V) during the first cycle. Peak location for (002) Miller plane labeled in figure for each curve. . . . .	122
A.4 Electrochemical impedance spectroscopy at various voltages for the first discharge for CNF and CNF-O material. . . . .	123
A.5 Galvanostatic intermittent titration technique with charge and discharge profiles for (a) CNF, (b) CNF-O, and (c) and graphite. (d) Plot of voltage vs. square root of time for CNF. . . . .	124
A.6 Galvanostatic intermittent titration technique with diffusional coefficient calculated for graphite material as K-ion anode. . . . .	125
A.7 Cyclic voltammetry for conditioned cells for CNF (a), (b), & (c) and CNF-O (d), (e), & (f) taken at scan rates from $0.1 \text{ mV s}^{-1}$ to $500 \text{ mV s}^{-1}$ . . . . .	126
A.8 Plot showing linear relation of $\log(v)$ vs. $\log(i)$ for discharge sweeps of cyclic voltammetry for CNF (a) and CNF-O (b) samples at various voltages. Slope correlated to b, where the voltammetric sweep follows the power law relationship of $I = av^b$ . Diffusion limited processes (intercalation) can be described by $b = 0.5$ , according to Cottrell Equation, while capacitive processes can be described by $b = 1.0$ . . . . .	127

Figure	Page
A.9 Dependence of the slope $b$ determined by the linear fit of $\log(v)$ vs. $\log(i)$ as a function of cell voltage for CNF and CNF-O materials. Calculated using scan rates from 0.1 - 5.0 $\text{mV s}^{-1}$ . A value of $b$ closer to 1 correlates to capacitive charge storage mechanism, while a value closer to 0.5 correlates to intercalation charge storage mechanism. . . . .	128
A.10 Cyclic voltammetry for conditioned cells for CNF and CNF-O, with red line showing total current. Charge storage contribution from pseudo-capacitance shown by shaded region. (a) CNF at 0.1 $\text{mV s}^{-1}$ . (b) CNF-O at 0.1 $\text{mV s}^{-1}$ . (c) CNF at 1.0 $\text{mV s}^{-1}$ . (d) CNF-O at 1.0 $\text{mV s}^{-1}$ . . . .	129
B.1 (a) First cycle charge-discharge voltage profile for graphite electrode when cycled against Li and K metal, with 20 $\text{mA g}^{-1}$ current density. (b) Extended galvanostatic cycling of graphite electrode at 20 $\text{mA g}^{-1}$ current density, comparing discharge capacity and Coulombic efficiency for Li and K ion system. . . . .	131
B.2 (a) Raman spectroscopy of synthetic graphite collected at 633 nm. (b) XRD of synthetic graphite. (c) Nitrogen sorption isotherms of graphite with BET surface area of 3.4 $\text{m}^2 \text{g}^{-1}$ . (d) SEM image of graphite particles with scale bar of 40 $\mu\text{m}$ . . . . .	132
B.3 (a) DSC profile of 0.8 M $\text{KPF}_6$ in 1:1 EC/DEC (volumetric) electrolyte. (b) DSC profile of 1 M $\text{LiF}_6$ in 1:1 EC/DEC (volumetric) electrolyte. (c) DSC profile of $\text{KPF}_6$ salt. (d) DSC profile of $\text{LiPF}_6$ salt. . . . .	133
B.4 (a) DSC profile of K metal wetted with 0.8 M $\text{KPF}_6$ in 1:1 EC/DEC (volumetric) electrolyte. (b) DSC profile of K metal with PVDF powder. . . . .	134
B.5 XRD patterns of graphite (blue), $\text{KC}_8$ prepared electrochemically and equilibrated at 5 mV (vs $\text{K}^+/\text{K}$ ), and $\text{KC}_8$ synthesized by heating stoichiometric K metal and graphite under inert atmosphere. Kapton tape was utilized for air sensitive $\text{KC}_8$ samples and is responsible for the broad peak at $19^\circ$ . . . . .	134
B.6 (a) EIS spectra collected at 200 mV (vs. $\text{K}^+/\text{K}$ ) for cycle 1, 10, and 25 with a graphite electrode in a K-ion battery. (b) Circuit model utilized to fit parameters to EIS spectra. $R_{cell}$ is the cell resistance. $R_{SEI}$ and $\text{CPE}_{SEI}$ are the resistance and constant phase element in parallel for SEI in the high frequency range. $R_{CT}$ is charge transfer resistance, with $\text{CPE}_{DL}$ as its relative double layer capacitance. $Z_W$ is the Warburg impedance corresponding to diffusion of K-ions on the electrode-electrolyte interface at low frequencies. . . . .	135

Figure	Page
B.7 Material properties for ball milled and sieved ( $>25 \mu\text{m}$ & $<53 \mu\text{m}$ ) graphite particles. (a) Nitrogen sorption isotherms and BET calculated surface areas. (b) Raman spectra. (c) XRD spectra. . . . .	136
B.8 SEM images for ball milled and sieved ( $>25 \mu\text{m}$ & $<53 \mu\text{m}$ ) graphite particles. (a & b) 0-hour ball mill. (c & d) 1-hour ball mill. (e & f) 5-hours ball mill. . . . .	137
B.9 (a) Extended galvanostatic cycling of graphite electrode with CMCNa binder at $20 \text{ mA g}^{-1}$ current density as K-ion anode. (b) Extended galvanostatic cycling of graphite electrode with Na alginate binder at $20 \text{ mA g}^{-1}$ current density as K-ion anode. . . . .	138
B.10 DSC profiles for K-ion battery graphite, carbon nanofiber, and Super P electrodes. . . . .	138
C.1 Galvanostatic intermittent titration technique profiles. At $0^\circ\text{C}$ for (a) Li and (b) K. At $22^\circ\text{C}$ for (c) Li and (d) K. At $40^\circ\text{C}$ for (e) Li and (f) K. All profiles were conducted with 30-minute current pulses at $C/10$ ( $37.2 \text{ mA g}^{-1}$ for Li and $27.9 \text{ mA g}^{-1}$ for K) followed by 1-hour relaxations. . . . .	141
C.2 Current pulses for LIB graphite anode at various specific currents. (a) $0^\circ\text{C}$ . (b) $10^\circ\text{C}$ . (c) $22^\circ\text{C}$ . (d) $30^\circ\text{C}$ . (e) $40^\circ\text{C}$ . Linear relationship was used to determine $(dE/d\sqrt{t})$ for solid-state diffusion coefficient calculation, and performed at 60% SOC. . . . .	142
C.3 Current pulses for graphite anode in KIB at various specific currents. (a) $0^\circ\text{C}$ . (b) $10^\circ\text{C}$ . (c) $22^\circ\text{C}$ . (d) $30^\circ\text{C}$ . (e) $40^\circ\text{C}$ . Linear relationship was used to determine $(dE/d\sqrt{t})$ for solid-state diffusion coefficient calculation, and performed at 60% SOC. . . . .	143
C.4 Dependence of $(dE/d\sqrt{t})$ on specific current across temperatures. (a) Li. (b) K. . . . .	144
C.5 Equivalent circuit utilized for fitting of electrochemical impedance spectra data. Equivalent circuit consists of a cell resistance, a constant phase element for SEI capacitance, a SEI resistance, a constant phase element for double layer capacitance, a charge-transfer resistance, and a Warburg diffusion element. . . . .	144
C.6 Coulombic efficiencies for each operating temperature during initial cycles at $50 \text{ mA g}^{-1}$ , corresponding to the data in Figure 5.3a-b. (a) Li. (b) K. . . . .	148
C.7 Nyquist plots for electrochemical impedance spectra of cells conditioned with three formation cycles at $5 \text{ mA g}^{-1}$ at each corresponding temperature. All electrochemical impedance spectra were measured at $22^\circ\text{C}$ and (a) $200 \text{ mV}$ for Li, and (b) $500 \text{ mV}$ for K. . . . .	149

Figure	Page
C.8 Nyquist plots for electrochemical impedance spectra of cells after aging for 100 cycles at 50 mA g <sup>-1</sup> at each corresponding temperature. All electrochemical impedance spectra were measured at 22°C and (a) 200 mV for Li, and (b) 500 mV for K. . . . .	150
C.9 Charge-discharge voltage profiles of 3-electrode cells at 20 mA g <sup>-1</sup> (after five conditioning cycles). (a) Li at 22°C. (b) Li at 40°C. (c) K at 22°C. (d) K at 40°C. . . . .	151
C.10 Voltage profiles of cells before and after aging during cycle 6 of Figure 5.6a. (a) Li at 50 mA g <sup>-1</sup> . (b) K at 50 mA g <sup>-1</sup> . (c) Open circuit voltage profile of cells stored at 50°C for 7 days. . . . .	152
C.11 Material characterization of synthesized Prussian blue cathode. (a) Thermogravimetric analysis conducted in argon atmosphere at 10°C min <sup>-1</sup> from 50 - 450°C. (b) X-ray diffraction pattern, with JCPDS 52-1907 reference card for Prussian blue Fe <sub>4</sub> [Fe(CN) <sub>6</sub> ] <sub>3</sub> . (c) Raman spectrum. . . . .	153
C.12 Electrochemical analysis of Prussian blue cathode in half-cell configuration. (a) Charge-discharge voltage profile for cycle 1, 2, and 5 conducted at 20 mA g <sup>-1</sup> from 2 - 4 V. (b) Charge-discharge voltage profile at various specific currents of 20 - 400 mA g <sup>-1</sup> . (c) Rate study from 20 - 400 mA g <sup>-1</sup> . (d) Long-term galvanostatic cycling conducted at 200 mA g <sup>-1</sup> . . . . .	154
D.1 Nitrogen adsorption/desorption isotherms obtained at 77 K for each carbon material. . . . .	162
D.2 Rate study of the three carbon materials, with 1C defined as 372 mA g <sup>-1</sup> . . . . .	163
D.3 Full cell data for tested carbon materials against a LiCoO <sub>2</sub> cathode. First two cycle voltage profiles for (a) graphite, (b) spherical carbon, and (c) spiky carbon. Long-term cycling data with Coulombic efficiencies are shown in (d), using a current density of 100 mA g <sup>-1</sup> , based on the weight of carbon. . . . .	164
D.4 Accelerated aging of carbon anodes with 1C rate conducted at 50°C for 100 cycles. EIS measurements were conducted before and after at 200 mV (vs. Li/Li <sup>+</sup> ). . . . .	165
D.5 Equivalent circuit utilized for electrochemical impedance spectra data fitting. . . . .	165
E.1 K 2p X-ray photoelectron spectra for Ti <sub>3</sub> CNT <sub>z</sub> electrodes before cycling (black), after fully discharging down to 5 mV (orange), and after recharging back to 3V (purple). . . . .	168

Figure	Page
E.2 The electrochemical performance of $\text{Ti}_3\text{C}_2\text{T}_z$ electrode. (a) Galvanostatic voltage profile for cycle number 1, 2, 50 and 100 at $20 \text{ mA g}^{-1}$ between 5.0 mV and 3.0 V vs. $\text{K}/\text{K}^+$ . (b) The corresponding $dQ/dV$ for the results presented in (a). The inset is a higher magnification for the potassiation part of the plot in (b). (c) Capacity vs. cycle number at $20 \text{ mA g}^{-1}$ . (d) Capacity vs. cycle number at rates of 10 - $100 \text{ mA g}^{-1}$ . . . . .	169
E.3 The electrochemical performance of $\text{Nb}_2\text{CT}_z$ electrode. (a) Galvanostatic voltage profile for cycle number 1, 2, 50 and 100 at $20 \text{ mA g}^{-1}$ between 5.0 mV and 3.0 V vs. $\text{K}/\text{K}^+$ . (b) The corresponding $dQ/dV$ for the results presented in (a). The inset is a higher magnification for the potassiation part of the plot in (b). (c) Capacity vs. cycle number at $20 \text{ mA g}^{-1}$ . (d) Capacity vs. cycle number at rates of 10 - $100 \text{ mA g}^{-1}$ . . . . .	170
E.4 Electrochemical impedance spectroscopy (EIS) Nyquist plot of $\text{Ti}_3\text{C}_2\text{T}_z$ and $\text{Ti}_3\text{CNT}_z$ at open circuit voltage. . . . .	171
E.5 The electrochemical performance of a carbon black electrode (90:10 carbon black to PVDF wt. ratio) in a KIB half cell. (a) Galvanostatic cycling at various current densities between 5 mV and 1.5 V. (b) Galvanostatic voltage profiles at various current densities. . . . .	172

## ABSTRACT

Adams, Ryan A. Ph.D., Purdue University, May 2019. Carbon Anode Performance and Safety Evaluation of Potassium-ion Batteries. Major Professors: Arvind Varma, Vilas G. Pol.

Potassium-ion batteries (PIBs) recently emerged as a next-generation energy storage technology, utilizing abundant and inexpensive potassium as the charge carrier cation. PIBs operate by an analogous mechanism to lithium-ion batteries (LIBs), with reversible potassium intercalation in anode and cathode through an inorganic salt - organic solvent electrolyte medium. Despite its larger size, potassium exhibits several electrochemical advantages over sodium, including a higher affinity for intercalation into graphitic (carbonaceous) anodes, forming a stage-one  $KC_8$  structure in graphite for a specific capacity of  $279 \text{ mAh g}^{-1}$ . This thesis aims to provide a thorough foundation for PIB carbon anodes, through a comprehensive experimental approach combining electrode synthesis, advanced material characterization and electrochemical-analytical techniques.

Safety concerns have consistently plagued LIBs despite almost three decades of widespread commercialization. Thermal runaway of LIBs can initiate as early as  $80^\circ\text{C}$  from exothermic breakdown of the solid electrolyte interphase (SEI) layer that covers the carbon anode surface. The subsequent reaction of lithiated carbon with electrolyte solvent leads to cathode decomposition and oxygen release for cell gassing and combustion. This thesis investigates the thermal runaway behavior of graphite anode for PIBs via differential scanning calorimetry analysis, determining the effect of electrode material, state-of-charge, and cycling history on heat generation. Notably, the PIB system emits significantly less heat overall than for LIBs, albeit an earlier and more intense onset reaction at  $100^\circ\text{C}$  raises safety concerns. Strategies to mitigate

this exothermic reaction are presented, including electrode binder manipulation to improve graphite particle coverage and enhance SEI layer stability.

To further evaluate the practicality of PIBs, the electrochemical behavior of graphite anode was investigated from 0 - 40°C operating temperature, in comparison to standard LIBs. The poor rate capability of potassium is attributed to sluggish solid-state diffusion and augmented cell impedance, where 3-electrode studies revealed dramatic polarization of the potassium metal counter electrode at low temperatures. Accelerated cell aging at elevated temperatures is attributed to SEI layer growth induced by the 61% volumetric expansion of graphite during potassiation, as well as the extreme reactivity of potassium metal. A full-cell system with a Prussian blue nanoparticle cathode and graphite anode showed enhanced rate performance at low temperatures by removing potassium metal counter electrode. These results provide valuable mechanistic insight for potassium intercalation in graphite and offer a practical evaluation of temperature dependent electrochemical performance for PIBs.

Supplementary research includes the exploration of carbon nanofibers electrospun from polyacrylonitrile precursor with subsequent pyrolysis as PIB anode. The design of an amorphous, low density carbon with a nanoscale one-dimensional morphology enables mitigation of the 61% volumetric expansion of graphite during potassiation. Remarkable stability (2000 charge-discharge cycles) is thus achieved by preventing electrode pulverization, SEI layer growth, and impedance rise during cycling. Electrochemical analysis revealed a pseudo-capacitance mechanism, enabling rapid charging through surface storage of potassium that could be enhanced by surface functionalization via plasma oxidation treatment. Moreover, two dimensional MXene transition carbonitride sheets were explored as PIB anode with X-ray diffraction and X-ray photoelectron spectroscopy used to study structural changes during potassium insertion.

Finally, the effect of particle morphology was investigated for LIB carbon anodes, wherein commercial graphite is compared with synthesized spherical and spiky carbons. Intercalation dynamics, side reaction rates (e.g. SEI growth), self-heating, and thermal runaway behavior were studied through a combination of electrochem-

ical analysis and modeling by a finite volume method. Spherical particles outperform irregular commercial graphite by eliminating unstructured inhomogeneities that lead to non-uniform current distributions. Interestingly, spiky particles offer a non-trivial response, where the ordered irregularities enhance intercalation dynamics to prevent degradation at extreme operating conditions. These findings emphasize the importance of tailoring particle morphology and structure in promoting desired LIB behavior and suppressing unwanted problems.

## 1. INTRODUCTION TO ENERGY STORAGE

### 1.1 Energy Storage Technologies

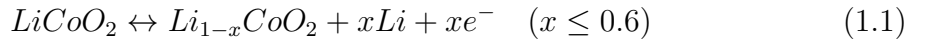
As global energy production shifts to renewable green sources, such as solar and wind, due to the environmental issues and limited supply of fossil fuels, the importance of electrical energy storage (EES) will increase.[1, 2, 3] Large scale EES systems must be established to buffer between supply (varying production of renewable energy) and demand (accommodation of peak hour usages).[4] Small scale systems are also of great importance to society, with ubiquitous applications such as powering electric vehicles (EVs), hybrid electric vehicles (HEVs), and electrical portable devices.[2, 5] Many energy storage technologies have been explored and proposed as possible solutions to these upcoming technological changes in society, e.g. mechanical storage via pumped hydro and compressed air, chemical storage through hydrogen fuel cells or biofuels, or electrical storage in supercapacitors or batteries.[1] All technologies have advantages and disadvantages in terms of energy storage scalability, cost of storage ( $\text{USD kWh}^{-1}$ ), storage efficiency, and power, making certain technologies appropriate for different applications.[1] Battery energy storage results in pollution-free operation, flexibility in power and energy densities, high efficiency, long cycle life, low maintenance, and compact size ( $\text{kWh L}^{-1}$ ).[6] While batteries remain the preferred solution to many applications, current technologies are too expensive and inefficient to satisfy many future requirements on a global scale.[6, 7, 8]

### 1.2 Lithium-ion Batteries

Since their introduction into commercial markets by Sony in the early 1990s, lithium-ion batteries (LIBs) have dominated rechargeable energy storage applications, with an annually growing market in portable consumer electronics (e.g. smartphones,

laptops, etc.).[9] LIBs offer higher operating voltages and greater energy densities than other commercial rechargeable batteries (NiMH, NiCd, Lead-Acid). However, lithium is a scarce resource that is primarily imported internationally from South America and China. The scarcity of lithium ores both domestically and globally could result in drastically inflated production costs in the next few decades.[6, 10] Furthermore, sourcing lithium through LIB recycling is only a medium-to-short term solution, as high cost, excessive energy requirements, lacking innovations in recycling processes impede long-term applications.[11] In this context, alternative battery storage technologies with lower production and operation costs than LIBs are essential, particularly for low-energy density applications such as electric grid storage.

Commercial LIB cells consist of four major components: cathode, anode, electrolyte, and separator. Compared to other energy storage systems, the LIBs demonstrate exceptionally high energy densities due to the low atomic weight and low redox potential [ $E_0$  (Li/ Li<sup>+</sup> = -3.04 V vs. standard hydrogen electrode (SHE))] of lithium.[12] LIBs are rechargeable across an extended time period due to the intercalation storage mechanism. Also known as the rocking chair mechanism, intercalation enables the shuttling of lithium back and forth between two host materials, resulting in relatively high cycle efficiency and low hysteresis.[12] Typical materials are the LiCoO<sub>2</sub> layered oxide material cathode (160 mAh g<sup>-1</sup>) and graphite anode (372 mAh g<sup>-1</sup>). In the charge process, Li ions are shuttled from the cathode to anode as follows:



The reverse reaction set illustrates the discharge process. A schematic displaying these charge and discharge processes is shown in Figure 1.1.

Despite the appealing performance values of lithium metal (viz. theoretical gravimetric capacity 3860 mAh g<sup>-1</sup>), the uncontrolled formation of Li outgrowths (i.e., dendrites) and poor Coulombic efficiency prevent safe and efficient operation, respectively. [13] An alternate to the lithium metal anode is graphite due to a higher

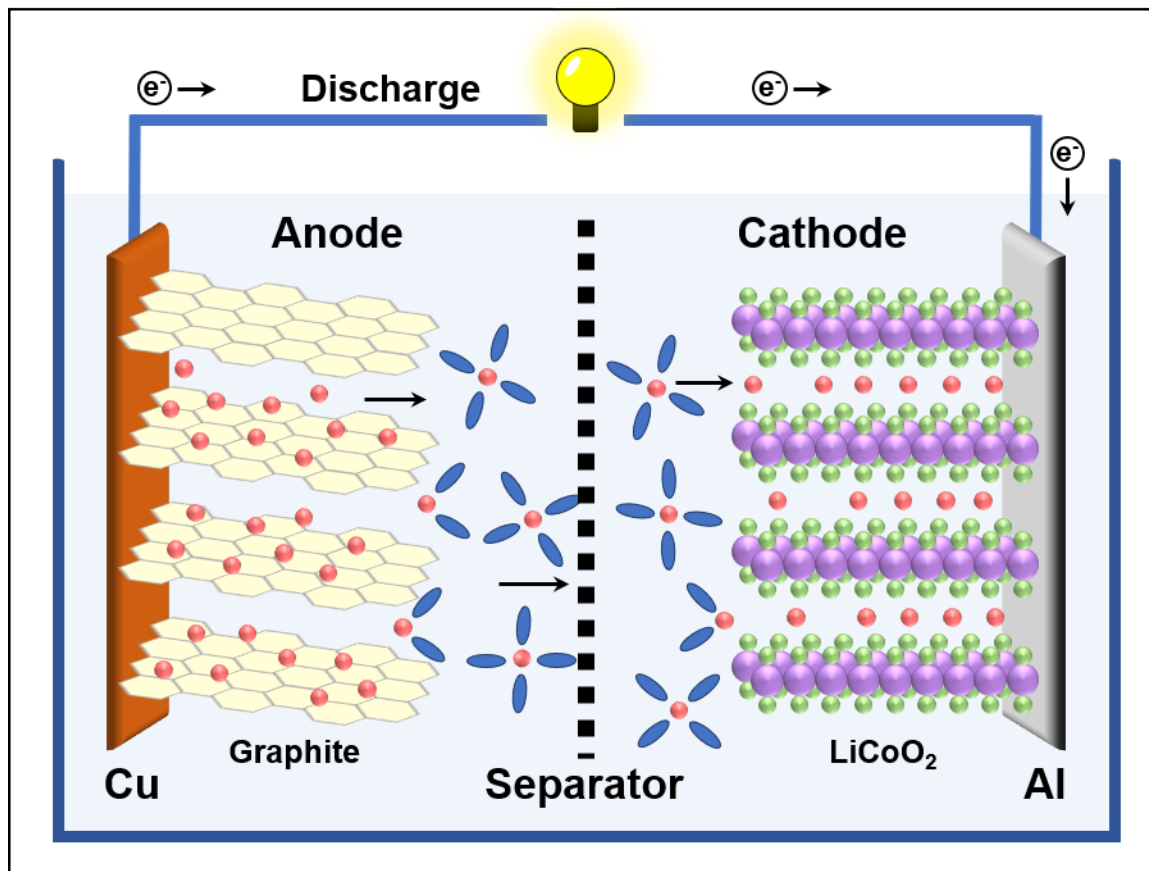


Figure 1.1. Schematic of a Lithium-ion Battery.

lithium intercalation voltage: the operating voltage of graphite (i.e., ca. 0.1 V vs.  $\text{Li}/\text{Li}^+$ ) enables safer operation well above the unstable lithium deposition and plating voltage (i.e., 0.0 V). However, cycling of graphite anodes at higher current densities or low temperature operation can eventually result in local Li metal deposition.[14] Another strategy is the utilization of alternative lithium storage mechanisms. The alloying mechanism enables lithium storage via formation of metal or covalent bonds with lithium ions (e.g., silicon anode). The conversion mechanism enables lithium storage via a series of redox reactions that incorporate or strip lithium (e.g., iron oxide anode). However, both types involve unresolved issues of large hysteresis and capacity fade due to dramatic chemical changes during cycling prevent widespread

commercialization.[12] As a result, many first-generation electrode materials developed in the 1980s are still manufactured for commercial LIBs today.

The electrolyte is an ionically-conductive and electronically-insulating medium, preferentially transporting lithium-ions between the cathode and anode. Typical organic electrolytes consist of an inorganic lithium salt (e.g.,  $\text{LiPF}_6$ ) in an organic solvent blend (e.g., ethylene carbonate, EC; and dimethyl carbonate, DMC) due to the high stability and ionic conductivity of such mixtures at high voltages. However, many commercial electrolytes experience partial decomposition into a polymeric interface on standard graphitic electrodes: voltage-sensitive reduction of EC and DMC forms a passivation layer known as a solid electrolyte interphase (SEI). Advantageously, the SEI has a high Li-ion conductivity and low electron conductivity that enables reversible lithium-ion diffusion,[15] and protects graphite from exfoliation and further SEI formation during repeated lithiation. However, the formation of the SEI severely reduces the availability of electrochemically-active lithium, and uncontrolled buildup results in capacity loss and greater impedance that may eventually terminate electrochemical performance.[12] This passivation layer, formed via multi-component decomposition reactions, is composed of densely packed inorganic Li salts (e.g., LiF,  $\text{Li}_2\text{O}$ ,  $\text{Li}_2\text{CO}_3$ ) on the anode side and oligomer organic layers (e.g.,  $\text{ROCO}_2\text{Li}$ ) on the electrolyte side. The particular properties of SEI are highly dependent upon material properties of the electrodes, the electrolyte composition, and cell cycling parameters. Chemical manipulation of SEI by electrolyte additives (e.g. vinylene carbonate (VC)) has improved cycling stability in LIBs.[16]

The battery separator imposes a physical separation between the cathode and anode electrodes to prevent instantaneous charge transfer or dissipation. A typical separator utilized in LIBs is the microporous polymer thin film, that serves as an insulating barrier between electrodes while conducting Li-ions through the pores.[17] Separators also play a vital role in LIB safety and thermal runaway shutdown: by adopting a multilayer structure (e.g., polyethylene (PE) - polypropylene (PP)), PE can melt and fill pores to dramatically increase cell resistance to terminate cell operation.[17]

### 1.3 Alternative Alkali Metal-ion Batteries

During the past few decades, extensive research has identified additional reversible metal-ion chemistries for electrochemical energy storage (i.e., Na-ion, Mg-ion, and Al-ion).[18] Of particular commercial interest is the Na-ion battery (NIB), which has much in common with the LIB due to its proximity in the periodic table and similar cationic charge of +1.[18] While the natural abundance of sodium is a clear scalability advantage, NIBs have lower energy densities than LIBs due to the greater atomic mass, cation size, and lower ionization voltage of sodium metal.[19] NIBs utilize similar organic solvent-inorganic salt electrolyte mixtures, in which Na-ions are shuttled between two host materials via an intercalation mechanism.[19] Many promising cathodes have been demonstrated, with layered metal oxide  $O_3/P_2$  structures or polyanionic compounds demonstrating specific capacities and voltages approaching those of LIBs.[20, 21, 22]

Analogous to the concerns regarding lithium metal in LIBs, pure sodium metal cannot be utilized as an anode material for NIBs due to safety and performance concerns. The traditional LIB graphite anode (specific capacity  $372 \text{ mAh g}^{-1}$ ) cannot effectively intercalate sodium - sodiation without prior graphitic expansion or co-solvent molecules, limiting it to a  $\text{NaC}_{64}$  structure ( $35 \text{ mAh g}^{-1}$ ).[23, 24] Hard carbon, derived from pyrolysis of various biomasses, has been demonstrated to produce moderate gravimetric capacities as a NIB anode, but the lower volumetric capacity and Coulombic efficiency limit practical applications.[25] In addition, hard carbons demonstrate low tap density and suffer from production scalability issues (compared to graphite anodes). Recently, potassium-ion batteries (KIBs) have received extensive interest, due to the discovery in 2015 that potassium can reversibly intercalate in graphite to stage-one  $\text{KC}_8$  for a capacity of  $279 \text{ mAh g}^{-1}$ .[26] Additionally, several cathode materials have since been developed with promise for high voltage KIBs.

## 1.4 Dissertation Overview

This thesis is motivated by the recent surge in research interest for KIBs. Chapter 2 provides a detailed literature background of non-aqueous KIBs, with the scientific and economic motivation for their development. The mechanism of potassium intercalation in carbon anodes is discussed due to the practical interest for a graphite anode system. Battery failure via thermal runaway is introduced for the well-known LIB system. The role of SEI in thermal runaway initiation is described along with explored mitigation strategies. Finally, the research objectives of this thesis are listed.

Chapter 3 presents my work on the utilization of carbon nanofibers for KIB anode for the first time. Due to the larger ionic size, graphite expands by 61% upon potassiation, as opposed to 11% of lithiation, causing electrode pulverization and capacity fade upon repeated cycling. By designing a one-dimensional, low-density amorphous carbon material, I mitigated this issue and obtained exceptional cycling stability for KIBs. Additionally, I explored oxygen surface functionalization to amplify the pseudo-capacitance storage of potassium ions.

Chapter 4 contains my work in elucidating the unknown thermal runaway behavior of KIBs. The exothermic reactions of standard graphite anode at various conditions (e.g. state-of-charge, cycling history) were investigated via differential scanning calorimetry, and compared across Li-ion and K-ion chemistries. Through *ex-situ* X-ray diffraction and Raman spectroscopy, a mechanistic model was proposed wherein exothermic reaction of potassiated carbon with electrolyte initiates thermal runaway of KIBs at 100°C.

Chapter 5 describes my work analyzing the effect of operating temperature on performance for KIBs. All prior investigations of KIBs have been conducted at room temperature, while it is known from LIBs that operating temperature plays a significant role in performance, lifetime, and safety. Standard graphite anode was utilized as a model system, with comparisons made between Li and K-ion chemistries in terms of kinetics, aging, and polarization. The non-ideal potassium metal counter

electrode limits cell performance, with significant polarization at low temperatures and accelerated aging at elevated temperatures.

Chapter 6 explores the hypothesis that irregular particle morphology leads to electrochemical performance and safety concerns from non-uniform current distributions. I synthesized and compared spherical carbon particles with spiky carbon particles and irregular graphite particles for LIB anode material to determine the geometry-functionality relationship via experimental and modeling studies in collaboration with Aashutosh Mistry and Dr. Partha Mukherjee at Purdue University. Notably, a designed material morphology and structuring mitigated thermal runaway heat generation and enhanced lithiation dynamics.

Chapter 7 details the exploration of two-dimensional transition metal carbonitrides, MXenes, for the first time as anode material for KIBs. In collaboration with Dr. Michael Naguib and Dr. Jagjit Nanda at Oak Ridge National Laboratory, I utilized electrochemical testing and *ex-situ* materials characterization to determine the structural and SEI layer development of titanium carbonitride,  $\text{Ti}_3\text{CNT}_z$ , upon potassium intercalation, providing valuable insight into KIBs and this class of materials.

Chapter 8 briefly summarizes the key findings of this dissertation, as well as suggests possible future research directions. While K-ion thermal runaway was probed by differential scanning calorimetry studies, detailed kinetic analysis via accelerating rate calorimetry studies and resulting modeling analysis could provide further insight into the exothermic degradation reactions and possible engineering methods for mitigation of safety concerns. As observed throughout my thesis, the KIB SEI layer governs the power, cycle life, and safety of the battery system. Due to its complexity and the technical difficulty of its characterization, the properties of the SEI layer remains largely mysterious and warrants further investigation via X-ray photoelectron spectroscopy. Electrochemical impedance spectroscopy analysis remains a valuable analytic technique to further SEI layer understanding via an electrolyte study.

## 1.5 References

- [1] B. Dunn, H. Kamath, and J. M. Tarascon, *Science* **334**, 928 (2011).
- [2] J. Liu et al., *Advanced Functional Materials* **23**, 929 (2013).
- [3] H. D. Abruña, *Journal of Chemical Education* **90**, 1411 (2013).
- [4] C. Weiller, *Energy Policy* **39**, 3766 (2011).
- [5] W. Kempton and J. Tomić, *Journal of Power Sources* **144**, 280 (2005).
- [6] M. Armand and J. M. Tarascon, *Building better batteries*, 2008.
- [7] J.-M. Tarascon, *Philosophical Transactions of the Royal Society A: Mathematical, Physical and Engineering Sciences* **368**, 3227 (2010).
- [8] J. B. Goodenough and Y. Kim, *Chemistry of Materials* **22**, 587 (2010).
- [9] M. Yoshio, R. J. Brodd, and A. Kozawa, *Lithium-ion batteries*, volume 1, Springer, 2009.
- [10] J. M. Tarascon, *Nature Chemistry* **2**, 510 (2010).
- [11] X. Zeng, J. Li, and N. Singh, *Critical Reviews in Environmental Science and Technology* **44**, 1129 (2014).
- [12] V. Etacheri, R. Marom, R. Elazari, G. Salitra, and D. Aurbach, *Energy & Environmental Science* **4**, 3243 (2011).
- [13] W. Xu et al., *Energy Environ. Sci.* **7**, 513 (2014).
- [14] R. V. Bugga and M. C. Smart, *Lithium Plating Behavior in Lithium-Ion Cells*, in *ECS Transactions*, volume 25, pages 241–252, 2010.
- [15] S. J. An et al., *Carbon* **105**, 52 (2016).
- [16] X. Zhang, Y. Huang, T. Wang, and L. Liu, *Composites Part A: Applied Science and Manufacturing* **38**, 936 (2007).
- [17] S. Zhang, *Journal of Power Sources* **162**, 1379 (2006).
- [18] Y. Wang et al., *Energy Storage Materials* **4**, 103 (2016).
- [19] N. Yabuuchi, K. Kubota, M. Dahbi, and S. Komaba, *Chemical Reviews* **114**, 11636 (2014).
- [20] M. Sathiya, A. S. Prakash, K. Ramesha, J. M. Tarascon, and A. K. Shukla, *Journal of the American Chemical Society* **133**, 16291 (2011).
- [21] J. Kang et al., *Journal of Materials Chemistry* **22**, 20857 (2012).
- [22] X. Li et al., *Electrochemistry Communications* **49**, 51 (2014).
- [23] P. Ge and M. Fouletier, *Solid State Ionics* **28**, 1172 (1988).
- [24] Y. Wen et al., *Nature Communications* **5**, 4033 (2014).

- [25] D. A. Stevens and J. R. Dahn, *Journal of The Electrochemical Society* **147**, 1271 (2000).
- [26] Z. Jian, W. Luo, and X. Ji, *Journal of the American Chemical Society* **137**, 11566 (2015).

## 2. POTASSIUM-ION BATTERIES AND SAFETY

### 2.1 Non-aqueous Potassium-ion Batteries

The potassium-ion battery (KIB) is a rechargeable battery system enabled by the reversible intercalation and storage of  $K^+$ . The KIB is analogous to the lithium-ion battery (LIB): reversible storage of the alkali metal-ion occurs between the anode and cathode, isolated by a separator, through the ionically-conductive electrolyte medium. The first non-aqueous KIB was introduced by Eftekhari in 2004. The prototype utilizes a host cathode of Prussian blue (PB) and an anode of potassium metal in a non-aqueous electrolyte of 3:7 ethylene carbonate (EC)/ ethyl methyl carbonate (EMC) + 1M  $KBF_4$ . [1] Since then, many additional cathode materials have been evaluated, including amorphous  $FePO_4$ , layered potassium oxide structures, Prussian green, and organic cathodes. [2, 3, 4, 5, 6] For example, the layered  $K_{0.7}Fe_{0.5}Mn_{0.5}O_2$  cathode, paired with soft carbon anode, has demonstrated a reversible specific capacity of  $119 \text{ mAh g}^{-1}$  at  $20 \text{ mA g}^{-1}$ , with a 76% capacity retention over 250 cycles. [5]

As observed in the research of LIBs and sodium-ion batteries (NIBs), graphite has been studied with particular interest for KIBs due to its abundance and sustainability. Recently, the reversible interaction between potassium and graphite has been identified as a three-step mechanism. Revealed through *ex-situ* XRD, the saturated graphitic intercalation compound (GIC) is  $KC_8$ :  $KC_{24}$  (stage-three)  $\rightarrow$   $KC_{16}$  (stage-two)  $\rightarrow$   $KC_8$  (stage-one). This experiment demonstrated a specific capacity of  $273 \text{ mAh g}^{-1}$  at a C/40 rate ( $1C = 279 \text{ mA g}^{-1}$ ) [7], an experimental value approaching the theoretical gravimetric capacity  $279 \text{ mAh g}^{-1}$ . In contrast, ab-initio calculations in combination with experiments revealed  $KC_{24}$  (stage-three)  $\rightarrow$   $KC_{16}$  (stage-two)  $\rightarrow$   $KC_8$  (stage-one) intercalation mechanism. [8] Additionally, Share *et al.* utilized *in-situ* Raman spectroscopy to propose the formation of a dilute stage-one compound above

0.24 V, with the transition from stage-six  $\text{KC}_{72}$  (0.24 V) to stage-two  $\text{KC}_{24}$  (0.15 V), and the subsequent formation of stage-one  $\text{KC}_8$  below 0.15 V.[9] These discrepancies illustrate the necessity for further *in-situ* characterization and modeling to elucidate the intercalation mechanism. The quasi-equilibrium potential of  $\text{KC}_8$  occurs at 0.24 V (determined via galvanostatic intermittent titration technique (GITT)). The higher K-ion intercalation potential (vs.  $\text{K}/\text{K}^+$ ) compared to the Li-ion intercalation potential (vs.  $\text{Li}/\text{Li}^+$ ) implies decreased risk of metal plating and dendrite formation: this suggests KIBs are a safer alternative to LIBs for high voltage applications.[7, 8] However, the bulky  $\text{K}^+$  ions do result in poor rate capabilities (e.g., 80 mAh  $\text{g}^{-1}$  at 1C and 20 mAh  $\text{g}^{-1}$  at 2C) when intercalated between the graphene sheets.[8]

Despite mechanistic similarity to LIBs and NIBs, KIB graphite anodes show poor electrochemical performance with conventional battery binders and electrolytes. Using the conventional LIB binder PVDF, graphite is susceptible to rapid electrode pulverization and interminable solid electrolyte interphase (SEI) growth, with a capacity decrease of 50% by cycle 50 at cycling rate C/2.[8] In lieu, elastic cross-linked binders such as sodium polyacrylate (PANa) demonstrate a first cycle Coulombic efficiency of 79%, over 30% greater than PVDF binder.[10] Similarly, optimized electrolyte systems decrease first cycle capacity losses and improve extended cycling stability (e.g., 220 mAh  $\text{g}^{-1}$  after 200 cycles).[10, 11] Despite accelerated progress over the past year, KIBs still remain in infancy. Significant work needs to be done to optimize secondary components for efficient and improved performance in KIBs.

The electrochemical properties of the three practical alkali metals are shown in Table 2.1. Principally, the technical challenges of the KIB are a result of the large atomic mass and atomic radius of the potassium atom. Interestingly however, the Stoke radius of the solvated K-ion is smaller than that of either the Li-ion or Na-ion in organic solvents as shown for acetonitrile, with a corresponding decreasing solvation number correspondingly. This improves the ionic conductivity, transference number, and diffusion coefficient of the K-ion compared to the Li-ion or Na-ion.[12] The lower Lewis acidity and charge density of the K-ion enables faster ion transfer

Table 2.1.  
Comparison of Alkali Metal Properties

Property	Lithium (Li)	Sodium (Na)	Potassium (K)
Atomic Mass (Da)	6.94	23.00	39.10
Shannon ionic radius (Å)	0.76	1.02	1.38
Solvation number in Acetonitrile at 25°C[17]	4.4	3.7	3.0
$E_0(A_{PC}^+/A)/V$ vs. SHE[10]	-2.79	-2.56	-2.88
Theoretical capacity of ACoO <sub>2</sub> (mAh g <sup>-1</sup> )[18]	274	235	206
Theoretical capacity of Graphite (mAh g <sup>-1</sup> )	372	35	279
Melting Point (°C)	180.5	97.7	63.5
Abundance (%)	0.0017	2.8	2.6
Cost of Carbonate (US \$ ton <sup>-1</sup> )[10]	23000	200	1000

at the electrolyte-electrode interface.[13] Practically, the greater abundance of potassium ores compared to lithium ores, both domestically and globally, suggests KIBs are more sustainable than LIBs. On an absolute scale (viz., versus the standard hydrogen electrode), the ionization redox potential of potassium is lower than that of both sodium and lithium.[10, 14, 15] This trend is conserved in both organic and aqueous electrolytes such that potassium plating and stripping occurs at lower potentials than lithium, enabling higher voltage cells. Furthermore, potassium does not form alloy compounds with aluminum at lower potentials, whereas Li does ( $< 0.5$  V vs. Li/Li<sup>+</sup>).[16] This necessitates copper current collectors when utilizing carbon anodes in LIBs, resulting in additional costs, whereas KIBs can use the inexpensive and lighter aluminum current collector for both cathodes and anodes.

During intercalation, competing trends in ionization energy and ion-substrate coupling means that Na has the weakest chemical binding of alkali metals, explaining its

inability to effectively intercalate into graphite and also its lower cathodic voltage.[19] Potassium graphite intercalation compound (GIC) is a strong reducing agent, and highly pyrophoric material that is more thermodynamically stable than  $\text{LiC}_6$ , forming a stage-one structure  $\text{KC}_8$  chemical structuring with significantly expanded graphene layers, corresponding to its Miller index (002).[20, 21]

While the chemical advantages of potassium over lithium and sodium cannot be understated, the viability of KIBs is limited due to safety concerns with potassium metal. Potassium metal is exceptionally dangerous as it reacts violently with oxygen in air or water, and forms peroxide ( $\text{O}_2^-$ ) and superoxide ( $\text{O}_2^{2-}$ ) species, which can spontaneously combust. Therefore, in establishing a KIB battery, the potassium metal must be replaced with a safer host material, to prevent K metal deposition and dendrite formation like in LIBs.

## 2.2 Carbon Anodes

Due to sustainability, abundance, and overall practicality, carbon materials are the most popularly studied anodes for rechargeable batteries. Graphite has been studied extensively in LIBs, and is the conventional anode of LIBs today. As the most stable allotrope of carbon, graphite is composed of  $\text{sp}^2$  hybridized carbon graphene sheets stacked either in an ABAB... ( $\alpha$ -hexagonal) or ABCABC ( $\beta$ -rhombohedral) configuration held together by van-der-Waals bonding forces. It has a moderate density of  $2.2 \text{ g cm}^{-3}$  and can be obtained either by mining (natural graphite) or by graphitization of petroleum coke precursor at high temperatures of  $2500\text{-}3000^\circ\text{C}$  (synthetic graphite). Typically, low surface area ( $<5 \text{ m}^2 \text{ g}^{-1}$ ), micron sized particles are utilized for electrodes, to minimize the first cycle inefficiency inevitably caused by SEI formation and to increase the tap density and weight loading. As a semimetal, it is highly conductive within the graphene plane due to the conjugated  $\pi$ -band electron network. Its anisotropic behavior is further demonstrated by the selective intercalation of alkali metal ions through the edges, versus the basal plane, where the native interlayer spacing of  $0.335 \text{ nm}$  between the graphene layers expands due to the en-

hanced electrostatic repulsion.[20] While graphite is capable of intercalating a variety of compounds (covalent and ionic), ionic graphite intercalation compounds (GICs), including alkali-metal intercalation compounds, have attracted great interest due to the resulting change in electronic properties.[22] GICs are typically classified by their staging, which refers to the number of graphene sheets between two intercalated layers, according to Rudorff and Daumas-Herold models.[23, 24] This mechanism stems from several competing energetics, including van-der-Waals binding energy disruption between adjacent graphene layers by the intercalant, intralayer attraction between intercalants, and electrostatic repulsion between different intercalant layers.[25] During electrochemical intercalation, graphite undergoes phase transformations from dilute to more concentrated staging (e.g. stage-one), resulting in c-axis expansion of the GIC perpendicular to the (002) hexagonal plane.

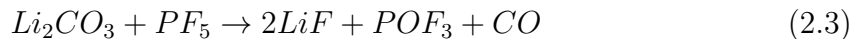
The electrochemical performance of carbonaceous materials - including graphite - is sensitive to morphology and material properties (e.g. surface area, porosity, crystallinity).[26] Thus, under defined circumstances, some disordered carbons demonstrate better performance than graphite. For LIBs, nanostructured carbon structures often have greater gravimetric capacities and rate capability due to more available electrolyte-electrode contact area. However, larger surface area decreases the first cycle Coulombic efficiency due to greater passivation volume.[27] The mechanisms of  $\text{Li}^+$  storage also alter, with pseudo-capacitance, pore filling, reversible binding at functional sites, and storage in interfacial regions all augmented due to the dramatically increased surface area.[28]

With the affinity of  $\text{K}^+$  storage in graphite, it follows to explore other carbonaceous anodes for KIBs. Due to the large volumetric change (61%) upon potassium intercalation, mechanical pulverization of graphite results in continual SEI growth and electrode degradation over extended cycling. Amorphous or nanostructured materials with lower density can help alleviate mechanical stresses due to expansion, as shown for Si anodes.[29] Jian *et al.* demonstrated that a soft carbon synthesized by pyrolysis of PTCDA at  $900^\circ\text{C}$  improved its rate capability to  $140 \text{ mAh g}^{-1}$  at 5C

and stability with 81.4% capacity retention after 50 cycles at 2C rate.[7] Hard carbon microspheres (by hydrothermal reaction of sucrose followed by pyrolysis) show superior rate capability with potassium vs. sodium and 83% capacity retention of 216 mAh g<sup>-1</sup> after 100 cycles at C/10.[30] Various graphene materials with N-doping or F-doping can augment the specific capacity of the material, rivaling that of graphite for LIBs, showing the affinity of K<sup>+</sup> intercalation in different carbon materials.[31, 9]

### 2.3 Safety Concerns of Lithium-ion Batteries

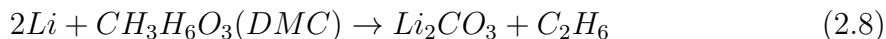
One of the primary concerns of rechargeable LIBs is their safety, in terms of operating range, flammability, and stability.[32] Due to the utilization of organic electrolyte to obtain a wide operating voltage window, these systems are flammable resulting in thousands of reported instances of electric vehicles, airplanes, and personal electronics catching fire or exploding due to defective cells, possibly poor manufacturing, cell puncturing, or other hazards.[33] Careful maintenance and control of operating conditions is required for safe operation, as heat generation in larger battery packs can lead to thermal runaway.[34] Thermal runaway initiates primarily because of the SEI layer breakdown on the carbon anode, initiating typically at around 100°C.[35] The following exothermic reactions have been proposed,[180,181]



where generally metastable species formed by acid-base reactions with electrolyte decompose. This releases low thermal energy to more stable species (LiF / Li<sub>2</sub>CO<sub>3</sub>), while increasing cell pressure via gassing.[36, 37, 38] These reactions consume the SEI layer, leading to an observed deceleration of heat release over time.[36] The carbon

material properties significantly alter the heat generation for this reaction, where increasing surface area augments the heat generation of SEI decomposition, seemingly from the excess SEI layer formation.[39, 35] From there, the polymer separator melts at around 130°C, causing short circuiting.[33]

At elevated temperatures, stronger exothermic reactions between intercalated lithium in the carbon and electrolyte occur, rapidly self-heating the system and leading to cathode decomposition and cell combustion. The following reactions have been proposed to occur, depending on electrolyte solvent as follows,



where generally, lithium carbonate and other thermally stable SEI components precipitate, along with further gassing and pressure rise. This can initiate by 100°C, but strongly depends on the SEI layer, as its growth in thickness with the above reactions does prevent electrolyte - intercalated lithium contact.[39] It is known however, that these reformed SEI can possibly decompose and generate more heat at higher temperatures, leading to several cycles of SEI formation and consumption during thermal runaway.[40] Additionally, above 200°C, the increased cell pressure can cause solvent intercalation in graphite, which exfoliates the graphene layers and provides fresh contact between intercalated lithium and electrolyte for additional consumption of lithium and heat generation.[41]

Eventually, the heat generation from these exothermic reactions and electrolyte breakdown results in decomposition of metal oxide cathode and oxygen gas release, enabling combustion of electrolyte and released gases in the cell.[42, 43, 44] By 200°C, 2 kJ g<sup>-1</sup> of electrode mass is released, with cell combustion and explosions observed in previous LIB safety incidents.[33] Decomposition of electrolyte, electrode, and polymer binder releases species such as O<sub>2</sub>, CO<sub>2</sub>, HF, H<sub>2</sub>, and POF<sub>3</sub>, causing further

increase of pressure and temperature.[45, 46, 40] Due to the complexity of breakdown mechanisms, all these reactions and phenomena are interconnected and fuel each other, and are similar to thermal runaway problems encountered in industrial chemical and catalytic reactors.[47]

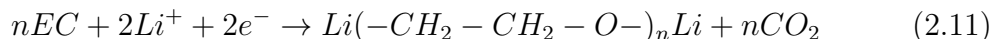
Due to its role in initiating LIB thermal runaway, the degradation reactions and exothermic heat generation of SEI breakdown on carbon anodes is vitally important to understand and mitigate. In fact, the differential scanning calorimetry (DSC) profile for a carbon anode depends greatly on the testing conditions of the cell. Factors such as state of charge (SOC), material surface area, electrolyte, electrode binder, and cycling history will significantly impact the resulting profile.[35] Thus, fundamental understanding of the breakdown mechanism can enable logical design of engineering solutions to mitigate the SEI decomposition. Practically speaking, safe operation of these LIB systems requires careful design and regulation, thus inflating the manufacturing cost by inclusion of fail-safe mechanisms (safety vents, gas relief valves, etc.) and thorough safety testing (e.g. oven tests, nail puncture, mechanical impact, short-circuit, overcharging).[33] Dangers can also occur at lower temperatures and high current densities, as plating of lithium metal can result in dendrite formation that can short circuit the cell.[32]

## 2.4 SEI Layer Relation to Thermal Runaway

Formation of a proper SEI can increase cycle lifetime and efficiency, due to its stabilization against exfoliation and further electrolyte decomposition, while being ionically conductive. LIBs have shown a two-layered structure, consisting of lithium salts such as  $\text{Li}_2\text{CO}_3$ ,  $\text{LiOH}$ ,  $\text{LiF}$ ,  $\text{Li}_2\text{O}$  near the electrode and oligomers near the electrolyte, with a variety of characterization techniques used to elucidate the SEI such as X-ray photoelectron spectroscopy (XPS), *in-situ* electrochemical scanning tunneling microscopy, Fourier-transform infrared spectroscopy, atomic force microscopy, and Raman microscopy.[48, 49, 50, 51] The SEI layer is important to understand and engineer in terms of combating thermal runaway safety concerns, as its decomposi-

tion is the first exothermic reaction to begin at elevated temperatures ( $>70^\circ\text{C}$ ). For example, manipulation of the SEI composition by 2% addition of vinylene carbonate (VC) to the electrolyte decreased heat generation of SEI breakdown from  $806 \text{ J g}^{-1}$  to  $394 \text{ J g}^{-1}$ , through formation of a radial poly(VC) compound in the SEI.[52, 53] Additionally, fluoroethylene carbonate (FEC), vinyl ethylene carbonate (VEC), and VC have exhibited benefits as electrolyte additive for the DSC profile and exothermic heat generation.[54, 55] Another strategy is manipulation of SEI by variation of the charge carrier salt, as LiFSI showed a profile with a sharp exothermic peak at  $200^\circ\text{C}$  as opposed to the lower  $100^\circ\text{C}$  of standard  $\text{LiPF}_6$ , resulting in higher resistance to thermal runaway start.[56, 57] Utilization of other binders also has a large impact in terms of electrochemical performance and thermal stability, with CMC-SBR binder showing promise compared to PVDF.[37, 58] There are also ways to mitigate the explosion and cell combustion, by adding nonflammable electrolyte additives such as organic phosphate compounds (e.g. triphenylphosphate, tributylphosphate), but this decreases electrochemical performance.[59, 60]

Currently, very little is understood of SEI formation in KIBs. It is known that usage of functionalized binders (e.g. CMCNa and PANa) enables a pre-formed SEI effect to decrease first cycle capacity loss, similar to NIB systems.[10] The addition of 10 mM KPF<sub>6</sub> to standard 1 M LiPF<sub>6</sub> EC/DMC electrolyte mitigated dendritic growth of lithium by generating a more inorganic SEI layer with higher conductivity.[61] In typical electrolyte compositions, lithium ions are solvated almost exclusively by EC, with the three following SEI formation reactions resulting in  $\text{Li}_2\text{CO}_3$  (2.9),  $(\text{CH}_2\text{OCO}_2\text{Li})_2$  oligomer (2.10), and polyethylene glycol (PEO) (2.11),



Due to charge density differences, potassium ions are solvated by one EC molecule as opposed to four EC molecules for lithium ions. The Marcus reorganization energy is

subsequently much smaller for  $K^+$  electro-reduction than for  $Li^+$ . Addition of  $KPF_6$  increase the rate for Eqn. 2.9, resulting in a SEI layer rich with carbonates as opposed to polymeric species.[61] Inclusion of  $K_2CO_3$  to LIBs as film forming electrolyte additive modified the SEI layer, resulting in a worm mesh structure with improved electrochemical performance and viscoelasticity.[62] Moshkovich *et al.* demonstrated that the cation has a strong effect on stability of surface species formed in a SEI.[63] As the cation decreases in size, its charge density is higher and it interacts with solvent more strongly, for increased solubility of the SEI layer. Thus, K-ion SEI is more stable in PC than Na-ion SEI, while Li-ion SEI forms strong bonds in its oxides, hydroxides, and carbonates, to make it insoluble and stable. While there are no studies yet of the compositional nature of the KIB SEI layer, early predictions indicate that it may have favorable electrochemical properties as compared with NIBs and possibly LIBs. This will impact not just the electrochemical performance but the safety, as LIB SEI decomposition plays a significant role in thermal runaway sensitivity.

## 2.5 Research Objectives

With the recent rising interest in KIBs for energy storage, many unknown parameters and aspects remain to be studied before possible commercialization. Much of the novelty of the KIB lies in the ability for graphite to intercalate  $K^+$ , but this mechanism and the resulting electrochemical behavior remains largely ambiguous. Additionally, poor cycling retention due to repeated 61% volumetric expansion and electrode pulverization limits the lifetime for current graphite anodes. The safety and stability of this system remains completely unknown, as all electrochemical evaluation of KIBs have only been performed at room temperature thus far. Thus, the research objectives of this thesis are as follows:

- Develop a stable cycling anode system via a materials design approach to augment electrochemical storage of  $K^+$ .

- Determine the mechanism of thermal runaway for graphite anode in KIBs, along with its cycling history dependence and mitigation strategies.
- Evaluate the effect of operating temperature on cell performance in terms of kinetics, aging, and polarization for graphite KIB anode.
- Understand the relationship between active particle morphology and electrochemical behavior such as intercalation dynamics, side reaction rates, self-heating, and thermal abuse behavior.
- Explore novel anode materials for KIBs, such as two-dimensional transition metal carbonitrides MXenes, and understand the intercalation mechanism and resulting structural changes.

## 2.6 References

- [1] A. Eftekhari, *Journal of Power Sources* **126**, 221 (2004).
- [2] P. Padigi et al., *Electrochimica Acta* **166**, 32 (2015).
- [3] V. Mathew et al., *NPG Asia Materials* **6**, e138 (2014).
- [4] C. Vaalma, G. A. Giffin, D. Buchholz, and S. Passerini, *Journal of The Electrochemical Society* **163**, A1295 (2016).
- [5] X. Wang et al., *Nano Letters* **17**, 544 (2017).
- [6] Z. Jian, Y. Liang, I. A. Pérez, Y. Yao, and X. Ji, *Electrochemistry Communications* **71**, 5 (2016).
- [7] Z. Jian, W. Luo, and X. Ji, *Journal of the American Chemical Society* **137**, 11566 (2015).
- [8] W. Luo et al., *Nano Letters* **15**, 7671 (2015).
- [9] K. Share, A. P. Cohn, R. E. Carter, and C. L. Pint, *Nanoscale* **8**, 16435 (2016).
- [10] S. Komaba, T. Hasegawa, M. Dahbi, and K. Kubota, *Electrochemistry Communications* **60**, 172 (2015).
- [11] J. Zhao, X. Zou, Y. Zhu, Y. Xu, and C. Wang, *Advanced Functional Materials* **26**, 8103 (2016).
- [12] S. H. Lee and J. C. Rasaiah, *Journal of Physical Chemistry* **100**, 1420 (1996).
- [13] F. Sagane, T. Abe, Y. Iriyama, and Z. Ogumi, *Journal of Power Sources* **146**, 749 (2005).

- [14] N. Matsuura, K. Umemoto, and Z. Takeuchi, *Bulletin of the Chemical Society of Japan* **47**, 813 (1974).
- [15] A. Eftekhari, Z. Jian, and X. Ji, *ACS Applied Materials and Interfaces* **9**, 4404 (2017).
- [16] S.-T. Myung, Y. Hitoshi, and Y.-K. Sun, *Journal of Materials Chemistry* **21**, 9891 (2011).
- [17] A. k. Covington, *Physical chemistry of organic solvent systems*, Springer Science & Business Media, 2012.
- [18] N. Yabuuchi, K. Kubota, M. Dahbi, and S. Komaba, *Chemical Reviews* **114**, 11636 (2014).
- [19] Q. Liu et al., *RSC Advances* **6**, 88683 (2016).
- [20] M. Dresselhaus and G. Dresselhaus, *Advances in Physics* **30**, 139 (1981).
- [21] Z. Wang, S. M. Selbach, and T. Grande, *RSC Adv.* **4**, 3973 (2014).
- [22] M. Noel and R. Santhanam, *Journal of Power Sources* **72**, 53 (1998).
- [23] G. Schmuelling et al., *Journal of Power Sources* **239**, 563 (2013).
- [24] C. Sole, N. E. Drewett, and L. J. Hardwick, *Faraday Discussions* **172**, 223 (2014).
- [25] S. A. Safran, *Physical Review Letters* **44**, 937 (1980).
- [26] Y. Wu, E. Rahm, and R. Holze, *Journal of Power Sources* **114**, 228 (2003).
- [27] A. Caballero, L. Hernán, and J. Morales, *ChemSusChem* **4**, 658 (2011).
- [28] H. Azuma, H. Imoto, S. Yamada, and K. Sekai, *Journal of Power Sources* **81-82**, 1 (1999).
- [29] V. Etacheri, R. Marom, R. Elazari, G. Salitra, and D. Aurbach, *Energy & Environmental Science* **4**, 3243 (2011).
- [30] Z. Jian, Z. Xing, C. Bommier, Z. Li, and X. Ji, *Advanced Energy Materials* **6**, 1 (2016).
- [31] Z. Ju et al., *ACS Applied Materials and Interfaces* **8**, 20682 (2016).
- [32] J. B. Goodenough, *Journal of Solid State Electrochemistry* **16**, 2019 (2012).
- [33] Q. Wang et al., *Journal of Power Sources* **208**, 210 (2012).
- [34] H. Maleki, G. Deng, A. Anani, and J. Howard, *Journal of The Electrochemical Society* **146**, 3224 (1999).
- [35] A. D. Pasquier, *Journal of The Electrochemical Society* **145**, 472 (1998).
- [36] M. N. Richard and J. Dahn, *Journal of The Electrochemical Society* **146**, 2068 (1999).
- [37] C. Forestier et al., *Journal of Power Sources* **330**, 186 (2016).

- [38] G. Gachot et al., *Electrochimica Acta* **83**, 402 (2012).
- [39] M. N. Richard and J. Dahn, *Journal of The Electrochemical Society* **146**, 2078 (1999).
- [40] H. Yang, H. Bang, K. Amine, and J. Prakash, *Journal of The Electrochemical Society* **152**, A73 (2005).
- [41] O. Haik et al., *Journal of The Electrochemical Society* **158**, A913 (2011).
- [42] J.-i. Yamaki et al., *Journal of Power Sources* **119-121**, 789 (2003).
- [43] J. R. Dahn, E. W. Fuller, M. Obrovac, and U. von Sacken, *Solid State Ionics* **69**, 265 (1994).
- [44] O. S. Mendoza-Hernandez, H. Ishikawa, Y. Nishikawa, Y. Maruyama, and M. Umeda, *Journal of Power Sources* **280**, 499 (2015).
- [45] H. Maleki, G. Deng, I. Kerzhner-Haller, A. Anani, and J. N. Howard, *Journal of The Electrochemical Society* **147**, 4470 (2000).
- [46] E. P. Roth, D. H. Doughty, and J. Franklin, *Journal of Power Sources* **134**, 222 (2004).
- [47] A. Varma, M. Morbidelli, and H. Wu, *Parametric sensitivity in chemical systems*, Cambridge University Press, 2005.
- [48] V. Eshkenazi, E. Peled, L. Burstein, and D. Golodnitsky, *Solid State Ionics* **170**, 83 (2004).
- [49] F. Kong et al., *Journal of Power Sources* **97-98**, 58 (2001).
- [50] G. V. Zhuang and P. N. Ross, *Electrochemical and Solid-State Letters* **6**, A136 (2003).
- [51] L. Seidl, S. Martens, J. Ma, U. Stimming, and O. Schneider, *Nanoscale* **8**, 14004 (2016).
- [52] S. Amiruddin, J. Prakash, H. J. Bang, and K. Amine, *ECS Transactions* **2**, 41 (2007).
- [53] L. El Ouatani et al., *Journal of The Electrochemical Society* **156**, A103 (2009).
- [54] L. Ma, J. Xia, X. Xia, and J. R. Dahn, *Journal of the Electrochemical Society* **161**, A1495 (2014).
- [55] I. A. Profatilova, C. Stock, A. Schmitz, S. Passerini, and M. Winter, *Journal of Power Sources* **222**, 140 (2013).
- [56] G. G. Eshetu et al., *Electrochimica Acta* **102**, 133 (2013).
- [57] M. Nie and B. L. Lucht, *Journal of the Electrochemical Society* **161**, A1001 (2014).
- [58] K. Ui et al., *Journal of Power Sources* **247**, 981 (2014).

- [59] Y. E. Hyung, D. R. Vissers, and K. Amine, *Journal of Power Sources* **119-121**, 383 (2003).
- [60] X. L. Yao et al., *Journal of Power Sources* **144**, 170 (2005).
- [61] S. M. Wood et al., *ACS Energy Letters* **1**, 414 (2016).
- [62] Q. C. Zhuang, J. Li, and L. L. Tian, *J. Power Sources* **222**, 177 (2013).
- [63] M. Moshkovich, Y. Gofer, and D. Aurbach, *Journal of The Electrochemical Society* **148**, E155 (2001).

### 3. FLEXIBLE, BINDER-FREE, N- AND O- RICH CARBON NANOFIBER ANODES FOR LONG CYCLE LIFE K-ION BATTERIES

The original publication of this work appears in ACS Applied Materials and Interfaces, volume 9, issue 21, 17872-17881. Material characterization, electrochemical testing, and data analysis was carried out by Ryan A. Adams and Yunpu Zhao. Carbon nanofiber preparation was carried out by Jia-Min Syu and Chieh-Tsung Lo. Manuscript preparation was performed by Ryan A. Adams.

DOI: 10.1021/acsami.7b02476

#### 3.1 Summary

Carbon nanofibers produced by electrospinning of polyacrylonitrile polymer and subsequent carbonization were tested as freestanding Potassium-ion anodes. The effect of oxygen functionalization on K-ion carbon anode performance was tested for the first time via plasma oxidation of prepared carbon nanofibers. The produced materials exhibited exceptional cycling stability through the amorphous carbon structuring and 1-dimensional architecture accommodating significant material expansion upon K<sup>+</sup> intercalation, resulting in a stable capacity of 170 mAh g<sup>-1</sup> after 1900 cycles at 1C rate for N-rich carbon nanofibers. Excellent rate performance of 110 mAh g<sup>-1</sup> at 10C rate, as compared to 230 mAh g<sup>-1</sup> at C/10 rate, resulted from the pseudo-capacitance storage mechanism and the increased K<sup>+</sup> solid diffusion coefficient in carbon nanofibers as compared to graphite. Plasma oxidation treatment augmented pseudo-capacitive storage of K<sup>+</sup> but increased material charge transfer resistance as compared to N-rich carbon fibers. *Ex-situ* characterization revealed that the 1-dimensional structure was maintained throughout cycling, despite the increase in graphitic interlattice spacing from 0.37 nm to 0.46 nm. The carbon nanofibers demonstrate great potential as an

anode material for Potassium-ion batteries with superior cycling stability and rate capability over previously reported carbon materials.

### 3.2 Introduction

Exploration of alternative metal-ion systems for inexpensive electrochemical energy storage has recently unveiled the potassium-ion battery (KIB), with some significant advantages over its competitor, the sodium-ion battery.[1] For anodes, electrochemical intercalation of  $K^+$  in graphite was recently demonstrated, despite the larger Shannons ionic radius of  $K^+$  (1.38 Å) as compared to  $Na^+$  (1.02 Å) and  $Li^+$  (0.76 Å), and that Na cannot reversibly intercalate without prior graphitic expansion or co-solvent molecules.[2, 3, 4] A three stage transition from  $KC_{24} \Rightarrow KC_{16} \rightarrow KC_8$  for a theoretical capacity of 279 mAh g<sup>-1</sup> results in a volume expansion of 61%, causing significant capacity fade due to electrode pulverization and solid electrolyte interphase (SEI) formation with standard polyvinylidene fluoride binder.[5, 6, 7] Utilization of functionalized binders, e.g. Na carboxymethyl cellulose or Na alginate, and optimized electrolyte solvent system decreased the first cycle capacity loss and improved long-term cycling stability, for a capacity retention of 220 mAh g<sup>-1</sup> after 200 cycles.[2, 8] Despite this optimization, poor performance at high current densities still resulted (120 mAh g<sup>-1</sup> at 100 mA g<sup>-1</sup> and 50 mAh g<sup>-1</sup> at 200 mA g<sup>-1</sup>), due to the poor diffusion kinetics of the bulky  $K^+$  between the graphene layers.[8] Hard and soft carbon micro-particles exhibited improved cycling stability and impressive rate performance, attributed to the increased capacity of low density carbon to expand.[4, 9] The decreased charge density of  $K^+$  results in a higher diffusional coefficient for superior rate capability as compared to  $Na^+$  in hard carbon microspheres.[9] A few potential cathode systems have been demonstrated for KIBs, including Prussian blue/green, amorphous  $FePO_4$  and  $K_{0.3}MnO_2$ . [10, 11, 12, 13, 14, 15]

Nanostructured carbons (fibers, tubes, spheres, sheets) have shown promise as Lithium-ion anode materials due to shorter diffusional distances and  $Li^+$  storage in interfacial regions, resulting in improved specific capacities and rate capabilities over

graphite.[16, 17, 18, 19] In particular, carbon nanofibers are unique due to a binder-free, entwined web morphology, resulting in electrical conducting pathways, material flexibility, and robust structural integrity.[20] Carbon nanofibers can be synthesized by the inexpensive and simple electrospinning process, followed by thermal treatment for carbonization of the polymer precursor.[21] Electrospinning enables tailoring of carbon nanofibers (CNFs), as depending on the polymer solution and processing conditions, properties such as diameter, porosity, electrical conductivity, tensile strength, etc. will change.[21, 22] augmenting oxygen functionalities of CNFs and increasing material capacitance.[23] As anode material, CNFs have exceptional mechanical strength enabling flexible battery applications and binder-free manufacturing for increased active material loading.[24] Extensive electrochemical testing of CNF anodes with Li-ion chemistry has been performed over the past decade, exploring various polymer precursors and processing conditions.[20, 25, 26, 27, 28, 29] Recently, Li et al. synthesized a porous CNF by partial carbonization in air ( $583 \text{ m}^2 \text{ g}^{-1}$  surface area), giving a Li-ion storage capacity of  $1780 \text{ mAh g}^{-1}$  after 40 cycles at  $50 \text{ mA g}^{-1}$ . [30] Wang et al. showed impressive cycling stability for a nitrogen doped CNF (Na-ion anode) prepared from polyamic acid, with  $200 \text{ mAh g}^{-1}$  capacity over 7000 cycles at  $5 \text{ A g}^{-1}$ . [31]

Currently, few studies exist on the application of potassium into nanostructured carbons, such as reduced graphene oxide and F-doped or N-doped graphene.[6, 32, 33] Liu et al. explored sodiation and potassiation of carbon nanofibers via *in-situ* transmission electron microscopy (TEM), finding that disordered carbon expanded 3 times more than crystalline carbon and that cracks developed along their interface.[34] Galvanostatic cycling showed poor cyclability and Coulombic efficiency (84% after 20 cycles) for K-ion anode material as compared to Na-ion, due to fracturing of the disordered/crystalline carbon bilayer structure.[34] In this work, carbon nanofibers are explored in detail as anode material for K-ion batteries. Flexible carbon nanofiber mats are prepared by electrospinning with PAN polymer precursor and subsequent carbonization (Figure A.1). The additional effect of surface functionalization via

plasma oxidation on carbon anodes is studied in terms of material properties and K-ion electrochemical storage mechanisms. Nitrogen doping can enhance electrochemical reactivity and electronic conductivity for carbonaceous materials with Li and Na-ion chemistries.[35, 36] Surface oxygen functionalization of carbons has improved pseudo-capacitance behavior and specific capacity.[37, 38] While some studies on the effect of carbon structuring (amorphous vs. graphitic) for K-ion anodes exist, this is the first study exploring the effect of carbon surface functionalization for K-ion electrochemical performance. As compared to prior carbon materials studied previously as KIB anode, the CNFs show superior cycling stability and Coulombic efficiency over 1900 cycles at a 1C rate, due to the pseudo-capacitive storage mechanism and stable carbon architecture.

### 3.3 Experimental Section

Polyacrylonitrile (PAN) with a molecular weight of  $150,000 \text{ g mol}^{-1}$  (Sigma-Aldrich Co.) was dissolved in N,N-dimethylformamide (DMF, J. T. Baker) for preparing the 7 wt. % precursor solution. Electrospinning was carried out at room temperature with a conventional single nozzle connected to a power supply (You-Shang Technical Corporation). During electrospinning, the precursor solution was extracted from the needle at a flow rate of  $0.7 \text{ mL h}^{-1}$ , controlled by a digital syringe pump (KDS 100, KD Scientific), under a voltage of 15 kV. The electrospun fibers were collected by an aluminum foil, which was placed vertically at a horizontal distance of 15 cm from the needle tip. To convert polymer fibers to carbon fibers, stabilization was conducted by heating the fibers to  $250^\circ\text{C}$  at a heating rate of  $1.8^\circ\text{C min}^{-1}$  in air. After maintaining the fibers at  $250^\circ\text{C}$  for 4 hours, carbonization occurred in nitrogen at  $800^\circ\text{C}$  for 1 hour with a heating rate of  $5^\circ\text{C min}^{-1}$  to produce carbon nanofibers (CNF). Oxygen-plasma treatment was used to modify the carbon nanofiber surface via a PDC-001 plasma cleaner (Harrick Plasma), with a plasma power of 30 W. The carbon fibers were treated for 6 min with an oxygen flow rate of  $50 \text{ mL min}^{-1}$  and resulted in functionalized carbon nanofibers (CNF-O).

The morphology of produced materials was observed by using a Hitachi SU8010 scanning electron microscope (SEM), operated at an accelerating voltage of 10 kV. Samples for SEM analysis were sputter-coated with platinum by using a JEOL JFC-1600 coater for enhancing image capture. Transmission electron microscopy (TEM) was performed with a FEI-Titan microscope operated at 300 kV. Energy-dispersive X-ray spectroscopy (EDS) was performed using an Oxford Instruments X-Max Silicon Drift Detector. X-ray diffraction (XRD) was conducted on carbon fibers using a Rigaku RINT-2000 diffractometer with a filtered  $\text{CuK}\alpha$  radiation source ( $\lambda = 0.154$  nm). The measurements were performed at 40 kV and 40 mA with a scattering angle  $2\theta$  from  $10^\circ$  to  $60^\circ$  at a scan rate of  $4^\circ \text{ min}^{-1}$ . Raman spectroscopy was carried out using a Thermo Fisher Scientific DXR Raman microscope with a laser excitation wavelength of 532 nm. The nitrogen sorption isotherms were measured at 77K (ASAP-2020, Micromeritics). Prior to measurements, carbon fibers were degassed at  $200^\circ\text{C}$  under vacuum. The specific surface area and pore size distribution of carbon fibers were analyzed through the nitrogen sorption isotherms using the Brunauer-Emmett-Teller (BET) and Barrett-Joyner-Halenda (BJH) methods, respectively. X-ray photoelectron spectroscopy (XPS, PHI 5000 VersaProbe) was used to determine the surface functionality of carbon nanofibers before and after oxygen plasma treatment.

Electrodes with 12 mm diameter were punched out from prepared carbon fiber sheets and dried in a vacuum oven overnight prior to assembly, with typical mass loadings of  $1.5 \text{ mg cm}^{-2}$ . Coin-type 2032 half-cells with potassium metal as the counter electrode were constructed in a high-purity glovebox (99.998% Argon) with  $\text{O}_2$  and  $\text{H}_2\text{O}$  concentrations  $<1$  ppm. Whatman glass fiber was used as separator and 0.8 M  $\text{KPF}_6$  (Sigma Aldrich 98%) dissolved in a 1:1 volume ratio of ethylene carbonate (EC, Sigma-Aldrich Anhydrous 99%) and diethyl carbonate (DEC, Sigma-Aldrich anhydrous  $>99\%$ ) was used as electrolyte. Galvanostatic cycling was performed using an Arbin cycler with a voltage range of 0.005 - 3 V and current densities calculated by assuming  $1\text{C} = 279 \text{ mA g}^{-1}$ . A Gamry-600 reference system was utilized to perform po-

tentiostatic electrochemical impedance spectroscopy (EIS), cyclic voltammetry (CV), and Galvanostatic intermittent titration technique (GITT) testing. EIS was taken with a fresh cell from 0.01 Hz to  $10^6$  Hz with an AC voltage of 10 mV at open current voltage (2.5 V). Galvanostatic intermittent titration technique (GITT) was performed for cycled cells at a C/10 current density with a 10-minute charge/discharge time followed by 10-minute rest periods from 0 - 2 V. Graphite electrodes for comparison were prepared by taking a ratio of 80 wt. % active material (artificial graphite MTI), 10 wt. % conductive material (Timcal Super C65), and 10 wt. % polyvinylidene difluoride (PVDF) binder with N-Methyl-2-pyrrolidone (NMP), as solvent. All potentials mentioned are versus  $K^+/K$  unless otherwise stated.

### 3.4 Results and Discussion

Carbon nanofibers were synthesized by the electrospinning process utilizing PAN precursor, with nontreated carbon nanofibers denoted as CNF and plasma oxidized sample denoted as CNF-O, respectively. SEM images of prepared fibers are shown in Figure 3.1a (CNF) and Figure 3.1b (CNF-O). Pristine CNF sample exhibited a network of smooth, bending, and randomly arranged fibers with an average diameter  $324 \text{ nm} \pm 57 \text{ nm}$ . The CNF-O material consisted of a similar morphology of randomly distributed fibers with an average diameter  $290 \text{ nm} \pm 39 \text{ nm}$ . The energetic plasma oxidation process partially etched away the surface carbon layer through ion bombardment, removing surface atoms and increasing surface roughness, as previously observed.[39, 40] Further investigation of surface and internal morphology was carried out through TEM imaging as shown in Figure 3.1c (CNF) and Figure 3.1d (CNF-O). Both samples display similar internal amorphous carbon structuring, indicating that plasma oxidation only impacts the surface functionality.

Further structural analysis was carried out through XRD characterization, shown in Figure 3.2a. Broad peaks centered at a  $2\theta$  value of  $24^\circ$  appear for both materials, corresponding to the (002) Miller plane. This peak represents the graphitic layering within the fibers, while the low intensity for the (100) peak signifies a lack of individ-

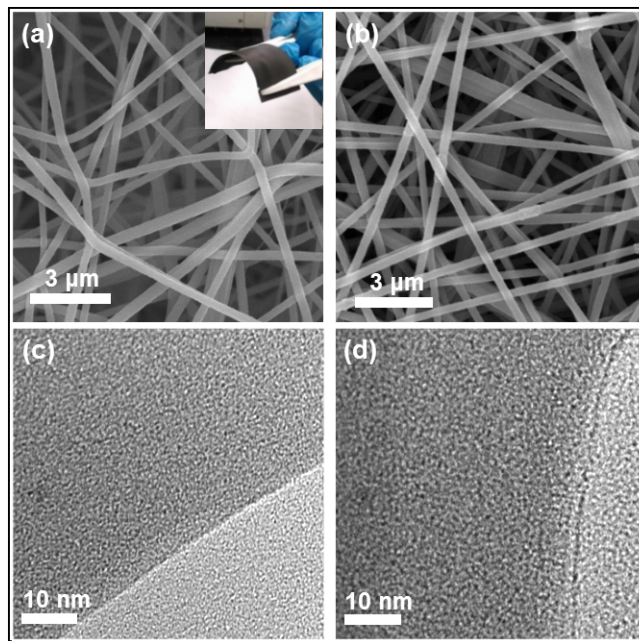


Figure 3.1. (a) SEM image of prepared electrospun CNF after carbonization at 800°C. Inset: Flexible CNF mat. (b) SEM image of electrospun CNF post oxygen plasma treatment (CNF-O). (c) TEM image of CNF. (d) TEM image of CNF-O.

ual graphene sheets.[41] Calculation via Braggs Law results in an average interlattice spacing of 0.37 nm for both materials, compared to 0.335 nm of bulk graphite.[41] Raman spectroscopy analysis is shown in Figure 3.2b, with the corresponding peaks labeled for graphitic (G) ordering at  $1580\text{ cm}^{-1}$  and disordered (D) ordering at  $1350\text{ cm}^{-1}$ . [42] The D band represents defect structuring such as carbon plane edges, correlating to  $\text{sp}^3$  carbon, while the G band is associated with  $\text{sp}^2$  carbon and in-plane structuring.[42] Similar intensity ratios for the peaks,  $I_D/I_G$ , are calculated for both samples, with ratios of 1.31 (CNF) and 1.34 (CNF-O) signifying substantial disorder in the fibers. The carbonization of electrospun PAN results in three stages, stabilization (200-300°C), carbonization (1000°C), and graphitization (1500-3000°C).[43] The stabilization step involves stretching and simultaneous oxidation of PAN into a non-plastic cyclic by conversion of nitrile groups (CN) into double bonds (C=N).[43]

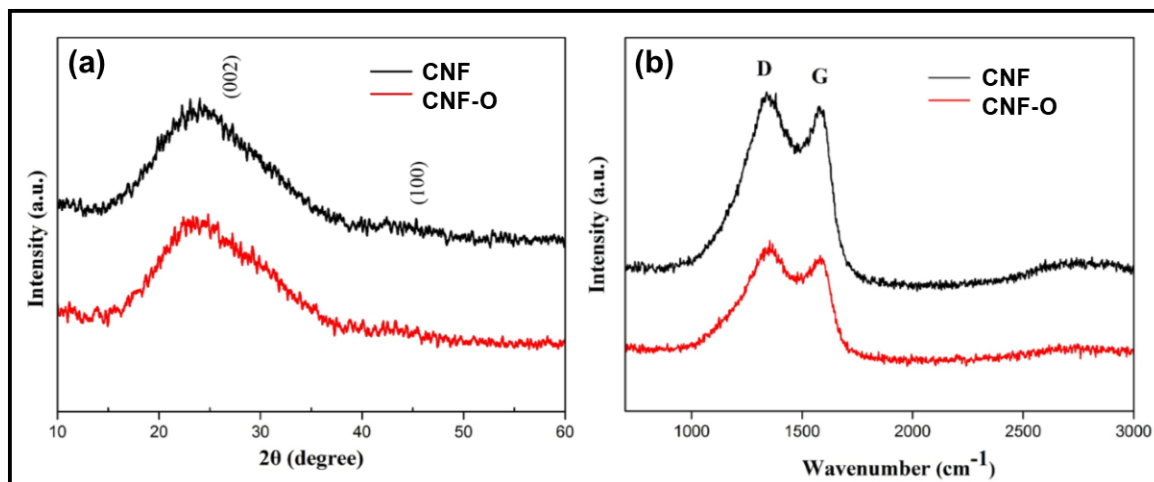


Figure 3.2. (a) XRD pattern for CNF samples with graphitic Miller indices indicated. (b) Raman spectroscopy for CNF samples with disordered and graphitic peaks labeled.

Table 3.1.  
Elemental composition of CNF samples via XPS analysis.

Element	CNF	CNF-O
C	85.8	79.5
O	4.2	12.8
N	10.0	7.8

The carbonization at 800°C in nitrogen results in the turbostratic structure evident in the CNF material and correlates to XRD and Raman results.[44]

XPS analysis was utilized to quantitatively determine the effect of plasma oxidation on the fibers, with the elemental compositions described in Table 3.1. Application of oxygen plasma treatment increased the oxygen content (3.2% to 12.8%), at the cost of carbon (85.8% to 79.5%) and nitrogen (10.0% to 7.8%). The C-C and C=C bonds are broken by free radicals and form carbonyl groups and some carboxyl groups after extended exposure.[45] Length of exposure increases the surface area, and oxygen

Table 3.2.  
Material properties and porosity for CNF samples.

Sample	Surface Area ( $\text{m}^2 \text{g}^{-1}$ )	Pore Volume ( $\text{cm}^3 \text{g}^{-1}$ )	Pore Volume (1.7 - 300 nm) ( $\text{cm}^3 \text{g}^{-1}$ )	Average ad- sorption pore width (nm)
CNF	139	0.087	0.054	3.4
CNF-O	153	0.087	0.048	3.1

content of the carbon nanofibers, but does cause fractures and loss of nitrogen.[23] Nitrogen adsorption-desorption isotherms were performed on each material at 77K to determine the surface structural properties (Figure A.2). These profiles indicate reversible Type II isotherms, corresponding to a nonporous adsorbent, with the first increase at low  $P/P_0$  related to monolayer completion and the increase at high  $P/P_0$  caused by multi-layer adsorption.[46] Resulting BET and BJH calculations of surface area and pore distribution are summarized in Table 3.2. Plasma oxygen treatment increased surface area from  $139 \text{ m}^2 \text{ g}^{-1}$  to  $153 \text{ m}^2 \text{ g}^{-1}$ , primarily through the creation of local surface pores and irregularities. Similar total pore volumes of  $0.087 \text{ cm}^3 \text{ g}^{-1}$  were obtained for both samples, with 60% of the porosity obtained in the 1.7 - 300 nm range.

The synthesized CNF and CNF-O were tested as anode in half cells against potassium metal. Differential capacity-versus-voltage ( $dQ/dV$ ) curves for the first five cycles at C/10 rate are shown in Figure 3.3a (CNF) and Figure 3.3b (CNF-O), to determine the K-ion storage mechanism. For the first discharge cycle of each material, peaks beginning at 1.4 V (CNF) and 1.3 V (CNF-O) represent initial solid electrolyte interface (SEI) formation, caused by reduction of the unstable electrolyte at the anode surface. A sharper peak for CNF-O possibly resulted from irreversible bonding of  $\text{K}^+$  to surface oxygen functionalities and increased SEI formation from higher surface area. Intercalation of  $\text{K}^+$  into the carbon nanofibers begins at 0.4

V for both, with several reduction peaks correlated to graphite staging mechanisms or SEI formation. After the first cycle, similar broad profiles indicate  $K^+$  storage occurring through pseudo-capacitance, as previously observed in carbon nanofibers anodes.[23] Pseudo-capacitance results from reversible faradaic reactions at the surface, but  $K^+$  storage in disordered interfacial regions can contribute as well.[47, 48] The charge profile stabilizes after the second cycle with oxidation peaks at 0.3 V and 0.7 V, but the discharge profile for both materials does not completely stabilize by cycle 5, possibly due to volumetric changes during potassiation and carbon restructuring. *Ex-situ* XRD analysis in Figure A.3 demonstrated the (002) Miller peak shift to  $19.5^\circ$  (CNF) and  $19.3^\circ$  (CNF-O) in the first discharge (0.005 V), and shift back to  $19.7^\circ$  and  $19.6^\circ$  after charging (3.0 V). Due to the low-density carbon and lack of graphitic ordering, the average interlattice spacing expands to 0.46 nm, with little contraction upon depotassiation. Charge and discharge voltage profiles for the formation cycles are shown in Figure 3.3c (CNF) and Figure 3.3d (CNF-O), with both showing characteristic sloping of amorphous carbon anodes. First cycle efficiencies of 41% (CNF) and 35% (CNF-O) resulted, with losses due to SEI formation and CNF-O exhibiting additional losses possibly due to surface oxygen reactivity or the increased surface area. However, CNF-O has increased Coulombic efficiencies for the second cycle (CNF: 70%, CNF-O: 76%) and fifth cycle (CNF: 80%, CNF-O: 86%).  $K_2CO_3$  has been shown to form effective SEI layers in Li-ion systems, and the oxygen functionalities of CNF-O could similarly result in an optimal SEI layer as compared to CNF.[49, 50]

Long term galvanostatic cycling performance was evaluated at 1C rate for the CNF (Figure 3.4a) and CNF-O (Figure 3.4b) materials. Exceptionally stable capacity was demonstrated by both, with a specific capacity of  $170 \text{ mAh g}^{-1}$  after 1900 cycles (CNF), and  $160 \text{ mAh g}^{-1}$  (CNF-O) after 300 cycles at 1C rate. By cycle number 100, the Coulombic efficiency was 97.5% (CNF) and 99.5% (CNF-O), showing superior SEI stabilization of the CNF-O material. It is worth noting that graphite electrodes with PVDF binder had an initial irreversibly capacity loss of 41%, and

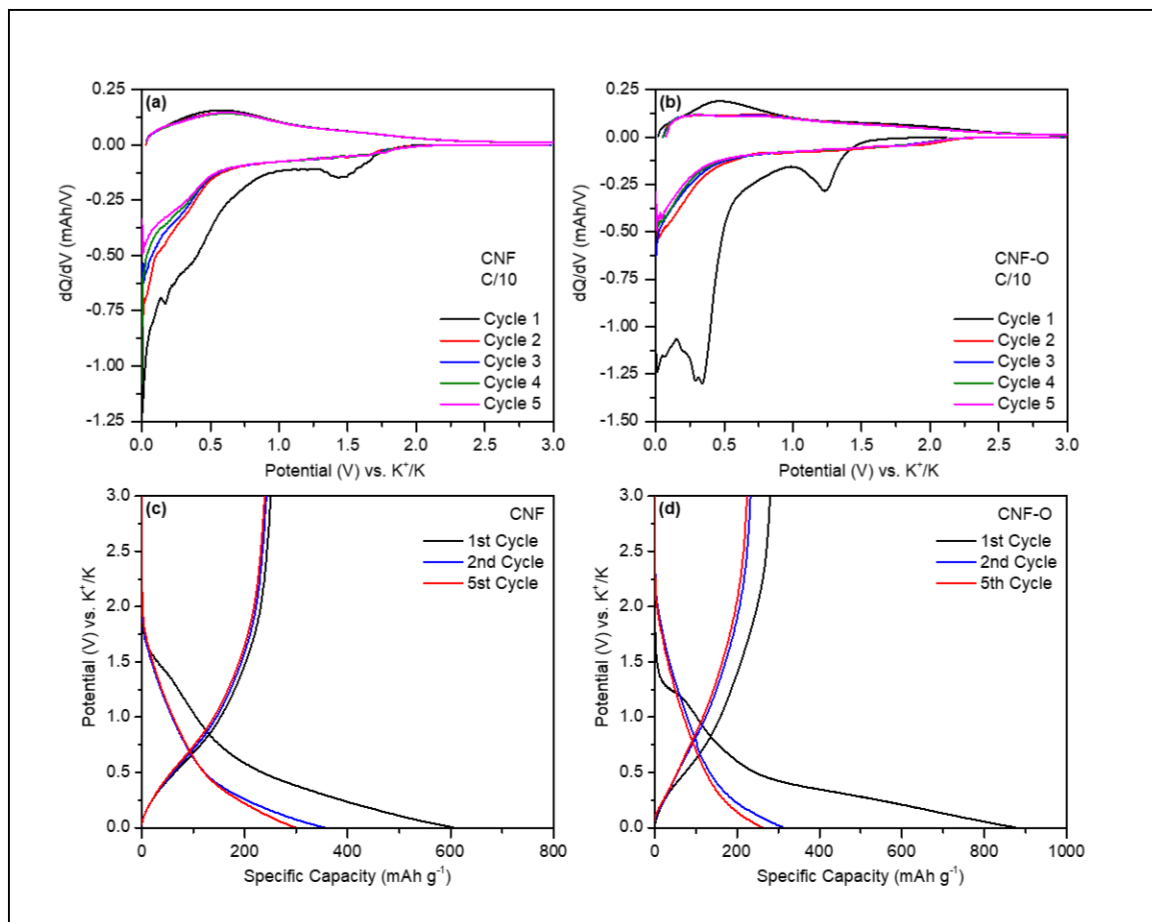


Figure 3.3. (a) & (b) Differential capacity curves for the first five cycles of CNF (a) and CNF-O (b) at C/10 rate (current density =  $27.9 \text{ mA g}^{-1}$ ). (c) & (d) Charge-discharge curves for the first, second, and fifth cycle of the CNF (c) and CNF-O (d) samples at C/10 rate.

functionalized binders mitigated this by a pre-formed SEI effect.[7] The freestanding carbon nanofibers tested contained no binder, so inefficiencies may be characteristic of the K-ion chemistry and the 1C current density rather than the material itself. The carbon nanofibers showed remarkable rate capability, with galvanostatic cycling at various current densities (C/10 to 10C) shown in Figure 3.4c (CNF) and Figure 3.4d (CNF-O). Both materials showed poor initial Coulombic efficiencies that improved with the current density, possibly due to pseudo-capacitance storage at high

current densities causing less structural changes than intercalation. At C/10, stable charge capacities of 220 mAh g<sup>-1</sup> resulted for both materials, due to the similar carbon morphology and structuring. Capacities of 110 mAh g<sup>-1</sup> (CNF) and 70 mAh g<sup>-1</sup> (CNF-O) were achieved at 10C rate, with the pristine CNF showing superior stability. Charge-discharge profiles at C/10, 1C, 5C, and 10C rates are shown in Figure 3.4e (CNF) and Figure 3.4f (CNF-O). While they exhibit similar sloping behavior, the CNF-O sample shows considerable hysteresis as compared to the CNF sample at 10C rate. Ohmic losses from resistance appear to dramatically increase above 1C, despite the natural conductivity of carbon nanofibers.

Electrochemical impedance spectroscopy (EIS) for the carbon nanofiber samples in fresh cells at the OCV potential are shown in Figure 3.5a. The plots consisted of a depressed semicircle in the high-medium frequency region and a linear Warburg impedance in the high frequency region.[51] The semicircle resulted from charge transfer resistance, since SEI had not formed yet on the material (circuit model shown in inset). Notably, the CNF-O material had increased resistance over the CNF material, likely due to the decreased nitrogen content and increased oxygen content. Nitrogen has been shown to increase conductivity of amorphous carbons, and this could explain the noticeable hysteresis difference at 10C rate.[35] EIS was also taken at 1 V and 0.1 V for both samples (Figure A.4), where SEI formation results in an additional semicircle. The CNF and CNF-O materials have similar profiles, indicating that SEI layer dominates the total material resistance at those voltages, but CNF shows less overall resistance.

Galvanostatic intermittent titration technique (GITT) for the materials was performed for CNF, CNF-O, and graphite with profiles shown in Figure A.5. The diffusion coefficient of K<sup>+</sup> in these materials was determined by Fick's second law (when cell voltage is linearly proportional to t<sup>1/2</sup>) and the corresponding equation:

$$D = \frac{4}{\pi\tau} \left( \frac{m_b}{\rho S} \right)^2 \left( \frac{\Delta E_s}{\Delta E_t} \right)^2 \quad (3.1)$$

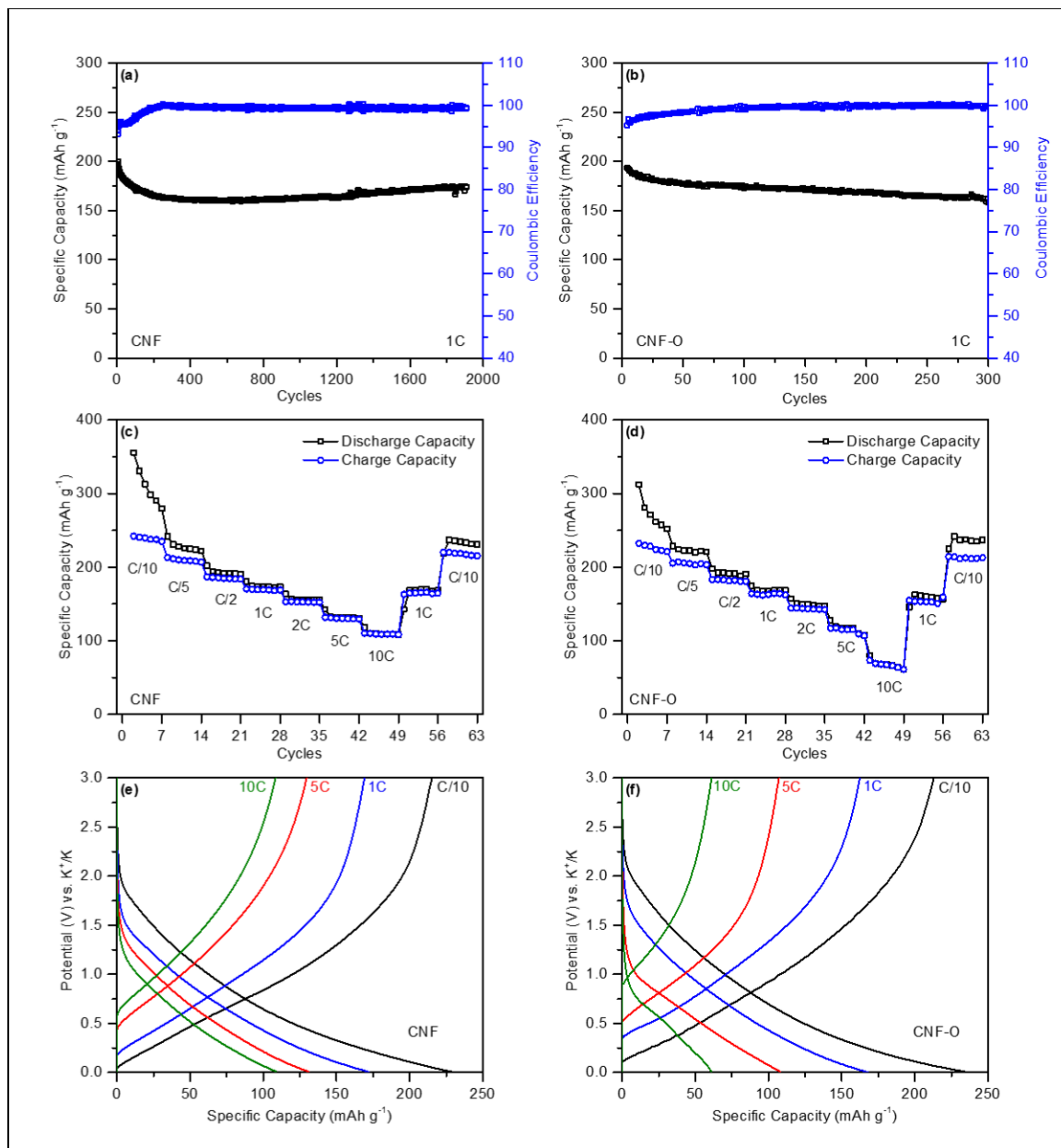


Figure 3.4. (a) & (b) Cycling performance of CNF (a) and CNF-O (b) at 1C current density. (c) & (d) Cycling performance of CNF (c) and CNF-O (d) at various rates. (e) & (f) Charge-discharge curves of CNF (e) and CNF-O (f) for stable performance at various rates. 1C = 279 mA g<sup>-1</sup>.

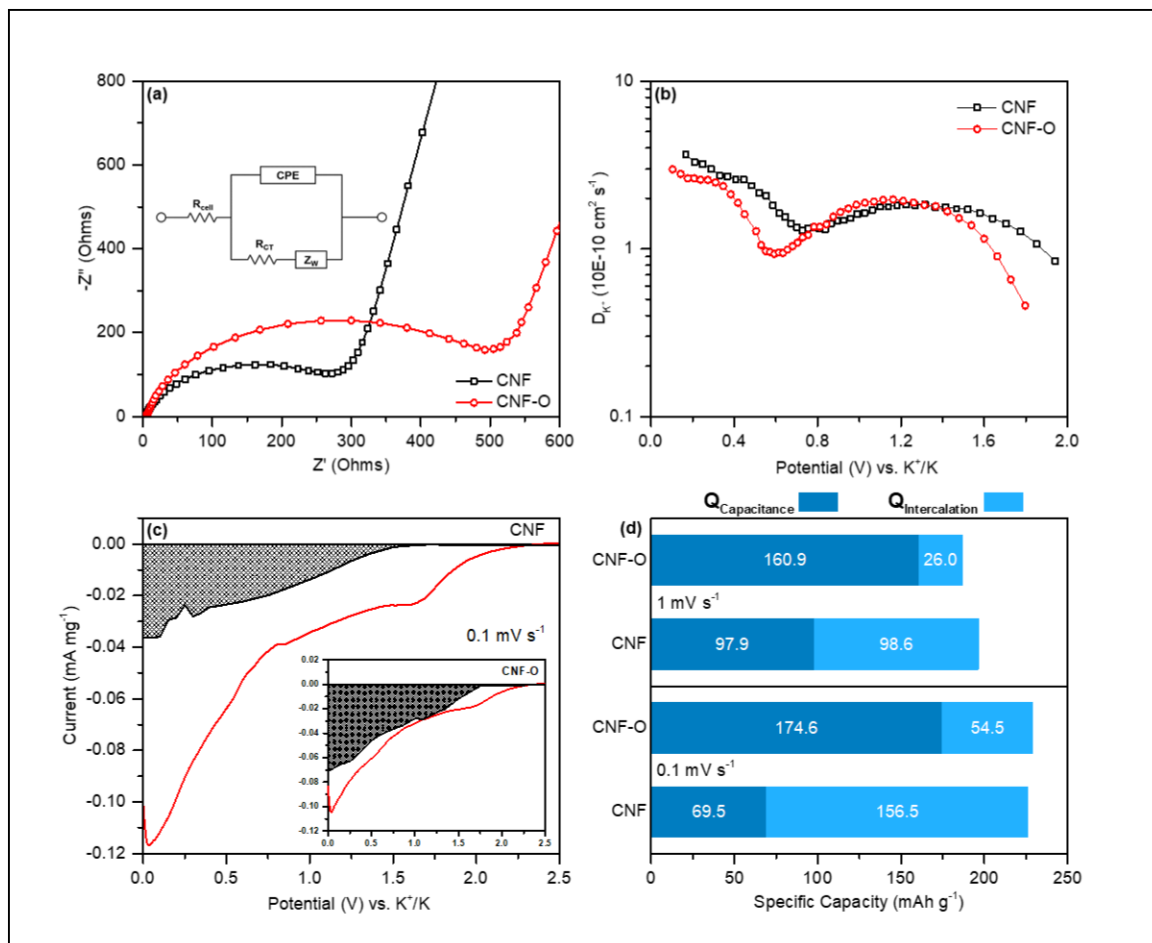


Figure 3.5. Electrochemical characterization of CNF and CNF-O materials. (a) Electrochemical impedance spectroscopy for fresh cells at OCV (2.5 V vs.  $K/K^+$ ). (b) Diffusional coefficient of  $K^+$  in the carbon nanofiber materials, calculated by GITT. (c) Cyclic voltammetry ( $0.1 \text{ mV s}^{-1}$ ) for conditioned cells for CNF and CNF-O (inset), with red line showing total current. Charge storage contribution from pseudocapacitance shown by shaded region. (d) Comparison of charge storage mechanism from intercalation and capacitance contributions for CNF and CNF-O at  $0.1$  and  $1 \text{ mV s}^{-1}$  scan rates.

where  $\tau$  is the pulse length;  $m_b$  is the electrode active mass;  $\rho$  is the material density;  $S$  is the geometric area of the electrode;  $\Delta E_s$  is the steady-state voltage change due to the pulse; and  $\Delta E_t$  is the voltage change during the constant current

pulse. The carbon nanofiber materials showed similar diffusion coefficients in the range of  $10^{-8}$ - $10^{-7}$   $\text{cm}^2 \text{s}^{-1}$ , with CNF-O having increased diffusivity through the 0.6-1.6 V range (Figure 3.5b). This likely resulted from the increased surface area and porosity, meaning significant Ohmic losses from decreased conductivity caused the CNF-O material to perform worse at high current densities. In comparison, graphite for  $\text{K}^+$  shows a diffusion constant  $\sim 10^{-9}$   $\text{cm}^2 \text{s}^{-1}$ , due to ionic diffusivity limitations from the 2D intercalation mechanism (Figure A.6). With both samples displaying a pseudo-capacitance mechanism and similar  $\text{K}^+$  diffusional coefficients, the rate limitations for CNF-O likely derive from Ohmic resistance losses as indicated by EIS, indicating the advantages of nitrogen doping.

To further understand the impact of pseudo-capacitive storage, cyclic voltammetry studies were performed on CNF and CNF-O materials in a wide range of scan rates from 0.1  $\text{mV s}^{-1}$  to 500  $\text{mV s}^{-1}$  (Figure A.7). These curves can be modeled by a power law type equation:  $i = av^b$ , where  $v$  is the scan rate, and  $a$  and  $b$  are adjustable parameters.[47] The parameter  $b$  can be determined by the slope of  $\log(i)$  vs.  $\log(v)$ , as shown in Figure A.8. A value of  $b = 0.5$  correlates to ideal diffusion-controlled faradaic processes (intercalation) per Cottrells equation, and a value of  $b = 1.0$  relates to capacitance type behavior, i.e. pseudo-capacitance  $\text{K}^+$  storage.[52, 53] The CNF-O anode has higher  $b$  values throughout the voltage range (Figure A.9), indicating increased pseudo-capacitance storage as compared to CNF. The total current extracted can be divided into its two main contributions by the following equation:

$$i(V) = a_1v + a_2v^{1/2} \quad (3.2)$$

with  $a_1$  and  $a_2$  as adjustable parameters for pseudo-capacitance and intercalation processes respectively. By plotting  $v^{1/2}$  vs.  $i(V)/v^{1/2}$  (Figure A.8),  $a_1$  and  $a_2$  can be determined by the slope and y-intercept respectively. Figure 3.5c shows the current contribution as a function of voltage for CNF and CNF-O (inset) at 0.1  $\text{mV s}^{-1}$  scan rate, where the shaded portion is pseudo-capacitance charge storage. Figure 3.5d

summarizes the results at 0.1 and 1.0 mV s<sup>-1</sup> (Figure A.10), where oxygen functionalization at the surface increased pseudo-capacitance behavior as previously observed for carbon anodes.[37, 38] Both materials show an increasing percentage of pseudo-capacitance as the scan rate increases, explaining the exceptional rate capabilities of these materials.

To explain the superior cycling stability, *ex-situ* analysis of cycled CNF was performed to observe structural and morphological changes after 100 cycles at 1C rate. A SEM image of the post cycled CNF sample is shown in Figure 3.6a, where some nanofibers have large agglomerates on them. EDS analysis (C, P, K) in Figure 3.6b-e showed that the globules correlated to phosphorus signal, possibly due to KPF<sub>6</sub> electrolyte breakdown. While SEI formed across all the material (uniform K signal), the globules likely formed at the intersection of several fibers, where increased current density could result in continuous SEI formation. Overall though, the morphology is well preserved, explaining how 1900 cycles can be achieved with minimal loss in capacity. Liu *et al.* noted that the *in-situ* TEM study of potassiation of carbon nanofibers showed internal fracturing at the crystalline/disordered carbon interface, while the electrospun CNF did not due to its uniform amorphous nature.[34] *Ex-situ* XRD was performed for fully potassiated and depotassiated CNF as shown in Figure 3.6f. The degree of potassiation has little effect, with the (002) Miller peak at 19.4° for potassiated CNF and 19.7° for depotassiated CNF, resulting in an average interlattice spacing of 0.46 nm (0.37 nm for pristine CNF). Significant expansion took place during the first discharge (Figure A.3) that is largely irreversible, with the degree of potassiation causing little change in the XRD spectra, likely due to how much of the K<sup>+</sup> charge storage occurs via pseudo-capacitance. *Ex-situ* Raman spectroscopy for potassiated and depotassiated CNF materials are shown in Figure 3.6g. After cycling, the I<sub>D</sub>/I<sub>G</sub> peak ratios increased to 1.44 for both cases, confirming that the carbon structure expands significantly upon potassiation, but that there is little change after the initial discharge.

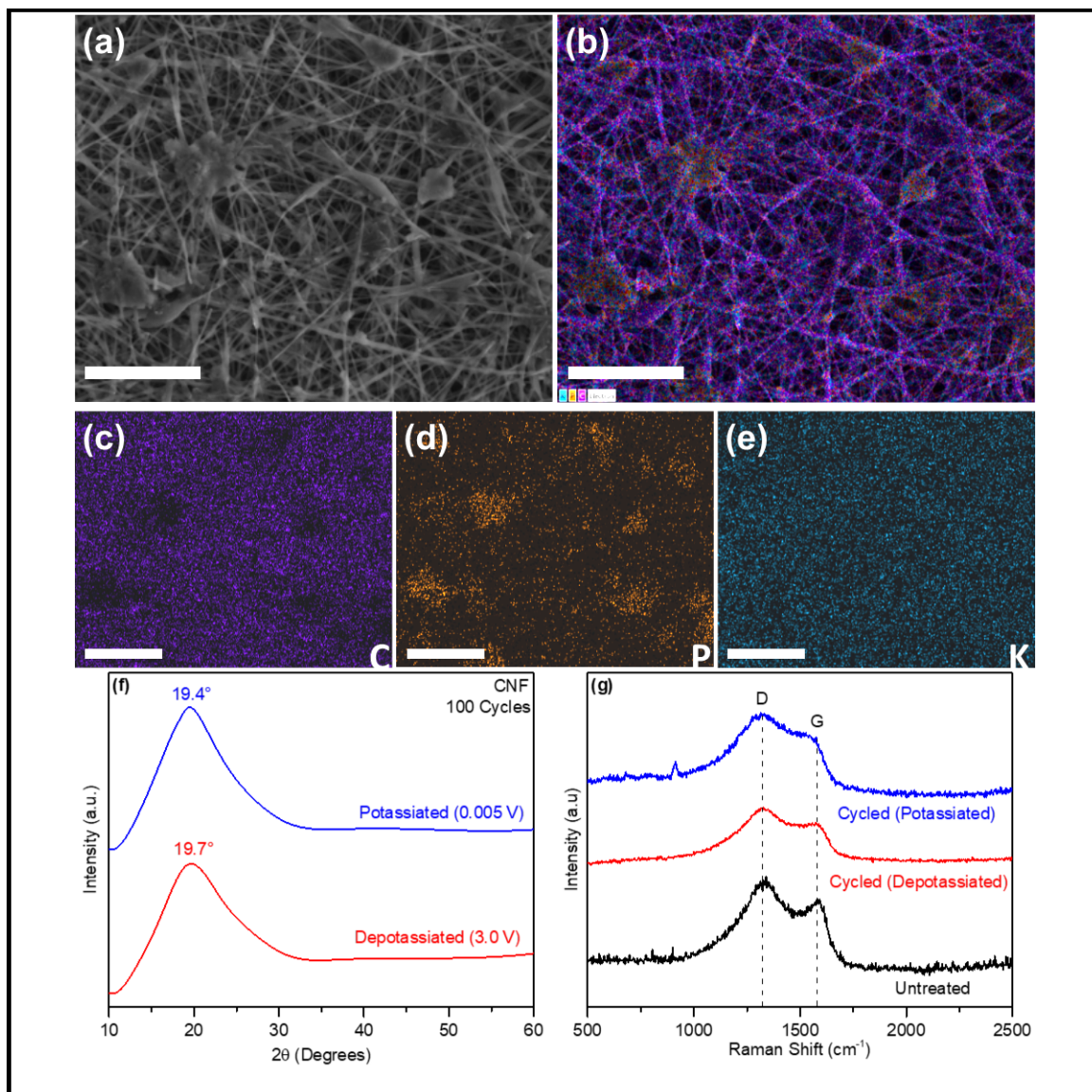


Figure 3.6. *Ex-situ* material characterization of CNF after 100 cycles at 1C rate (a) SEM image. (b) EDS analysis with (c) carbon, (d) phosphorous, and (e) potassium, shown in purple, orange, and blue respectively. The scale bar for all images is 10  $\mu\text{m}$ . (f) Post-cycling XRD patterns. (g) Post-cycling Raman spectra.

As compared to performance of previous K-ion anodes, this material improves upon two facets: poor long-term cyclability and rate performance. The ability of

the CNF material to accommodate the volumetric changes of potassiation and the pseudo-capacitive storage mechanism enables stable capacity through 1900 cycles at 1C rate. While air activation does augment the pseudo-capacitive storage of CNF-O, lessened intercalation storage from the decreased carbon content results in similar total electrochemical performance for both samples. Previously, air activation of Li-ion carbon anode materials has improved capacity and rate capability, through pseudo-capacitance via Faradaic redox reactions at the surface functionalities, and some similar benefits are seen in the K-ion system.[54] The CNF-O materials showed additional first cycle losses, but the improved SEI, possibly from  $K_2CO_3$  formation, did improve Coulombic efficiencies through the rest of formation cycles. Future work could involve a composite of these carbon nanofiber materials with Sn nanoparticles to further increase capacity, as reversibly alloying of Sn with  $K^+$  has already been demonstrated, utilizing the stable architecture for improved cyclability.[55]

### 3.5 Conclusions

In this work, we demonstrated that electrospun carbon nanofibers perform as exceptional binder-free and flexible anode materials for K-ion batteries. To investigate the effects of elemental composition and surface functionalization, two materials were tested: nitrogen-doped pristine carbon nanofibers (CNF) and plasma oxidized carbon nanofibers (CNF-O). XRD and Raman spectroscopy revealed analogous bulk carbon amorphous structuring and interlattice spacing for both materials, but the etching plasma oxidation process decreased the fiber diameter and increased oxygen composition from 4.2% to 12.8% by surface oxygen functionalities. When the CNF material was cycled against K metal, a sloping voltage profile resulted, exhibiting excellent cycling stability for a capacity of  $170 \text{ mAh g}^{-1}$  at 1C rate after 1900 cycles. Excellent rate performance resulted as well, with capacities of  $110 \text{ mAh g}^{-1}$  at 10C rate and  $230 \text{ mAh g}^{-1}$  at C/10 rate respectively. Electrochemical characterization showed that while oxygen functionalization did not significantly increase the specific capacity, pseudo-capacitive type storage did increase, albeit with increased mate-

rial resistance as compared to nitrogen doped CNF. *Ex-situ* analysis after 100 cycles showed that CNF fiber structure was maintained, despite the generation of SEI globules. Interlattice (002) expansion from 0.37 nm to 0.46 nm after the first potassiation shifted little during later cycles, due to the lower carbon density and nanofiber morphology, preventing mechanical pulverization and SEI buildup/capacity fade. This study demonstrates how material engineering of carbon can address some of the issues resulting from bulkier  $K^+$  intercalation, and may elucidate possible strategies to improve performance of K-ion batteries in the future.

### 3.6 Acknowledgements

V.P. thanks Purdue University and its School of Chemical Engineering for the generous start-up funding. Electron microscopy studies at Birck Nanotechnology Center were funded by a Kirk exploratory research grant. Thermo Scientific is thanked for DXR Raman microscope studies. The Slayter Discretionary Fund was used to purchase chemical and laboratory supplies. Arthur Dysart is thanked for assistance with scanning electron microscopy studies.

### 3.7 References

- [1] A. Eftekhari, Z. Jian, and X. Ji, *ACS Applied Materials and Interfaces* **9**, 4404 (2017).
- [2] N. Yabuuchi, K. Kubota, M. Dahbi, and S. Komaba, *Chemical Reviews* **114**, 11636 (2014).
- [3] Y. Wen et al., *Nature Communications* **5**, 4033 (2014).
- [4] Z. Jian, W. Luo, and X. Ji, *Journal of the American Chemical Society* **137**, 11566 (2015).
- [5] Z. Xu et al., *Carbon* **107**, 885 (2016).
- [6] W. Luo et al., *Nano Letters* **15**, 7671 (2015).
- [7] S. Komaba, T. Hasegawa, M. Dahbi, and K. Kubota, *Electrochemistry Communications* **60**, 172 (2015).
- [8] J. Zhao, X. Zou, Y. Zhu, Y. Xu, and C. Wang, *Advanced Functional Materials* **26**, 8103 (2016).

- [9] Z. Jian, Z. Xing, C. Bommier, Z. Li, and X. Ji, *Advanced Energy Materials* **6**, 1 (2016).
- [10] A. Eftekhari, *Journal of Power Sources* **126**, 221 (2004).
- [11] P. Padigi et al., *Electrochimica Acta* **166**, 32 (2015).
- [12] V. Mathew et al., *NPG Asia Materials* **6**, e138 (2014).
- [13] C. Vaalma, G. A. Giffin, D. Buchholz, and S. Passerini, *Journal of The Electrochemical Society* **163**, A1295 (2016).
- [14] X. Wang et al., *Nano Letters* **17**, 544 (2017).
- [15] Z. Jian, Y. Liang, I. A. Pérez, Y. Yao, and X. Ji, *Electrochemistry Communications* **71**, 5 (2016).
- [16] P. G. Bruce, B. Scrosati, and J. M. Tarascon, *Angewandte Chemie - International Edition* **47**, 2930 (2008).
- [17] P. Lian et al., *Electrochimica Acta* **55**, 3909 (2010).
- [18] V. G. Pol and M. M. Thackeray, *Energy and Environmental Science* **4**, 1904 (2011).
- [19] C. De Las Casas and W. Li, *Journal of Power Sources* **208**, 74 (2012).
- [20] C. Kim et al., *Advanced Functional Materials* **16**, 2393 (2006).
- [21] M. Inagaki, Y. Yang, and F. Kang, *Advanced Materials* **24**, 2547 (2012).
- [22] Z. M. Huang, Y. Z. Zhang, M. Kotaki, and S. Ramakrishna, *Composites Science and Technology* **63**, 2223 (2003).
- [23] C.-C. Lai and C.-T. Lo, *RSC Adv.* **5**, 38868 (2015).
- [24] X. Li et al., *Electrochemistry Communications* **49**, 51 (2014).
- [25] A. K. Shukla and T. Prem Kumar, *Current Science* **94**, 314 (2008).
- [26] L. Ji et al., *Journal of Power Sources* **195**, 2050 (2010).
- [27] L. Qie et al., *Advanced Materials* **24**, 2047 (2012).
- [28] Y.-T. Peng and C.-T. Lo, *Journal of Solid State Electrochemistry* **19**, 3401 (2015).
- [29] B. Zhang, F. Kang, J. M. Tarascon, and J. K. Kim, *Progress in Materials Science* **76**, 319 (2016).
- [30] W. Li, M. Li, M. Wang, L. Zeng, and Y. Yu, *Nano Energy* **13**, 693 (2015).
- [31] S. Wang et al., *Advanced Energy Materials* **6**, 1502217 (2016).
- [32] Z. Ju et al., *ACS Applied Materials and Interfaces* **8**, 20682 (2016).
- [33] K. Share, A. P. Cohn, R. E. Carter, and C. L. Pint, *Nanoscale* **8**, 16435 (2016).

- [34] Y. Liu et al., *Nano Letters* **14**, 3445 (2014).
- [35] L. G. Bulusheva et al., *Carbon* **49**, 4013 (2011).
- [36] L. Wang, Z. Schnepf, and M. M. Titirici, *Journal of Materials Chemistry A* **1**, 5269 (2013).
- [37] T. Bhardwaj, A. Antic, B. Pavan, V. Barone, and B. D. Fahlman, *Journal of the American Chemical Society* **132**, 12556 (2010).
- [38] Y. Shao et al., *Nano Letters* **13**, 3909 (2013).
- [39] L. Y. Yuan, C. S. Chen, S. S. Shyu, and J. Y. Lai, *Composites Science and Technology* **45**, 1 (1992).
- [40] M. A. Montes-Morán, A. Martínez-Alonso, J. M. Tascón, and R. J. Young, *Composites Part A: Applied Science and Manufacturing* **32**, 361 (2001).
- [41] Z. Q. Li, C. J. Lu, Z. P. Xia, Y. Zhou, and Z. Luo, *Carbon* **45**, 1686 (2007).
- [42] A. Ferrari and J. Robertson, *Physical Review B - Condensed Matter and Materials Physics* **61**, 14095 (2000).
- [43] M. S. A. Rahaman, A. F. Ismail, and A. Mustafa, *Polymer Degradation and Stability* **92**, 1421 (2007).
- [44] V. G. Pol et al., *Electrochimica Acta* **127**, 61 (2014).
- [45] X. Zhang, Y. Huang, T. Wang, and L. Liu, *Composites Part A: Applied Science and Manufacturing* **38**, 936 (2007).
- [46] M. Thommes et al., *Pure and Applied Chemistry* **87**, 1051 (2015).
- [47] J. Wang, J. Polleux, J. Lim, and B. Dunn, *The Journal of Physical Chemistry C* **111**, 14925 (2007).
- [48] V. Augustyn et al., *Nature Materials* **12**, 518 (2013).
- [49] Q. C. Zhuang, J. Li, and L. L. Tian, *J. Power Sources* **222**, 177 (2013).
- [50] S. M. Wood et al., *ACS Energy Letters* **1**, 414 (2016).
- [51] M. Umeda et al., *Electrochimica Acta* **47**, 885 (2001).
- [52] M. Sathiya, A. S. Prakash, K. Ramesha, J. M. Tarascon, and A. K. Shukla, *Journal of the American Chemical Society* **133**, 16291 (2011).
- [53] L. Fu et al., *Nanoscale* **6**, 1384 (2014).
- [54] E. Frackowiak and F. Béguin, *Carbon* **39**, 937 (2001).
- [55] I. Sultana, T. Ramireddy, M. M. Rahman, Y. Chen, and A. M. Glushenkov, *Chem. Commun.* **52**, 9279 (2016).

## 4. MECHANISTIC ELUCIDATION OF THERMAL RUNAWAY IN POTASSIUM-ION BATTERIES

The original publication of this work appears in Journal of Power Sources, volume 375, 131-137. Material characterization, electrochemical testing, data analysis, and manuscript preparation was carried out by Ryan A. Adams.

DOI: 10.1016/j.jpowsour.2017.11.065

### 4.1 Summary

For the first time, thermal runaway of charged graphite anodes for K-ion batteries is investigated, using differential scanning calorimetry (DSC) to probe the exothermic degradation reactions. Investigated parameters such as state of charge, cycle number, surface area, and binder demonstrate strong influences on the DSC profiles. Thermal runaway initiates at 100°C owing to  $K_xC_8$  - electrolyte reactions, but the K-ion graphite anode evolves significantly less heat as compared to the analogous Li-ion system (395 J g<sup>-1</sup> vs. 1048 J g<sup>-1</sup>). The large volumetric expansion of graphite during potassiation cracks the SEI layer, enabling contact and reaction of  $KC_8$  - electrolyte, which diminishes with cycle number due to continuous SEI growth. High surface area graphite decreases the total heat generation, owing to thermal stability of the K-ion SEI layer. These findings illustrate the dynamic nature of K-ion thermal runaway and its many contrasts with the Li-ion graphite system, permitting possible engineering solutions for safer batteries.

### 4.2 Introduction

Safety remains a primary concern of lithium ion batteries (LIBs) despite more than two decades of commercialization and widespread usage.[1, 2] Thermal runaway

can initiate from exothermic breakdown of the SEI layer on carbon anodes, which starts typically at 120°C.[3, 4, 5] Heat generation from electrolyte breakdown and reaction with lithiated carbon leads to cathode decomposition and release of oxygen, increasing system pressure and reactivity.[6, 7, 8] By 200°C, total exothermic heat generation of 2 kJ g<sup>-1</sup> electrode material occurs, resulting in intense explosions and flames.[9] Evolution of CO<sub>2</sub>, O<sub>2</sub>, H<sub>2</sub>, POF<sub>3</sub>, and HF from decomposition reactions of electrolyte, salt, polymer binder, and electrodes contributes to increased heat and pressure, accelerating the process.[10] As the initiating process for thermal runaway of LIBs, the degradation reactions of SEI breakdown are of great interest to understand and mitigate.[11] Factors including state of charge (SOC), electrolyte composition, binder, and carbon material properties significantly impact thermal runaway.[3] Various strategies, including alternative binders, electrolyte components, and flame retardant additives, can mitigate heat generation in the Li-ion battery system, but typically adversely affect electrochemical performance.[12, 13] In practice, LIBs must be carefully designed and regulated for safe operation, leading to manufacturing cost increases for failsafe mechanisms (gas relief valves, safety vents, etc.) and rigorous testing by heating, short-circuiting, overcharging, nail puncturing, and crushing of cells.[9]

Recently, non-aqueous potassium-ion batteries (KIBs) have received interest as a novel energy storage technology, utilizing inexpensive and abundant potassium as the charge carrier ion. KIBs operate in a manner similar to LIBs, with K ion intercalation between cathode and anode through an organic solvent-inorganic salt electrolyte medium.[14, 15] Despite its larger ionic size, KIBs have an advantage over its competitor, the sodium-ion battery, as K ions can electrochemically intercalate into graphite to form stage-one KC<sub>8</sub> structure for 279 mAh g<sup>-1</sup>, whereas Na is limited to NaC<sub>64</sub> for 35 mAh g<sup>-1</sup>. [16, 17] Formation of KC<sub>8</sub> causes 61% volumetric expansion of graphite however, resulting in electrode pulverization and excessive solid electrolyte interphase (SEI) formation over time.[17, 18] Utilization of functionalized binders, such as sodium carboxymethylcellulose (CMCNa), and opti-

mized electrolyte significantly improve electrochemical performance, with increased first cycle Coulombic efficiency and long-term cycling stability.[19, 20] Many carbon materials have been evaluated for KIB anodes, including hard carbon microspheres, carbon nanofibers, F- or N-doped graphene, polynanocrystalline graphite, and tire-derived hard carbon.[21, 22, 23, 24, 25, 26, 27] The expanded graphitic interlattice spacing mitigates electrode pulverization induced by volumetric changes, resulting in exceptional rate capability and cycling stability. Several KIB cathode materials have shown promising performance, including layered K metal oxide materials, such as  $\text{K}_{0.3}\text{MnO}_2$ ,  $\text{K}_{0.7}\text{Fe}_{0.5}\text{Mn}_{0.5}\text{O}_2$ , and  $\text{K}_{0.6}\text{CoO}_2$ , as well as vanadium phosphate  $\text{KVPO}_4\text{F}$  and  $\text{KVOPO}_4$ . [28, 29, 30, 31] Despite this exceptional electrochemical performance, no prior studies have been reported regarding KIB carbon anode safety to evaluate the practicality of this novel battery system.

Possible safety concerns for KIBs arise from several aspects: (1) Potassium metal is dangerous due to its formation of highly reactive superoxide compounds. (2) K metal melts at  $63.5^\circ\text{C}$ , as compared to  $97.8^\circ\text{C}$  for Na and  $180.5^\circ\text{C}$  for Li. (3) Stage-one  $\text{KC}_8$  is pyrophoric. (4) An organic based electrolyte is utilized, making the system flammable and self-sustaining in exothermic breakdown reactions. While K metal anode is not utilized per se in the full cell, the possibility of K metal deposition and plating on the carbon anode remains. Additionally, properties of the K-ion SEI layer remain largely unknown, although some studies have predicted it to be more stable than Li-ion and Na-ion SEI with increased fraction of inorganic salts, such as  $\text{K}_2\text{CO}_3$ . [32, 33, 34] In this study, graphite is the primary electrode material investigated, due to its favorable energy density, voltage plateau, and commercialization viability. Differential scanning calorimetry (DSC) is the primary technique used to study the KIB graphite system, with selective sample preparation to determine the thermal runaway mechanism and heat generation in comparison to LIBs. To our knowledge, this is the first study to explore safety aspects of KIBs, analyze thermal runaway of graphite anode, and evaluate its practicality for commercialization.

### 4.3 Experimental

Electrodes were prepared with a ratio of 80 wt. % active material (e.g. synthetic graphite), 10 wt. % conductive additive (Timcal Super C65), and 10 wt. % polymer binder (polyvinylidene fluoride). Using N-methyl-2-pyrrolidone as solvent, a slurry was mixed for 20 minutes and tape-cast onto aluminum foil via doctor-blade. For laminates constructed with functionalized binders, such as CMCNa or Na-alginate, water was utilized as solvent. The laminate was dried for 12 h in a vacuum oven set to 80°C, and then 12 mm diameter electrodes were punched out with an active material density of 2.5 mg cm<sup>-2</sup>. Electrochemical tests were performed in a coin-type 2032 half-cell, using potassium metal as the counter and reference electrode. Whatman 934-AH glass microfiber was used as separator and 0.8 M KPF<sub>6</sub> in a 1:1 (by volume) mixture of ethylene carbonate (EC) / diethyl carbonate (DEC) was utilized as electrolyte. Galvanostatic cycling was performed with an Arbin cycler in a voltage range of 0.005-1.5 V at room temperature. To condition for differential scanning calorimetry (DSC) analysis, half-cells were cycled at C/10 current density (determined by theoretical capacity of 279 mAh g<sup>-1</sup>, according to KC<sub>8</sub> stage-one structure) for 5 cycles for the base case, with the corresponding voltage set at equilibrium condition (<1 A current). To remove electrolyte, the electrode was washed with dimethyl carbonate (DMC) three times, with vacuum drying in-between. Lithium-ion coin cells were prepared using copper-foil cast graphite electrodes, with Li metal as the counter electrode, Celgard 2500 as separator, and 1 M LiPF<sub>6</sub> in 1:1 (by volume) EC/DEC.

DSC was performed with a TA Instruments Q20 instrument, at a scan rate of 5°C min<sup>-1</sup>. To perform DSC analysis, the conditioned coin cell was disassembled in an argon glovebox, with the potassiated electrode material scraped off the current collector into a hermetically sealed aluminum pan. A Mettler Toledo XS3DU microbalance was used to precisely measure mass loading of wetted electrode material, with an average 1 - 2 mg sample size. Low mass loading was used to prevent gassing and breakage of the hermetic seal at higher temperatures due to electrolyte evapo-

ration, and results showing irregular jumps or weight loss after DSC measurements were removed. To ensure consistency of results, multiple coin cells were constructed for each trial, with 2 samples run from each individual electrode, and representative data is provided in this study. Scanning electron microscopy (FE-SEM) images were recorded using a Hitachi S-4800 microscope. Powder X-ray diffraction (XRD) was utilized to characterize the crystalline phase via the BraggBrentano method (Rigaku SmartLab X-ray diffractometer). A Cu-K $\alpha$  X-ray source ( $\lambda = 0.154\ 184\ \text{nm}$ ) was used to obtain the XRD patterns ( $2\theta = 5\text{-}80^\circ$ ) at a scanning rate of  $2^\circ\ \text{min}^{-1}$  with samples sealed by Kapton tape. Raman spectra were collected with a 633 nm laser utilizing a Thermo Scientific DXR Raman microscope and an inert sample holder loaded in an argon glovebox. Surface area analysis (Quantachrome Instruments NOVA 2200e) was conducted using nitrogen adsorption/desorption isotherm measurements at 77 K. Samples were degassed for 12 h at  $300^\circ\text{C}$  prior to measurements. Multipoint specific surface area calculations were performed using the linear portion ( $P/P_0 = 0.05\text{-}0.30$ ) of the Brunauer-Emmett-Teller (BET) model. Stage-one KC $_8$  was chemically synthesized by taking stoichiometric ratios of graphite and K metal, and heating in an inert atmosphere under stirring at  $200^\circ\text{C}$  for 2 hours. High surface area graphite was produced by ball milling (Quantachrome Instruments MillPrep-Micro Ball Mill) for either 1 or 5 hours, followed by particle sieving (Endecotts  $>25\ \mu\text{m}$  &  $<53\ \mu\text{m}$  stainless steel sieve) to improve particle size homogeneity.

#### 4.4 Results and Discussion

A typical second cycle charge-discharge voltage profiles for a graphite anode tested in Li-ion and K-ion systems are shown in Figure 4.1. At  $20\ \text{mA}\ \text{g}^{-1}$ , the graphite anode achieves close to the theoretical capacities of  $279\ \text{mAh}\ \text{g}^{-1}$  for KC $_8$  and  $372\ \text{mAh}\ \text{g}^{-1}$  for LiC $_6$ . The higher intercalation potential of K versus Li reduces the risk of plating and dendrite formation on the anode, which can occur at very low potentials, high currents, and low operating temperatures.[35] The first cycle voltage profile is shown in Figure B.1a, where the K-ion system has a Coulombic efficiency of 43%,

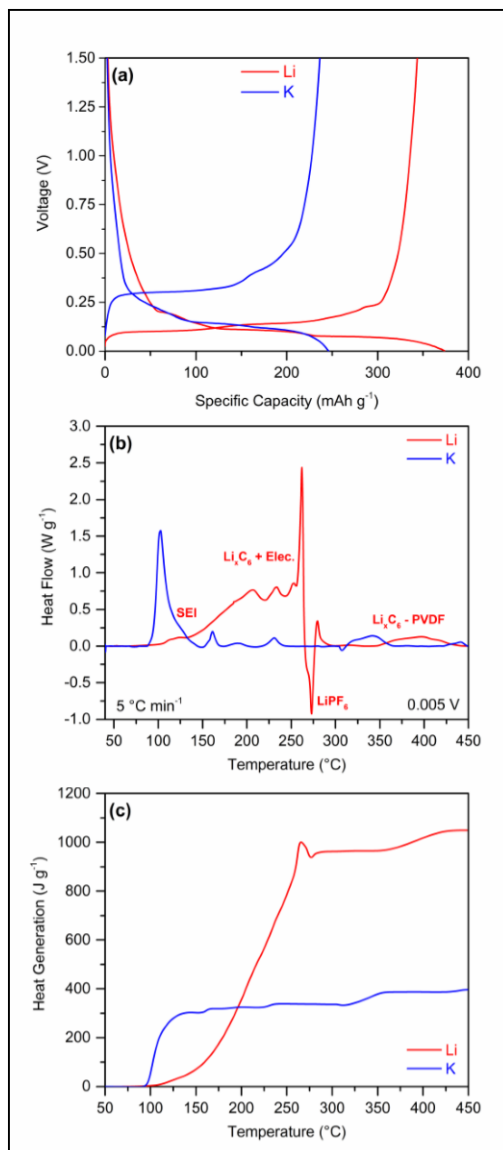


Figure 4.1. (a) Typical charge-discharge voltage profile for graphite electrode in Li-ion and K-ion battery configuration at 20 mA g<sup>-1</sup> current density. (b) DSC profiles of fully charged graphite electrodes prepared by a Li-ion or K-ion battery configuration, with Li-ion degradation reactions labeled. (c) Total heat generation as a function of temperature of DSC profiles.

as compared to 80% for Li-ion, likely occurring due to excessive SEI formation from the 61% volume expansion during potassiation.[17] Extended galvanostatic cycling, as shown in Figure B.1b, reveals a capacity fade of 35% over 50 cycles for the K-

ion graphite anode, due to electrode pulverization and SEI buildup as signified by 95% average Coulombic efficiency. In contrast, the Li-ion graphite anode shows rapid stabilization and 99.9% average Coulombic efficiency over 50 cycles. The synthetic graphite material properties are characterized in Figure B.2, with Raman spectrum, XRD pattern, SEM imaging, and N<sub>2</sub> sorption isotherms, giving a BET surface area 3.4 m<sup>2</sup> g<sup>-1</sup>. For these DSC studies, the electrodes with polyvinylidene fluoride (PVDF) binder were analyzed, to analyze the influence of the native K-ion SEI layer and volumetric changes on thermal runaway.

Figure 4.1b presents typical DSC profiles for charged graphite anodes in Li-ion and K-ion batteries. The Li-ion profile matches well with prior literature, where SEI degradation initiates thermal runaway at 110°C, followed by exothermic reactions of intercalated Li with the electrolyte solvents over 150 - 250°C.[3, 10] At higher temperatures (>250°C), the LiPF<sub>6</sub> electrolyte salt melts and the PVDF binder reacts with Li<sub>x</sub>C<sub>6</sub> by dehydrofluorination.[3, 13] In comparison, the K-ion thermal runaway profile contains a large exothermic peak centered at 100°C, as well as several minor peaks at 160°C, 225°C, and 325°C. While the early peak at 100°C initiates thermal runaway at a lower temperature than for LIB, the total heat evolved over the whole temperature range (50 - 450°C) is significantly lower for K-ion (395 J g<sup>-1</sup> vs. 1048 J g<sup>-1</sup>) (Figure 4.1c). After 195°C, the Li-ion system generates more heat, indicating the greater stability of KIBs at higher temperatures. Depending on battery pack configuration and operation, these differences could present opportunities for safer operation. The sources of these exothermic peaks in the K-ion system cannot be determined by analogous comparison with the Li-ion profile. There are six species present in charged graphite electrodes, including K<sub>x</sub>C<sub>8</sub>, electrolyte, SEI, carbon black, PVDF, and possibly K metal. To determine the source of the peak at 100°C, each of these species were individually tested to evaluate their contribution to thermal runaway.

To determine the effect of the degree of potassium intercalation, DSC profiles at various states of charge (SOC) from 0% (1.5 V) to 100% (5 mV) are shown in Figure

4.2a. As the SOC increases, the total heat evolved increases from  $85 \text{ J g}^{-1}$  at 0% to  $325 \text{ J g}^{-1}$  at 100%, which is consistent with the trend for LIBs.[7] Remarkably, the primary exothermic peak shifts its center from  $90$  to  $100^\circ\text{C}$  as the SOC increases from 25% to 100%, indicating that the full potassiation improves the thermal stability over partial potassiation. At 0% SOC, broad exotherms from  $110^\circ\text{C}$  to  $160^\circ\text{C}$  evolve, which could arise from SEI decomposition, as the metastable species should decompose regardless of K intercalation. This would indicate similar overall SEI thermal stability as LIBs, such that charged graphite electrode is required for thermal runaway in both systems.

Electrolyte was removed by washing the cycled electrode with dimethyl carbonate (DMC) and vacuum drying prior to DSC analysis, with the profiles shown in Figure 4.2b. Regardless of the SOC, electrolyte removal results in complete loss of the peak at  $100^\circ\text{C}$ , implying that intercalated K and electrolyte are required for chemical reaction. This exothermic reaction occurs in the Li-ion system, to generate SEI and heat, but from  $150 - 250^\circ\text{C}$ . [3] Figure B.3 exhibits DSC profiles of K-ion and Li-ion electrolyte, showing that these exotherms occur only in the presence of electrolyte and intercalated graphite. In Figure B.4a, an exothermic peak occurs due to reaction of electrolyte and K metal from  $140$  to  $170^\circ\text{C}$ , correlating with the observed peak at  $160^\circ\text{C}$ , which is present only in the fully charged sample where K metal plating is most likely to occur. Figure B.4b shows the interactions of PVDF with K metal, where dehydrofluorination of PVDF to form KF likely occurs above  $315^\circ\text{C}$  as seen in Figure 4.1b.

To verify the proposed reaction mechanism at  $100^\circ\text{C}$ , chemically synthesized  $\text{KC}_8$  was prepared, with the structure verified by XRD in Figure B.5. This  $\text{KC}_8$  sample does not have SEI formation, PVDF binder, or carbon black. It was found in Figure 4.2c, that peaks centered at  $90^\circ\text{C}$  and  $140^\circ\text{C}$  were generated only by the combination of  $\text{KC}_8$  and electrolyte. One proposed reaction, in analogy to the Li case, could be  $2\text{K} + \text{C}_3\text{H}_4\text{O}_3 \rightarrow \text{K}_2\text{CO}_3 + \text{C}_2\text{H}_4$ , which can be verified by additional characterization in future studies. The discrepancy in the peak center ( $90 - 100^\circ\text{C}$ ) could be due to the SEI layer preventing contact of potassiated graphite with electrolyte, as Figure 4.2a

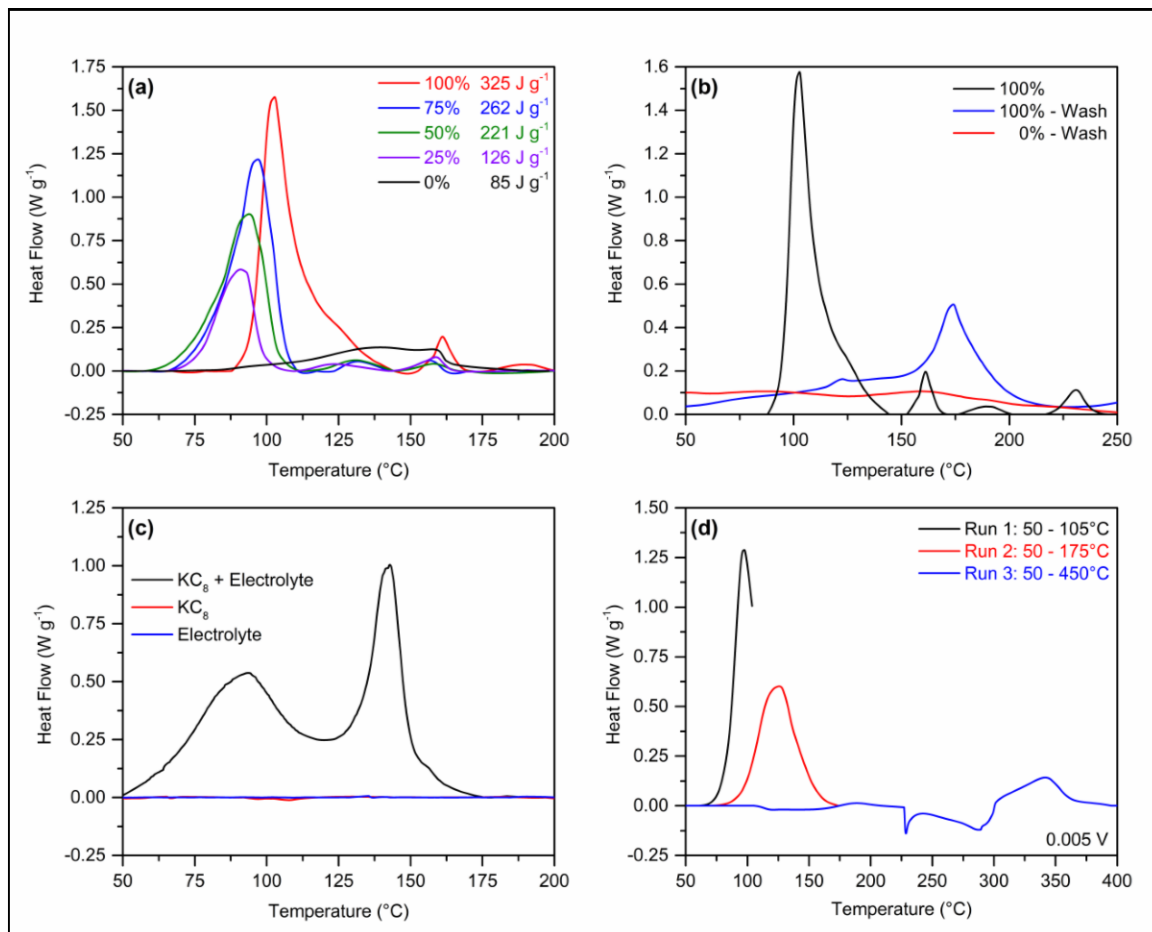


Figure 4.2. (a) DSC profiles for K-ion graphite anode prepared at various states of charge from 0% (depotassiated) to 100% (potassiated). (b) DSC profiles of washed graphite electrodes to remove electrolyte. (c) DSC profiles of chemically synthesized  $\text{KC}_8$  with electrolyte. (d) Repeated DSC analysis of K-ion graphite electrode with incrementing temperature.

showed a shift with SOC and the 61% volumetric contraction could crack the SEI during depotassiation. The two peaks in Figure 4.2c could correlate to phase changes, such as stage-one  $\text{KC}_8$  to  $\text{KC}_{24}$ . To assess the reversibility of these exothermic reactions, a hermetically sealed pan was heated three times to increasing temperatures, with the DSC profiles shown in Figure 4.2d. In subsequent runs, the earlier peaks

disappeared, suggesting these exothermic reactions are irreversible, similarly to the Li-ion system.[3, 4]

To evaluate how volumetric changes upon potassiation/depotassiation affect thermal runaway, DSC was conducted at different cycles in Figure 4.3a. While thermal runaway of graphite in the Li-ion system is consistent over various cycles, KIBs decrease dramatically from cycle 1 ( $1170 \text{ J g}^{-1}$ ) to 10 ( $528 \text{ J g}^{-1}$ ) to 25 ( $280 \text{ J g}^{-1}$ ), due to mitigation of the peak at  $100^\circ\text{C}$ . For LIB silicon anodes with 300% volume expansion, the continuous growth of SEI over time has been observed, increasing the SEI layer resistance.[36] To determine if similar phenomena occur in the K-ion graphite system, electrochemical impedance spectroscopy (EIS) spectra were collected at 200 mV (vs.  $\text{K}^+/\text{K}$ ) during cycle 1, 10, and 25 with the Nyquist plot of the high frequency region shown in Figure 4.3b. Figure B.6 shows Nyquist plots for the full range EIS spectra and the corresponding equivalent circuit model. The semicircle correlating to the SEI resistance and capacitance is located at high frequencies for Li-ion graphite anodes.[37] In Figure 4.3b, evolution of a distinguishable semicircle near the origin over later cycles is seen, describing the continuous growth of SEI. After fitting the equivalent circuit,  $R_{SEI}$  increases from  $8.2 \Omega$  (cycle 1) to  $119.3 \Omega$  (cycle 10) to  $279.9 \Omega$  (cycle 25). This data supports that SEI acts as a blocking mechanism for the  $\text{K}_x\text{C}_8$  electrolyte reaction; a similar mechanism has been proposed previously, as in LIB thermal runaway not all of the intercalated lithium is consumed, due to SEI layer growth during thermal runaway.[4]

To probe the impact of SEI decomposition on thermal runaway, high surface area graphite created by ball milling was analyzed, with material properties shown in Figure B.7. Ball milling did not impact the chemical properties or crystal structuring, but only increased surface area from  $2.9 \text{ m}^2 \text{ g}^{-1}$  (0 h) to  $43 \text{ m}^2 \text{ g}^{-1}$  (1 h) to  $194 \text{ m}^2 \text{ g}^{-1}$  (5 h), with SEM images in Figure B.8 showing decreased particle size due to fracturing. The first cycle charge-discharge voltage profile is shown in Figure 4.4a; with increasing surface area, the Coulombic efficiency decreases from 43% (0 h) to 33% (1 h) to 20% (5 h), signifying additional SEI formation. The corresponding DSC

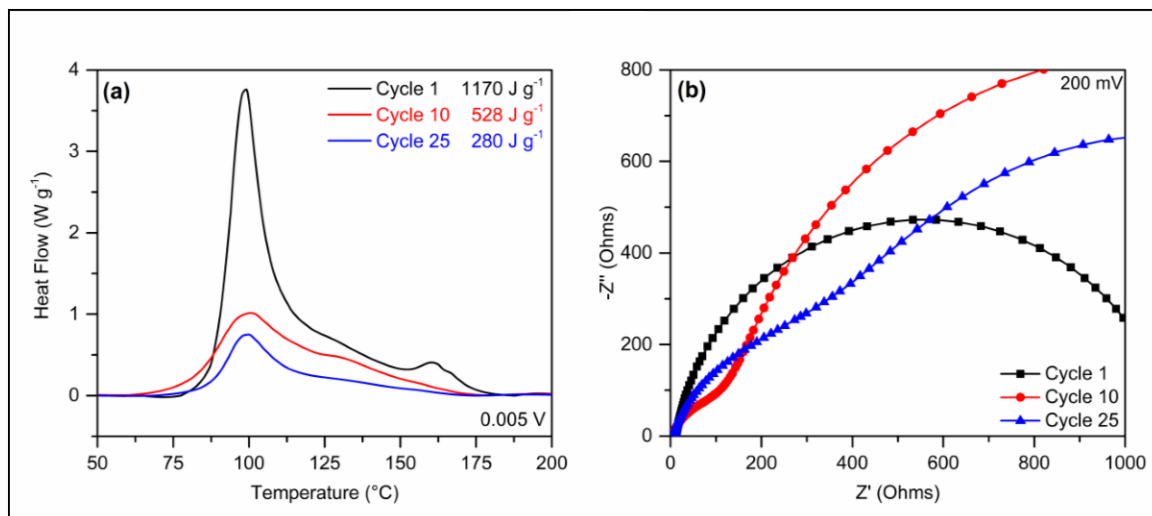


Figure 4.3. (a) DSC profiles of K-ion graphite electrodes after different numbers of cycles. (b) EIS of K-ion graphite electrodes after different numbers of cycles at 200 mV vs. K<sup>+</sup>/K.

profiles are compared in Figure 4.4b, where ball milling decreases heat generation from 550 J g<sup>-1</sup> (0 h) to 455 J g<sup>-1</sup> (1 h) to 354 J g<sup>-1</sup> (5 h). In the Li-ion graphite system, higher surface area significantly augments thermal runaway, increasing the heat contribution from both SEI decomposition and Li<sub>x</sub>C<sub>6</sub> electrolyte reaction.[3, 4] This unexpected result substantiates two previous claims: 1. The SEI layer blocks and prevents the K<sub>x</sub>C<sub>8</sub> - electrolyte reaction. 2. K-ion SEI decomposition is comparatively insignificant in KIB thermal runaway.

Currently, little is known about SEI formation in KIBs. Wood et al. demonstrated that addition of 10 mM KPF<sub>6</sub> to a standard 1 M LiPF<sub>6</sub> in EC/DMC electrolyte significantly decreased the growth of dendrites on lithium metal by increasing the quantity of inorganic salts for a thinner and more conductive SEI.[34] Li<sup>+</sup> is solvated almost exclusively by ethylene carbonate (EC) in EC/DMC, with the following reactions

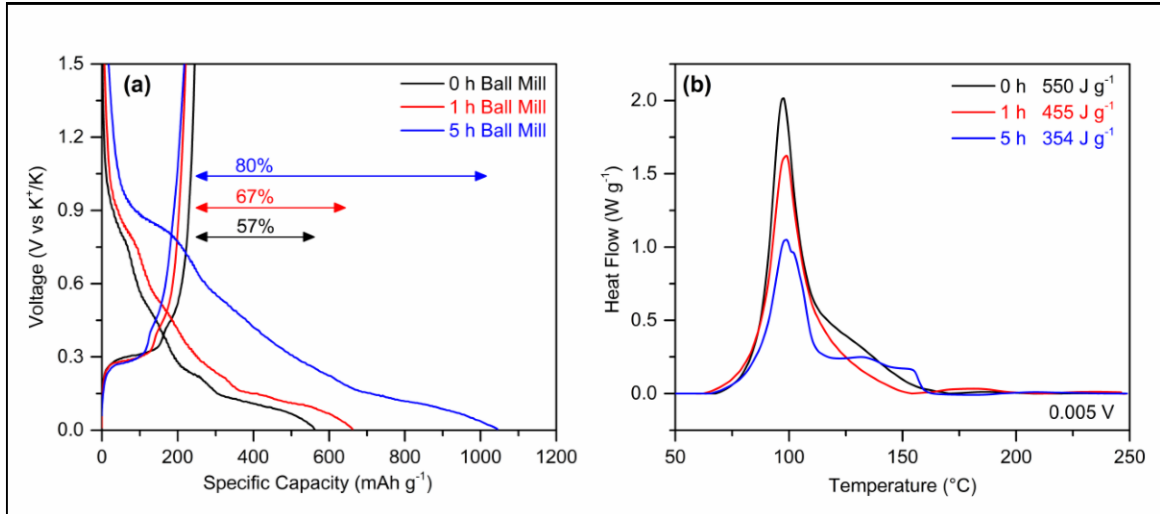
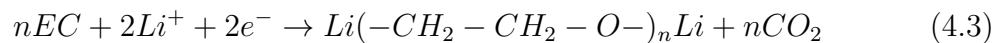
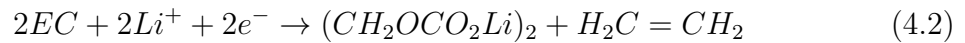
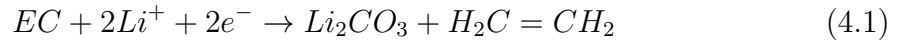


Figure 4.4. (a) First cycle charge-discharge voltage profile for graphite ball milled for varying lengths of time. (b) DSC profiles for potassiated graphite electrodes after ball milling.

resulting in SEI species of  $\text{Li}_2\text{CO}_3$ ,  $(\text{CH}_2\text{OCO}_2\text{Li})_2$  oligomer, and polyethylene glycol (PEO), respectively,[34]



$\text{Li}^+$  is solvated by four EC molecules on average, whereas  $\text{K}^+$  is solved by one, due to cationic size differences.[38, 39] The Marcus reorganization energy for  $\text{K}^+$  electroreduction is consequently much lower than for  $\text{Li}^+$ , and the rate constant for (4.1) is augmented by addition of  $\text{KPF}_6$ , favoring formation of stable carbonate species relative to PEO polymer.[34] While there have not been direct studies of the SEI film formed in KIBs with carbon anodes, this study predicts that KIB SEI layer may be composed of thermally stable species, such as  $\text{K}_2\text{CO}_3$ , as opposed to metastable oligomers and PEO, whose degradation initiates thermal runaway in LIBs.

To probe the influence of binder on thermal runaway, graphite electrodes with CMCNa and Na alginate binders were analyzed. As expected, improved Coulombic efficiencies were obtained for these functionalized binders as compared to PVDF, as shown in Figure 4.5a. This is due to their pre-formed SEI effect, improved coatability, and favorable mechanical properties to create a robust SEI layer.[19, 20] Extended cycling is shown in Figure B.9, where CMCNa and Na alginate demonstrate superior capacity retention over 50 cycles than PVDF. The thermal runaway profiles for each binder are compared in Figure 4.5b, where essentially similar heat is generated, with  $373 \text{ J g}^{-1}$  for PVDF,  $481 \text{ J g}^{-1}$  for CMCNa, and  $353 \text{ J g}^{-1}$  for Na alginate. The exothermic peak at  $100^\circ\text{C}$  is broader for the functionalized binders, with the peak intensity decreasing by 35% for CMCNa and 55% for Na alginate. Instead, thermal runaway initiates earlier, at  $73^\circ\text{C}$  for CMCNa and  $82^\circ\text{C}$  for Na alginate, as compared to  $88^\circ\text{C}$  for PVDF. While PVDF generates 86.5% of its total heat from  $50\text{-}130^\circ\text{C}$ , CMCNa and Na alginate generate 54.0% and 71.8% respectively. This could be due to the pre-formed SEI, resulting in a composition reflective of Na-ion carbon SEI that is more vulnerable to thermal decomposition.[40, 41] The decreased intensity at  $100^\circ\text{C}$  correlating to the  $\text{K}_x\text{C}_8$  electrolyte reaction could result from improved SEI coverage and flexibility on the graphite particles throughout cycling.

*Ex-situ* material characterization was performed after quenching at varying temperatures during DSC to analyze the change in potassium staging during thermal runaway. The resulting XRD patterns are shown in Figure 4.6a, where the broad peak centered at  $19^\circ$  is due to Kapton tape used to prevent sample oxidation. At  $100^\circ\text{C}$ , two peaks at  $30.5^\circ$  and  $33.3^\circ$  belong to  $\text{KC}_{24}$  and  $\text{KC}_8$  respectively.[42] At  $150^\circ\text{C}$ , the (002) graphite peak at  $26.5^\circ$  appears, along with small peaks for  $\text{KC}_{36}$  ( $22.0^\circ$ ,  $30.4^\circ$ ).[42] By  $250^\circ\text{C}$ , only the graphite peaks at  $26.5^\circ$  (002) and  $54.5^\circ$  (004) remain, implying that all the intercalated potassium is consumed during thermal runaway. Raman spectra in Figure 4.6b confirm the presence of these intercalation stages at each quenching temperature, although some overlap between peaks complicates the analysis.[42] Stage-two  $\text{KC}_{24}$  and stage-three  $\text{KC}_{36}$  were detected previously

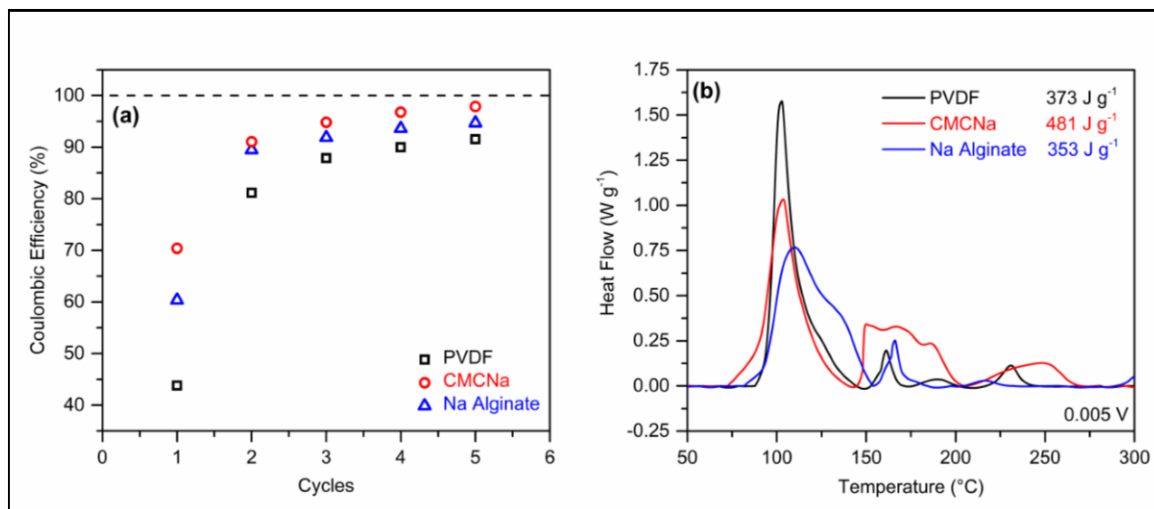


Figure 4.5. (a) Coulombic efficiency for the first five cycles of K-ion graphite electrodes using either PVDF, CMCNa, or Na alginate as binder. (b) DSC profiles of potassiated graphite electrodes prepared with different binders.

by *ex-situ* XRD and *in-situ* Raman spectroscopy, correlating with this degradation mechanism.[17, 43] In comparison to the Li-ion graphite system, analogous experiments concluded that for  $\text{Li}_x\text{C}_6$ , the change in the amount of intercalated Li was  $\Delta x = 0.3$  after thermal runaway, regardless of the initial SOC, as SEI layer growth eventually prevents further reaction.[4] The divergence results from cracking of the SEI layer during cycling, and matches with the DSC profiles where 90% of heat is generated by 150°C, as only graphite and  $\text{KC}_{36}$  remain.

Besides graphite, many carbons materials have been explored as K-ion anodes with exceptional cycling stability and rate capabilities. The lower density of these amorphous carbons allow them to tolerate the strain associated with insertion of bulky  $\text{K}^+$ .[21] DSC profiles of high surface area carbon nanofiber (CNF) and Super P electrodes are shown in Figure B.10.[23] The CNFs generated significantly lower heat of 62 J g<sup>-1</sup>, as compared to 169 J g<sup>-1</sup> for Super P and 324 J g<sup>-1</sup> for graphite. Thermal runaway initiates at a lower temperature of 70°C, but the low heat generation

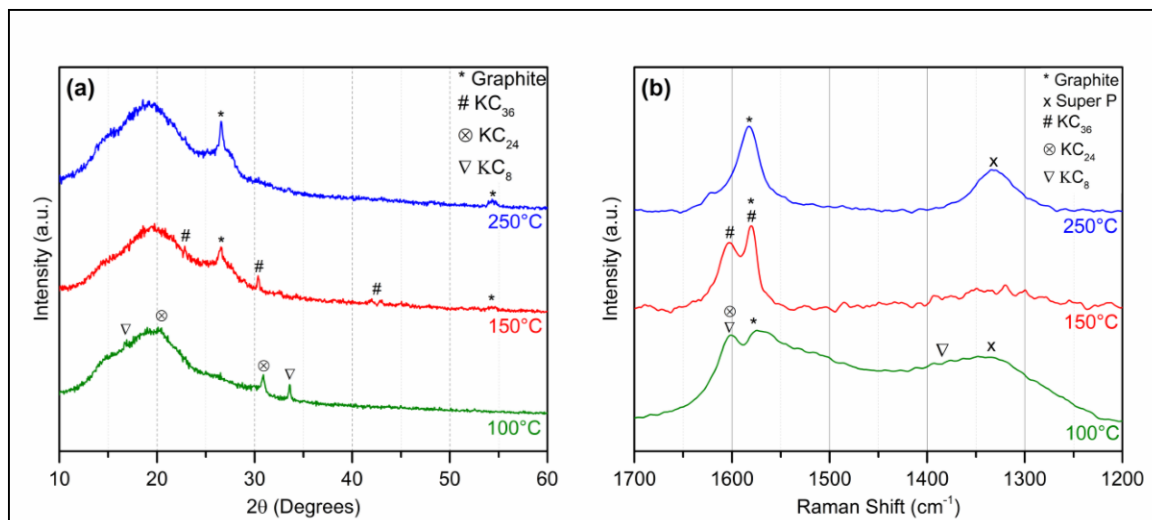


Figure 4.6. (a) XRD patterns of potassiated graphite quenched at 100°C, 150°C, or 250°C. (b) Raman spectra of potassiated graphite quenched at 100°C, 150°C, or 250°C.

in conjunction with their promising electrochemical performance warrants further investigation.[23] The thermal stability of KIB cathodes also requires exploration, as oxygen release during breakdown of metastable Li-ion cathodes (e.g.  $\text{Li}_x\text{CoO}_2$ ) initiates cell combustion during thermal runaway.[6] The matter of electrolytes also warrants further investigation, as while so far only carbonate-based electrolytes (e.g. EC, DEC) have been utilized in non-aqueous KIBs, alternative systems and electrolyte additives could possibly provide benefits of electrochemical performance and safety.[44]

#### 4.5 Conclusions

Thermal runaway of graphite anodes for KIBs was investigated for the first time utilizing DSC analysis. The KIB graphite anode initiates thermal runaway at 100°C, due to exothermic reaction of  $\text{KC}_8$  - electrolyte, but generates only  $395 \text{ J g}^{-1}$  versus  $1048 \text{ J g}^{-1}$  for Li-ion from 50-450°C. A strong dependence on SOC, cycle number,

and carbon material properties was found, due to the large volumetric expansion of graphite upon potassiation, causing SEI layer cracking and growth over time. Functionalized binders (CMCNa and Na alginate) mitigate the exothermic peak at 100°C by preventing  $K_xC_8$  - electrolyte contact through improved SEI layer coverage, but decrease the inherent thermal stability of K-ion SEI. *Ex-situ* XRD and Raman spectroscopy verified the complete consumption of intercalated K, explaining the strong intensity of the exotherm at 100°C. These findings suggest future strategies to improve KIB safety, where establishment of a robust SEI layer with complete graphite particle coverage can mitigate this initiating reaction. The significantly decreased heat generation and promise of non-graphitic carbon anodes also warrant further investigation into the safety of K-ion batteries for rechargeable energy storage. In summary, potassium battery graphitic anodes are prone to thermal runaway at lower temperature but overall heat generation is less as compared to conventional lithium ion battery anodes.

#### 4.6 Acknowledgements

V.P. thanks Purdue University and its Davidson School of Chemical Engineering for the generous start-up funding. The Slayter Discretionary Fund (A.V.) was used to purchase chemical and laboratory supplies. V.P. thanks the Office of Naval Research for supporting this project under Naval Enterprise Partnership Teaming with Universities for National Excellence (NEPTUNE Phase I and II) at Purdue Center for Power and Energy Research provided under grant number N00014-15-1-2833.

#### 4.7 References

- [1] T. M. Bandhauer, S. Garimella, and T. F. Fuller, *Journal of The Electrochemical Society* **158**, R1 (2011).
- [2] X. Feng et al., *Energy Storage Materials* **10**, 246 (2018).
- [3] A. D. Pasquier, *Journal of The Electrochemical Society* **145**, 472 (1998).
- [4] M. N. Richard and J. Dahn, *Journal of The Electrochemical Society* **146**, 2068 (1999).

- [5] Y. Fu et al., *Journal of Power Sources* **273**, 216 (2015).
- [6] J. R. Dahn, E. W. Fuller, M. Obrovac, and U. von Sacken, *Solid State Ionics* **69**, 265 (1994).
- [7] Q. Wang, J. Sun, X. Yao, and C. Chen, *Journal of The Electrochemical Society* **153**, A329 (2006).
- [8] O. S. Mendoza-Hernandez, H. Ishikawa, Y. Nishikawa, Y. Maruyama, and M. Umeda, *Journal of Power Sources* **280**, 499 (2015).
- [9] Q. Wang et al., *Journal of Power Sources* **208**, 210 (2012).
- [10] G. Gachot et al., *Electrochimica Acta* **83**, 402 (2012).
- [11] H. H. Lee, C. C. Wan, and Y. Y. Wang, *Journal of The Electrochemical Society* **151**, A542 (2004).
- [12] L. Ma, J. Xia, X. Xia, and J. R. Dahn, *Journal of the Electrochemical Society* **161**, A1495 (2014).
- [13] C. Forestier et al., *Journal of Power Sources* **330**, 186 (2016).
- [14] A. Eftekhari, Z. Jian, and X. Ji, *ACS Applied Materials and Interfaces* **9**, 4404 (2017).
- [15] J. C. Pramudita, D. Sehwat, D. Goonetilleke, and N. Sharma, *Advanced Energy Materials* **7**, 1602911 (2017).
- [16] N. Yabuuchi, K. Kubota, M. Dahbi, and S. Komaba, *Chemical Reviews* **114**, 11636 (2014).
- [17] Z. Jian, W. Luo, and X. Ji, *Journal of the American Chemical Society* **137**, 11566 (2015).
- [18] W. Luo et al., *Nano Letters* **15**, 7671 (2015).
- [19] S. Komaba, T. Hasegawa, M. Dahbi, and K. Kubota, *Electrochemistry Communications* **60**, 172 (2015).
- [20] J. Zhao, X. Zou, Y. Zhu, Y. Xu, and C. Wang, *Advanced Functional Materials* **26**, 8103 (2016).
- [21] Z. Jian, Z. Xing, C. Bommier, Z. Li, and X. Ji, *Advanced Energy Materials* **6**, 1 (2016).
- [22] Y. Liu et al., *Nano Letters* **14**, 3445 (2014).
- [23] R. A. Adams et al., *ACS Applied Materials & Interfaces* **9**, 17872 (2017).
- [24] Z. Ju et al., *ACS Applied Materials and Interfaces* **8**, 20682 (2016).
- [25] K. Share, A. P. Cohn, R. E. Carter, and C. L. Pint, *Nanoscale* **8**, 16435 (2016).
- [26] Z. Xing, Y. Qi, Z. Jian, and X. Ji, *ACS Applied Materials and Interfaces* **9**, 4343 (2017).

- [27] Y. Li et al., *Journal of The Electrochemical Society* **164**, A1234 (2017).
- [28] C. Vaalma, G. A. Giffin, D. Buchholz, and S. Passerini, *Journal of The Electrochemical Society* **163**, A1295 (2016).
- [29] X. Wang et al., *Nano Letters* **17**, 544 (2017).
- [30] H. Kim et al., *Advanced Energy Materials* **7**, 1700098 (2017).
- [31] K. Chihara, A. Katogi, K. Kubota, and S. Komaba, *Chemical Communications* **53**, 5208 (2017).
- [32] M. Moshkovich, Y. Gofer, and D. Aurbach, *Journal of The Electrochemical Society* **148**, E155 (2001).
- [33] Q. C. Zhuang, J. Li, and L. L. Tian, *J. Power Sources* **222**, 177 (2013).
- [34] S. M. Wood et al., *ACS Energy Letters* **1**, 414 (2016).
- [35] M. Ouyang et al., *Journal of Power Sources* **286**, 309 (2015).
- [36] M. Nie et al., *Journal of Physical Chemistry C* **117**, 1257 (2013).
- [37] S. Zhang, *Journal of Power Sources* **162**, 1379 (2006).
- [38] I. Skarmoutsos, V. Ponnuchamy, V. Vetere, and S. Mossa, *Journal of Physical Chemistry C* **119**, 4502 (2015).
- [39] H. Wang and M. Yoshio, *Journal of Power Sources* **195**, 1263 (2010).
- [40] M. Dahbi, N. Yabuuchi, K. Kubota, K. Tokiwa, and S. Komaba, *Physical Chemistry Chemical Physics* **16**, 15007 (2014).
- [41] S. J. An et al., *Carbon* **105**, 52 (2016).
- [42] J. Purewal, *Hydrogen adsorption by alkali metal graphite intercalation compounds*, PhD thesis, California Institute of Technology, 2010.
- [43] K. Share, A. P. Cohn, R. E. Carter, and C. L. Pint, *Nanoscale* **8**, 16435 (2016).
- [44] P. Balakrishnan, R. Ramesh, and T. Prem Kumar, *Journal of Power Sources* **155**, 401 (2006).

## 5. TEMPERATURE DEPENDENT ELECTROCHEMICAL PERFORMANCE OF GRAPHITE ANODES FOR K-ION AND LI-ION BATTERIES

The original publication of this work appears in Journal of Power Sources, volume 410-411, 124-131. Material characterization, electrochemical testing, data analysis, and manuscript preparation was carried out by Ryan A. Adams.

DOI: 10.1016/j.jpowsour.2018.11.007

### 5.1 Summary

The electrochemical behavior of graphite anode for potassium-ion batteries (KIBs) is investigated in detail over varying operating temperatures (0 - 40°C) with comparisons made to lithium-ion batteries (LIBs). Three main categories of cell performance are analyzed and evaluated, namely, kinetics, aging, and polarization. At 10°C and below, the KIBs exhibit poor rate capability, which can be attributed to the decreased solid-state diffusion coefficient, and the amplified charge-transfer and SEI resistances. In comparison to LIBs, KIBs exhibit rapid cell aging at elevated temperatures, owing to augmented SEI growth induced by the significant volumetric change of graphite during potassiation. 3-electrode cell studies reveal the dramatic polarization of K metal at 0°C (161 mV), while the extreme reactivity of K metal causes a severe rise in impedance from cell storage at 50°C. A full cell system comprising Prussian blue cathode and graphite anode is evaluated, which removes the issues associated with the K metal counter electrode and enhances rate performance at 0°C. These findings provide a thorough basis for understanding the temperature dependent behavior of graphite anode for KIBs and its performance concerns at low and elevated temperatures.

## 5.2 Introduction

Rechargeable lithium-ion batteries (LIBs) are currently the dominant electrical energy storage technology with widespread usage in portable electronics and electric vehicles due to their high energy density and reasonable lifetime. However, the scarcity and poor distribution of Li resources limit the scalability of this technology proceeding into the future, especially for large scale applications, such as grid storage of renewable energy (e.g. solar and wind).[1, 2] While efforts have been made towards the recovery of valuable cobalt and lithium resources from spent LIBs, the economics and complexity of these recycling processes limit their viability.[3, 4] Thus, researchers have become interested in alternative alkali metal-ion chemistries, replacing Li with Na, and more recently K, for applications where kWh \$<sup>-1</sup> is more important than energy density.[5, 6, 7] These batteries operate with an analogous mechanism to LIBs, with intercalation storage between cathode and anode in a non-aqueous electrolyte. Despite its larger cationic size, potassium-ion batteries (KIBs) have some intrinsic advantages over sodium-ion batteries (NIBs), including a higher operating voltage and increased electrolyte transference number in organic solvents due to the weaker Lewis acidity of K<sup>+</sup>. [8, 9] A variety of electrode materials have been explored for KIBs, with promising cathodes including layered metal oxides (K<sub>0.3</sub>MnO<sub>2</sub>, K<sub>0.7</sub>Fe<sub>0.5</sub>Mn<sub>0.5</sub>O<sub>2</sub>, K<sub>0.6</sub>CoO<sub>2</sub>), [10, 11, 12] polyanionic compounds (KVPO<sub>4</sub>F and KVOPO<sub>4</sub>), [13] and hexacyanoferrates (Prussian blue, K<sub>1.89</sub>Mn[Fe(CN)<sub>6</sub>]<sub>0.92</sub>•0.75H<sub>2</sub>O) [14, 15, 16]. For the anode side, graphitic and carbonaceous materials are the most viable choices, including hard carbon microspheres, N-doped carbon nanofibers, tire-derived carbon, soft carbon nanorods as well as MXenes. [17, 18, 19, 20, 21]

The key advantage of KIBs over NIBs comes from the ability of graphite to reversibly intercalate K<sup>+</sup> to a stage-one KC<sub>8</sub> structure (279 mAh g<sup>-1</sup>), whereas Na<sup>+</sup> is limited to a stage-eight NaC<sub>64</sub> structure (35 mAh g<sup>-1</sup>). [22, 23, 24] Commercial LIBs have primarily used graphite as anode for over two decades, due to its good cycling stability, favorable low voltage profile, high tap density (as compared to non-

graphitic carbons), low first cycle inefficiency, and reasonable reversible capacity. In fact, the main hurdle to NIB commercialization comes from the lack of a suitable anode material, where the front-runner hard carbon materials suffer from poor first cycle Coulombic efficiency and long-term cycling stability.[25] Intercalation of  $K^+$  into graphite is mechanistically similar to that of  $Li^+$ , with multiple phase changes occurring from stage-three  $KC_{36} \rightarrow$  stage-two  $KC_{24} \rightarrow$  stage-one  $KC_8$  structures, resulting in voltage plateaus near 0.2 V (vs.  $K/K^+$ ).[23] The slightly higher average voltage for  $K^+$  insertion into graphite, as compared to  $Li^+$ , is beneficial in preventing K metal plating and dendrite growth under high current or low temperature conditions, which is a severe safety concern. Due to the bulkier size of  $K^+$  as compared to  $Li^+$ , a larger volumetric expansion of 61% occurs upon full potassiation (vs. 11% for lithiation); however, full reversibility of this intercalation process has been demonstrated without graphene exfoliation.[23, 24] Cell optimization of electrode binder, such as functionalized sodium carboxymethyl cellulose (CMCNa), and electrolyte have significantly improved the first cycle Coulombic efficiency and long-term cycling stability, despite the large volumetric expansion.[24, 26]

With KIB research still in its infancy, there remain many challenges and unexplored aspects that require further investigation to evaluate the viability of this chemistry for commercialization. For example, the effect of operating temperature on KIB performance remains completely unknown, where all experimental studies thus far have been conducted at room temperature only. It is well known that operating temperature plays a significant role in LIB performance, lifetime, and safety.[27] At low temperatures ( $< 10^\circ C$ ), reduced energy and power capability result from the sluggish kinetics, with severe safety concerns arising from possible Li metal plating and dendrite formation on the graphite anode at high currents.[28, 29] At elevated temperatures ( $> 40^\circ C$ ), accelerated battery aging occurs due to irreversible solid electrolyte interphase (SEI) growth.[30, 31] Additionally, thermal runaway remains a significant issue for LIBs, where the metastable electrode materials and flammable organic electrolyte result in self-propagated cell combustion at extreme temperatures

(> 80°C).[32] Recently, we investigated the thermal runaway behavior of graphite anode in KIBs via differential scanning calorimetry, where exothermic reactions of  $K_xC_8$  - electrolyte initiate as early as 100°C, with a strong dependence on state of charge, cycle number, electrode binder, and graphite surface area.[33] This illustrates the need to evaluate the KIB graphite anode system over a wide operating temperature range, and to determine the effects of temperature on battery performance, aging, and safety.

In this study, we conducted thorough electrochemical evaluation of graphite anode for KIBs and LIBs to compare their behavior across a wide temperature range (0 - 40°C). Three major parameters were evaluated: (1) diffusion kinetics and rate capability, (2) cell aging and impedance growth, and (3) cell polarization. Coin cells were constructed using analogous electrolytes ( $LiPF_6$  /  $KPF_6$  salt dissolved in a mixed carbonate solvent), with the non-idealities of the K metal reference/counter electrode determined via 3-electrode cell and full cell studies. Through this work, we aim to provide further mechanistic insight into  $K^+$  - graphite intercalation electrochemistry and its differences with the well-known Li system.

### 5.3 Experimental

To facilitate comparisons between chemistries, the same graphite electrode was utilized for K-ion and Li-ion battery testing, comprising of 80 wt. % synthetic graphite (MTI Corp), 10 wt. % conductive additive (Super P carbon black), and 10 wt. % CMCNa binder (Sigma-Aldrich). Material characterization for this standard graphite powder can be found in our prior related work.[33] These materials were mixed in a slurry utilizing water as solvent for 30 minutes and cast onto copper foil (MTI Corp) prior to drying in a vacuum oven at 80°C for 12 hours. For coin cell testing, 12 mm diameter electrodes were punched out with an average graphite loading of 2 mg  $cm^{-2}$ . Electrochemical testing was performed in coin-type 2032 half-cells, with Li (MTI Corp) or K metal (Sigma-Aldrich) foils used as reference and counter electrode. 3-electrode cells were constructed using the methodology of Juarez-Robles *et al.*,

albeit with Li or K metal as the reference electrode.[34] Glass microfiber (Whatman 934-AH) was utilized as separator, while the electrolyte was 1 M LiPF<sub>6</sub> in ethylene carbonate (EC):diethyl carbonate (DEC) (1:1 volumetric ratio) for LIBs and 0.8 M KPF<sub>6</sub> in EC:DEC (1:1) for KIBs (all salts and solvents obtained from Sigma-Aldrich).

Galvanostatic cycling was performed via an Arbin cycler with cells contained in an ESPEC environmental chamber for temperature control, with five temperatures chosen for analysis: 0°C, 10°C, 22°C, 30°C, and 40°C. Due to the low melting temperature of K metal (63.5°C), the thermal analysis of cells was conducted at a maximum temperature of 40°C for safety. Cycling was performed in the voltage range of 0.01 - 1.5 V (vs. Li/Li<sup>+</sup> or K/K<sup>+</sup>) with specific currents provided in terms of mA g<sup>-1</sup>. Galvanostatic intermittent titration technique was conducted with 30-minute pulses at C/10 (1C = 372 mA g<sup>-1</sup> for LIBs & 1C = 279 mA g<sup>-1</sup> for KIBs) and 1-hour relaxations between pulses. Potentiostatic electrochemical impedance spectroscopy (EIS) was performed with a Gamry-600+ instrument, in the frequency range of 0.01 - 10<sup>6</sup> Hz, with an amplitude of 5 mV and prior cell conditioning to a voltage of 200 mV (LIBs) or 500 mV (KIBs). EIS spectra were fit using Echem Analyst software from Gamry Instruments. To analyze battery self-discharge and aging, cells conditioned at 22°C were discharged (i.e. lithiated / potassiated), stored at 50°C for 1 week at open circuit voltage (OCV), and then cycled at room temperature again, with EIS collected before and after storage at 50°C.

## 5.4 Results and Discussion

### 5.4.1 Kinetics

To analyze the effect of temperature on kinetics, an initial inquiry was conducted via galvanostatic cycling at various specific currents (20 - 500 mA g<sup>-1</sup>), with obtained charge capacities shown in Figure 5.1a for Li and Figure 5.1b for K. At 22°C, both chemistries achieve their theoretical capacities of 279 mAh g<sup>-1</sup> and 372 mAh g<sup>-1</sup> for K and Li respectively, after initial cell conditioning and SEI formation. At higher

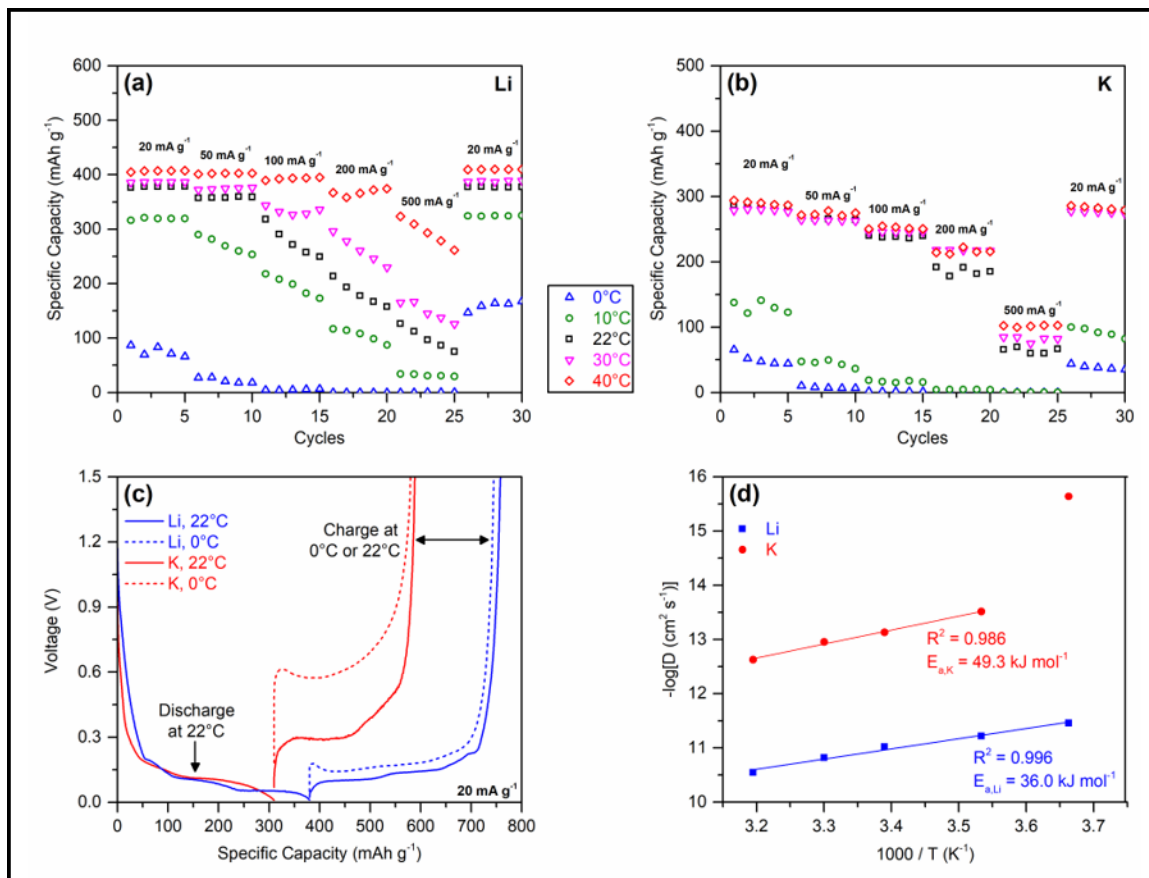


Figure 5.1. Kinetic analysis of graphite across temperatures. (a) Charge capacity of Li at various specific currents. (b) Charge capacity of K at various specific currents. (c) Voltage profile for discharge at 22°C with subsequent charge at 0°C or 22°C, at 20 mA g<sup>-1</sup> and cycle 5. (d) Solid-state diffusion coefficients of Li<sup>+</sup> and K<sup>+</sup> in graphite from 0 - 40°C, with calculated diffusion activation energies determined by the Arrhenius equation.

temperatures, the theoretical capacity of 372 mAh g<sup>-1</sup> is exceeded for LIBs, likely due to the storage of Li<sup>+</sup> in Super P carbon black, as previously observed.[35] Due to the low surface area (3.4 m<sup>2</sup> g<sup>-1</sup>), larger particle diameters, and limited diffusion of K<sup>+</sup>/Li<sup>+</sup> through the edge of the graphene sheets, both chemistries suffer from poor rate capability at higher currents of 500 mA g<sup>-1</sup>. [33] As expected, increased temperatures augment the capacity achieved for LIBs, from 100 mAh g<sup>-1</sup> (22°C) to

300 mAh g<sup>-1</sup> (40°C) at 500 mA g<sup>-1</sup>, while decreased temperatures lower the capacity dramatically. In comparison, graphite anode for KIB shows less improvement at elevated temperatures, and already starts failing at moderate currents by 10°C.

To provide further insight into the kinetic limitations at 0°C, a coin cell was discharged fully (i.e. lithiated or potassiated) at 22°C after 5 conditioning cycles, and subsequently charged (i.e. delithiated or depotassiated) at 0°C or 22°C as shown in Figure 5.1c. Both systems obtain nearly the full capacity upon charging at 0°C, indicating that the rate limiting step involves insertion of the alkali ion into graphite, rather than extraction, agreeing with previous observations for LIBs.[36] However, the hysteresis between the charge voltage curves at 0°C and 22°C is significantly higher for the KIB. Additionally, the charge profiles for both systems at 0°C display an initial overpotential hump, likely due to a charge-transfer related activation energy barrier amplified by the low temperature.[37] As shown in Figure 5.1c, the poor rate capability at low temperatures could originate from several factors, such as cell polarization, diffusional resistance, or poor charge-transfer kinetics. Evaluation of both electrolyte compositions indicates that no freezing or salt precipitation occurs at 0°C (Table C.1).

To determine the source of these kinetic limitations, the diffusion coefficients of Li<sup>+</sup> and K<sup>+</sup> in graphite were determined as a function of temperature, using the method of Kulova *et al.* (experimental details in Supporting Information).[38, 39] The calculated diffusion coefficients are shown in Figure 5.1d, where  $D_{Li^+}$  is in the range of 10<sup>-11</sup> cm<sup>2</sup> s<sup>-1</sup>, agreeing well with previously calculated values.[40] As expected, the diffusion coefficient observes an Arrhenius relationship with temperature as follows,

$$D = D_0 \exp^{-E_A/RT} \quad (5.1)$$

where  $E_A$  is the activation energy for cation diffusion in graphite. An activation energy of 36.0 kJ mol<sup>-1</sup> is obtained for Li<sup>+</sup>, showing a good linear fit and matching previously obtained values.[39] Contrarily, the diffusion coefficient for K<sup>+</sup> is on the order of 10<sup>-13</sup> cm<sup>2</sup> s<sup>-1</sup>, indicating much more sluggish solid-state diffusion, as expected

from the larger cationic size of  $K^+$  and the poor observed rate capability. A linear trend is also observed for  $D_{K^+}$ , with an activation energy of  $49.3 \text{ kJ mol}^{-1}$ , ignoring the data point at  $0^\circ\text{C}$ , which has a significantly lower diffusion coefficient value of  $10^{-16} \text{ cm}^2 \text{ s}^{-1}$ . Much lower specific currents were required to achieve a linear response at  $0^\circ\text{C}$  (even using a 3-electrode cell), with extreme polarization preventing cell operation. Interestingly, first-principles calculations have predicted decreased site jump energy barriers for  $K^+$  as compared to  $Li^+$ , suggesting that larger cations should diffuse more smoothly in graphite, suggesting a discrepancy between experimental and computational results.[41]

To investigate this inconsistency, EIS analysis was utilized to probe and compare the impedance of the two battery chemistries. To determine the effect of temperature, EIS was performed on well-conditioned cells (C/10 for 10 cycles at  $22^\circ\text{C}$ ) at a specified state-of-charge (200 mV for Li, 500 mV for K) in an environmental chamber for temperature control. The spectra are displayed in Figure 5.2a for Li and Figure 5.2b for K, with insets for the high frequency region. Both systems demonstrate a strong relationship of impedance with temperature, albeit K even more so, with increasing temperature lowering cell impedance as expected.[42] Both sets of spectra include several overlapping semicircles, which can be ascribed to SEI layer resistance and capacitance (at high frequencies), as well as a Randles circuit for charge-transfer resistance and double layer capacitance (at medium frequencies). Additionally, a linear region of  $45^\circ$  at low frequencies is observed representing solid-state diffusion impedance via a Warburg element. The equivalent circuit utilized to fit the EIS data is shown in Figure C.5, where constant phase elements (CPEs) are used for modeling to improve the fitting, which physically arises from inhomogeneities in the particle surface.

After fitting, the values corresponding to charge-transfer and SEI resistance are plotted in Figure 5.2c and Figure 5.2d, respectively, with additional fitting parameters listed in Tables C.2-3. An Arrhenius relationship is observed for charge-transfer resistance, with calculated activation energies of  $80.8 \text{ kJ mol}^{-1}$  for K and  $51.7 \text{ kJ}$

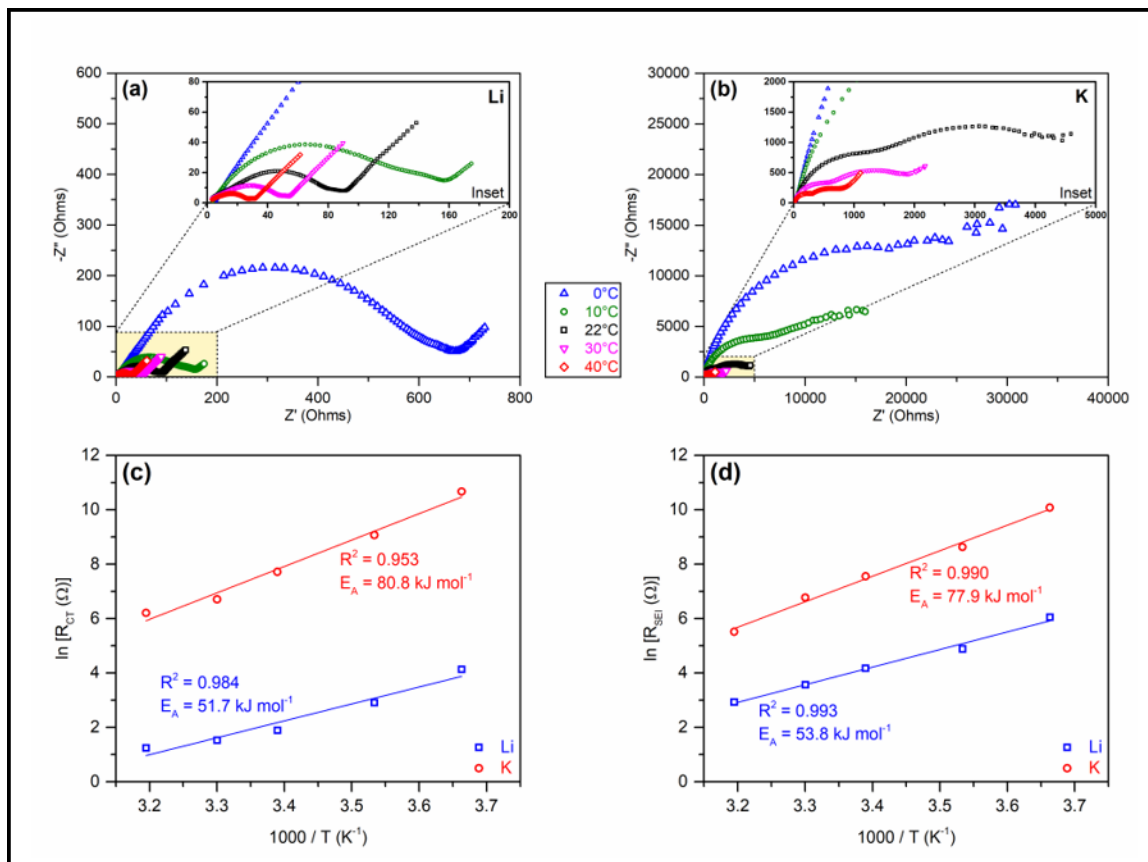


Figure 5.2. Dependence of cell impedance with temperature. Nyquist plots of electrochemical impedance spectra conducted at various temperatures for (a) Li at 200 mV and (b) K at 500 mV. (c) Charge-transfer resistance and (d) SEI resistance, with corresponding activation energies determined by the Arrhenius equation.

mol<sup>-1</sup> for Li, which agrees well with prior obtained values for LIBs.[42, 43, 44] The impedance of KIBs is significantly higher than that of LIBs, which suggests that the augmented energy barrier caused by insertion of a larger cation is a stronger effect than the beneficial weaker Lewis acidity of K<sup>+</sup>. [26] The SEI resistances also follow Arrhenius relationships, with activation energies of 77.9 kJ mol<sup>-1</sup> for K and 53.8 kJ mol<sup>-1</sup> for Li. While the properties of the KIB SEI layer remain largely undetermined, it was shown that K<sup>+</sup> possesses low ionic conductivity within the

SEI as compared to  $\text{Li}^+$ , resulting in significant overpotentials.[45] Additionally, SEI surface films consisting on ionic Na compounds are much more resistive than those comprised of ionic Li compounds, with the trend continuing for the soft K cations due to the resulting formation of less compact and ionically conductive compounds.[46] Computational studies have predicted a disordered and flexible solvation structure for  $\text{K}^+$  in ethylene carbonate, enabling easier electrode - electrolyte migration than with the well-defined  $\text{Li}^+$  solvation shell, meaning this discrepancy in rate behavior likely arises from sluggish transport through the KIB SEI layer.[47] Since this EIS was conducted with half-cells, SEI from the metal counter electrodes will also contribute to the measured impedance. Due to the increased reactivity of K metal over Li metal, it is likely that K metal will have increased SEI formation and impedance, and that its composition may vary across temperatures. The influence of the counter electrode will be discussed in further detail later.

#### 5.4.2 Aging

Besides affecting kinetic parameters, extreme operating temperatures can significantly increase the rate of cell degradation and aging. For an initial probe into the effect of temperature on aging, long term galvanostatic cycling was conducted at  $50 \text{ mA g}^{-1}$  over the range of  $0 - 40^\circ\text{C}$ , with discharge capacities shown in Figure 5.3a (Li) and Figure 5.3b (K). For LIBs, stable capacities are observed from  $22 - 40^\circ\text{C}$ , with minor increases in capacity values for the higher temperatures. The lower temperatures display an increase in capacity over cycle number, likely due to material activation or improving electrolyte-electrode contact over time.[48] In contrast, KIBs exhibit a slight capacity fade with cycling, due to the 61% volumetric expansion during potassiation. The rate of this capacity fade increases with temperature, arising from augmented SEI growth on exposed graphite caused by SEI cracking during repeated material expansion and contraction. The average capacity loss per cycle is 0.167% for  $22^\circ\text{C}$ , 0.236% for  $30^\circ\text{C}$ , and 0.390% for  $40^\circ\text{C}$ . The lower temperatures give minimal capacity, agreeing well with the prior rate study in Figure 5.1b, and do not

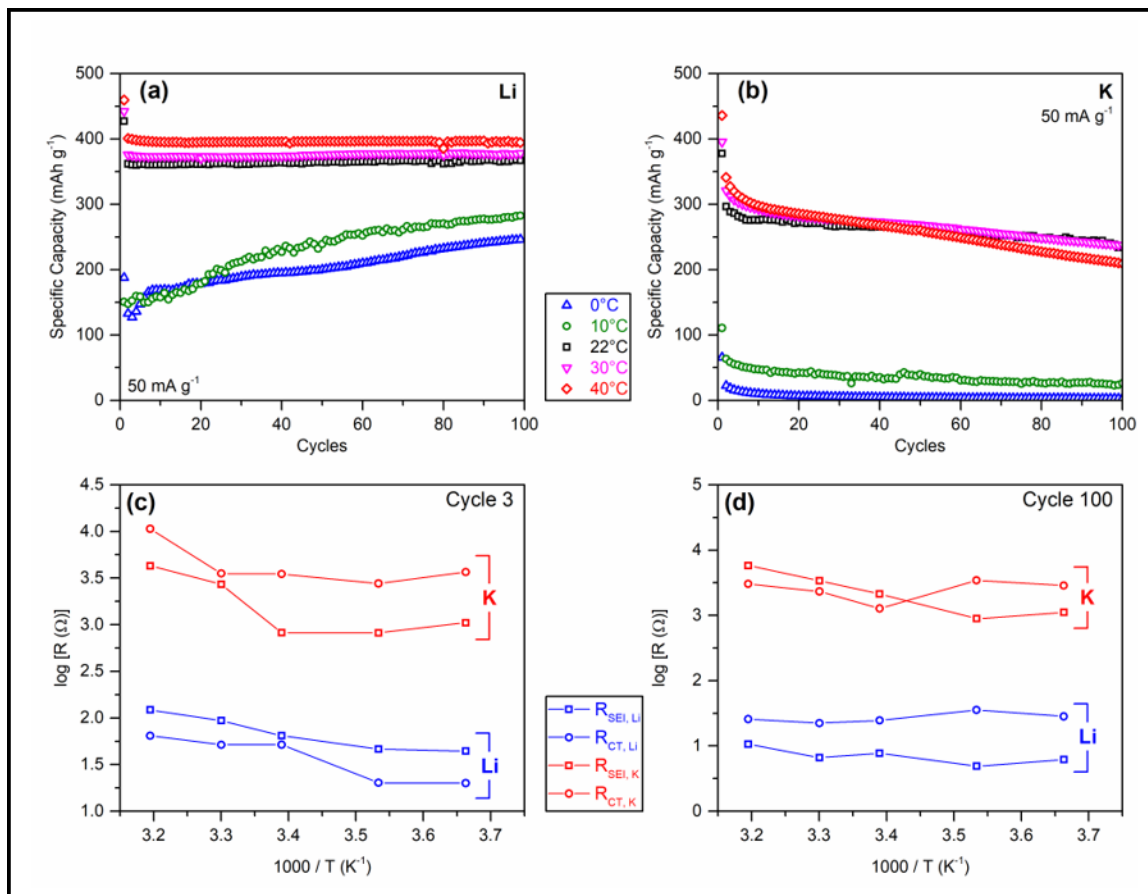


Figure 5.3. (a) Discharge capacity of LIB cycled at 50 mA g<sup>-1</sup>. (b) Discharge capacity of KIB cycled at 50 mA g<sup>-1</sup>. Aging of cells conditioned at various temperatures, with subsequent electrochemical impedance spectroscopy analysis conducted at 22°C. (c) SEI and charge-transfer resistances after 3 slow formation cycles conducted at 5 mA g<sup>-1</sup>. (d) SEI and charge-transfer resistances after 100 cycles at 50 mA g<sup>-1</sup>.

activate over time in contrast to LIBs, indicating that the high cell impedance results in nominal capacity. The Coulombic efficiencies for the initial cycles are shown in Figure C.6, where both chemistries show the greatest stability at room temperature, with excessive SEI growth at elevated temperatures and possible alkali metal plating at lower temperatures. Additionally, LIBs stabilize in Coulombic efficiency across all temperatures more quickly, plateauing by cycle 15, as compared to cycle 25 for KIBs.

To elucidate the aging mechanisms of the batteries more clearly, EIS analysis was conducted at 22°C, to study the change in impedance for cells previously conditioned at varying temperatures. EIS was conducted for conditioned cells (three slow cycles at 5 mA g<sup>-1</sup>), as well as cells that had undergone extended cycling (100 cycles at 50 mA g<sup>-1</sup>) to determine the evolution of impedance over cycling, with spectra displayed in Figures C.7-8. All spectra were fit to an equivalent circuit (Figure C.5), with the values for charge-transfer and SEI resistance shown in Figure 5.3c (three cycles) and Figure 5.3d (100 cycles), and additional fitting parameters listed in Tables C.4-7. After three slow conditioning cycles, LIBs increase in SEI resistance with cycling temperature from 44.1 Ω at 0°C to 122.2 Ω at 40°C, due to the enhanced SEI formation kinetics. In comparison, the KIBs exhibit similar SEI resistance from 0 - 22°C, but have a significant increase at elevated temperatures, with 820.5 Ω at 22°C, 2708 Ω at 30°C, and 4275 Ω at 40°C, indicating the augmented SEI growth and its poor stabilization. The charge-transfer resistances increase with temperature for both chemistries, likely arising from changes in electrolyte-electrode interfacial contact and the SEI composition and thickness.[49] Overall, slow conditioning suggests that the impedance is directly related to the cycling temperature of the cells, with increased temperature detrimental to electrochemical performance.

After extended cycling, the LIB charge-transfer resistances are independent of temperature, with any slight variation likely arising from cell to cell discrepancies, agreeing with previous results.[50] While there is a slight increase in SEI resistance with cycling temperature, from 7.7 Ω at 22°C to 10.6 Ω at 40°C, the system exhibits relatively minor changes as expected of the stable LIB graphite anode. Since the cycling was conducted at a low specific current of 50 mA g<sup>-1</sup>, the extent of Li plating on graphite should not be significant, which agrees with the small increase in SEI resistance of 4.8 Ω to 6.2 Ω, from 10°C to 0°C, respectively.[51] In contrast, the KIB SEI resistance increases dramatically with temperature, from 2121 Ω at 22°C to 5792 Ω at 40°C, reflecting the accelerated capacity fade during cycling at 40°C in Figure 5.3b. Xiao *et al.* demonstrated that the 0.8 M KPF<sub>6</sub> EC/DEC electrolyte utilized

in this study exhibits poor Coulombic efficiency for reversible plating/stripping of K on Cu substrate, due to poor SEI stabilization on the K metal.[52] The minimum value for SEI resistance is observed after 10°C cycling, with 0°C likely resulting in K metal plating. The charge-transfer resistance for KIBs is the lowest at 22°C, reflecting its optimal electrochemical performance and stability, with higher temperatures augmenting SEI growth and lower temperatures resulting in cell polarization. In comparison, LIBs exhibit a wider optimal operating range of 22 - 40°C and still function at lower temperatures, showing the practicality and flexibility of LIBs over KIBs.

### 5.4.3 Polarization

The effect of operating temperature on the voltage profile of graphite anode was probed via slow galvanostatic cycling (5 mA g<sup>-1</sup>) at temperatures of 0°C, 22°C, and 40°C, with the first charge-discharge cycle shown in Figure 5.4a (Li) and Figure 5.4c (K). Typical voltage profiles are observed, with several plateaus due to phase changes between different staging structures at ~0.1 V for Li<sup>+</sup> and ~0.23 V for K<sup>+</sup>. First cycle inefficiencies caused by SEI formation have values of 15%, 16%, and 22% for LIBs at 0°C, 22°C, and 40°C, respectively. In comparison, the first cycle for KIBs have inefficiencies of 28%, 35%, and 39% at 0°C, 22°C, and 40°C, respectively. While both chemistries have augmented SEI formation at higher temperatures, due to enhanced reaction kinetics, LIBs display less variation due to its greater SEI stability across temperatures and the decreased reactivity of Li metal as compared to K metal. Differential capacity curves were generated for these voltage profiles to elucidate the redox peak locations and the hysteresis between charge and discharge processes, as shown in Figure 5.4b (Li) and Figure 5.4d (K). As expected, the voltage hysteresis increases at lower temperatures due to higher cell impedance, resulting in poorer energy efficiency. This is much more apparent in the KIB profile, with its significant hysteresis of 343 mV between the corresponding reduction and oxidation peaks at 0°C, as compared to 52 mV for Li. In fact, even at 5 mA g<sup>-1</sup>, the full theoretical capacity is not achieved at 0°C, with the potassiation peak interrupted by the lower voltage

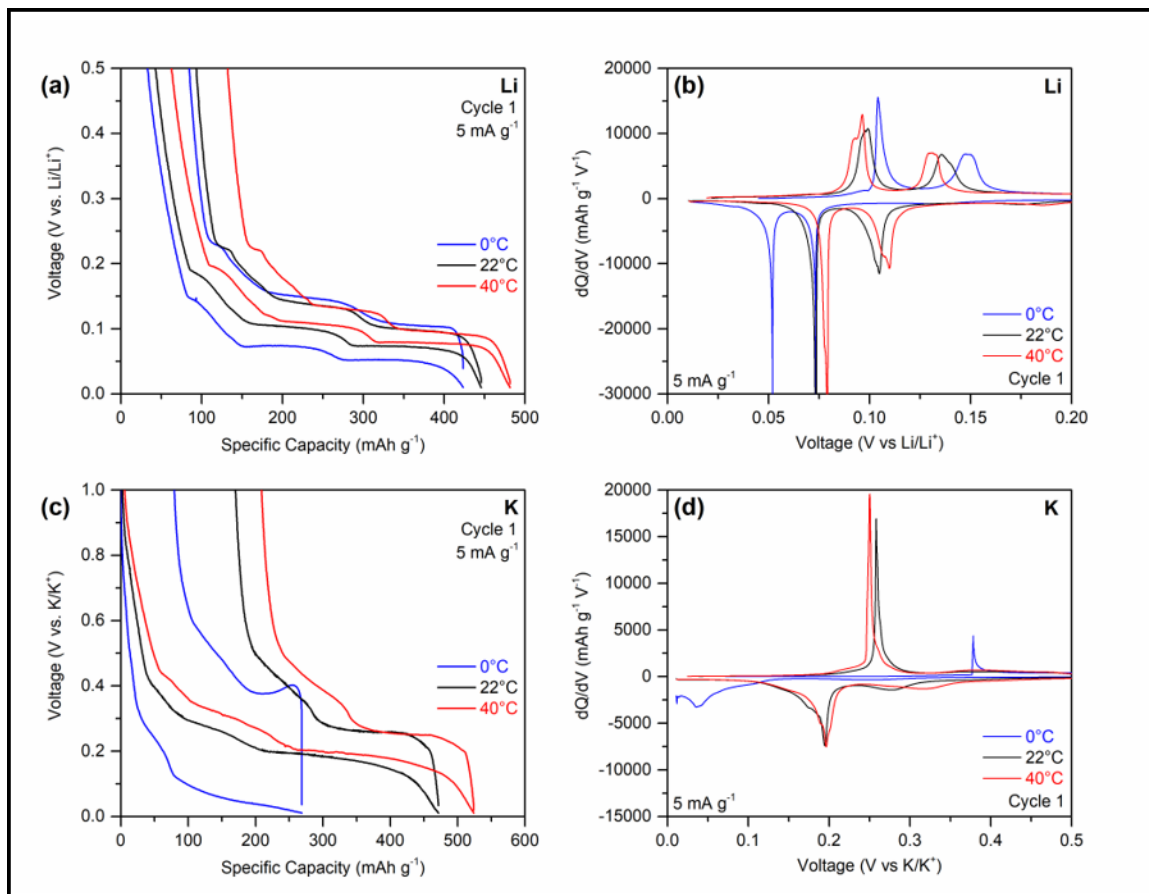


Figure 5.4. First cycle charge-discharge voltage profile variation with temperature. (a) Voltage profile for LIB at 0°C, 22°C, and 40°C at 5 mA g<sup>-1</sup>, and corresponding (b) differential capacity plot of LIB voltage profile. (c) Voltage profile for KIB at 0°C, 22°C, and 40°C at 5 mA g<sup>-1</sup>, and corresponding (d) differential capacity plot of KIB voltage profile.

limit of 0.01 V (vs. K/K<sup>+</sup>). This severe polarization contributes significantly to the poor rate performance observed before; however, it is unsure whether this polarization arises from the graphite working electrode or the K metal counter electrode.

3-electrode cells were constructed for each battery chemistry to quantify the polarization originating from the alkali metal counter electrode. The deconvoluted voltage profiles for the graphite anode and alkali metal counter electrode, after prior condi-

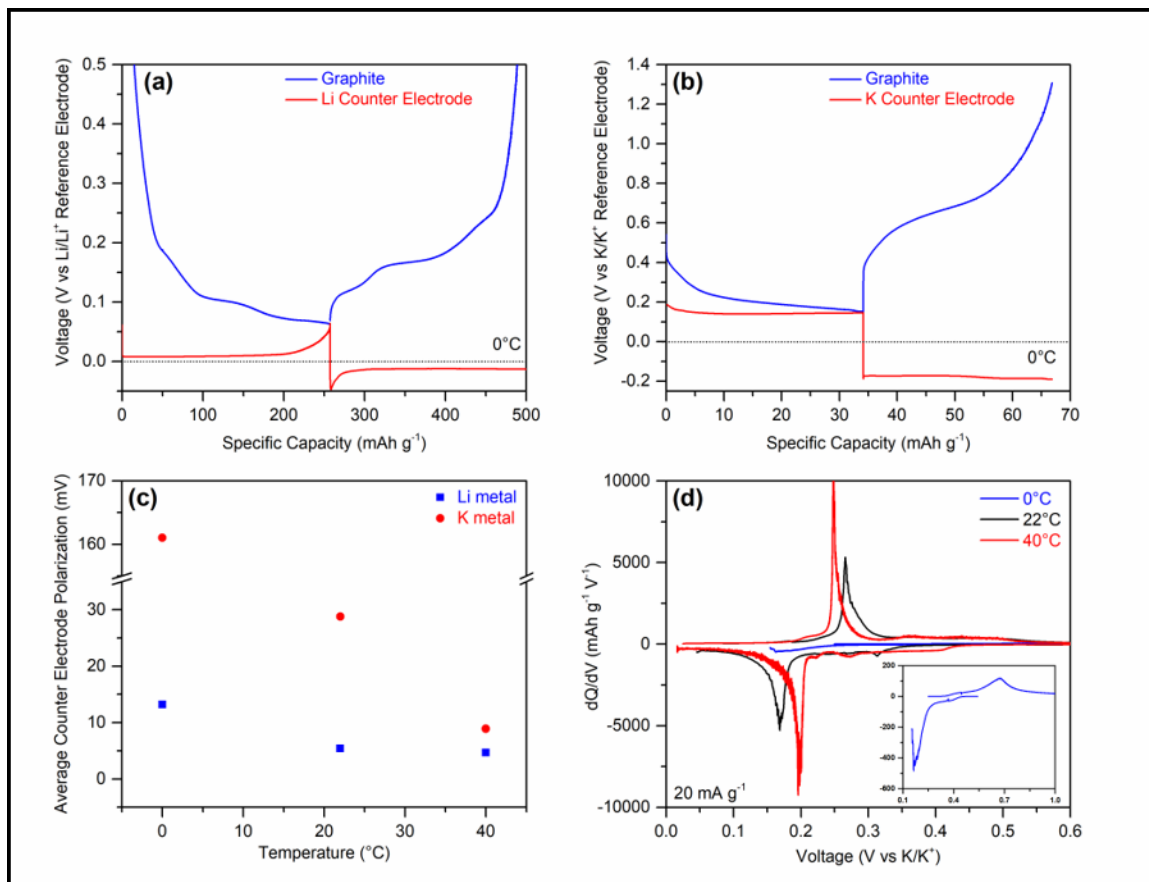


Figure 5.5. Polarization of the alkali metal counter electrode. (a) Voltage profile of 3-electrode LIB cell at 20 mA g<sup>-1</sup> and 0°C. (b) Voltage profile of 3-electrode KIB cell at 20 mA g<sup>-1</sup> and 0°C. (c) Dependence of the average alkali metal counter electrode polarization with temperature. (d) Differential capacity plot of the graphite voltage profile across temperatures in a 3-electrode KIB cell.

tioning for 5 cycles, are shown in Figure 5.5a (Li) and Figure 5.5b (K) for 0°C at 20 mA g<sup>-1</sup>. The corresponding voltage profiles at 22°C and 40°C are shown in Figure C.9. Noticeably, the Li metal has minimal polarization at 0°C, with a sharp increase occurring only after the graphite is mostly lithiated. In contrast, the K metal has consistently high polarization across the entire state-of-charge, ending the discharge step after only 35 mAh g<sup>-1</sup>. The average alkali metal counter electrode polarization

was calculated across the three tested temperatures and plotted in Figure 5.5c. The Li metal shows relatively low variation from 0 - 40°C, indicating its suitability as a reference electrode for half-cell testing. In contrast, there was a dramatic decrease in polarization from 0°C (161 mV) to 40°C (8.9 mV) for K metal, reflecting the higher activation energy calculated for SEI resistance in KIBs. In agreement with our results, Hess demonstrated the strong effect the cation has on the SEI overpotential, with its non-linear behavior resulting in enlarged polarization for K at low specific currents as compared to Li.[53] It should be noted that even after neglecting K metal polarization, graphite itself displays a significant hysteresis between the charge-discharge voltage profiles as compared to the LIB case. The differential capacity curves for graphite in the 3-electrode KIB cell at different temperatures are shown in Figure 5.5d, where a strong dependence of voltage hysteresis on temperature is observed, reflecting the higher activation energy for KIB charge-transfer resistance.

It is known that K metal is much more reactive than Li, such that it should never be utilized as anode in commercial KIBs for safety reasons. While KIB half-cells have shown promising performance at room temperature, it is unknown how reactive the K metal will be at elevated temperatures in the non-aqueous electrolyte. For safety reasons, an upper limit of 40°C was chosen for all cycling in this study due to the low melting point (63.5°C) of K metal. To study this behavior, cell aging was explored for fully discharged half-cells (i.e. lithiated or potassiated) by holding them at 50°C for a week under OCV. Similar tests have been conducted previously in the literature to analyze the rate of self-discharge and impedance growth for LIBs, albeit usually at higher temperatures, such as 70°C.[54, 55] The charge-discharge capacities before and after aging are shown in Figure 5.6a, where all galvanostatic cycling was conducted at room temperature, and the aging process occurred between the discharge and charge steps of the sixth cycle. The LIB shows a minor decrease of 9.4% in charge capacity after aging, which can be attributed to self-discharge, but recovers its full capacity in later cycles, thus indicating the systems stability at 50°C.

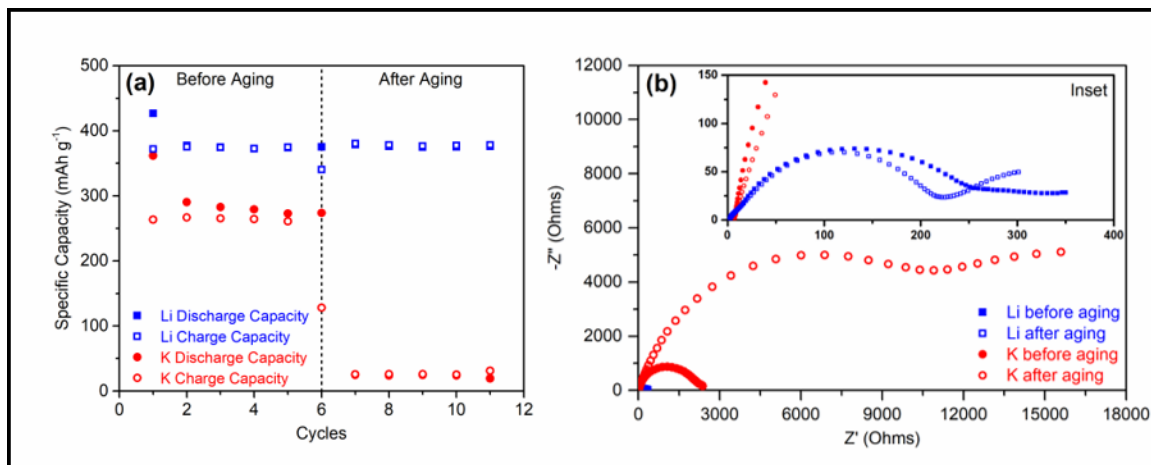


Figure 5.6. Cell aging from high temperature storage. (a) Specific capacity before and after aging, at  $50 \text{ mA g}^{-1}$  and  $22^\circ\text{C}$ . Aging was performed in the middle of cycle 6 at  $50^\circ\text{C}$  for 7 days for fully lithiated / potassiated (discharged) batteries under open circuit voltage. (b) Nyquist plots for electrochemical impedance spectra immediately before and after aging.

In contrast, the KIB has a significant capacity loss of 53.2% after aging, with a subsequent dramatic decrease in reversible capacity during cycling. The voltage profile for the sixth cycle in Figure C.10 reveals the dramatic increase in impedance for the KIB, with the charge plateau occurring at  $\sim 1 \text{ V}$  instead of  $\sim 0.3 \text{ V}$ . Additionally, the decreased length of this plateau indicates that the capacity loss in the sixth cycle after aging is likely due to self-discharge. The dramatic rise in impedance after aging, as portrayed by EIS analysis in Figure 5.6b, demonstrates the reactivity of K metal, with augmented SEI formation occurring at  $50^\circ\text{C}$ . Lei *et al.* showed that DEC solvent is highly reactive in KIBs, and is more electrochemically unstable with K metal than graphite, due to its strong reducibility.[56] Additionally,  $\text{KPF}_6$  salt causes a higher voltage hysteresis, due the resulting continuous SEI formation and dendrite growth, when used with K metal.[57] These results indicate that K metal is a poor counter and reference electrode for KIB electrode testing, especially at extreme temperatures where increased polarization and reactivity occur.

#### 5.4.4 Full Cell

In light of these findings, a KIB full cell was constructed utilizing graphite as anode and Prussian blue (PB) nanoparticles as cathode (experimental details in Supporting Information). Material characterization of the synthesized PB cathode (Figure C.11) matches well with the prior report, including the crystallinity from X-ray diffraction analysis (JCPDS: 52-1907).[14] The PB cathode exhibits typical electrochemical behavior in a half-cell, with a specific capacity of  $70 \text{ mAh g}^{-1}$  resulting from the Fe(II) Fe(III) redox behavior at  $\sim 3.3 \text{ V}$ , as seen in Figure C.12.[14] The PB cathode exhibits exceptional rate capability due to its open 3D network, achieving  $50 \text{ mAh g}^{-1}$  at  $200 \text{ mA g}^{-1}$  and  $40 \text{ mAh g}^{-1}$  at  $400 \text{ mA g}^{-1}$ . Coupled with the high mass ratio of PB to graphite (to achieve 1:1 cathode to anode charge ratio in the full cell), any limitation in rate capability for the full cell system will likely originate from the graphite anode. Additionally, good cycling stability is observed for PB cathode, with minimal capacity loss occurring after 150 cycles at  $200 \text{ mA g}^{-1}$  (Figure C.12d). The first cycle charge-discharge voltage profiles for the PB cathode and graphite anode in the half-cell configuration (prior to disassembly and full cell construction) are shown in Figure 5.7a. Both electrodes exhibit initial irreversible capacity loss, due to SEI formation on graphite and decomposition of interstitial water in the PB lattice at higher potentials, explaining the need for half-cell conditioning prior to full cell testing.[14]

The voltage profiles for the full cell can be seen in Figure 5.7b, where cycling was performed at  $50 \text{ mA g}^{-1}$  of graphite at various temperatures, resulting in a specific energy of  $90 \text{ Wh kg}^{-1}$  (calculated using both electrode masses) and a corresponding specific power of  $25 \text{ W kg}^{-1}$  ( $\sim C/4$  discharge) at  $22^\circ\text{C}$ . In comparison, commercial LIBs have a much higher specific energy of  $150 \text{ Wh kg}^{-1}$  and specific power of  $50 \text{ W kg}^{-1}$  ( $\sim C/3$  discharge). This is due to the low capacity of KIB graphitic anode as well PB cathodes. Notably, at  $0^\circ\text{C}$ , a capacity of  $100 \text{ mAh g}^{-1}$  was achieved, in contrast to the negligible value obtained for graphite in the half-cell configuration. A 50% loss in capacity was observed going from room temperature to  $0^\circ\text{C}$ , with an

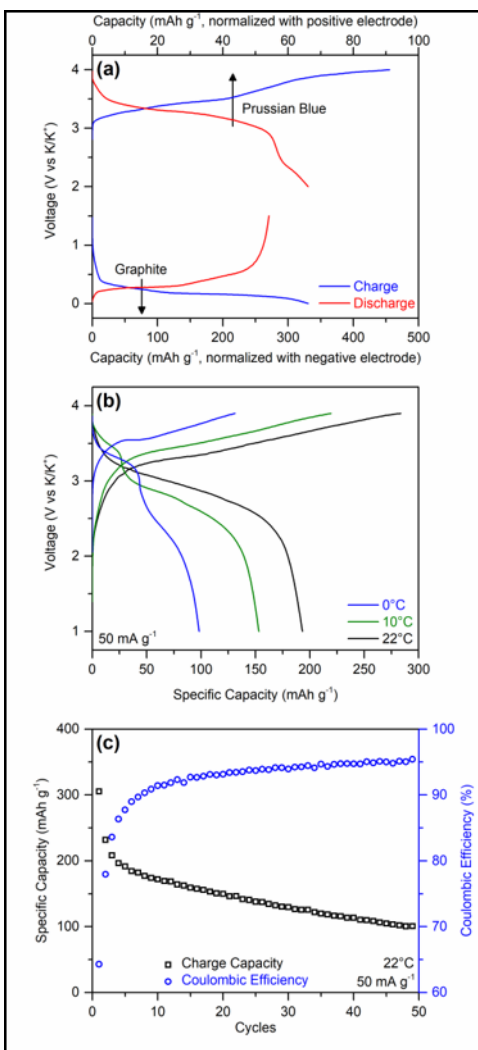


Figure 5.7. KIB full cell evaluation. (a) First cycle voltage profiles of Prussian blue cathode and graphite anode half-cells at  $50 \text{ mA g}^{-1}$ . The capacities are normalized to show the positive to negative charge ratio of the full cell. (b) Full cell charge-discharge voltage profiles across various temperatures from 1.0 - 3.9 V at  $50 \text{ mA g}^{-1}$  of graphite. (c) Charge capacities and Coulombic efficiencies for full cell cycling conducted from 1.0 - 3.9 V at  $50 \text{ mA g}^{-1}$  of graphite and  $22^\circ\text{C}$ . Specific current and capacity values in (b) and (c) are normalized by the weight of active material in the graphite anode.

associated increase in cell hysteresis, albeit not to the extent observed in the half-cell. These results confirm the issues of using K metal as a counter electrode for half-cell testing for KIBs. Long term cycling of this full cell, as shown in Figure 5.7c, results

in a capacity retention of 50% from cycle 3 to 50, which can be attributed to the poor Coulombic efficiency ( $< 96\%$ ). Upon inspection of the cell after cycling, the electrolyte had turned a dark color, likely due to side reactions at high potentials and the release of water in PB cathode, resulting in a rise in cell impedance over time. This study indicates that while KIBs have shown promise in optimal conditions in the prior literature, there remains much improvement to be made in terms of cycling stability and performance, especially at non-ideal conditions.

## 5.5 Conclusions

For the first time in the literature, we have investigated the temperature dependent behavior of KIBs, specifically with reference to the promising graphite anode. Comparisons between KIB and LIB electrochemical performance were made in terms of three categories, namely: rate capability, cell aging, and polarization. Notably, severe kinetic limitations are observed for KIBs at low temperatures, which can be attributed to the increased solid-state diffusion activation energy, charge-transfer resistance, and SEI resistance. The solid-state diffusion coefficient for  $\text{K}^+$  in graphite is two orders of magnitude smaller than that of Li ( $10^{-13} \text{ cm}^2 \text{ s}^{-1}$  vs.  $10^{-11} \text{ cm}^2 \text{ s}^{-1}$ ), which can be attributed to the larger cationic size. While LIB graphite anode demonstrated good cycling stability at  $40^\circ\text{C}$ , the KIBs exhibited accelerated capacity fade with increasing temperature, due to continuous SEI growth and impedance rise. Evaluation of K metal as the counter electrode revealed extreme polarization at low temperatures (161 mV at  $0^\circ\text{C}$  at  $20 \text{ mA g}^{-1}$ ) and poor stability at elevated temperatures due to dramatic electrolyte breakdown. Full-cell evaluation using graphite anode and Prussian blue cathode revealed enhanced performance at low temperatures, elucidating the issues of K metal for KIB electrode evaluation. These results provide valuable mechanistic insight into graphite anode for KIBs, providing a practical evaluation of the temperature dependent electrochemical performance and the K metal counter electrode used to study KIB performance.

## 5.6 Acknowledgements

We thank the National Science Foundation for supporting our potassium ion battery safety work under the CBET-1804300 grant. VP thanks the Office of Naval Research for supporting lithium ion battery safety work under the grant N00014-18-1-2397. RA acknowledges the Bilsland Dissertation Fellowship for financial support, as well as Arthur Dysart for his helpful discussions regarding electrochemical impedance spectroscopy analysis.

## 5.7 References

- [1] J. M. Tarascon, *Nature Chemistry* **2**, 510 (2010).
- [2] D. Larcher and J.-M. Tarascon, *Nature Chemistry* **7**, 19 (2015).
- [3] Y. Guo et al., *Journal of Materials Science* **53**, 13790 (2018).
- [4] J. Guan et al., *ES Energy & Environment* , 1 (2018).
- [5] K. Kubota and S. Komaba, *Journal of The Electrochemical Society* **162**, A2538 (2015).
- [6] X. Wu, D. P. Leonard, and X. Ji, *Chemistry of Materials* **29**, 5031 (2017).
- [7] K. Kubota, M. Dahbi, T. Hosaka, S. Kumakura, and S. Komaba, *The Chemical Record* **18**, 459 (2018).
- [8] K. Kim et al., *Carbon* **133**, 62 (2018).
- [9] A. Eftekhari, Z. Jian, and X. Ji, *ACS Applied Materials and Interfaces* **9**, 4404 (2017).
- [10] C. Vaalma, G. A. Giffin, D. Buchholz, and S. Passerini, *Journal of The Electrochemical Society* **163**, A1295 (2016).
- [11] X. Wang et al., *Nano Letters* **17**, 544 (2017).
- [12] H. Kim et al., *Advanced Energy Materials* **7**, 1700098 (2017).
- [13] K. Chihara, A. Katogi, K. Kubota, and S. Komaba, *Chemical Communications* **53**, 5208 (2017).
- [14] C. Zhang et al., *Advanced Functional Materials* **27**, 1604307 (2017).
- [15] L. Xue et al., *Journal of the American Chemical Society* **139**, 2164 (2017).
- [16] X. Bie, K. Kubota, T. Hosaka, K. Chihara, and S. Komaba, *Journal of Materials Chemistry A* **5**, 4325 (2017).

- [17] Z. Jian, Z. Xing, C. Bommier, Z. Li, and X. Ji, *Advanced Energy Materials* **6**, 1 (2016).
- [18] R. A. Adams et al., *ACS Applied Materials & Interfaces* **9**, 17872 (2017).
- [19] Y. Li et al., *Journal of The Electrochemical Society* **164**, A1234 (2017).
- [20] X. Wang et al., *Nanoscale* **9**, 18216 (2017).
- [21] M. Naguib et al., *Chemical Communications* **53**, 6883 (2017).
- [22] X. Wang et al., *Nature Communications* **6**, 6544 (2015).
- [23] Z. Jian, W. Luo, and X. Ji, *Journal of the American Chemical Society* **137**, 11566 (2015).
- [24] S. Komaba, T. Hasegawa, M. Dahbi, and K. Kubota, *Electrochemistry Communications* **60**, 172 (2015).
- [25] W. Luo et al., *Accounts of Chemical Research* **49**, 231 (2016).
- [26] J. Zhao, X. Zou, Y. Zhu, Y. Xu, and C. Wang, *Advanced Functional Materials* **26**, 8103 (2016).
- [27] M.-T. F. Rodrigues et al., *Nature Energy* **2**, 17108 (2017).
- [28] S. Zhang, K. Xu, and T. Jow, *Electrochimica Acta* **48**, 241 (2002).
- [29] M. Petzl, M. Kasper, and M. A. Danzer, *Journal of Power Sources* **275**, 799 (2015).
- [30] M. Levi, C. Wang, J. Gnanaraj, and D. Aurbach, *Journal of Power Sources* **119-121**, 538 (2003).
- [31] T. Waldmann, M. Wilka, M. Kasper, M. Fleischhammer, and M. Wohlfahrt-Mehrens, *Journal of Power Sources* **262**, 129 (2014).
- [32] Q. Wang et al., *Journal of Power Sources* **208**, 210 (2012).
- [33] R. A. Adams, A. Varma, and V. G. Pol, *Journal of Power Sources* **375**, 131 (2018).
- [34] D. Juarez-Robles, C.-F. Chen, Y. Barsukov, and P. P. Mukherjee, *Journal of The Electrochemical Society* **164**, A837 (2017).
- [35] R. Gnanamuthu and C. W. Lee, *Materials Chemistry and Physics* **130**, 831 (2011).
- [36] C. K. Huang, J. S. Sakamoto, J. Wolfenstine, and S. Surampudi, *Journal of The Electrochemical Society* **147**, 2893 (2000).
- [37] S. Müller et al., *Journal of The Electrochemical Society* **165**, A339 (2018).
- [38] T. L. Kulova and A. M. Skundin, *Russian Journal of Electrochemistry* **42**, 251 (2006).

- [39] T. L. Kulova, A. M. Skundin, E. A. Nizhnikovskii, and A. V. Fesenko, *Russian Journal of Electrochemistry* **42**, 259 (2006).
- [40] P. Yu, *Journal of The Electrochemical Society* **146**, 8 (1999).
- [41] K. Nobuhara, H. Nakayama, M. Nose, S. Nakanishi, and H. Iba, *Journal of Power Sources* **243**, 585 (2013).
- [42] S. Zhang, K. Xu, and T. Jow, *Electrochimica Acta* **49**, 1057 (2004).
- [43] K. Xu, Y. Lam, S. S. Zhang, T. R. Jow, and T. B. Curtis, *The Journal of Physical Chemistry C* **111**, 7411 (2007).
- [44] M. Steinhauer, S. Risse, N. Wagner, and K. A. Friedrich, *Electrochimica Acta* **228**, 652 (2017).
- [45] M. Hess, *Journal of The Electrochemical Society* **165**, A323 (2018).
- [46] E. de la Llave et al., *Israel Journal of Chemistry* **55**, 1260 (2015).
- [47] T. A. Pham, K. E. Kweon, A. Samanta, V. Lordi, and J. E. Pask, *The Journal of Physical Chemistry C* **121**, 21913 (2017).
- [48] Y. Chen et al., *Journal of The Electrochemical Society* **164**, A2000 (2017).
- [49] D. Abraham et al., *Electrochemistry Communications* **4**, 620 (2002).
- [50] W. Waag, S. Käbitz, and D. U. Sauer, *Applied Energy* **102**, 885 (2013).
- [51] Q. Liu et al., *RSC Advances* **6**, 88683 (2016).
- [52] N. Xiao, W. D. McCulloch, and Y. Wu, *Journal of the American Chemical Society* **139**, 9475 (2017).
- [53] M. Hess, *Electrochimica Acta* **244**, 69 (2017).
- [54] R. Yazami and Y. Reynier, *Electrochimica Acta* **47**, 1217 (2002).
- [55] T. Utsunomiya, O. Hatozaki, N. Yoshimoto, M. Egashira, and M. Morita, *Journal of Power Sources* **196**, 8598 (2011).
- [56] Y. Lei et al., *ACS Applied Energy Materials* **1**, 1828 (2018).
- [57] W. Zhang, W. K. Pang, V. Sencadas, and Z. Guo, *Joule* , 1 (2018).

## 6. MATERIALS BY DESIGN: TAILORED MORPHOLOGY AND STRUCTURES OF CARBON ANODES FOR ENHANCED BATTERY SAFETY

Material synthesis, characterization, and electrochemical testing was carried out by Ryan A. Adams. Modeling was performed by Aashutosh N. Mistry. The content in this chapter has been submitted for publication: R. A. Adams\*, A. N. Mistry\*, P. P. Mukherjee, V. G. Pol, *ACS Applied Materials and Interfaces*, 2019.

### 6.1 Summary

Next generation Li-ion battery technology awaits materials that not only store more electrochemical energy at finite rates but have superior control over side reactions and better thermal stability. Herein, we hypothesize that designing an appropriate particle morphology can provide a well-balanced set of physicochemical interactions. Given the anode-centric nature of primary degradation modes, we investigate three different carbon particles - commercial graphite, spherical, and spiky carbon, and analyze the correlation between particle geometry and functionality. Intercalation dynamics, side reaction rates, self-heating, and thermal abuse behavior have been studied. It is revealed that the spherical particle outperforms an irregular one (commercial graphite) under thermal abuse conditions, as it eliminates unstructured inhomogeneities. A spiky particle with ordered protrusions exhibits smaller intercalation resistance and attenuated side reactions, thus outlining the potential for controlled stochasticity. Such findings emphasize the importance of tailoring particle morphology to proffer selectivity among multimodal interactions

## 6.2 Introduction

Despite the long history of commercialization,[1, 2] next generation lithium ion battery technology[3, 4, 5, 6, 7, 8] faces three key challenges: (1) insufficient volume/ weight specific performance (2) cycle life and (3) safety risks. Scientifically, these directly relate to intercalation dynamics, uncontrolled side reactions, and internal heat generation. Lithium ion batteries are fundamentally multiscale systems where physicochemical interactions are strongly correlated across multiple length scales.[9] Traditional approaches have been quite disparate in their treatment of these concerns. For example, thermal management systems are often employed to constrain global temperature rise and represent a cell-level strategy. Alternatively, solutions such as electrolyte additives, functionalized binder, and particle coatings have also been employed to alter the behavior of the electrode-electrolyte interface (to mitigate degradation) and/or the bulk electrolyte response (to modulate thermal runaway). These are electrode-scale materials solutions and often they result in a compromise in terms of primary battery function, i.e., electrochemical energy storage.[10, 11, 12, 13, 14, 15, 16, 17]

Active material (e.g., graphite) is responsible for assimilating the electrochemical energy as well as the irreversible changes (in part). Hence, if intrinsic active material characteristics are targeted, it has the potential to considerably alter the energy storage landscape.[18, 19, 20, 21, 22, 23, 24, 25, 26, 27] Past studies reveal a nonmonotonic dependence on active material dimensions where larger particles are prone to mechanical degradation arising from intercalation induced stress and smaller nanoscale morphologies promotes chemical degradation, for example, excessive solid electrolyte interphase (SEI) formation.[28, 29, 30, 31, 32, 33, 34, 35] Here we investigate three distinct anode particle morphologies (Figure 6.1a-c) in terms of their multimodal interactions. Since in state-of-the-art Li-ion cells, degradation (intercalation-induced stress, SEI formation, Li plating etc.) is primarily anode-centric, carbon (conventional anode) is studied.

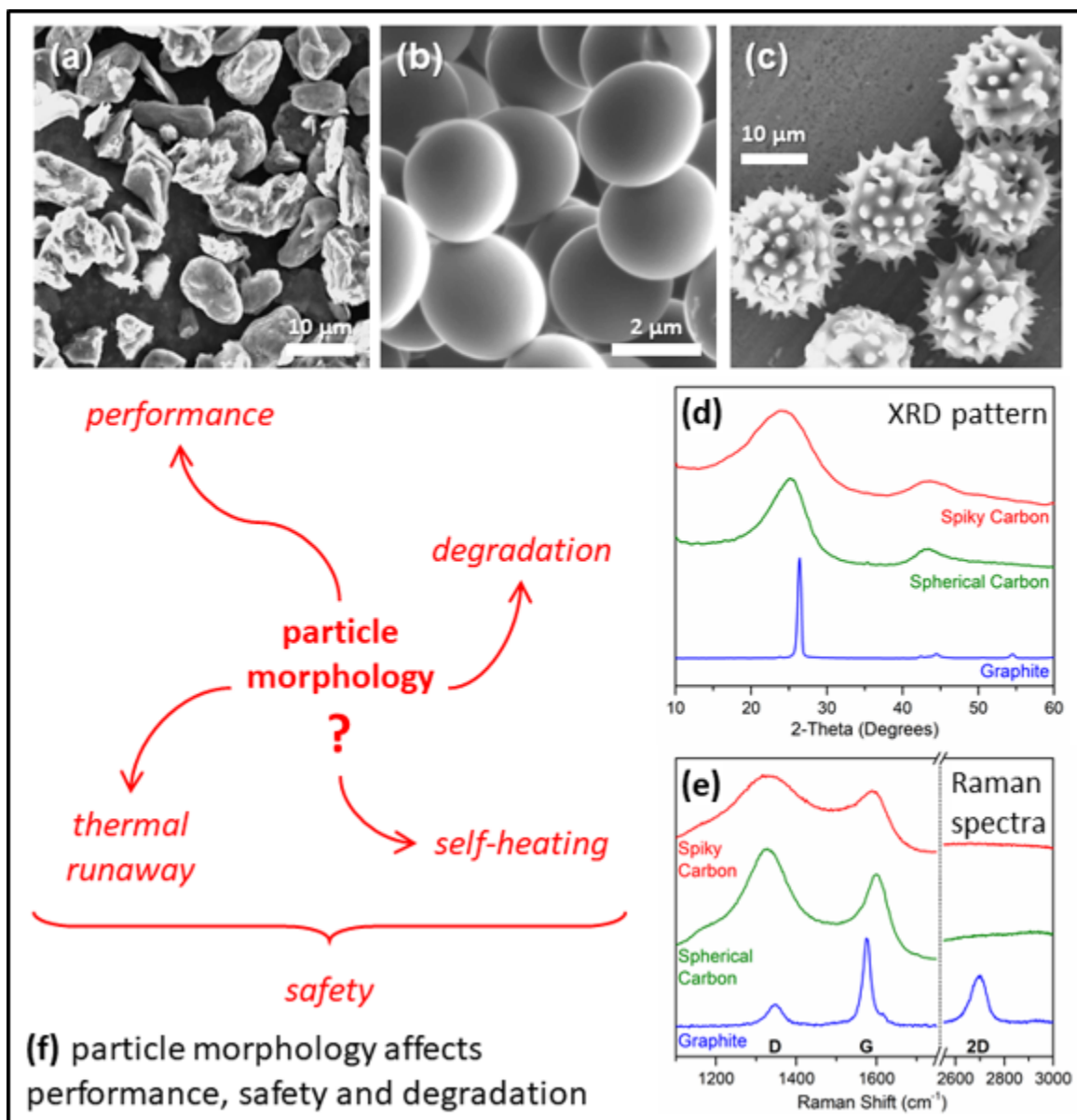


Figure 6.1. Different carbon-types studied here: (a) commercial graphite (b) spherical carbon and (c) spiky carbon. (a) and (c) are prepared in-house. Their (d) crystalline structure is examined by X-ray diffraction and (e) Raman spectroscopy. (f) Multimodal interactions related to particle morphology.

The commercial synthetic graphite has irregular particles (Figure 6.1a). Such geometrical irregularity fosters nonuniform intercalation dynamics and in turn localized

reactions.[36, 37] However, spherical particles (Figure 6.1b), given the absence of directional preference, should avoid the hot spot formation. A spiky particle (Figure 6.1c) represents an interesting possibility where controlled irregularity is introduced, while maintaining the spherical symmetry at large. Relevant materials and methods are summarized in the Supporting Information. Specific care has been exercised to ensure a proper comparison across these materials, e.g., using comparable electrode active material loading masses. The experiments are supplemented with mathematical analysis to understand inaccessible aspects such as reaction distribution and hot spot formation.

## 6.3 Results and Discussion

### 6.3.1 Materials Characterization

The morphologies of the three tested carbon materials are revealed via SEM imaging in Figure 6.1a-c. Commercial synthetic graphite particles (Figure 6.1a) showcase irregular and rough surfaces, with widely varying particle shape and size. In comparison, spherical carbon particles (Figure 6.1b), synthesized via autogenic reaction, exhibit smooth surfaces, with an average particle diameter of  $2.70 \mu\text{m} \pm 0.15 \mu\text{m}$ . These spherical particles are highly uniform in size and morphology, due to the nucleation and growth mechanism of the corresponding autogenic synthesis.[38] Carbon particles derived from the pyrolysis of bee pollen (Figure 6.1c), referred to as spiky carbon elsewhere in the text, have an average particle diameter of  $14.4 \mu\text{m} \pm 0.7 \mu\text{m}$ , and consist of a spherical core coated with numerous spikes. The designed morphologies of these micron-sized carbon particles were achieved by autogenic reaction of mesitylene to produce spherical carbon and pyrolysis of bee pollen biomass precursor to obtain spiky carbon material, as illustrated in prior studies.[26, 38, 39, 40] Given the constraints on particle synthesis, the spherical particle dimensions are different than the other two morphologies. The analysis of intercalation response discussed subsequently assist in isolating the purely morphological effects.

Furthermore, the nitrogen sorption isotherms were measured as shown in Figure D.1. Table D.1 summarizes the as obtained BET (Brunauer-Emmett-Teller) surface area for each material as well as the density functional theory (DFT) pore volume.[41] As seen in Table D.2, the graphite consists of mostly carbon (99%), whereas the spherical carbon contains 3 wt. % of hydrogen and oxygen heteroatoms from the mesitylene precursor. The spiky carbon consists of 94% carbon, with oxygen heteroatoms (2.8%) originating from the biomass source. For carbon anodes, the degree of crystallinity and carbon structuring plays a significant role in the lithium storage mechanism and electrochemical behavior and thus is important to characterize.[42, 43, 44] The XRD pattern for graphite in Figure 6.1d contains the characteristic (002) peak for the layered graphene sheets at a  $2\theta$  of  $26.4^\circ$ , resulting in an inter-lattice spacing of 0.347 nm via Bragg's law. In contrast, the spherical and spiky carbons demonstrate broad (002) peaks, indicating amorphous carbon characterized by defects, heteroatoms, and  $sp^3$  hybridization, as expected from the low pyrolysis temperature. The (002) peak for spherical carbon is centered at  $25.1^\circ$ , for an average inter-lattice spacing of 0.363 nm, in contrast to  $24.5^\circ$  and 0.371 nm for spiky carbon. Raman spectra were collected for these carbon materials, as shown in Figure 6.1e. The G band  $1580\text{ cm}^{-1}$  correlated to  $sp^2$  hybridized carbon and the overtone 2D band at  $2700\text{ cm}^{-1}$  are prominent in graphite as expected. In contrast, the D band at  $1330\text{ cm}^{-1}$  related to  $sp^3$  hybridized non-graphitic carbon (due to heteroatoms, edge defects, etc.) is much more prominent for the spiky and spherical carbon.

### 6.3.2 Electrochemical Implications

To compare the electrochemical performance of these carbon materials, lithium ion half cells were constructed, with the charge-discharge voltage profiles for the first two cycles (C/10 rate) shown in Figure 6.2a-c. The graphite exhibits its characteristic low voltage intercalation plateau and a reversible capacity of  $345\text{ mAh g}^{-1}$  (approaching the theoretical capacity of  $372\text{ mAh g}^{-1}$ ). In comparison, spherical and spiky carbon anodes display sloping voltage profiles and reversible capacities of  $300\text{ mAh g}^{-1}$  and

240 mAh g<sup>-1</sup>, respectively. The first cycle Coulombic inefficiency (demonstrated by the red arrow) is attributed to SEI layer formation on the carbon anode surface. This occurs due to electrochemical degradation of surrounding electrolyte on the lithiated graphite surface until quasi-equilibrium is established (often referred to as the formation cycle capacity loss). On the other hand, SEI growth upon repeated cycling later is related to an electrochemical reaction. Graphite and spherical carbon show similar irreversible capacities of 19% and 28% respectively, while spiky carbon has a higher value of 50%. The first cycle capacity loss is known to depend on surface area as well as carbon structuring, favoring increased SEI layer formation for amorphous carbon materials. Thus, the much higher first cycle loss of spiky carbon as compared to graphite can be attributed to its increased surface area, heteroatoms, and hard carbon structuring.

Intercalation stability over repeated cycling is further probed using constant current cycling at a C/2 rate as shown in Figure 6.2d. Close to 100% Coulombic efficiencies are observed, pointing to structural stability. By cycle 100, specific capacities of 240 mAh g<sup>-1</sup>, 250 mAh g<sup>-1</sup>, and 230 mAh g<sup>-1</sup> are obtained for graphite, spherical carbon, and spiky carbon, respectively. A separate rate study was performed (Figure D.2), with the capacity retention plotted in Figure 6.2e. The spiky carbon exhibits consistently higher rate capability than spherical carbon. Further full cells with LiCoO<sub>2</sub> cathode are tested to identify how anode morphological variations translate to a full cell setting. Figure D.3 recognizes similar trends as Figure 6.2d, thus confirming the relevance of such effects. Electrochemical impedance spectroscopy (EIS) analysis was performed for each carbon material before and after aging (Figure D.4), with spectra shown in Figure 6.2f-h. Modeling to an equivalent circuit (Figure D.5) revealed that both the graphite and spherical carbon materials increased in cell impedance, coming from charge-transfer resistance and SEI resistance (Tables D.3 and D.4). Comparatively, the spiky carbon material exhibits minor change, indicating that the preferential intercalation at spikes and reduced overpotential, as predicted through modeling, mitigates cell aging at harsh cycling conditions.

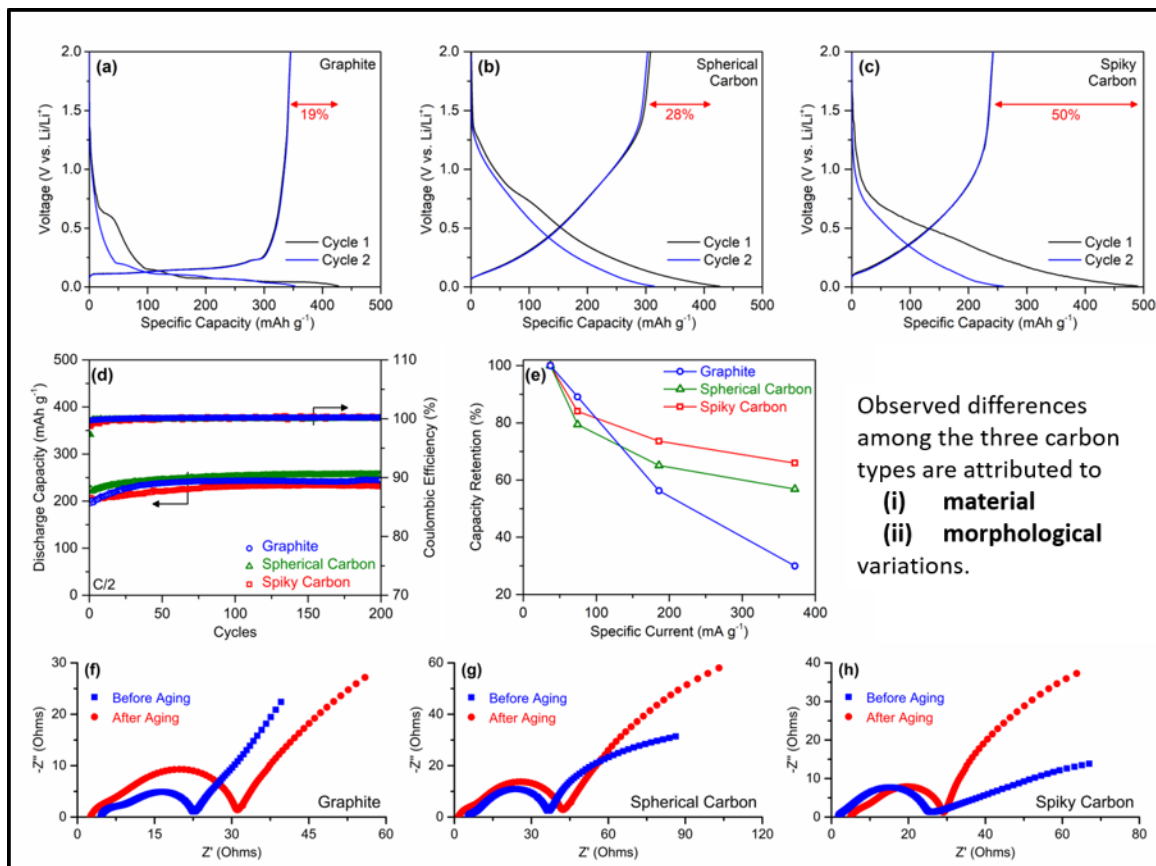


Figure 6.2. Electrochemical trends upon cycling. Initial cycles refer to the formation of a stable SEI film and accordingly large capacity variations are seen across all carbon types (a) graphite (b) spherical and (c) spiky. These tests are carried out at C/10. (d) Constant current cycling quantifies the capacity decay due to SEI growth on repeated cycling. (e) Capacity retention trends differ as SEI formation and intercalation dynamics vary across different particle types. Electrochemical impedance spectra of (f) graphite, (g) spherical carbon, and (h) spiky carbon. Cells were aged at 50°C for 100 cycles at 1C rate, and EIS was collected at 200 mV (vs. Li/Li<sup>+</sup>).

As revealed by Figure 6.2b-c (as well as Figure 6.1d-e) the intrinsic material characteristics for the two are similar, and in turn the electrochemical differences between the two in Figure 6.2d-e largely stem from geometrical features such as (i) different intercalation lengths (ii) morphology. To understand this intricate correlation between

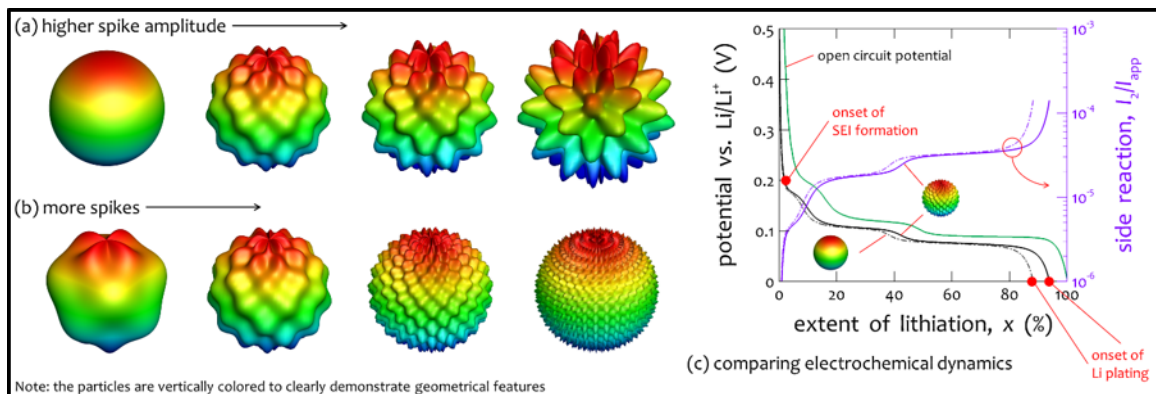


Figure 6.3. A spiky particle has two attributes (a) spike amplitude and (b) spike count. A spherical particle is a special instance of a spiky particle with vanishingly small spike amplitude. (c) Such geometrical features bring about complexities in the intercalation response which in turn affects side reaction rates.

surface features and intercalation dynamics, electrochemical dynamics was modeled for the spiky particles (Figure 6.3). These spikes (surface features) have two distinct attributes - length and count. Varying these two, one can obtain a range of particulate structures as shown in Figure 6.3a and 6.3b. Figure 6.3c compares potential evolution during intercalation for a spherical (smooth) and a spiky particle. These intercalations are carried out at identical rates (4C). A high rate (here 4C) is chosen to demonstrate the severity of these effects. The potentials are less than the open circuit potential (OCP) for a given state of (overall) lithiation as the intercalation flux is inwards. Both the profiles qualitatively match the OCP, with the potential of a spiky particle being closer to OCP. This indicates better electrochemical utilization, in terms of both the voltage as well as lithium storage. Carbon-based electrodes face two distinct modes of chemical degradation: (i) Solid electrolyte interphase (SEI) formation - 0.2 V reaction potential, and (ii) Lithium plating - 0.0 V reaction potential.

At any instant, the following identity holds (integration is performed over particle surface):

$$I_{app} = \int_S (i_{intercalation} + i_{side}) dS \quad (6.1)$$

where intercalation current refers to lithiation (a reversible reaction):

$$i_{intercalation} = k \sqrt{C_s C_e (C_s^{max} - C_s)} \left[ e^{\frac{F\eta}{2RT}} - e^{-\frac{F\eta}{2RT}} \right] = i_{intercalation}^0 \left[ e^{\frac{F(\phi-U)}{2RT}} - e^{-\frac{F(\phi-U)}{2RT}} \right] \quad (6.2)$$

and SEI formation reaction - an irreversible side reaction:

$$i_{side} = -i_{SEI}^0 e^{-\frac{F(\phi-U_{SEI})}{2RT}} \quad (6.3)$$

Since OCP for SEI reaction (Eqn. 6.3) is around 0.2 V, as soon as the particle potential drops below 0.2 V, SEI starts forming. The exchange current density,  $i_{SEI}^0$ , and OCP,  $U_{SEI}$ , are constants. Additionally, given the high electrical conductivity of carbon-based materials, no appreciable gradient exists in the solid phase potential,  $\phi$ . These assumptions amount to uniform SEI formation at different locations on the particle surface and the respective flux changes over time due to variation in the particle potential,  $\phi$ . Figure 6.3c also sketches this side reaction flux during intercalation. The total side reaction current is  $i_{side} = \int_S i_{side} dS$ . As the potential for the spherical particle is consistently lower than that for the spiky particle, the side reaction flux is higher for the spherical particle (Figure 6.3c). Moreover, since the spherical particle voltage drops to zero earlier, the onset of Li plating is earlier for the smooth spherical geometry. This is quite interesting since the introduction of these ordered geometrical features appears to improve intercalation behavior as well as subside the side reactions. Note that the two particles have similar volumes so the observed trends in Figure 6.3c clearly stem from morphological differences. These findings match with Figure 6.2e, where experimentally the spherical particle consistently under performs compared to the spiky one. Also note that Figure 6.2b-c quantify the initial (chemical) SEI formation, while SEI reaction (Eqn. 6.3) corresponds to capacity fade over repeated cycling. The capacity loss during formation cycling is a more complex phenomena, and accounts for the differences in Figure 6.2d,

while Figure 6.2e presents intercalation rate dependence once the formation cycles are over (i.e., normalized with respect to the stabilized capacity).

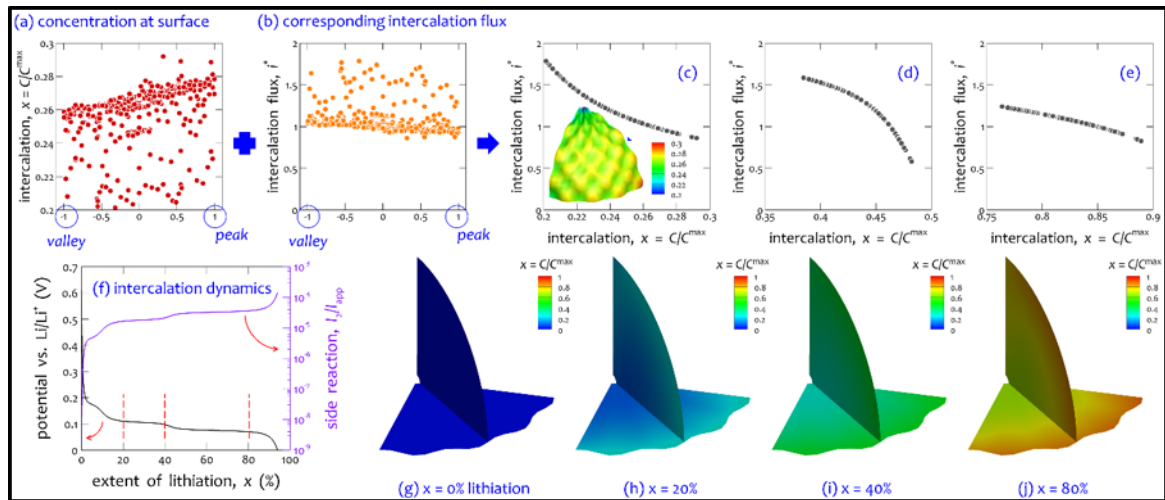


Figure 6.4. Intercalation nonuniformity due to geometrical features. (a) Concentration and (b) intercalation flux distribution on particle surface at 20% lithiation. (c) Corresponding intercalation flux as a function of concentration and surface map (inset). (d) and (e) show the progression of flux-concentration maps at higher lithiation extents, 40%, and 80%, respectively. (f) Potential evolution and contribution from side reaction. Concentration evolution upon lithiation in the interior of the particle (g) initial (h) 20% (i) 40% and (j) 80% lithiation. Vertical and horizontal sections are shown in (g) through (j).

To further understand the intercalation dynamics of a spiky particle, surface and bulk fields are sketched in Figure 6.4. First, consider the concentration distribution on the particle surface at 20% lithiation, as shown in Figure 6.4a. Surface points are identified by a dimensionless indicator where -1 refers to the valley, 0 to mean surface and 1 to peak locations. In general, the peak locations intercalate more than the valley points. This points to preferential intercalation as peak locations locally have more surface area available for reactions. Interestingly, not all the points at identical radial distances have identical intercalation. This is because the lateral dimensions of

the spikes are not identical and vary based on their surface location (refer to Figure 6.4c inset). This gives rise to overlapping lithiation fronts and breaks the symmetry. Next, refer to the local intercalation flux expression (Eqn. 6.2), where both the exchange current density and open circuit potential are dependent on local surface concentration. Also, given the high electronic conductivity, the entire particle is at a constant electric potential, (less than the smallest OCP during lithiation). At a given lithiation extent, the current distribution is dictated by the OCP variation as exponential terms represent a stronger nonlinearity (Eqn. (6.2)). As shown in Figure 6.3c, OCP decreases with lithiation. Hence, valley locations have a higher OCP and in turn a greater overpotential. This leads to a higher intercalation flux in valleys, with Figure 6.4b showing this distribution. As found in the concentration distribution, the intercalation flux also exhibits a nonmonotonic dependence on the radial location of the surface point. A clearer trend is obtained if intercalation flux is plotted against surface concentration (Figure 6.4c), where locations that are less intercalated have a higher intercalation flux. Figure 6.4c-e demonstrate the evolution of this flux - concentration relation with lithiation. Less intercalated locations consistently have a higher flux but the qualitative nature changes.

As a reference to the intercalation extent, Figure 6.4f presents the potential and side reaction flux evolution during the respective operation. Figure 6.4g-j provide a visual picture of the intercalation front propagation in the interior portions of the particles. The normalized lithium concentration,  $x = C/C^{max}$ , is plotted on vertical and horizontal planes. It appears that the intercalation front qualitatively follows a shape similar to the surface features. Note that these calculations only reveal the active material centered phenomena. In typical porous electrodes, secondary species as well as the electrolyte pore network contribute to overall dynamics.[45, 46, 47, 48, 49]

Revisit Figure 6.3c where the potential profiles largely differ during the transition stages for graphite. Graphite characteristically has three voltage plateaus, each of which correspond to a particular lithiation window. For a spherical particle, surface

concentration is uniform, and the voltage transitions take place simultaneously for all the points on the surface (recall that the OCP is a function of surface concentration). On the other hand, for a particle with surface protrusions, preferential intercalation takes place, and consequently about the transition points on the OCP profile (Figure 6.3c), surface inhomogeneity of the state of lithiation causes a prolonged transition. When the all the lithiation points are in the same plateau, the behavioral difference originates from difference in surface area. In either of the stages, the disparity grows with the operating current.

### 6.3.3 Inhomogeneity in Self-heating

When an intercalation reaction takes place, a portion of the reaction enthalpy gets stored electrochemically (correlated to OCP evolution with lithiation) and part dissipates as heat. This remaining portion is referred to as the reversible heat and is quantified as:

$$q_{reversible} = -i_{intercalation} T \frac{\partial U}{\partial T} \quad (6.4)$$

Additionally, to sustain a finite rate of electrochemical reactions, a penalty is incurred in the form of reaction overpotential that eventually manifests as heat generation at the active interface:

$$q_{kinetic} = -i_{intercalation} \eta \quad (6.5)$$

Intercalation flux ( $i_{intercalation}$ ), entropic coefficient  $\partial U/\partial T$ , and overpotential ( $\eta$ ), all depend on the local surface concentration, and in turn the heat generation rates also exhibit a location dependence. Figure 6.5 presents this progression with lithiation. First, consider the evolution of overpotential as shown in Figure 6.5a-d. At the start of intercalation, the concentration field is uniform and in turn, a constant overpotential exists (Figure 6.5a). Initially, the exchange current density is very low due to an inverse - quadratic dependence on lithium concentration (Eqn. 6.2). This leads to a fairly high reaction overpotential (50 mV). Exchange current density reaches its maxima at 50% lithiation, hence going from Figure 6.5a-c, the average color shifts

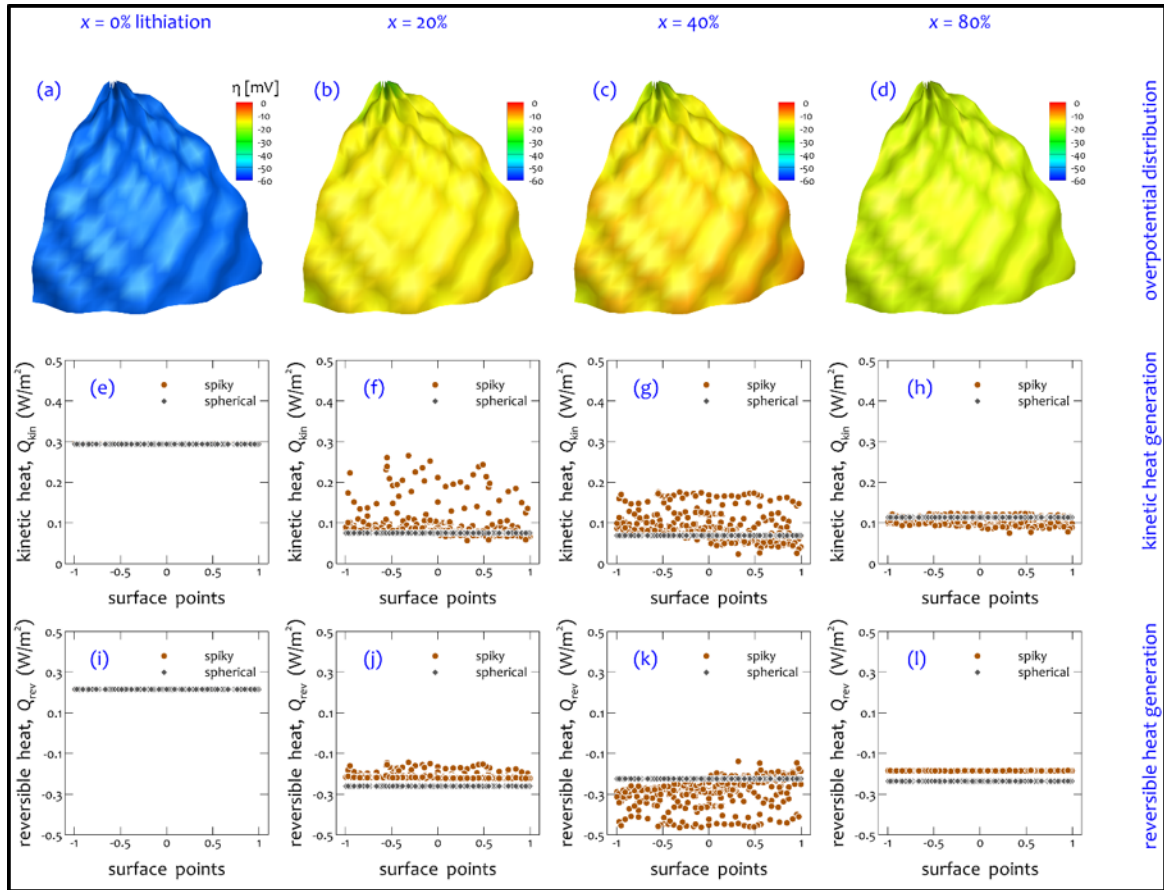


Figure 6.5. Progression of (a) - (d) local overpotential (e) - (h) kinetic and (i) - (l) reversible heat generation rates as lithiation takes place. The inhomogeneity translates to all the different fields and is observable during intermediate stages of lithiation. For comparison, states of an equivalent spherical particle are also shown. A spherical particle has a uniform surface state.

towards smaller overpotentials. The overpotential inhomogeneity is visible in these maps. Again beyond 50% lithiation, exchange current density decreases and equivalently average overpotential rises (Figure 6.5d). The remaining plots in Figure 6.5 demonstrate the evolution of kinetic heat (Figure 6.5e-h) and reversible heat (Figure 6.5i-l). For comparison, corresponding heat generation rate distribution of an equivalent spherical particle is also sketched simultaneously. As mentioned earlier, at the

onset of intercalation, the concentration field is uniform and in turn, every other field variable is spatially invariant. Hence, the respective data points overlap in Figure 6.5e and 6.5i. As lithiation proceeds, heat generation rates for the spiky particle exhibit spatial variations, while spherical particle continues to exhibit unique values (Figure 6.5f-h and Figure 6.5j-l). Given the nonlinear coupling between the lithiation fields and the heat generation modes, the average heat generation rate in the spiky particle is different than the singular value for the spherical particle. Also, the peak or the valley locations do not necessarily demonstrate the extreme behavior, since as the intercalation progresses, diffusion fronts propagate and break such an ordering. Note that the spread in heat generation rate values changes non-monotonically with the extent of lithiation. A spiky particle does not necessarily experience a higher heat generation than its spherical counterpart during intercalation (Figure 6.5g vs. 6.5h). The evolution of kinetic and reversible heat generation rates is also nontrivial. Such complexities give rise to behavioral transitions as the rate of operation is varied since  $q_{kinetic}$  and  $q_{reversible}$  scale differently with C-rate.

As the present discussion focuses on the particle scale thermal response, transport heat related with the electrolyte transport resistance in the pore-network is not discussed here. The self-heating signature for the spiky particle, quantitatively described as  $Q_{particle} = Q_{kinetic} + q_{reversible}$ , exhibits a quadratic departure from the corresponding (equal volume) spherical particle. At the start of lithiation, the concentration distribution is uniform and in turn little disparity exists between the two in Figure 6.5e and 6.5i. The interfacial stochasticity present in the spiky particle causes nonuniform intercalation resistance which is apparent through the preferential intercalation patterns. This effectively leads to distributions in both the heat generation terms, as is apparent in Figures 6.5f, 6.5g, 6.5j, and 6.5k. The reversible heating can become negative based on the direction of entropy exchange and give rise to situations where the total particle heat for a spiky particle is less than the equivalent spherical active material (Figure 6.5g, 6.5k in contrast to 6.5f, 6.5j). Towards the end of lithiation, when most of the low intercalation resistance locations

are nearly lithiated, the lagging spots get filled predominantly. Such a reversal in lithiation preference is responsible for the decreased field inhomogeneities in Figures 6.4e and 6.5d, 6.5h, 6.5l.

#### 6.3.4 Thermal Abuse Behavior

The previous discussion compared the self-heating rates of different particle morphologies. On the other hand, there are certain thermally activated side reactions that can trigger at higher temperatures. Given their exothermic nature, if allowed to carry on, these reactions prove to be autocatalytic where heat generated due to one reaction increases the local temperature and further activates another reaction. In the worst case, if the generated heat is not dissipated quickly, it leads to extremely high temperatures and possible cell combustion (often called thermal runaway). Safety concerns for lithium ion batteries arise from such poor thermal stability of electrode and electrolyte materials.[50, 51] Typically, thermal runaway initiates from degradation reactions occurring on the graphite anode, where metastable species in the SEI undergo exothermic breakdown, initiating as early as 90°C.[52, 53, 54] Hence, the anodes thermal stability, in turn, affects the thermal runaway response of the entire cell.

In order to characterize these thermally activated reactions for the three carbon types, differential scanning calorimetry (DSC) analysis was carried out. Figure 6.6c presents the DSC profiles for these materials, with two characteristic exothermic peaks shown. The first one corresponds to the decomposition of metastable components in the SEI. At higher temperatures, the intercalated lithium starts reacting with the electrolyte in another exothermic reaction. DSC information is somewhat difficult to interpret, as the temperature is continuously increased (at a constant rate) and in turn, the next reaction may get triggered before the previous reaction proceeds to completion. Given this complexity, past studies resort to accelerated rate calorimetry (ARC) in order to fingerprint these thermally activated reactions.

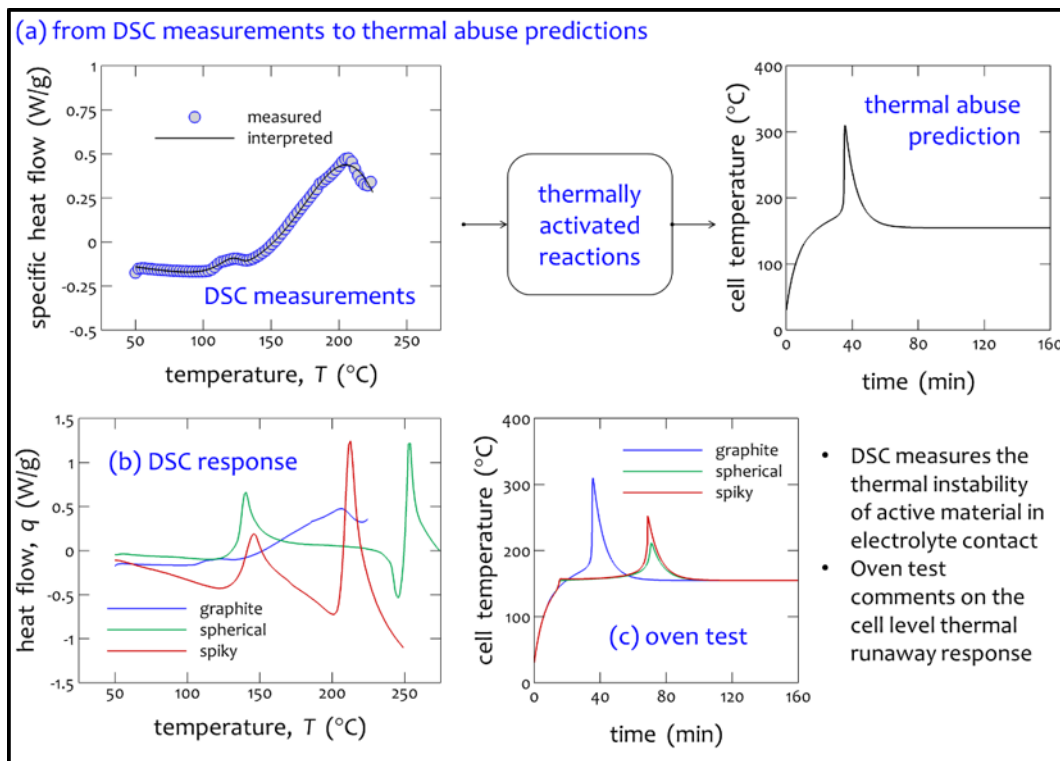


Figure 6.6. (a) Differential scanning calorimetry (DSC) captures the thermally activated reactions (endothermic and exothermic) of active material. This reaction information is further useful in estimating thermal abuse response of cells composed of the same active material. (b) DSC responses of the three carbon materials and corresponding (c) oven test trends. Note that a larger spike in the heat flow does not necessarily mean poorer thermal stability as reaction rate constant can change the rate of heat generation.

We have developed an inverse problem formulation to consistently interpret DSC data. For example, Figure 6.6a shows the DSC data for commercial graphite, along with the interpreted trend based on the inverse analysis. This gives us reaction information, essentially, the rate constant, activation energy (related to onset temperature) and reaction heat. While DSC comments on an individual materials thermal instability, this does not translate monotonically to the battery scale. For example, a battery with a lot of extra inert material will absorb all the heat generated due to thermally activated reactions and would never initiate thermal runaway. Given the sufficient

information regarding the abuse reactions, the cell-level thermal abuse tolerance can be predicted.

Figure 6.6a shows the thermal runaway response of a fully charged cylindrical cell with graphite anode and lithium cobalt oxide  $\text{LiCoO}_2$  cathode. Similar predictions have been carried out for other carbon materials by properly interpreting their DSC data (Figure 6.6b). Figure 6.6c presents the thermal abuse response of these materials. For a consistent comparison, identical active material loadings and cell dimensions are used. In other words, the observed differences purely stem from different carbon-types and is not contaminated by unequal loadings for example. Figure 6.6c reveals that the spherical carbon is the safest material as the smallest amount of heat is generated as well as the onset temperature for the thermal ramp is the highest. Also, notice a small kink in the temperature profiles (Figure 6.6c) for the spherical and spiky carbons. This results from an appreciable heat generation during SEI decomposition (visible in Figure 6.6b). But since the trigger temperatures for the second reaction between the intercalated Li and electrolyte are much higher, this does not trigger an early onset thermal runaway. In other words, sharper and taller peaks on DSC profile does not necessarily mean an inferior thermal stability. Thermal stability relies not only on reaction enthalpies but also on reaction rates and activation energies.

#### 6.4 Conclusions

Active material, the phase responsible for electrochemical energy storage, exhibits varying particle geometries. The physical aspects of the active particles dictate the distribution of intercalation flux and associated physicochemical complexations. Here we probe such morphological dependence of multimodal interactions responsible for observable battery characteristics, namely, performance, degradation and safety. Using complimentary experimental and analysis tools, we studied three distinct anode particle types: (i) irregular graphite, (ii) spherical carbon and (iii) spiky carbon. The irregular graphite exhibits poor rate dependence given the nonuniformity caused by particle geometry, as compared to a spherical carbon. Introducing controlled disor-

der, i.e., a spiky particle, results in a noncanonical response where improved particle electrolyte contact reduces the overpotential, enhances intercalation and attenuates the side reactions leading to better performance and slower capacity fade. Consequently, the self heating response also scales nonmonotonically with the particle surface features. However, the spiky particle demonstrates marginally poor thermal abuse response. In summary, tailored particle morphology provides a unique avenue to tuning particle scale energy storage through geometrical alterations.

## 6.5 Acknowledgements

The A-C010 LiCoO<sub>2</sub> cathodes were produced at the U.S. Department of Energys (DOE) CAMP (Cell Analysis, Modeling, and Prototyping) Facility, Argonne National Laboratory. The CAMP Facility is fully supported by the DOE Vehicle Technologies Program (VTP) within the core funding of the Applied Battery Research (ABR) for Transportation Program. VP and PPM wish to thank the Office of Naval Research (ONR) for supporting lithium ion battery safety work under the grant N00014-18-1-2397, and Dr. Michele Anderson from ONR for supporting this work. RA thanks the Bilisland Dissertation Fellowship for support.

## 6.6 References

- [1] D. H. Doughty and E. P. Roth, *Interface magazine* **21**, 37 (2012).
- [2] Q. Wang et al., *Journal of Power Sources* **208**, 210 (2012).
- [3] M. Armand and J. M. Tarascon, *Building better batteries*, 2008.
- [4] X. Feng et al., *Energy Storage Materials* **10**, 246 (2018).
- [5] M.-T. F. Rodrigues et al., *Nature Energy* **2**, 17108 (2017).
- [6] S. Sripad and V. Viswanathan, *Journal of The Electrochemical Society* **164**, E3635 (2017).
- [7] E. J. Cairns and P. Albertus, *Annual Review of Chemical and Biomolecular Engineering* **1**, 299 (2010).
- [8] T. M. Bandhauer, S. Garimella, and T. F. Fuller, *Journal of The Electrochemical Society* **158**, R1 (2011).

- [9] C.-F. Chen, P. Barai, and P. P. Mukherjee, *Current Opinion in Chemical Engineering* **13**, 82 (2016).
- [10] Y. E. Hyung, D. R. Vissers, and K. Amine, *Journal of Power Sources* **119-121**, 383 (2003).
- [11] G. G. Eshetu et al., *Electrochimica Acta* **102**, 133 (2013).
- [12] C. Forestier et al., *Journal of Power Sources* **330**, 186 (2016).
- [13] J. Vetter et al., *Journal of Power Sources* **147**, 269 (2005).
- [14] V. Agubra and J. Fergus, *Materials* **6**, 1310 (2013).
- [15] T. Daggar et al., *Journal of Power Sources* **396**, 519 (2018).
- [16] J. B. Habedank et al., *Journal of The Electrochemical Society* **165**, A1563 (2018).
- [17] Y.-S. Park, T.-W. Lee, M.-S. Shin, S.-H. Lim, and S.-M. Lee, *Journal of The Electrochemical Society* **163**, A3078 (2016).
- [18] H. Fujimoto, K. Tokumitsu, A. Mabuchi, N. Chinnasamy, and T. Kasuh, *Journal of Power Sources* **195**, 7452 (2010).
- [19] P. Zheng et al., *RSC Advances* **5**, 40737 (2015).
- [20] V. G. Pol and M. M. Thackeray, *Energy and Environmental Science* **4**, 1904 (2011).
- [21] E. Ventosa et al., *Electrochimica Acta* **65**, 22 (2012).
- [22] L. Wang, Z. Schnepf, and M. M. Titirici, *Journal of Materials Chemistry A* **1**, 5269 (2013).
- [23] A. D. Roberts, X. Li, and H. Zhang, *Chem. Soc. Rev.* **43**, 4341 (2014).
- [24] E. M. Lotfabad et al., *ACS Nano* **8**, 7115 (2014).
- [25] S. Goriparti et al., *Journal of Power Sources* **257**, 421 (2014).
- [26] J. Tang, V. Etacheri, and V. G. Pol, *Scientific Reports* **6**, 20290 (2016).
- [27] J. Tang, V. Etacheri, and V. G. Pol, *ACS Sustainable Chemistry & Engineering* **4**, 2624 (2016).
- [28] M. N. Richard and J. Dahn, *Journal of The Electrochemical Society* **146**, 2068 (1999).
- [29] F. Joho, P. Novak, and M. E. Spahr, *Journal of The Electrochemical Society* **149**, A1020 (2002).
- [30] Y.-S. Park and S.-M. Lee, *Electrochimica Acta* **54**, 3339 (2009).
- [31] C.-K. Back and J. Prakash, *Thermochimica Acta* **520**, 93 (2011).
- [32] M. Gauthier et al., *The Journal of Physical Chemistry Letters* **6**, 4653 (2015).

- [33] R. A. Adams et al., *Industrial & Engineering Chemistry Research* **55**, 8706 (2016).
- [34] O. Fromm et al., *Carbon* **128**, 147 (2018).
- [35] K. Kim et al., *Carbon* **133**, 62 (2018).
- [36] S. J. Harris and P. Lu, *The Journal of Physical Chemistry C* **117**, 6481 (2013).
- [37] N. Ghanbari, T. Waldmann, M. Kasper, P. Axmann, and M. Wohlfahrt-Mehrens, *The Journal of Physical Chemistry C* **120**, 22225 (2016).
- [38] H. Gershi, A. Gedanken, H. Keppner, and H. Cohen, *Carbon* **49**, 1067 (2011).
- [39] V. G. Pol, J. M. Calderon-Moreno, P. J. Chupas, R. E. Winans, and P. Thiyagarajan, *Carbon* **47**, 1050 (2009).
- [40] V. G. Pol, J. M. Calderon-Moreno, and P. Thiyagarajan, *Industrial & Engineering Chemistry Research* **48**, 5691 (2009).
- [41] M. Thommes et al., *Pure and Applied Chemistry* **87**, 1051 (2015).
- [42] K. Sato, M. Noguchi, A. Demachi, N. Oki, and M. Endo, *Science* **264**, 556 (1994).
- [43] J. R. Dahn, T. Zheng, Y. Liu, and J. S. Xue, *Science* **270**, 590 (1995).
- [44] J. Kang, H.-V. Kim, S.-A. Chae, and K.-H. Kim, *Small* **14**, 1704394 (2018).
- [45] A. Mistry, D. Juarez-Robles, M. Stein, K. Smith, and P. P. Mukherjee, *Journal of Electrochemical Energy Conversion and Storage* **13**, 031006 (2016).
- [46] M. Stein, A. Mistry, and P. P. Mukherjee, *Journal of The Electrochemical Society* **164**, A1616 (2017).
- [47] G. J. Nelson et al., *Journal of The Electrochemical Society* **164**, A1412 (2017).
- [48] P. P. Mukherjee, A. N. Mistry, and K. Smith, *Meeting Abstracts MA2018-01*, 1323 (2018).
- [49] A. N. Mistry, K. Smith, and P. P. Mukherjee, *ACS Applied Materials & Interfaces* **10**, 6317 (2018).
- [50] J.-i. Yamaki et al., *Journal of Power Sources* **119-121**, 789 (2003).
- [51] O. S. Mendoza-Hernandez, H. Ishikawa, Y. Nishikawa, Y. Maruyama, and M. Umeda, *Journal of Power Sources* **280**, 499 (2015).
- [52] A. D. Pasquier, *Journal of The Electrochemical Society* **145**, 472 (1998).
- [53] Q. Wang, J. Sun, X. Yao, and C. Chen, *Journal of The Electrochemical Society* **153**, A329 (2006).
- [54] Z. Chen et al., *Energy & Environmental Science* **4**, 4023 (2011).

## 7. ELECTROCHEMICAL PERFORMANCE OF MXENES AS K-ION BATTERY ANODES

The original publication of this work appears in *Chemical Communications*, volume 53, issue 51, 6883-6886. Material characterization, data analysis, and manuscript preparation was carried out by Ryan A. Adams and Michael Naguib. Material preparation was carried out by Michael Naguib. Electrochemical testing was carried out by Ryan A. Adams and Yunpu Zhao. XPS characterization and analysis was performed by Dmitry Zemlyanov.

DOI: 10.1039/C7CC02026K

### 7.1 Summary

Herein, we report on the electrochemical performance of two-dimensional transition metal carbonitrides as novel promising electrode materials in K-ion batteries. Titanium carbonitride,  $\text{Ti}_3\text{CNT}_z$ , was investigated in detail using electrochemical galvanostatic cycling at various current densities. X-ray diffraction and X-ray photoelectron spectroscopy were used to study the potassiation mechanism and its structural changes.

### 7.2 Introduction

With the growth of rechargeable batteries for electronic devices, electric vehicles and microgrid applications, there has been growing concern about the sustainability and cost of lithium (Li), which is the most widely used material for intercalation batteries. Therefore, in the last decade, there has been rapid progress in investigating metal-ion batteries beyond Li, such as Na and K. The large ionic radii of both Na

and K as compared to Li (0.76, 1.02 and 1.38 Å for Li<sup>+</sup>, Na<sup>+</sup> and K<sup>+</sup>, respectively) limit the choices of host materials for them.

Two-dimensional (2D) materials offer many advantages as electrode materials for metal-ion batteries due to their large number of accessible active sites and short diffusion distance pathways.[1, 2] Recently, a new family of electrically conductive 2D transition metal carbides and carbonitrides, the so-called MXenes, were developed by etching atomically thin metal layers from MAX phases.[3, 4] The latter are layered ceramics with a composition of  $M_{n+1}AX_n$ , where M is an early transition metal (e.g. Ti, V, Cr, Mo, and Nb), A is mostly from groups 13 and 14 (e.g. Al, Si, Sn, and Ga), X stands for carbon and/or nitrogen, and  $n = 1-3$ . [5] The etching process takes place in a fluoride containing aqueous solution.[6] Thus, the MXene surfaces are terminated with a mixture of O, OH, and F moieties (hereafter, this mixture of terminations is referred to as  $T_z$ ). To date, more than 15 different MXene compositions have been synthesized (e.g.  $Ti_3C_2T_z$ ,  $Ti_2CT_z$ ,  $Ti_3CNT_z$ ,  $V_2CT_z$ ,  $Nb_2CT_z$ , and  $Mo_2CT_z$ )[3, 4, 7, 8, 9] and many more are expected to be stable.[10]

One of the first applications for MXenes was their utilization as electrode materials for LIBs, where they exhibited exceptional performance, especially at high cycling rates.[7, 8, 11, 12, 13, 14] For example, when delaminated  $Mo_2CT_z$  was mixed with CNTs and tested as an electrode material, a reversible capacity of 560 mAh g<sup>-1</sup> at 0.4 A g<sup>-1</sup> and a reversible capacity of 76 mAh g<sup>-1</sup> at 10 A g<sup>-1</sup> over 1000 cycles were achieved.[8] More recently, MXenes were explored as electrode materials for Na-ion batteries and capacitors with promising performance.[15, 16, 17, 18] MXenes are also predicted to be capable of hosting other ions such as K<sup>+</sup>, Ca<sup>2+</sup>, [19] Mg<sup>2+</sup>, and Al<sup>3+</sup>. [18] Experimentally, there has been a single report exploring  $Ti_3C_2T_z$  in K-ion batteries (KIBs) by Xie *et al.*, [18] but in that report the electrode was a simple mixture of MXene and carbon black powders without any binder and was not cast on the current collector but was sprinkled on the separator. This was sufficient to show the possibility for  $Ti_3C_2T_z$  to host Na and K, but it was far from a practical battery electrode configuration and active material loading. Herein, we report for the first

time on the electrochemical performance of  $\text{Ti}_3\text{CNT}_z$ , an anode material for KIBs, and also explore  $\text{Ti}_3\text{C}_2\text{T}_z$  and  $\text{Nb}_2\text{CT}_z$  MXene phases.  $\text{Ti}_3\text{CNT}_z$  was selected since it showed exceptional performance as compared to  $\text{Ti}_3\text{C}_2\text{T}_z$  when tested in LIBs.[20]

### 7.3 Experimental

MXenes were synthesized by etching aluminum from their corresponding MAX phases. The detailed synthesis procedure can be found elsewhere.[3, 4, 7] Briefly, MAX phase powders with particle sizes less than 45 microns were immersed in aqueous hydrofluoric acid with various concentrations (as received concentration: 48%, Macron Fine Chemicals - Avantor Performance Materials, Center Valley, PA, USA) with a ratio of 1 g of powder:10 mL of HF solution. The etching time and HF concentrations varied from one MXene to the other;  $\text{Ti}_3\text{C}_2\text{T}_z$ -48% HF for 18 h,  $\text{Nb}_2\text{CT}_z$ -48% HF for 92 h, and  $\text{Ti}_3\text{CNT}_z$ -30% HF for 18 h (all at room temperature under continuous stirring). The etching conditions used here were selected based on previous reports to achieve the highest conversion from MAX phases to MXenes with minimum MXene dissolution in the acid.[4, 7] After etching the powders were washed as described in Appendix E.

Electrode slurries were prepared with a ratio of 75 wt% MXenes, 15 wt% conductive carbon additive (Timcal Super C65), and 10 wt% polymer binder, polyvinylidene fluoride (PVDF), using N-methyl-2-pyrrolidone (NMP) as a solvent. The resulting electrodes have an active material loading of  $1.75 \text{ mg cm}^{-2}$  (more details about the electrode preparation are provided in Appendix E).

### 7.4 Results and Discussion

At  $20 \text{ mA g}^{-1}$  (Fig. 7.1a), the  $\text{Ti}_3\text{CNT}_z$  electrode exhibited a 1st cycle potassiation capacity of  $710 \text{ mAh g}^{-1}$  and a 1st cycle de-potassiation capacity of  $202 \text{ mAh g}^{-1}$  ( $1.5 \text{ K}^+$  per  $\text{Ti}_3\text{CNOF}$ ) with a first cycle efficiency of 28.4%. The 2nd cycle resulted in a discharge capacity of  $275 \text{ mAh g}^{-1}$  and a charge capacity of  $154 \text{ mAh g}^{-1}$  with a cycle

efficiency of 56%. Then, as shown in Fig. 7.1c, the capacity faded during cycling until it reached  $75 \text{ mAh g}^{-1}$  after 100 cycles, which correlated with  $0.6 \text{ K}^+$  per  $\text{Ti}_3\text{CNOF}$ . The capacity obtained here is comparable to that reported for a carbon nanofiber anode (a 1st cycle capacity of  $700 \text{ mAh g}^{-1}$  and a reversible capacity of  $75 \text{ mAh g}^{-1}$  after 20 cycles).[21] The  $dQ/dV$  plot (Fig. 7.1b) indicates three peaks at 1.25, 0.81, and 0 V during the first potassiation cycle, with the corresponding de-potassiation peaks (inset in Fig. 7.1b) at 1.50, 0.80, and 0.50 V, respectively. The intensity of the potassiation peaks at 1.25 V and 0.80 V decreased significantly for the 2nd cycle and vanished completely after 50 cycles. While the potassiation peak close to 0 V and the corresponding de-potassiation peak at 0.50 V were still dominant for the 2nd cycle, after 50 cycles the de-potassiation peak became broader and shifted to 0.25 V.

The large 1st cycle irreversible capacity was observed for MXenes when tested in both LIBs and Na-ion batteries and was explained by the irreversible reaction of the alkali metal with the surface moieties of MXenes, water trapped between the MXene layers, or the etching products.[11, 12, 17] The same analogy is valid here when K is used instead of Li and Na. It is highly plausible that the MXene surface may have ample defect and passivation sites where K-ions can get trapped irreversibly, contributing to higher irreversible capacity loss. Additional factors such as decomposition of the electrolyte and formation of a solid electrolyte interphase (SEI) may contribute to this irreversibility.[17] X-ray photoelectron spectroscopy (XPS) was performed for pristine, fully discharged (5 mV), and fully charged (3 V) electrodes to probe the SEI layer composition, with their elemental composition described in Table E.1. The K 2p peaks, as shown in Fig. E.1, at 5 mV (24.4 at%) are similar to those at 3 V (23.9 at%), suggesting significant SEI formation of  $\text{K}_2\text{CO}_3$ , KF, and other species that can explain the large first cycle capacity loss.

The rate capability was analyzed at current densities from 10 to  $500 \text{ mA g}^{-1}$  (Fig. 7.1d) starting from cycle 3. After 10 cycles,  $\text{Ti}_3\text{CNT}_z$  exhibited a charge capacity of  $90 \text{ mAh g}^{-1}$  at  $10 \text{ mA g}^{-1}$ , which decreases with higher specific currents ( $65 \text{ mAh g}^{-1}$  at  $50 \text{ mA g}^{-1}$ ,  $52 \text{ mAh g}^{-1}$  at  $100 \text{ mA g}^{-1}$ ,  $42 \text{ mAh g}^{-1}$  at  $200 \text{ mA g}^{-1}$ , and

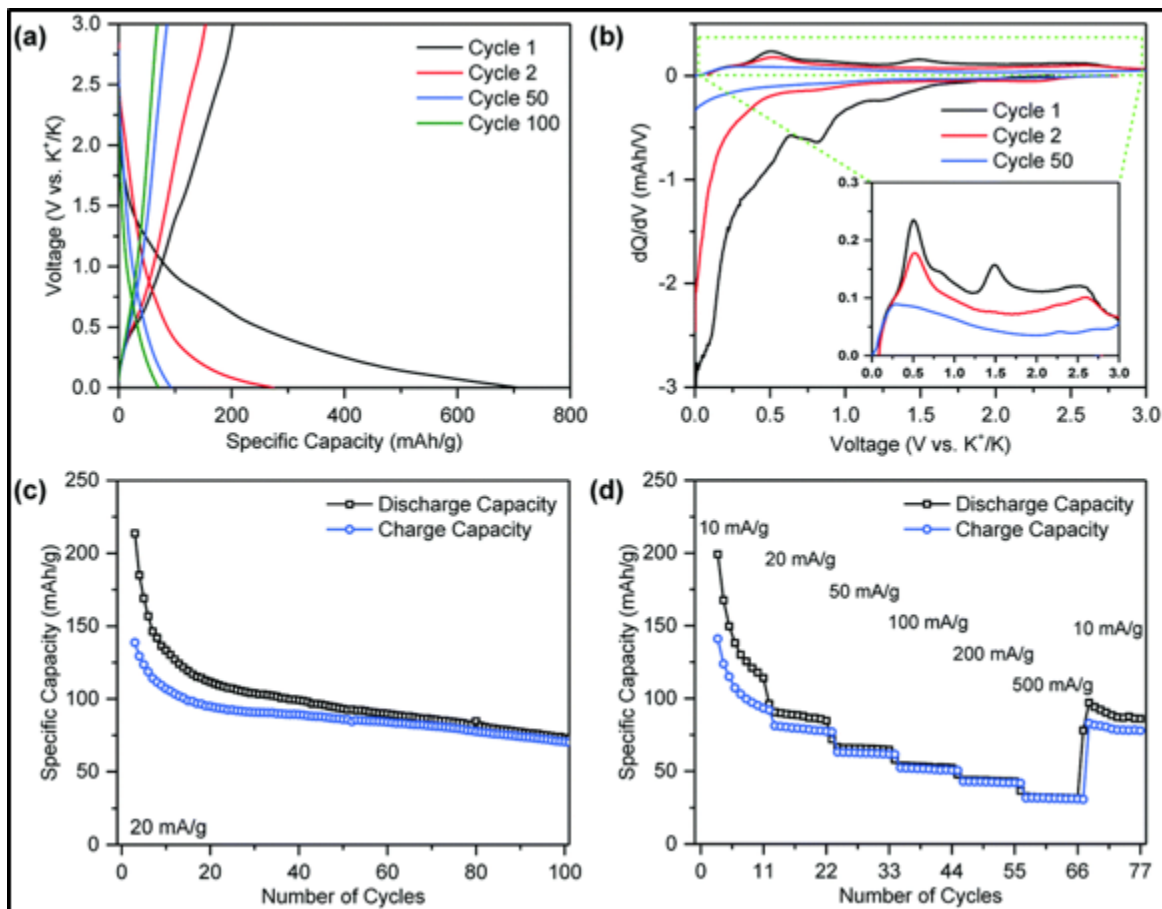


Figure 7.1. The electrochemical performance of the  $\text{Ti}_3\text{CNT}_z$  electrode. (a) Galvanostatic voltage profiles for cycles 1, 2, 50 and 100 at  $20 \text{ mA g}^{-1}$  between  $5.0 \text{ mV}$  and  $3.0 \text{ V}$ . (b) The corresponding  $dQ/dV$  for the results presented in 1a. The inset shows a higher magnification for the potassiation part of the plot in b. (c) Capacity vs. cycle number at  $20 \text{ mA g}^{-1}$ . (d) Capacity vs. cycle number at rates of 10 -  $500 \text{ mA g}^{-1}$ .

$32 \text{ mAh g}^{-1}$  at  $500 \text{ mA g}^{-1}$ ). While the specific capacity is low, the material shows excellent rate capability with minimal losses at high current densities (from 100 to  $500 \text{ mA g}^{-1}$ ), possibly due to the intercalation mechanism into the 2D MXene structure. Finally, it stabilizes back at a charge capacity of  $80 \text{ mAh g}^{-1}$  after returning to  $10 \text{ mA g}^{-1}$ , showing that the structure is maintained even after high cycling rates.

Although the capacity reported here is not as high as that reported for few-layer F-doped graphene, especially at high rates,[22] these results are encouraging for further investigation considering that the  $\text{Ti}_3\text{CNT}_z$  used in this study was as-synthesized multi-layers without any chemical modification. It is well established that delaminated MXenes exhibit a much higher capacity than the as-synthesized multi-layers when tested in Li and Na ion batteries.[13]

The  $\text{N}_2$  adsorption-desorption isotherms of  $\text{Ti}_3\text{CNT}_z$  are shown in Fig. 7.2a. The specific surface area (SSA) of  $\text{Ti}_3\text{CNT}_z$  was calculated using the BET equation[23] and was found to be around  $6 \text{ m}^2 \text{ g}^{-1}$ . Thus, it is reasonable to conclude that the measured capacity cannot be simply explained by adsorption of K-ions on the outer surface of MXenes. X-ray diffraction (XRD) was used to shed light on the changes in the MXene structure when cycled in KIBs. Fig. 7.2b shows the XRD patterns for  $\text{Ti}_3\text{CNT}_z$  electrodes: as-synthesized, fully discharged to 5 mV, recharged back to 3 V, and after 100 cycles.

The main broad diffraction peak in all the XRD patterns is the (0002) peak of  $\text{Ti}_3\text{CNT}_z$ . This peak shifted from a  $2\theta$  of  $7.83^\circ$  (c-lattice parameter, c-LP, of  $22.58 \text{ \AA}$ ) to  $5.89^\circ$  (c-LP  $30.00 \text{ \AA}$ ) upon discharging from the open-circuit-voltage (OCV) to 5 mV. When the electrode was re-charged back to 3 V, the peak shifted up slightly to  $6.07^\circ$   $2\theta$  (c-LP of  $29.11 \text{ \AA}$ ), but it did not return back to its initial position. After 100 cycles the c-LP decreased to  $27.94 \text{ \AA}$ . Although the increase in the c-LP is more than 30% after the first cycle, this does not necessarily mean that the increase in the electrode thickness is that high, because the accordion-like MXene morphology (inset in Fig. 7.2) can accommodate large increases in the layers' thicknesses without much effect on the outer dimensions of the multi-layer particles. Also, the fact that no new peaks were observed suggests that the potassiation mechanism is intercalation based without conversion reactions. It is worth noting that the  $\text{Ti}_3\text{CNT}_z$  sample contained a small amount of the unreacted MAX phase with higher order, i.e.  $\text{Ti}_4\text{Al}(\text{C}_{1-x}\text{N}_x)_3$ , which had a small sharp peak at a  $2\theta$  of  $7.57^\circ$  which is represented by the \* sign in Fig. 7.2. This peak did not shift during cycling since the MAX phases are electrochemically

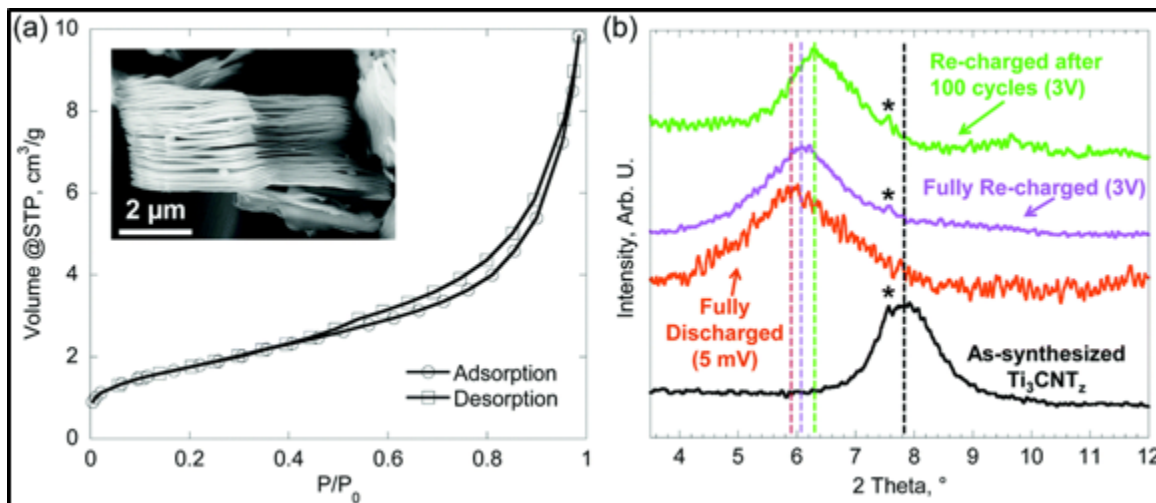


Figure 7.2. Nitrogen adsorption-desorption isotherms for  $\text{Ti}_3\text{CNT}_z$  measured at 77 K. The inset shows a typical SEM image for the as synthesized  $\text{Ti}_3\text{CNT}_z$  particle. (b) XRD patterns for  $\text{Ti}_3\text{CNT}_z$  electrodes that were as-synthesized (black), fully discharged from OCV to 5 mV (orange), re-charged to 3 V (purple), and cycled for 100 cycles (lime green). The vertical broken lines are for guiding the eye to show the changes in the peak position. The \* sign represents the peak position of the  $\text{Ti}_4\text{Al}(\text{C}_x\text{N}_{1-x})_3$  secondary phase.

inert to ion insertion, similar to what was observed for unreacted  $\text{Ti}_2\text{AlC}$  in the  $\text{Ti}_2\text{CT}_z$  sample when tested in LIBs.[11]

The XRD results are summarized in the schematic shown in Fig. 7.3. Unsurprisingly, during the 1st discharge cycle (potassiation), the potassium ions intercalated between the MXene sheets cause an increase in the c-lattice parameter. It is highly plausible that some of these potassium ions were trapped between the layers and could not be extracted by re-charging the battery back to 3 V, preventing the c-LP from returning to its initial value. This is in agreement with the large 1st cycle irreversibility discussed above, and with previous reports on MXenes when tested with Li[11] and Na.[24] The trapped potassium ions act as pillars between the MXene sheets that minimize large expansion/contraction during cycling. This in principle limits the breaking of the SEI formed every cycle and slows down the decomposition of the elec-

trolyte with cycling. The slight decrease in the c-LP after 100 cycles is most likely due to de-intercalation of a certain species from in-between the layers with extended cycling and/or time. The nature of this species is not obvious but it could be the solvent from the electrolyte that co-intercalated with the ions.[24]

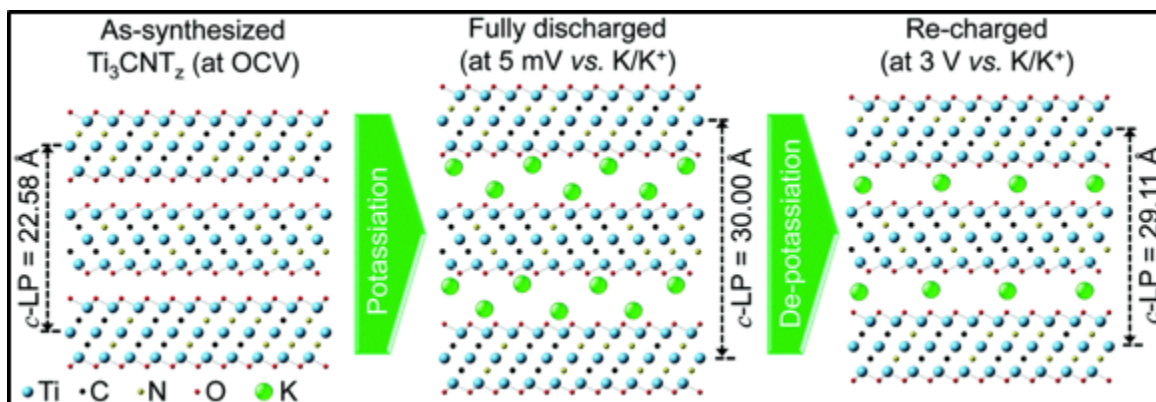


Figure 7.3. Schematic for the structure of  $\text{Ti}_3\text{CNO}_2$  before and after electrochemical potassiation and de-potassiation.  $\text{O}_2$  was used instead of  $\text{T}_z$  for simplicity (c-LP stands for the c-lattice parameter).

It is worth noting that when  $\text{Ti}_3\text{C}_2\text{T}_z$  and  $\text{Nb}_2\text{CT}_z$  were electrochemically cycled against K at  $20 \text{ mA g}^{-1}$  (Fig. E.2 and E.3), reversible capacities of  $30 \text{ mAh g}^{-1}$  were obtained for both materials after 50 cycles, as compared to  $90 \text{ mAh g}^{-1}$  in the case of  $\text{Ti}_3\text{CNT}_z$ . The superior performance of  $\text{Ti}_3\text{CNT}_z$  as compared to  $\text{Ti}_3\text{C}_2\text{T}_z$  can be attributed to the presence of nitrogen that is known to improve the electrochemical performance of other systems such as graphene due to enhanced conductivity.[25] Also,  $\text{Ti}_3\text{CNT}_z$  is predicted to store more electrons than  $\text{Ti}_3\text{C}_2\text{T}_z$ . [26]  $\text{Ti}_3\text{C}_2\text{T}_z$  shows an inferior rate capability compared to  $\text{Ti}_3\text{CNT}_z$ , with  $100 \text{ mA g}^{-1}$  decreasing the capacity to  $20 \text{ mAh g}^{-1}$ . Also, this is reflected in the electrochemical impedance spectroscopy data (Fig. E.4), with the  $\text{Ti}_3\text{CNT}_z$  electrode having lower charge transfer resistance as compared to  $\text{Ti}_3\text{C}_2\text{T}_z$ . The lower performance of  $\text{Ti}_3\text{C}_2\text{T}_z$  reported here compared to the previously reported performance by Xie *et al.*[18] ( $45 \text{ mAh g}^{-1}$  at  $100 \text{ mA g}^{-1}$ ) could be explained by the different electrode configurations. In the

present work the electrode materials were cast with a binder and carbon black with an active material loading of  $>1.5 \text{ mg cm}^{-2}$ , while in the previous work the electrode materials were mixed with 20% carbon black and sprinkled on the separator.

## 7.5 Conclusions

In conclusion, titanium carbonitride MXene,  $\text{Ti}_3\text{CNT}_z$ , showed encouraging performance as an anode material for K-ion batteries. At  $20 \text{ mA g}^{-1}$ , a first cycle capacity of  $710 \text{ mAh g}^{-1}$  was achieved that decreased to  $275 \text{ mAh g}^{-1}$  for the second cycle. After 100 discharge-charge cycles, a reversible capacity of  $75 \text{ mAh g}^{-1}$  was maintained. When cycled at a current density of  $10 \text{ mA g}^{-1}$ ,  $\text{Ti}_3\text{CNT}_z$  exhibited a stable capacity of  $90 \text{ mAh g}^{-1}$ , which decreased to  $65 \text{ mAh g}^{-1}$  at  $50 \text{ mA g}^{-1}$ , then further to  $42 \text{ mAh g}^{-1}$  at  $200 \text{ mA g}^{-1}$ , and finally to  $32 \text{ mAh g}^{-1}$  at  $500 \text{ mA g}^{-1}$ . X-ray diffraction showed an intercalation potassiation mechanism with an irreversible expansion in the c-lattice parameter upon potassiation of the first cycle. Other MXenes, viz.  $\text{Ti}_3\text{C}_2\text{T}_z$  and  $\text{Nb}_2\text{CT}_z$ , showed electrochemical activity for storing K but with decreased performance as compared to  $\text{Ti}_3\text{CNT}_z$ .

## 7.6 Acknowledgements

MN was supported by the Laboratory Directed Research and Development Program of the Oak Ridge National Laboratory, managed by UT-Battelle, LLC, for the U.S. Department of Energy. JN acknowledges support from the Assistant Secretary for Energy Efficiency and Renewable Energy, Office of Vehicle Technologies of the U.S. Department of Energy. The Slayter Discretionary Fund was used to purchase chemical and laboratory supplies (Purdue University). The XPS data were obtained at the Surface Analysis Facility of the Birck Nanotechnology Center, Purdue University.

## 7.7 References

- [1] L. Peng, Y. Zhu, D. Chen, R. S. Ruoff, and G. Yu, *Advanced Energy Materials* **6**, 1600025 (2016).

- [2] Y. Jing, Z. Zhou, C. R. Cabrera, and Z. Chen, *Journal of Materials Chemistry A* **2**, 12104 (2014).
- [3] M. Naguib et al., *Advanced Materials* **23**, 4248 (2011).
- [4] M. Naguib et al., *ACS Nano* **6**, 1322 (2012).
- [5] M. W. Barsoum, *MAX phases: properties of machinable ternary carbides and nitrides*, John Wiley & Sons, 2013.
- [6] M. Naguib, V. N. Mochalin, M. W. Barsoum, and Y. Gogotsi, *Advanced Materials* **26**, 992 (2014).
- [7] M. Naguib et al., *Journal of the American Chemical Society* **135**, 15966 (2013).
- [8] J. Halim et al., *Advanced Functional Materials* **26**, 3118 (2016).
- [9] J. C. Lei, X. Zhang, and Z. Zhou, *Frontiers of Physics* **10**, 276 (2015).
- [10] M. Khazaei et al., *Advanced Functional Materials* **23**, 2185 (2013).
- [11] J. Come et al., *Journal of The Electrochemical Society* **159**, A1368 (2012).
- [12] M. Naguib et al., *Electrochemistry Communications* **16**, 61 (2012).
- [13] O. Mashtalir et al., *Nature Communications* **4**, 1716 (2013).
- [14] Q. Tang, Z. Zhou, and P. Shen, *Journal of the American Chemical Society* **134**, 16909 (2012).
- [15] X. Xie et al., *Nano Energy* **26**, 513 (2016).
- [16] Y. Dall’Agnese, P.-L. Taberna, Y. Gogotsi, and P. Simon, *The Journal of Physical Chemistry Letters* **6**, 2305 (2015).
- [17] X. Wang et al., *Nature Communications* **6**, 6544 (2015).
- [18] Y. Xie et al., *ACS Nano* **8**, 9606 (2014).
- [19] D. Er, J. Li, M. Naguib, Y. Gogotsi, and V. B. Shenoy, *ACS Applied Materials & Interfaces* **6**, 11173 (2014).
- [20] M. N. Abdelmalak, No Title, 2014.
- [21] Y. Liu et al., *Nano Letters* **14**, 3445 (2014).
- [22] Z. Ju et al., *ACS Applied Materials and Interfaces* **8**, 20682 (2016).
- [23] S. Brunauer, P. H. Emmett, and E. Teller, *Journal of the American Chemical Society* **60**, 309 (1938).
- [24] S. Kajiyama et al., *ACS Nano* **10**, 3334 (2016).
- [25] A. L. M. Reddy et al., *ACS Nano* **4**, 6337 (2010).
- [26] W. Zhang et al., *Physical Chemistry Chemical Physics* **18**, 4376 (2016).

## 8. SUMMARY AND RECOMMENDATIONS

### 8.1 Summary

Throughout my thesis, I presented my results and developed understanding of carbon anodes for potassium-ion batteries (KIBs). Of recent particular interest is the graphite system, where a stage-one structure ( $\text{KC}_8$ ) results in  $279 \text{ mAh g}^{-1}$  capacity with a favorable voltage profile. However, the 61% volumetric expansion during potassium intercalation causes accelerated capacity fade for non-optimized electrode and electrolyte. To combat this, I explored carbon nanofibers as KIB anode. The one-dimensional morphology and low-density turbostratic carbon structuring enables highly stable capacity for over 1900 charge-discharge cycles. Pseudo-capacitance surface charge storage enabled by oxygen functionalization of the carbon surface improved the rate capability as well. Due to its higher tap density and commercial viability, I subsequently evaluated standard graphite anode and its practical performance parameters such as battery safety and temperature dependent performance. During thermal runaway, the KIB graphite anode system generates less heat in differential scanning calorimetry (DSC) studies than for lithium-ion batteries (LIBs), albeit KIB thermal runaway initiates earlier due to exothermic reaction of intercalated potassium and electrolyte. The KIB system demonstrated much greater variation in cell performance with operating temperature, where extreme polarization at low temperatures limited cell performance largely due to the non ideal potassium metal counter electrode. Additionally, cycling at elevated temperatures resulted in dramatic impedance rise, due to augmented solid electrolyte interphase (SEI) layer formation from the 61% volumetric expansion of graphite and the high reactivity of potassium metal. This thesis attempted to provide a practical basis in evaluating this novel electrochemical system, showing its complications as compared to standard LIBs. Next, I explored

the hypothesis that controlled particle morphology can prevent safety concerns arising from non-uniform current distributions, wherein spherical and spiky carbon particles were compared to irregular graphite particles. Experiments and modeling revealed the relationship between cell performance, aging, and safety with morphology wherein desired traits can be obtained by careful materials design. Finally, MXene type transition metal carbonitrides were evaluated as KIB anode, where the unique layered structure enables reversible intercalation of potassium ions. In particular,  $\text{Ti}_3\text{CNT}_z$  demonstrated reasonable reversible capacity and rate capability, with *ex-situ* characterization utilized to study the structural changes upon potassium insertion.

## 8.2 Recommendations

### 8.2.1 Accelerating Rate Calorimetry

As compared to using DSC to measure exothermic heat generation, accelerating rate calorimetry (ARC) has several advantages that can more accurately reflect real battery operating conditions, namely: (1) Larger cell and sample sizes (2) Self-heating rate can be determined accurately due to adiabatic condition (3) Full cell system analysis. While DSC is useful to identify the components participating in thermal runaway, the results do not provide information on the kinetics of the thermal runaway incident, preventing a full system evaluation of battery safety. ARC utilizes a heat-wait-search mode to slowly increment the system temperature, until an exothermic reaction occurs, and allows for careful measurement of onset temperature of self-heating that cannot be as accurately determined in DSC. Direct comparison of self-heating rates for different sample preparation, can elucidate the effects of parameters such as state of charge and electrolyte composition. Kinetic parameters (e.g. rate constants, activation energies) can be calculated for thermal reactions by ARC analysis, such as the degradation of metastable SEI to stable SEI. This will enable direct comparison between KIB and LIB thermal runaway kinetics, and enable modeling studies to determine if cooling is required for safe operation. Additionally, it will

enable full-cell system analysis, to elucidate the complete spectrum of K-ion battery safety, as the prior results suggest that K-ion batteries could be more thermally stable at higher temperatures and less likely to catch on fire.

### 8.2.2 K-ion Battery SEI Layer

Formation of a proper SEI layer can improve battery lifetime and safety, due to its stabilization against exfoliation and further electrolyte decomposition. The LIB SEI has a gradient structure, consisting of lithium salts (e.g.  $\text{Li}_2\text{CO}_3$ ,  $\text{LiOH}$ ,  $\text{LiF}$ ,  $\text{Li}_2\text{O}$ ) near the electrode and oligomers near the electrolyte, as revealed by X-ray photoelectron spectroscopy (XPS). Currently, very little is known of the SEI formed in KIBs. Usage of functionalized binders (e.g. CMCNa and PANa) enables a pre-formed SEI effect to decrease first cycle capacity loss, similar to NIB systems. We discovered that plasma oxidation, to impart oxygen functionalities on the CNF surface, augmented growth of a superior, faster stabilizing SEI layer, due to increased  $\text{K}_2\text{CO}_3$  and oxide salt formation. We also performed XPS analysis of post-cycled Mxene anode material ( $\text{Ti}_3\text{CNT}_z$ ), where K 2p, F 1s, O 1s, and P 2p signals increased, suggesting significant growth of  $\text{K}_2\text{CO}_3$ , KF, and other SEI components during cycling. These initial studies demonstrate that the SEI layer in KIBs forms similarly to the LIBs, with electrolyte decomposition, and that SEI composition plays an important role in electrochemical stability. Fundamental understanding of KIB SEI formation and thermal degradation should be evaluated: (1) before and after thermal runaway, (2) for cells cycled at low or high temperatures, and (3) for laminates with different binders and electrolyte compositions. Characterization via XPS with depth profiling analysis will enable penetration into precycled graphite electrodes, to determine compositional changes as a function of depth.

### 8.2.3 Electrochemical Impedance Spectroscopy

While electrochemical impedance spectroscopy (EIS) analysis was utilized frequently during my thesis work, issues arose for the KIB system. Firstly, the impedance values obtained for charge-transfer / SEI resistance are orders of magnitudes higher than those obtained for LIB (thousands vs. tens of ohms). Results from Chapter 5 indicate that the high reactivity and polarizability of potassium metal counter electrode cause this. Future EIS studies should be performed in a symmetric cell configuration, wherein half-cell graphite anodes are conditioned first, then reassembled into the symmetric configuration. This method of EIS, although more resource intensive, will provide more accurate results for modeling. Additional EIS studies can determine the effect of electrolyte solvent (ethylene carbonate, diethyl carbonate, propylene carbonate) and salt ( $\text{KFP}_6$ ,  $\text{KFSI}$ ) on cell impedance during the formation cycle, thus providing further insight into how to optimize the SEI layer of carbon anodes for KIBs.

## APPENDICES

## A. CHAPTER 3 SUPPORTING INFORMATION

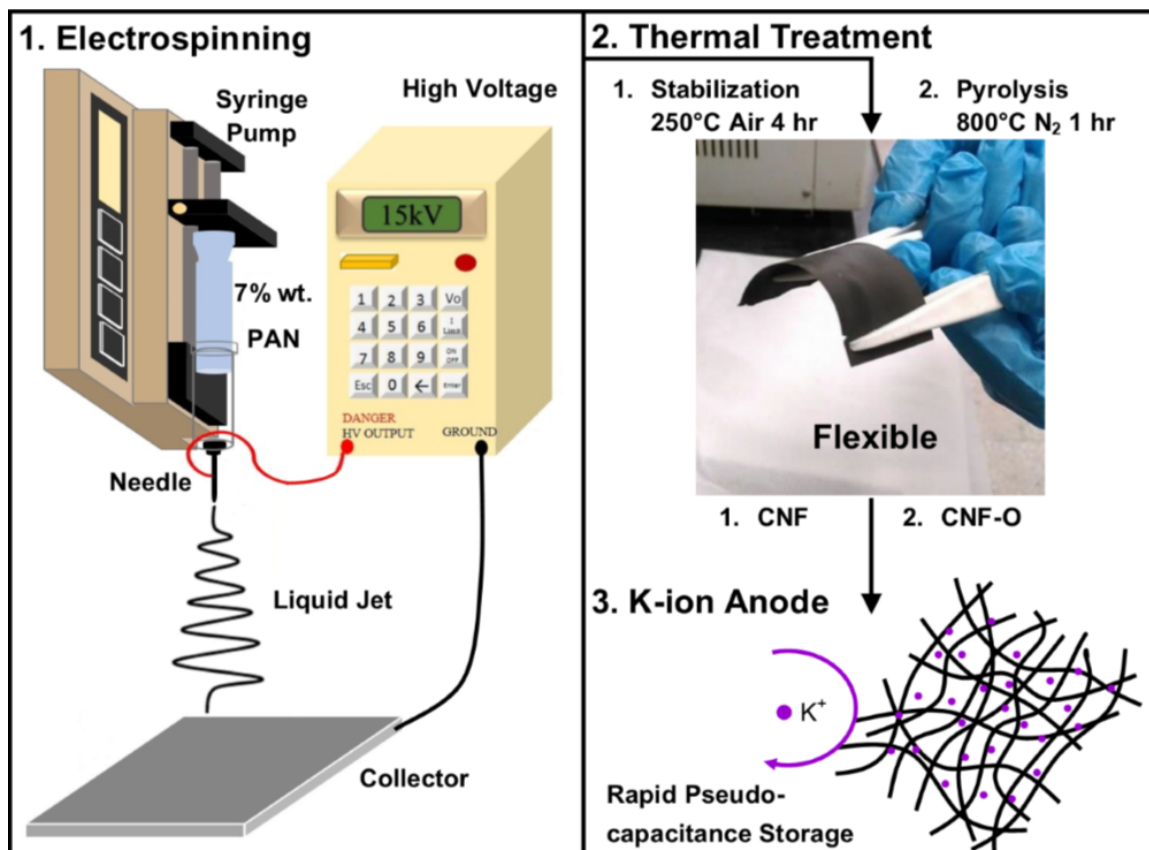


Figure A.1. Schematic of flexible carbon nanofiber mat electrospinning synthesis, thermal treatment, and application as K-ion anode material.

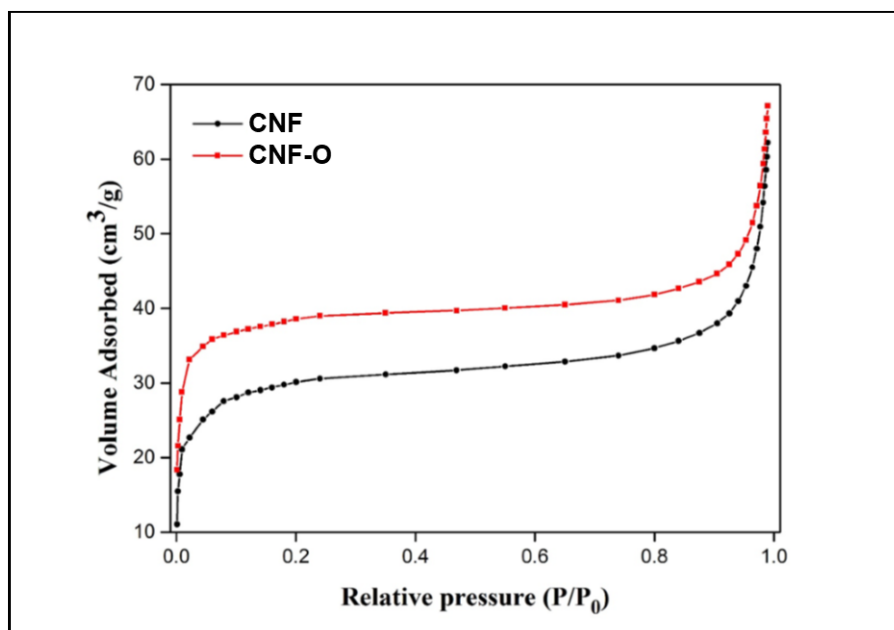


Figure A.2. Nitrogen adsorption isotherms taken at 77K for CNF and CNF-O.

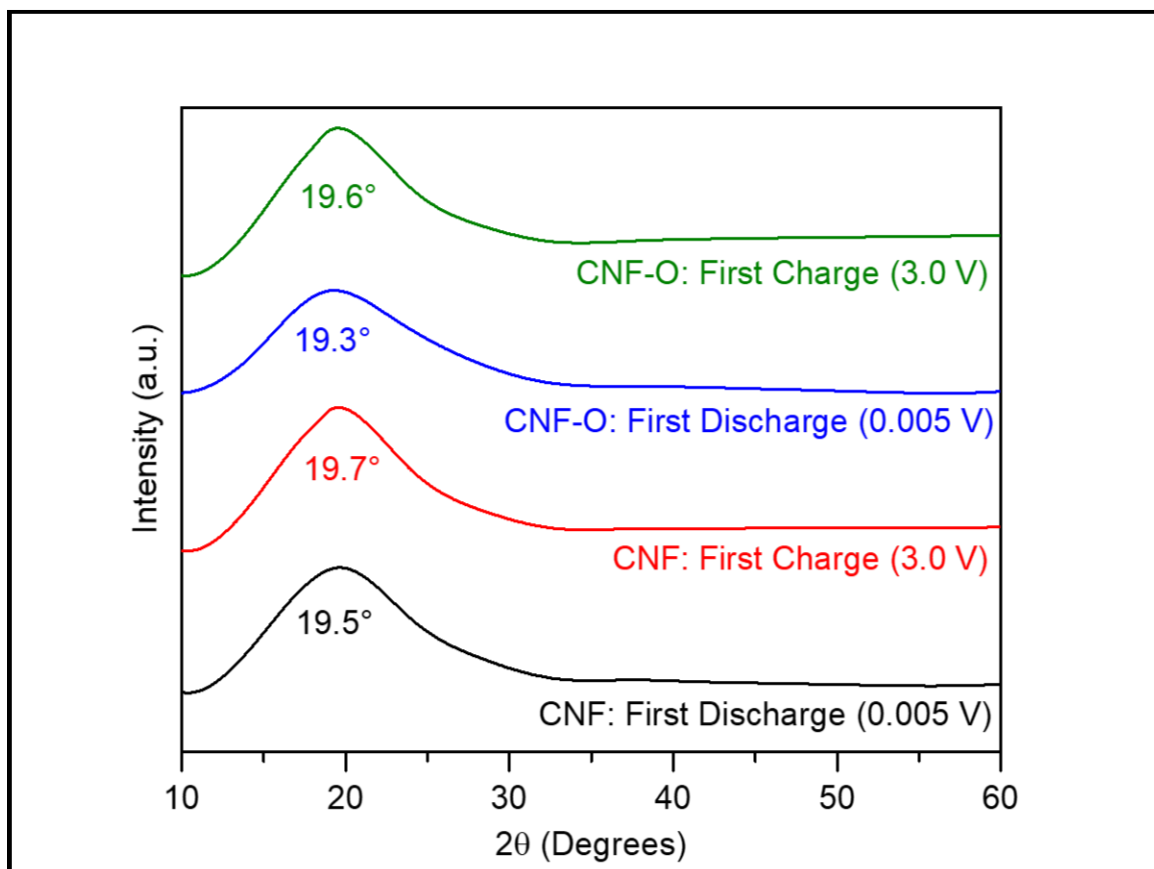


Figure A.3. *Ex-situ* XRD analysis of CNF and CNF-O materials after the first discharge (0.005 V) and charge (back to 3.0 V) during the first cycle. Peak location for (002) Miller plane labeled in figure for each curve.

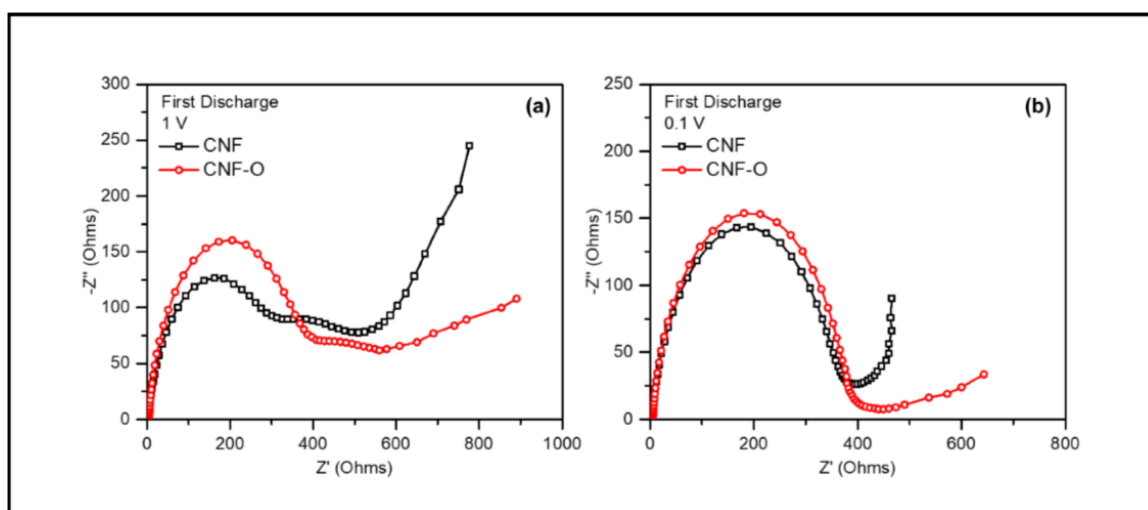


Figure A.4. Electrochemical impedance spectroscopy at various voltages for the first discharge for CNF and CNF-O material.

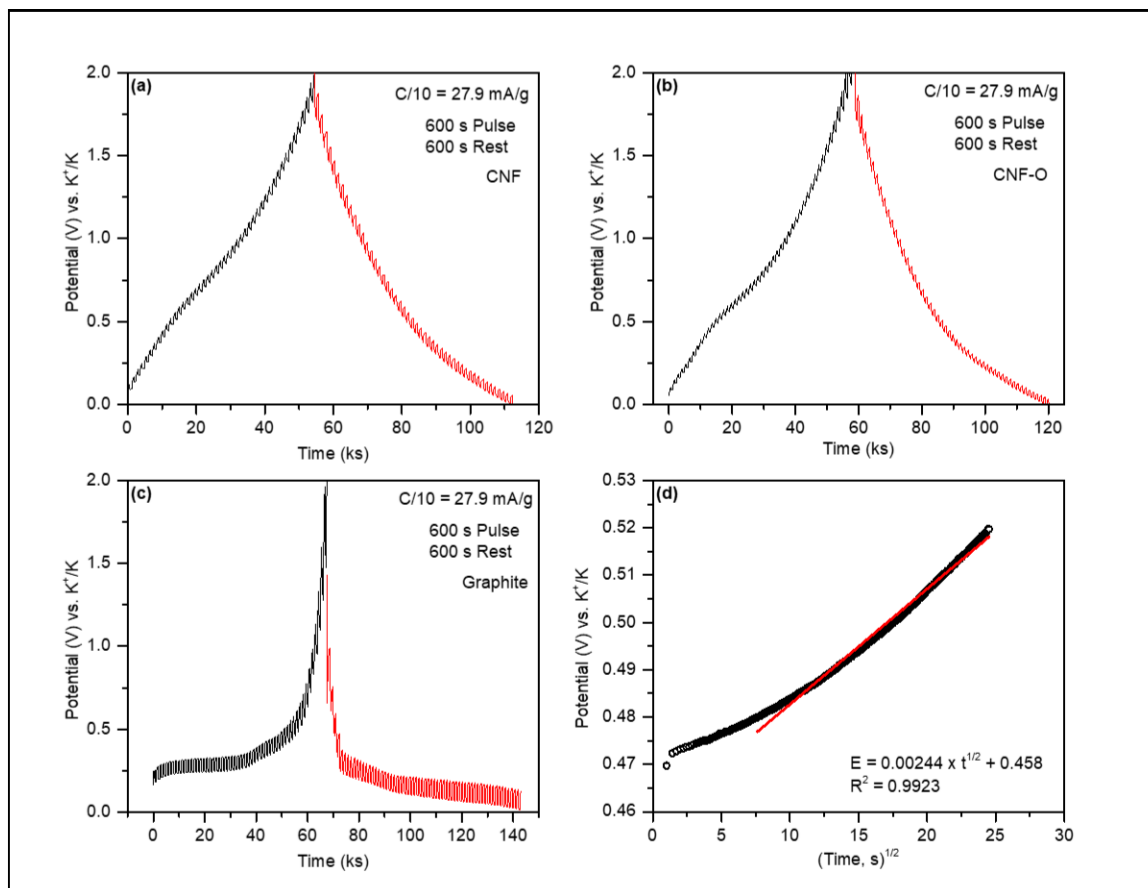


Figure A.5. Galvanostatic intermittent titration technique with charge and discharge profiles for (a) CNF, (b) CNF-O, and (c) and graphite. (d) Plot of voltage vs. square root of time for CNF.

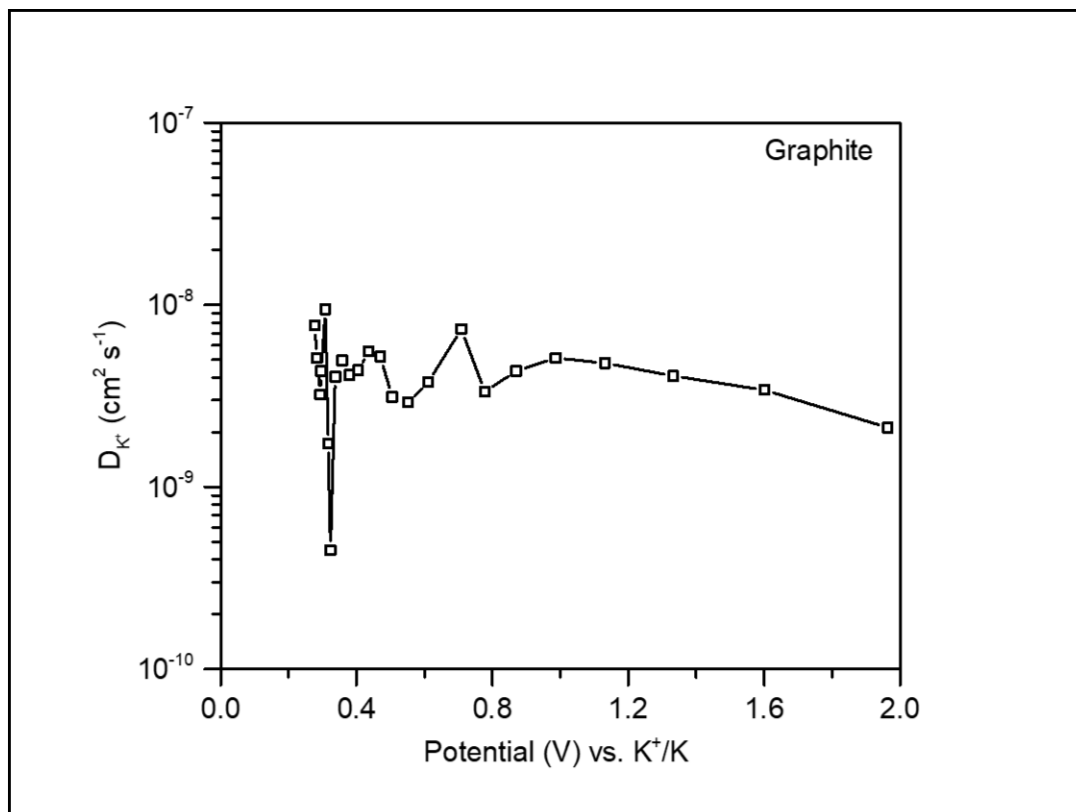


Figure A.6. Galvanostatic intermittent titration technique with diffusional coefficient calculated for graphite material as K-ion anode.

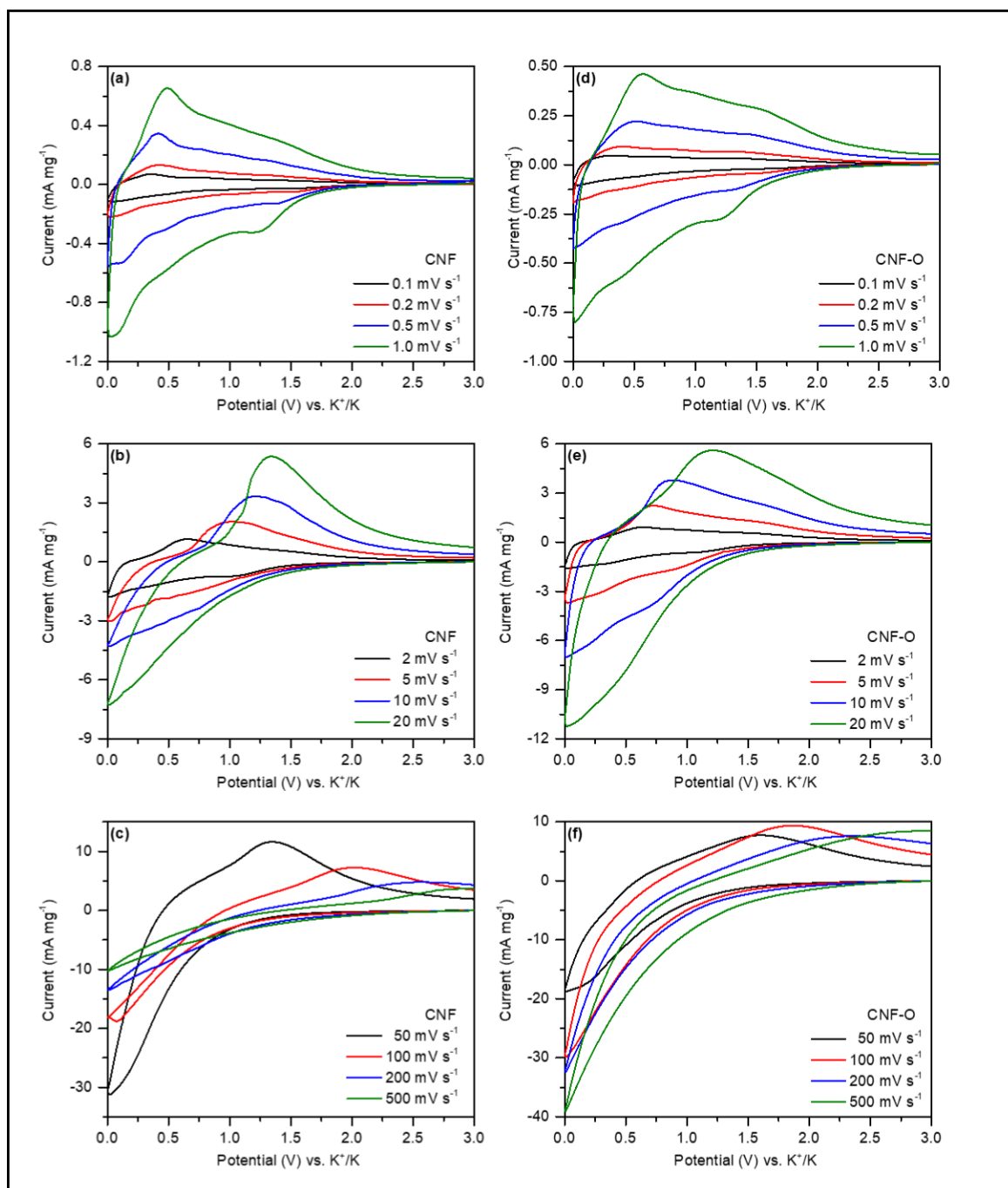


Figure A.7. Cyclic voltammetry for conditioned cells for CNF (a), (b), & (c) and CNF-O (d), (e), & (f) taken at scan rates from 0.1 mV s<sup>-1</sup> to 500 mV s<sup>-1</sup>.

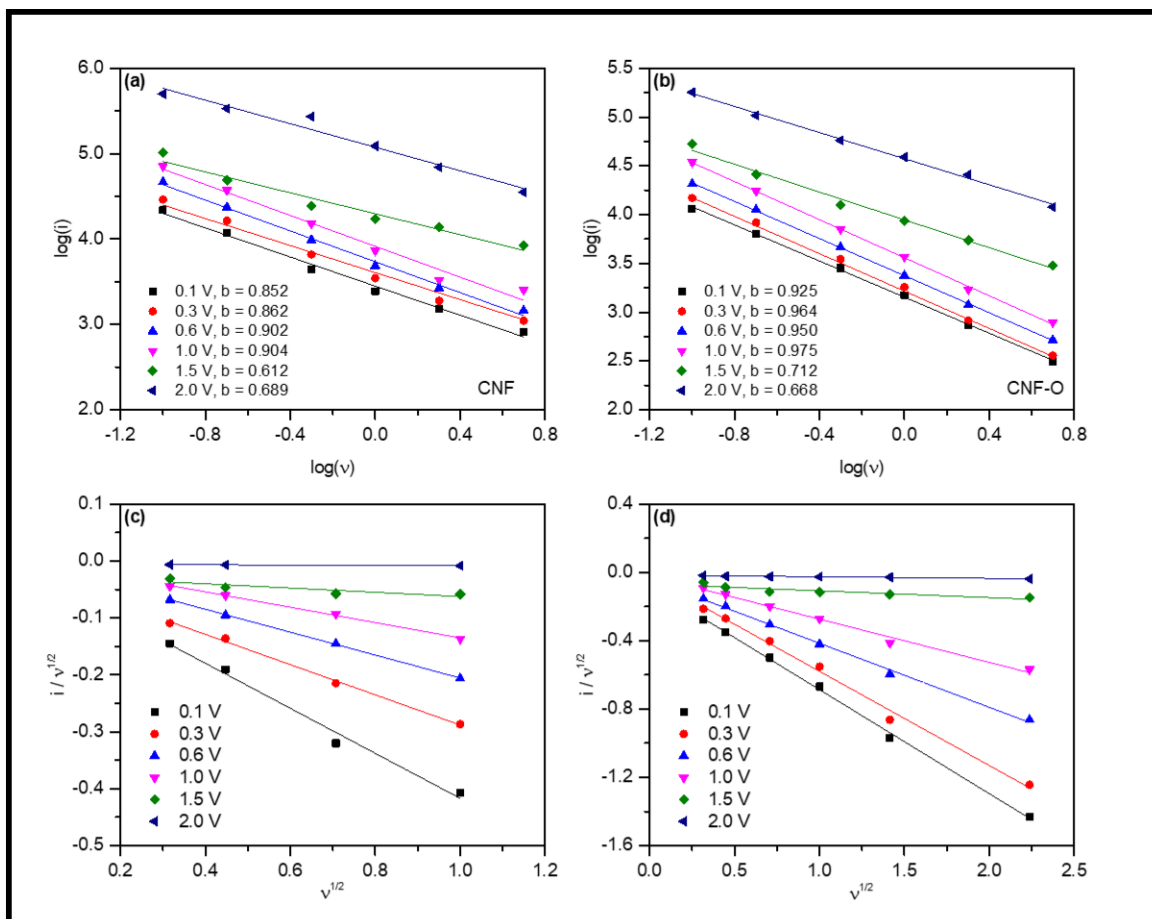


Figure A.8. Plot showing linear relation of  $\log(v)$  vs.  $\log(i)$  for discharge sweeps of cyclic voltammetry for CNF (a) and CNF-O (b) samples at various voltages. Slope correlated to  $b$ , where the voltammetric sweep follows the power law relationship of  $I = av^b$ . Diffusion limited processes (intercalation) can be described by  $b = 0.5$ , according to Cottrell Equation, while capacitive processes can be described by  $b = 1.0$ .

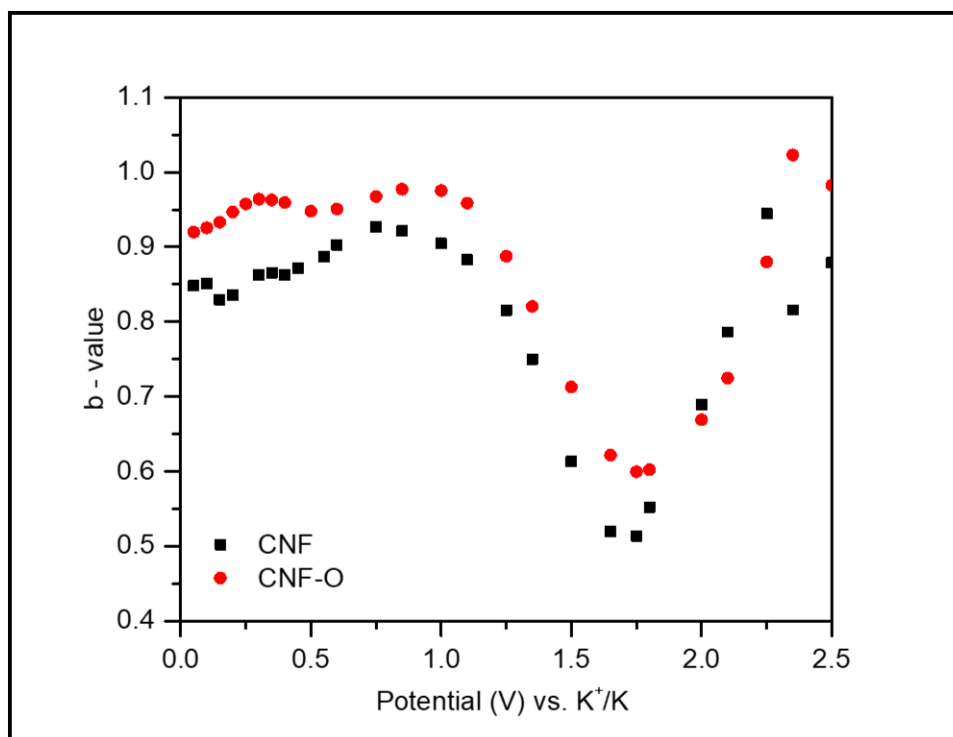


Figure A.9. Dependence of the slope  $b$  determined by the linear fit of  $\log(v)$  vs.  $\log(i)$  as a function of cell voltage for CNF and CNF-O materials. Calculated using scan rates from  $0.1 - 5.0 \text{ mV s}^{-1}$ . A value of  $b$  closer to 1 correlates to capacitive charge storage mechanism, while a value closer to 0.5 correlates to intercalation charge storage mechanism.

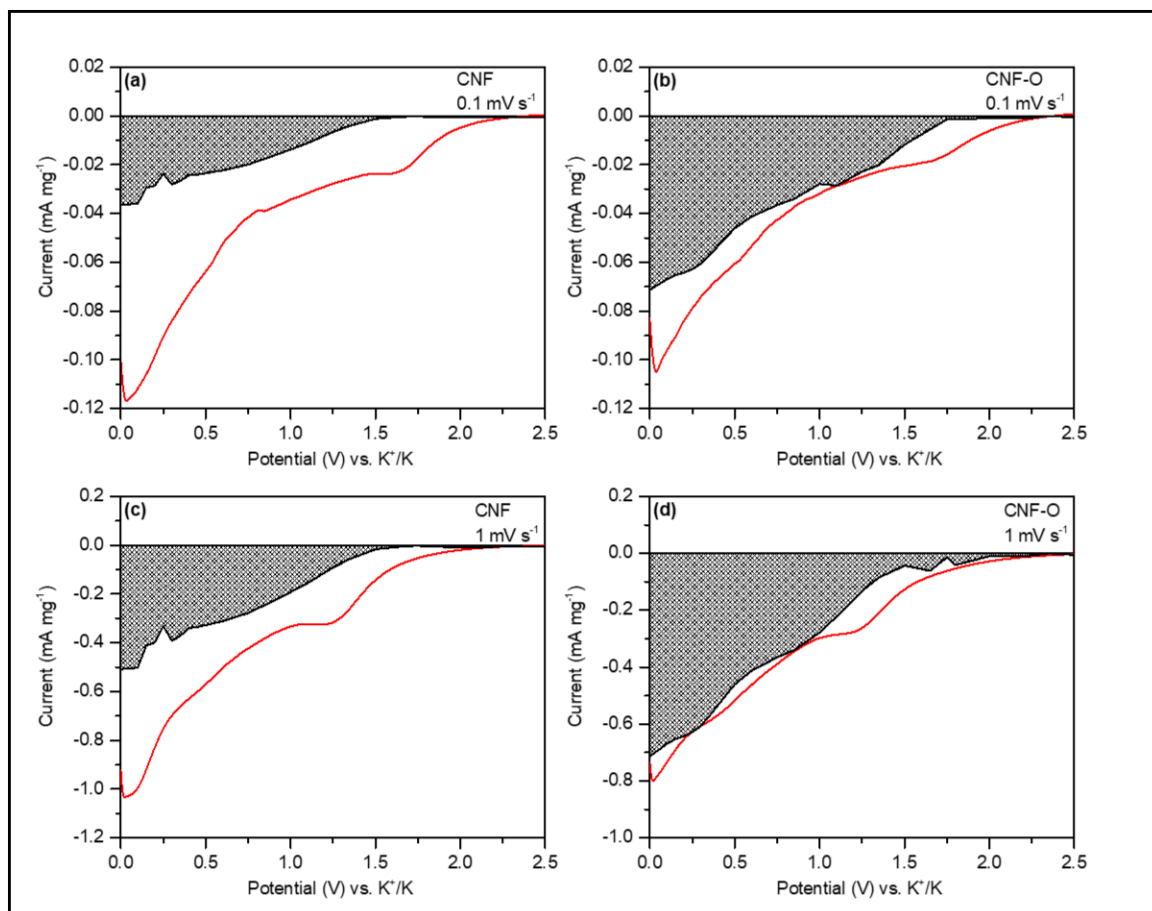


Figure A.10. Cyclic voltammetry for conditioned cells for CNF and CNF-O, with red line showing total current. Charge storage contribution from pseudo-capacitance shown by shaded region. (a) CNF at 0.1 mV s<sup>-1</sup>. (b) CNF-O at 0.1 mV s<sup>-1</sup>. (c) CNF at 1.0 mV s<sup>-1</sup>. (d) CNF-O at 1.0 mV s<sup>-1</sup>.

B. CHAPTER 4 SUPPORTING INFORMATION

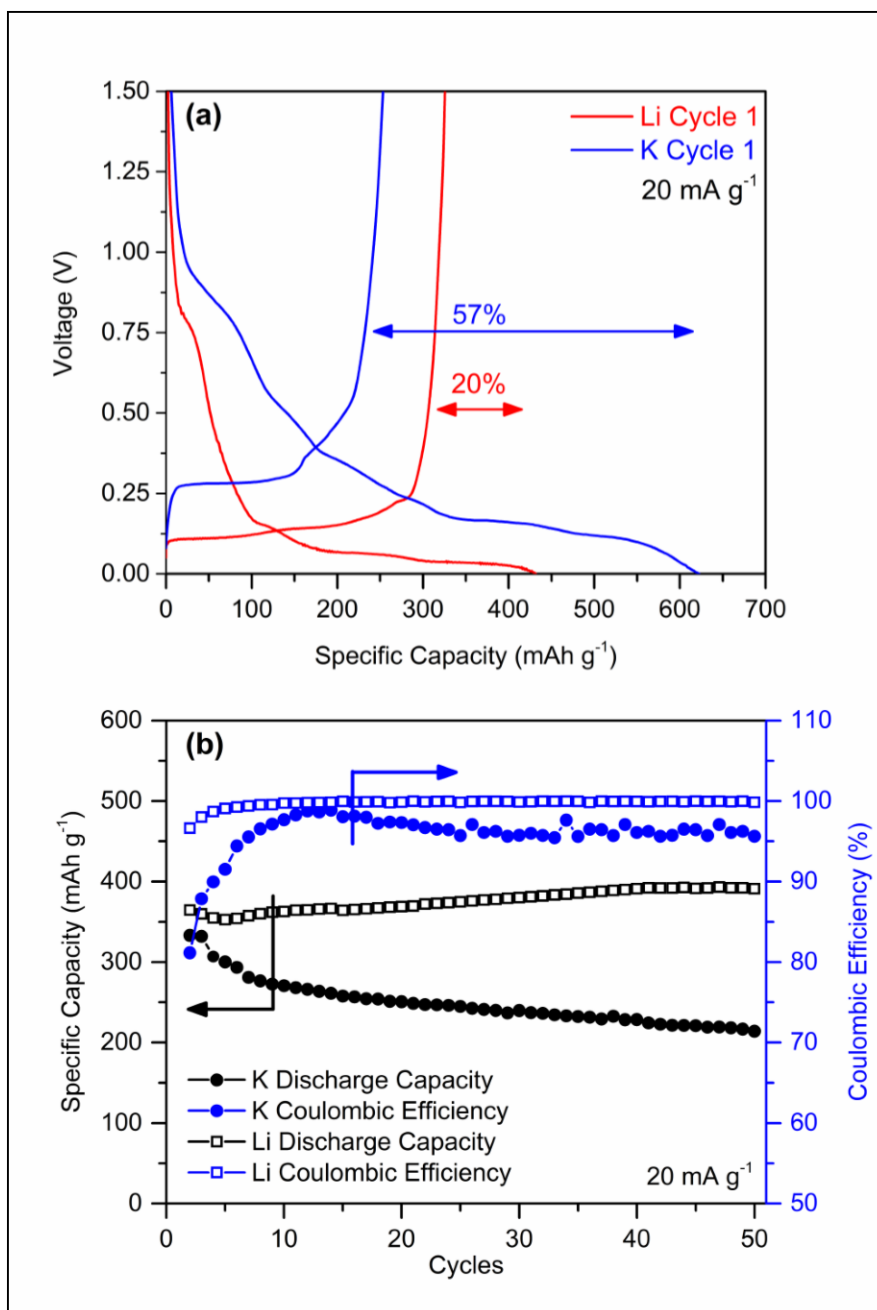


Figure B.1. (a) First cycle charge-discharge voltage profile for graphite electrode when cycled against Li and K metal, with  $20 \text{ mA g}^{-1}$  current density. (b) Extended galvanostatic cycling of graphite electrode at  $20 \text{ mA g}^{-1}$  current density, comparing discharge capacity and Coulombic efficiency for Li and K ion system.

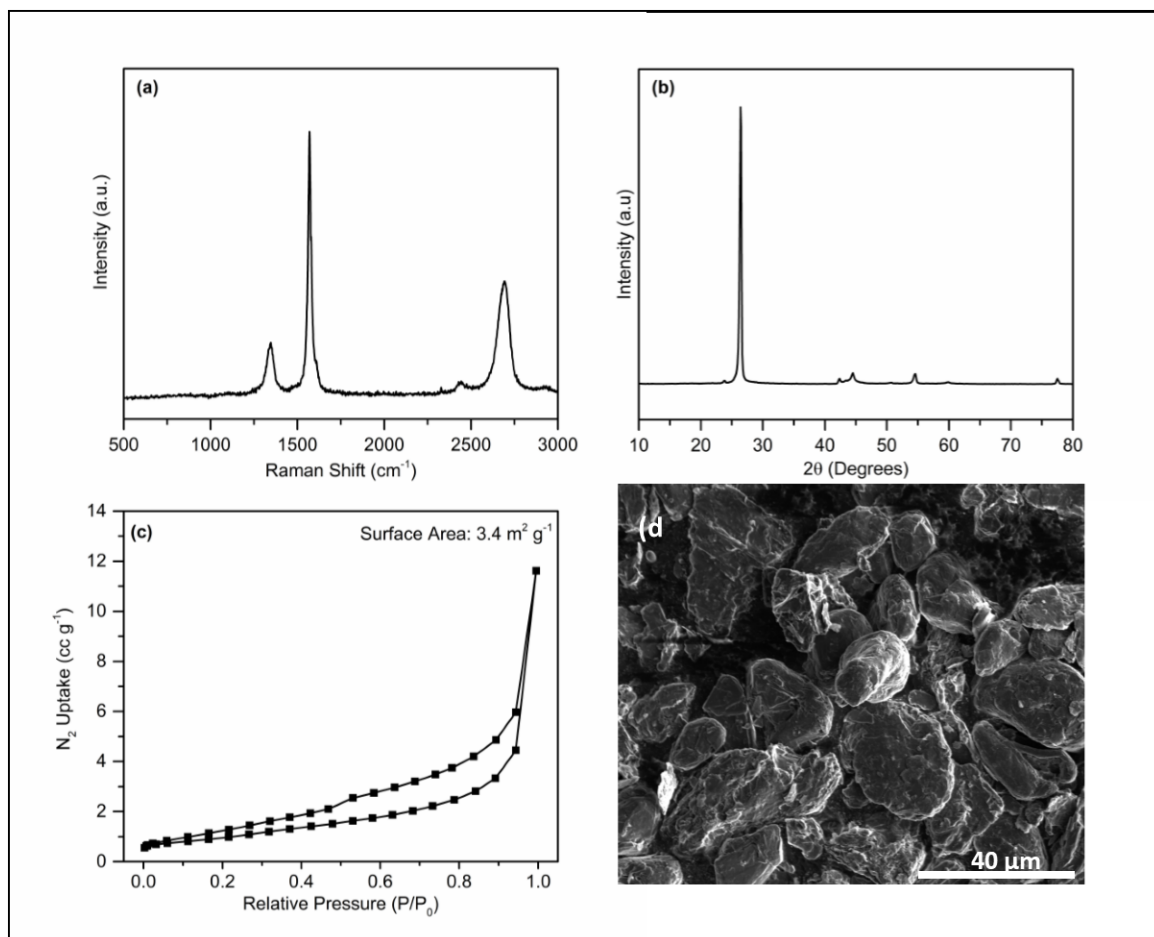


Figure B.2. (a) Raman spectroscopy of synthetic graphite collected at 633 nm. (b) XRD of synthetic graphite. (c) Nitrogen sorption isotherms of graphite with BET surface area of  $3.4 \text{ m}^2 \text{ g}^{-1}$ . (d) SEM image of graphite particles with scale bar of  $40 \mu\text{m}$ .

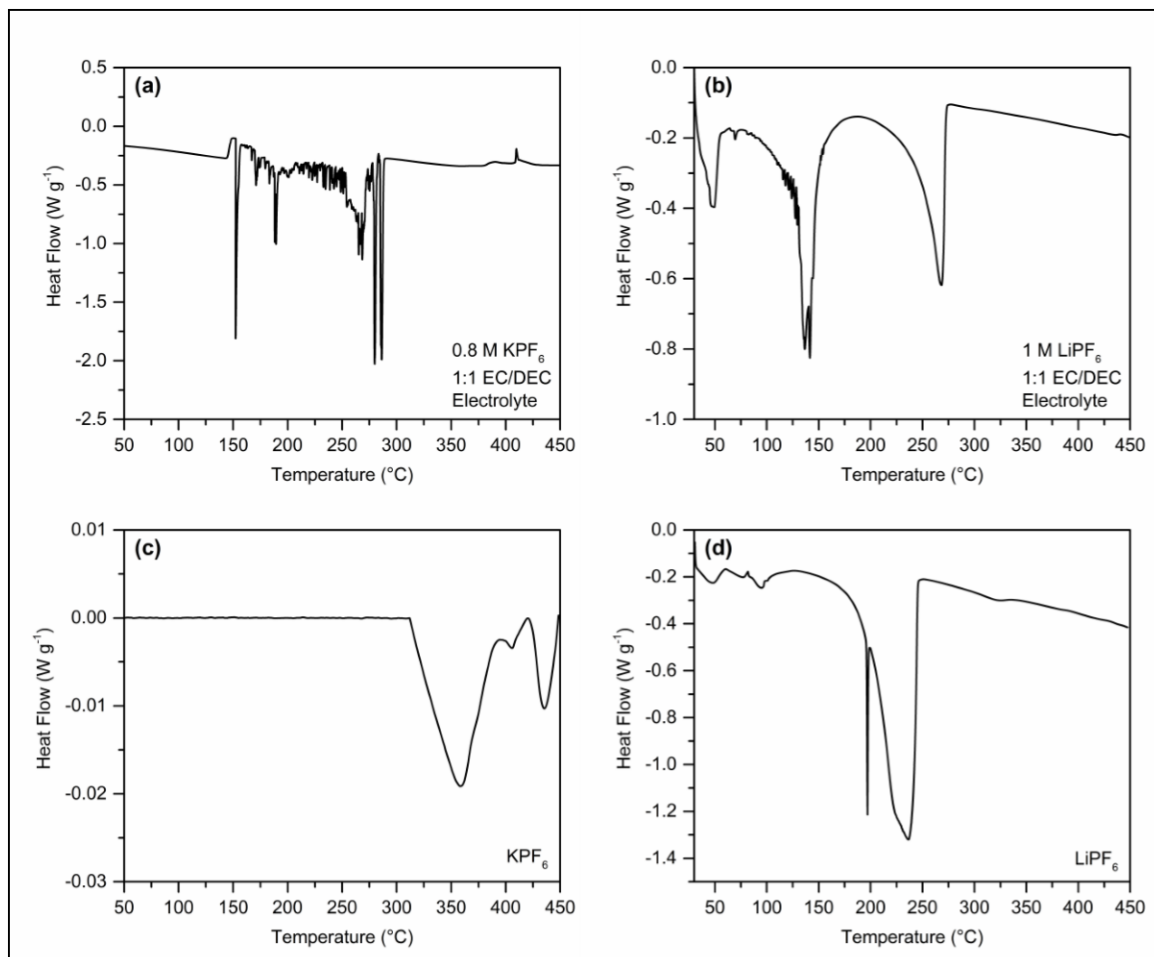


Figure B.3. (a) DSC profile of 0.8 M  $\text{KPF}_6$  in 1:1 EC/DEC (volumetric) electrolyte. (b) DSC profile of 1 M  $\text{LiPF}_6$  in 1:1 EC/DEC (volumetric) electrolyte. (c) DSC profile of  $\text{KPF}_6$  salt. (d) DSC profile of  $\text{LiPF}_6$  salt.

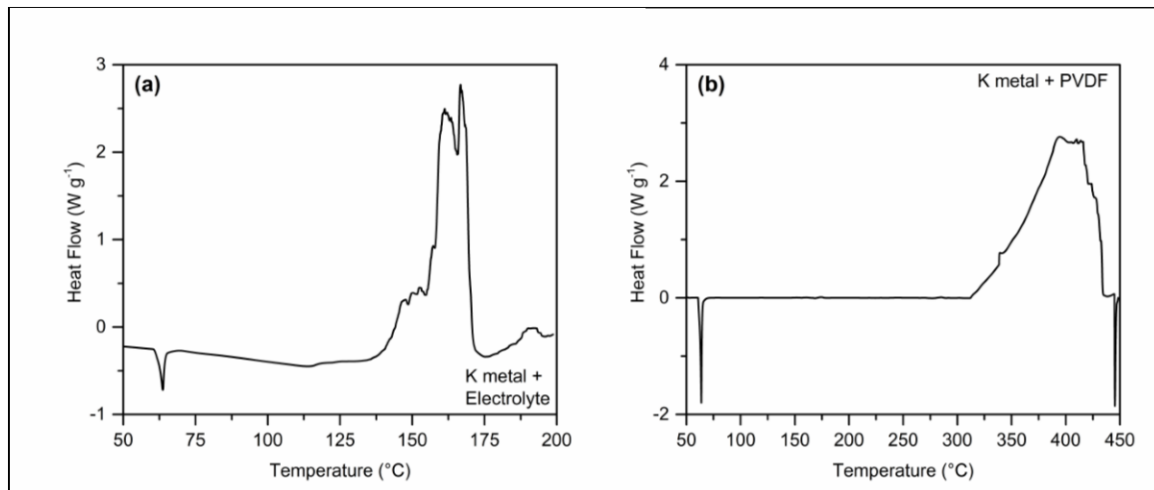


Figure B.4. (a) DSC profile of K metal wetted with 0.8 M  $\text{KPF}_6$  in 1:1 EC/DEC (volumetric) electrolyte. (b) DSC profile of K metal with PVDF powder.

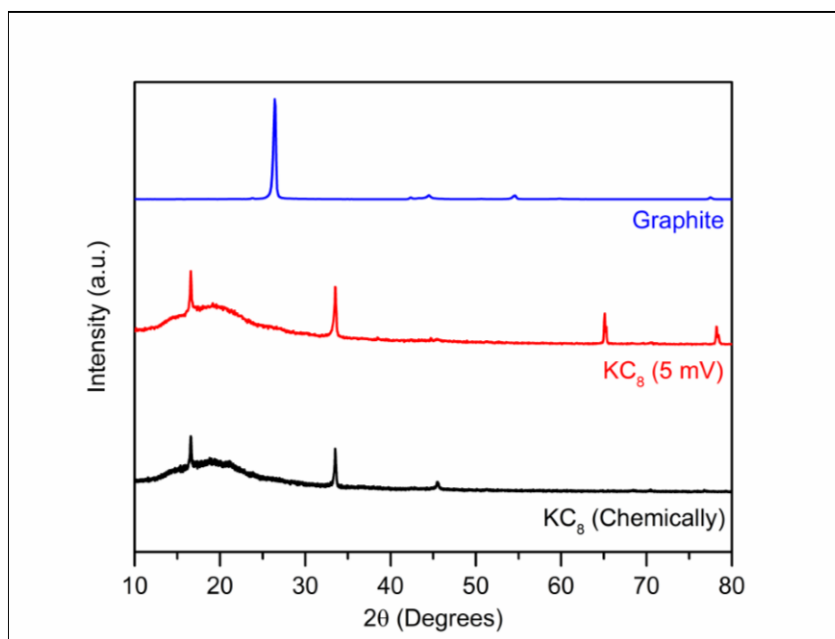


Figure B.5. XRD patterns of graphite (blue),  $\text{KC}_8$  prepared electrochemically and equilibrated at 5 mV (vs  $\text{K}^+/\text{K}$ ), and  $\text{KC}_8$  synthesized by heating stoichiometric K metal and graphite under inert atmosphere. Kapton tape was utilized for air sensitive  $\text{KC}_8$  samples and is responsible for the broad peak at 19°.

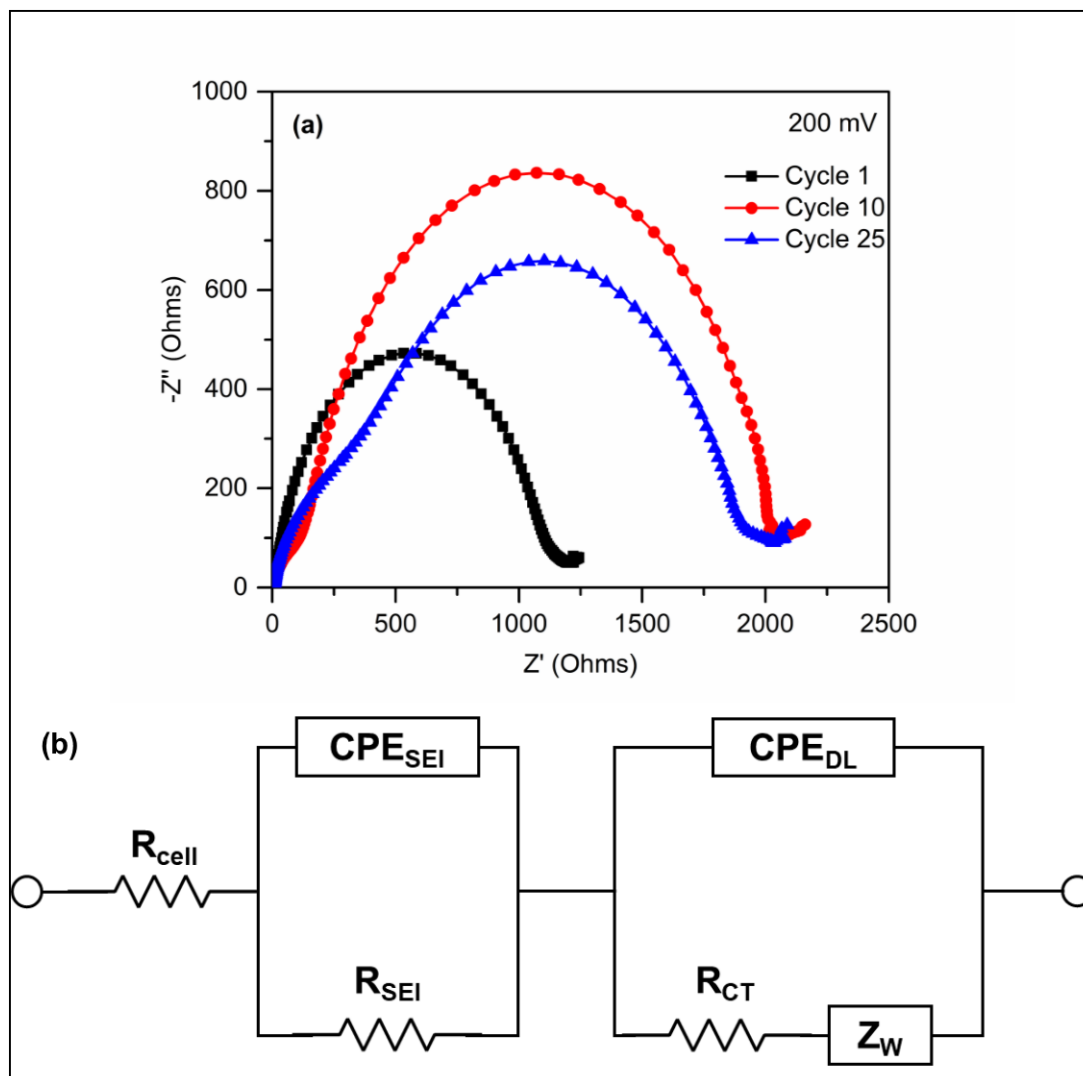


Figure B.6. (a) EIS spectra collected at 200 mV (vs.  $K^+/K$ ) for cycle 1, 10, and 25 with a graphite electrode in a K-ion battery. (b) Circuit model utilized to fit parameters to EIS spectra.  $R_{cell}$  is the cell resistance.  $R_{SEI}$  and  $CPE_{SEI}$  are the resistance and constant phase element in parallel for SEI in the high frequency range.  $R_{CT}$  is charge transfer resistance, with  $CPE_{DL}$  as its relative double layer capacitance.  $Z_W$  is the Warburg impedance corresponding to diffusion of K-ions on the electrode-electrolyte interface at low frequencies.

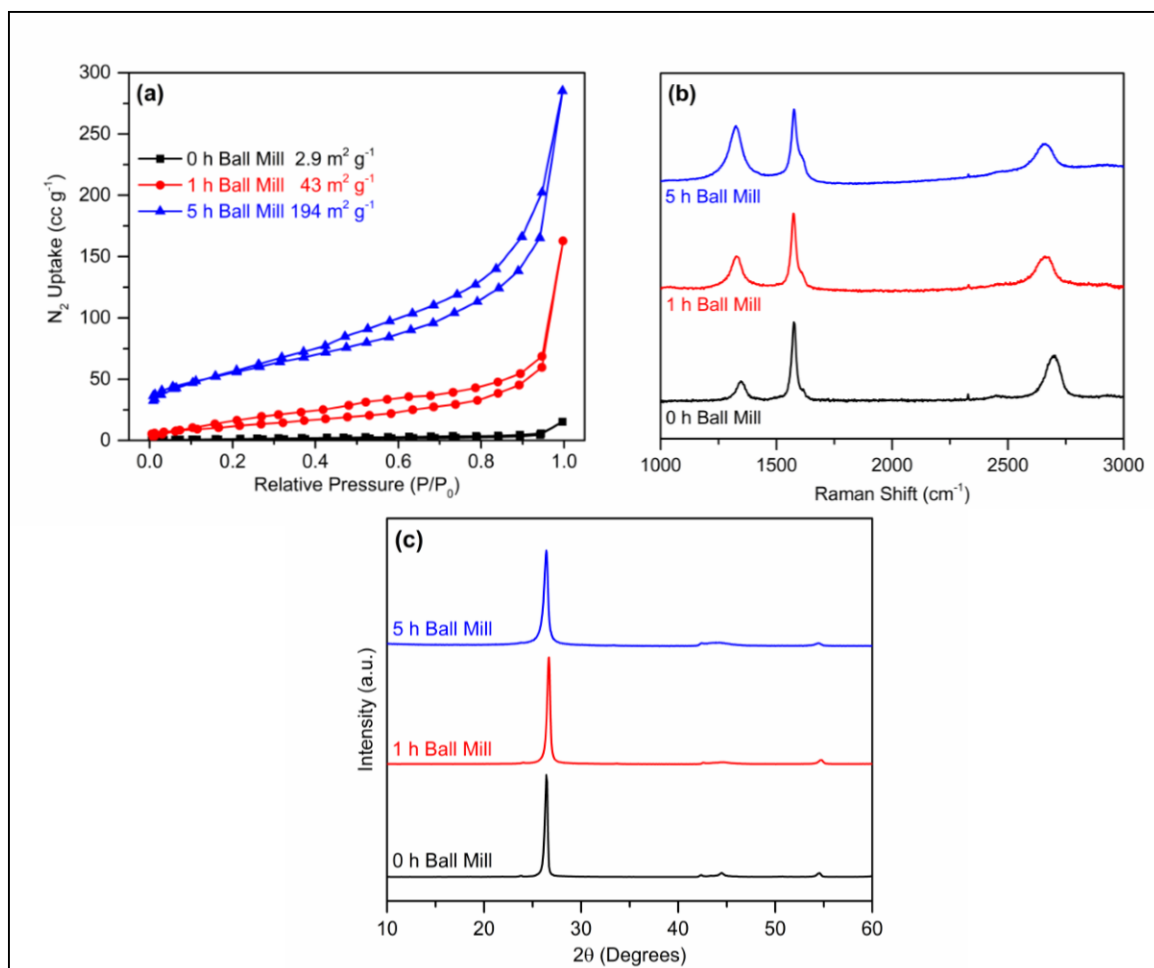


Figure B.7. Material properties for ball milled and sieved ( $>25\ \mu m$  &  $<53\ \mu m$ ) graphite particles. (a) Nitrogen sorption isotherms and BET calculated surface areas. (b) Raman spectra. (c) XRD spectra.

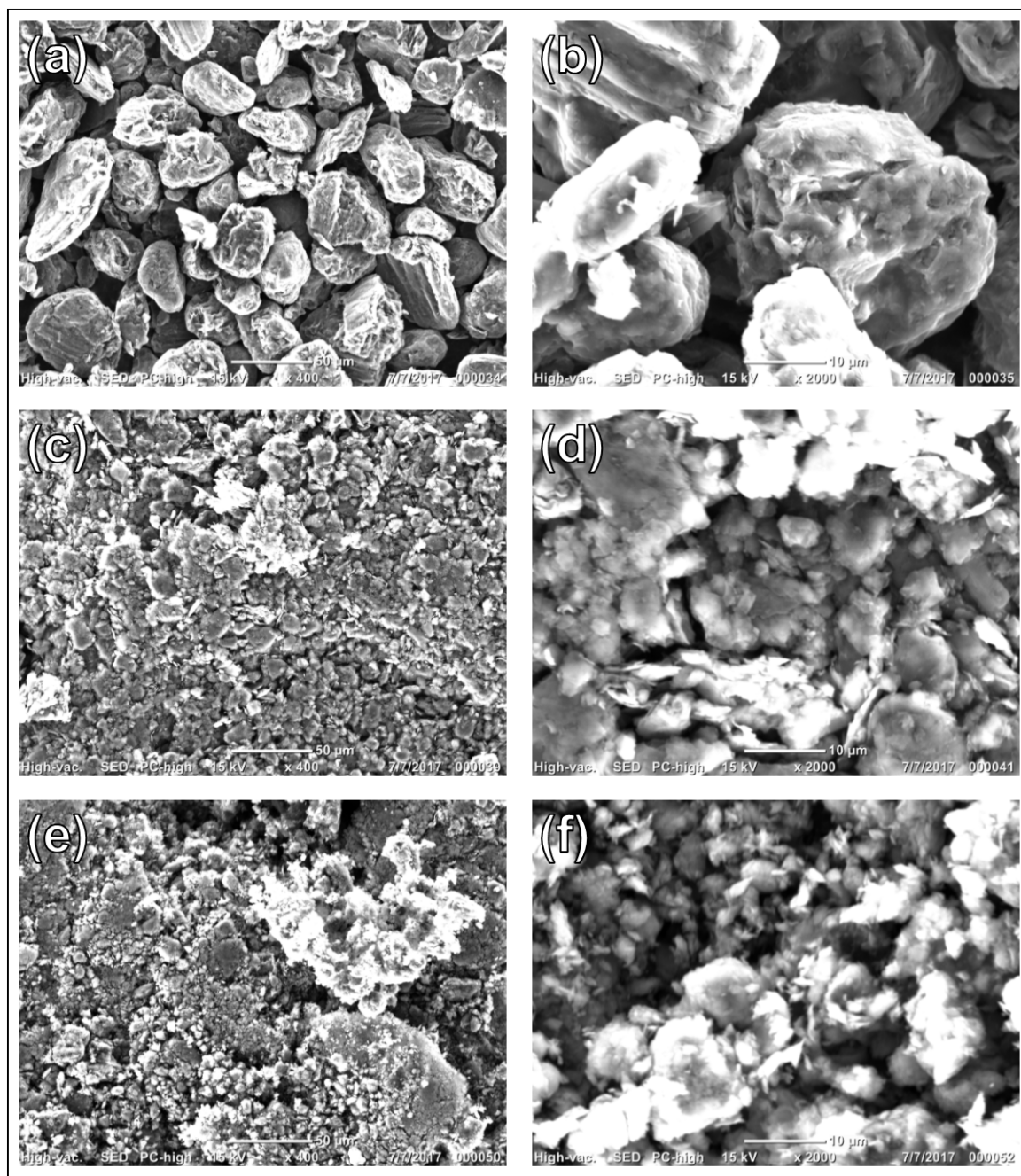


Figure B.8. SEM images for ball milled and sieved ( $>25 \mu\text{m}$  &  $\leq 53 \mu\text{m}$ ) graphite particles. (a & b) 0-hour ball mill. (c & d) 1-hour ball mill. (e & f) 5-hours ball mill.

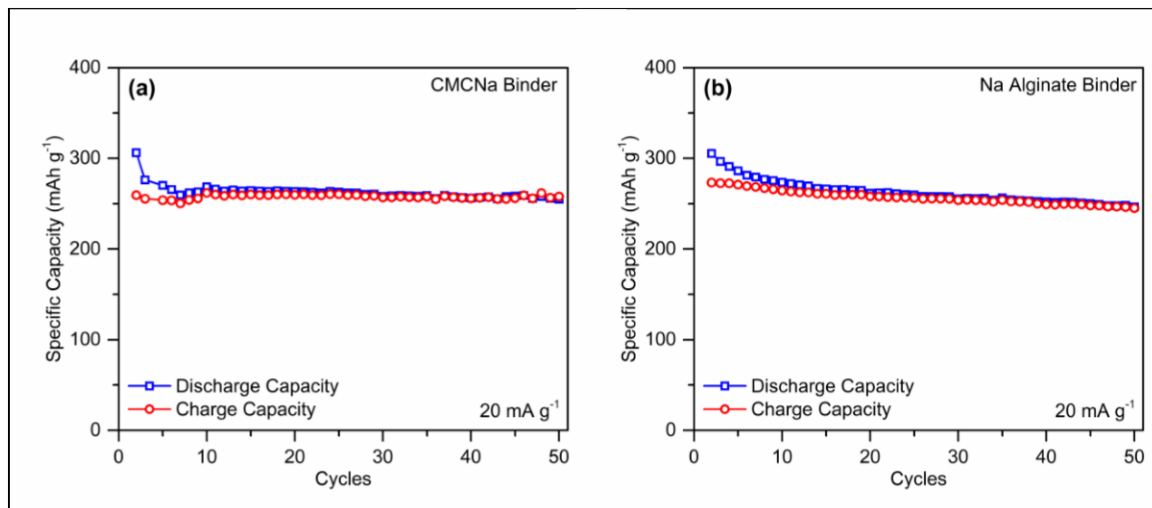


Figure B.9. (a) Extended galvanostatic cycling of graphite electrode with CMCNa binder at  $20 \text{ mA g}^{-1}$  current density as K-ion anode. (b) Extended galvanostatic cycling of graphite electrode with Na alginate binder at  $20 \text{ mA g}^{-1}$  current density as K-ion anode.

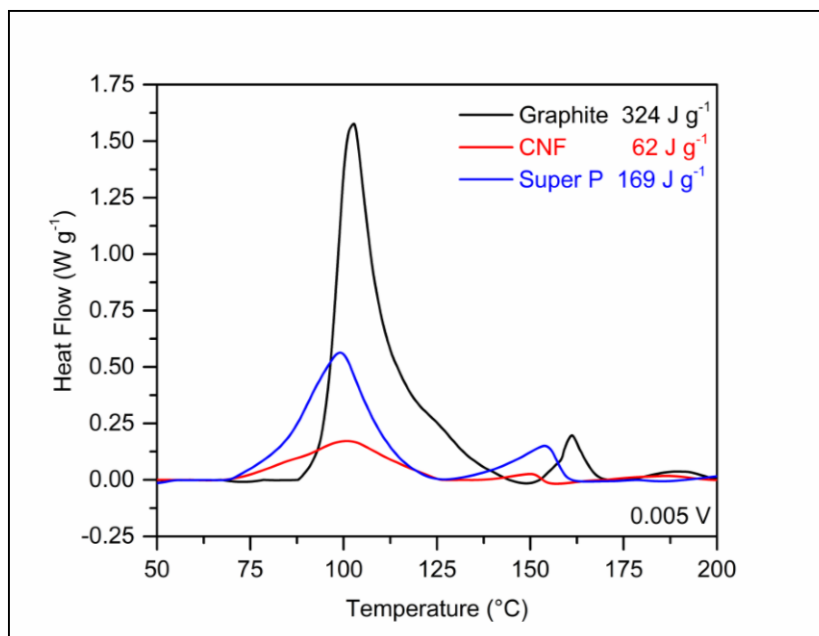


Figure B.10. DSC profiles for K-ion battery graphite, carbon nanofiber, and Super P electrodes.

## C. CHAPTER 5 SUPPORTING INFORMATION

*Effective Diffusion Coefficient*

To determine the effective diffusion coefficient ( $D_{Li^+} / D_{K^+}$ ) in graphite, the methodology of Kulova *et al.* was utilized, for cells conditioned to 60% state of charge.[1,2] This method is based on the fulfillment of Ficks laws of diffusion, and thus the diffusion coefficients are better treated as effective values due to the non-idealities of the electrode. To understand the sole effect of temperature on diffusion, it was calculated for one state of charge (60%) by applying various current pulses, via the following equation:

$$D = \frac{4}{\rho^2 \pi} \left( \frac{dE}{dQ} \right)^2 / \left( \frac{d^2E}{d(i)d(\sqrt{t})} \right)^2 \quad (C.1)$$

where  $dE/dQ$  is determined by the equilibrium voltage profile (obtained by the GITT profile Figure C.1). The second derivative term is calculated first by the linear change of voltage with respect to  $\sqrt{t}$  for each current pulse ( $dE/d\sqrt{t}$ ), and then by the derivative of that term with respect to specific current [ $dE^2/d(i)d(\sqrt{t})$ ], with linear responses obtained if semi-infinite diffusion is valid. The current pulses and dependence of ( $dE/d\sqrt{t}$ ) on specific current plots are shown in Figure C.2-4. From these linear fits, the above equation can be utilized to calculate the effective diffusion coefficients.

*Prussian Blue Cathode and Full Cell*

To perform full cell studies, Prussian blue nanoparticles were synthesized following the method of Zhang *et al.* via an aqueous-based precipitation method.[3] Thermogravimetric analysis was conducted in an argon atmosphere at  $10^\circ\text{C min}^{-1}$  using an Instrument Specialists Incorporated TGA i-1000. Powder X-ray diffraction patterns were measured with a Rigaku SmartLab X-ray diffractometer via a  $\text{Cu K}\alpha$

X-ray source ( $\lambda = 0.154$  nm) in the Bragg-Brentano mode. Raman spectra were collected with a Thermo Scientific DXR Raman microscope, using a 633 nm laser at 8 mW. Cathode electrodes were prepared by mixing 60 wt. % Prussian blue, 30 wt. % conductive additive, and 10 wt. % polyvinylidene difluoride (PVDF), with N-methyl-2-pyrrolidone (NMP) utilized as solvent to make a slurry. Full cells were constructed using Prussian blue cathode and graphite anode, with the same separator and electrolyte as used in KIB half-cells. Prussian blue cathode and graphite were both conditioned for 5 cycles at  $50 \text{ mA g}^{-1}$  in half-cells prior to full cell assembly. A positive to negative capacity ratio of 1.0 was targeted for proper cell balance, with cycling conducted from 1.0 - 3.9 V at  $50 \text{ mA g}^{-1}$  of graphite.

### References

- [1] T.L. Kulova, A.M. Skundin, Balance between reversible and irreversible processes during lithium intercalation in graphite, *Russ. J. Electrochem.* 42 (2006) 251-258.
- [2] T.L. Kulova, A.M. Skundin, E.A. Nizhnikovskii, A. V. Fesenko, Temperature effect on the lithium diffusion rate in graphite, *Russ. J. Electrochem.* 42 (2006) 259-262.
- [3] C. Zhang, Y. Xu, M. Zhou, L. Liang, H. Dong, M. Wu, et al., Potassium Prussian Blue Nanoparticles: A Low-Cost Cathode Material for Potassium-Ion Batteries, *Adv. Funct. Mater.* 27 (2017) 1604307.

Table C.1.  
Freezing point range of liquid electrolyte used in Li-ion and K-ion batteries.

<b>Temperature</b>	<b>1M LiPF<sub>6</sub> EC/DEC</b>	<b>0.8M KPF<sub>6</sub> EC/DEC</b>
0°C	Liquid	Liquid
-10°C	Liquid/Solid	Liquid
-20°C	Liquid/Solid	Solid

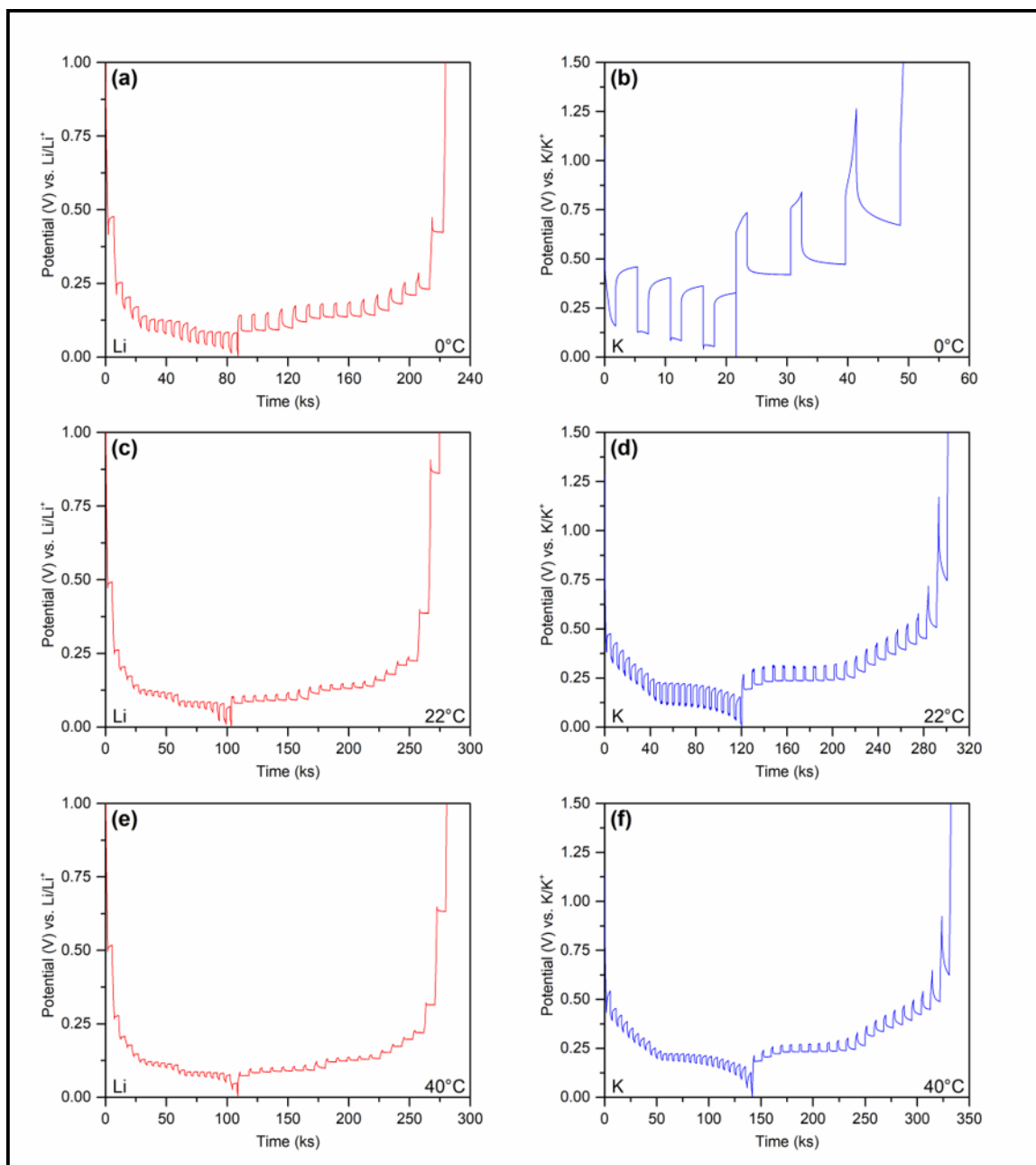


Figure C.1. Galvanostatic intermittent titration technique profiles. At 0°C for (a) Li and (b) K. At 22°C for (c) Li and (d) K. At 40°C for (e) Li and (f) K. All profiles were conducted with 30-minute current pulses at  $C/10$  ( $37.2 \text{ mA g}^{-1}$  for Li and  $27.9 \text{ mA g}^{-1}$  for K) followed by 1-hour relaxations.

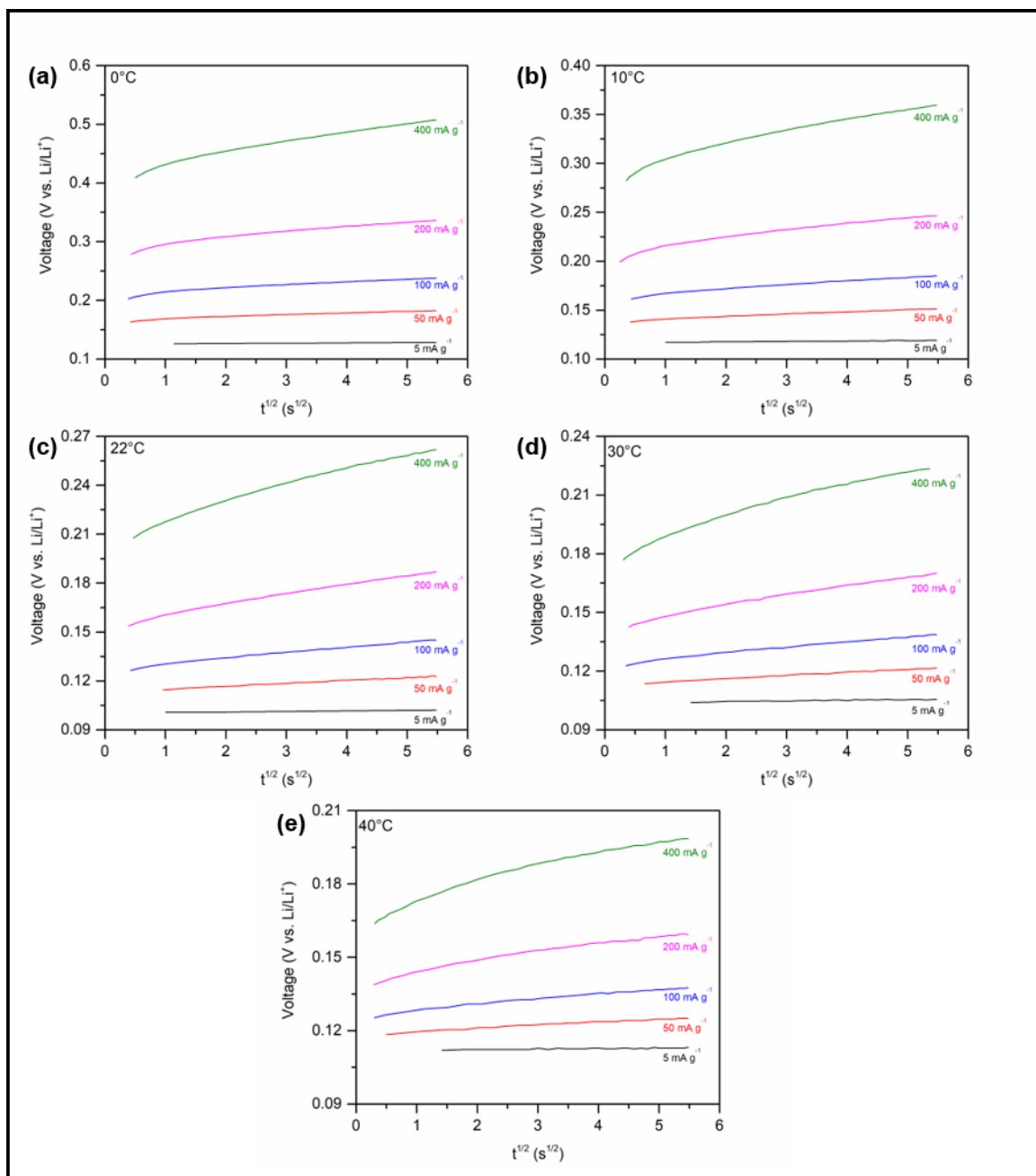


Figure C.2. Current pulses for LIB graphite anode at various specific currents. (a) 0°C. (b) 10°C. (c) 22°C. (d) 30°C. (e) 40°C. Linear relationship was used to determine  $(dE/d\sqrt{t})$  for solid-state diffusion coefficient calculation, and performed at 60% SOC.

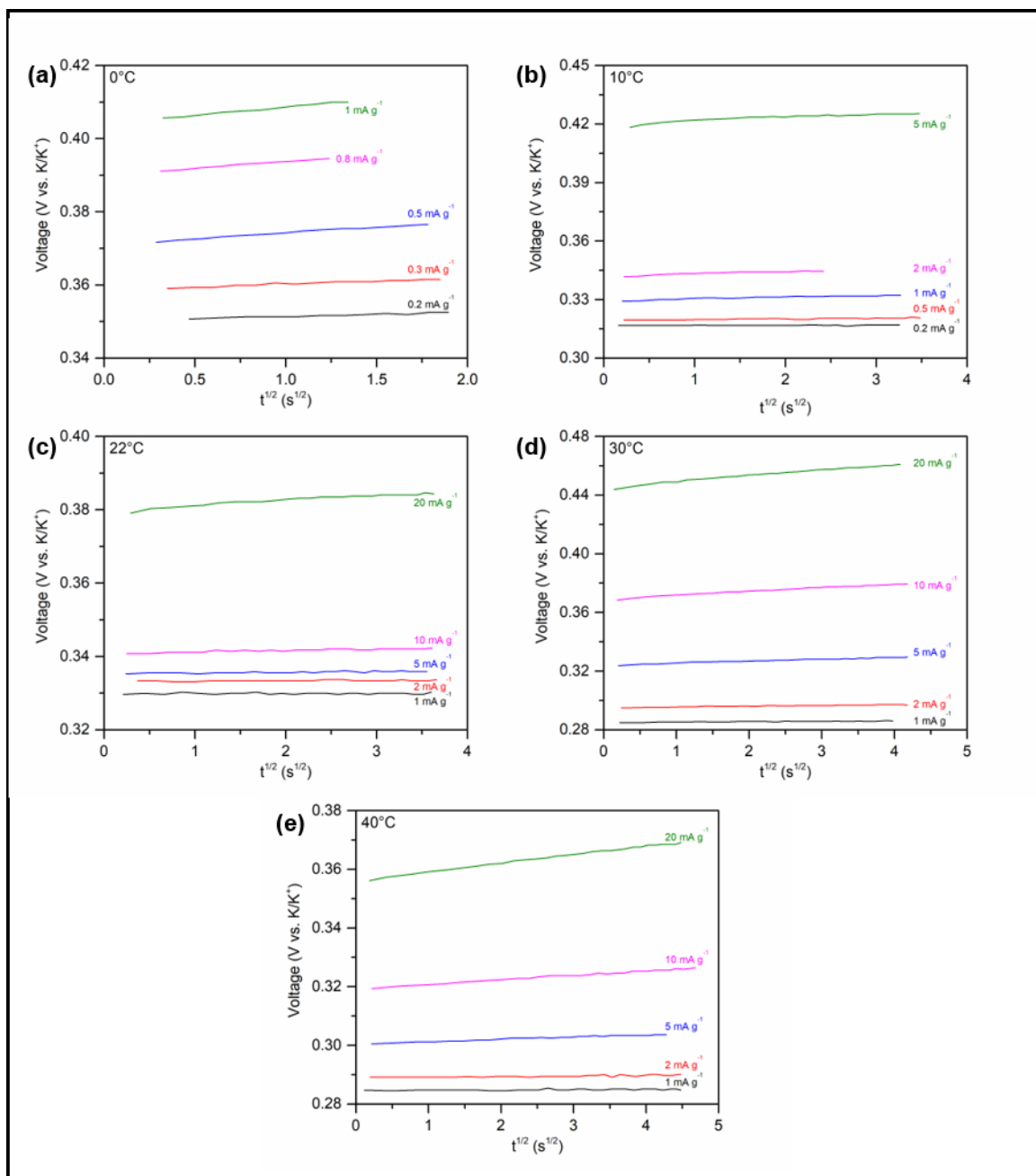


Figure C.3. Current pulses for graphite anode in KIB at various specific currents. (a) 0°C. (b) 10°C. (c) 22°C. (d) 30°C. (e) 40°C. Linear relationship was used to determine  $(dE/d\sqrt{t})$  for solid-state diffusion coefficient calculation, and performed at 60% SOC.

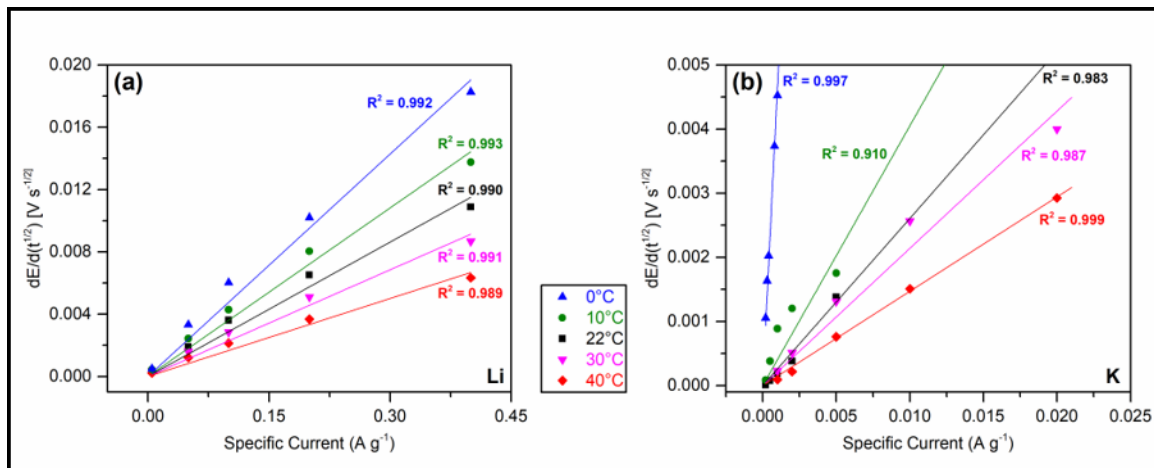


Figure C.4. Dependence of  $(dE/d\sqrt{t})$  on specific current across temperatures. (a) Li. (b) K.

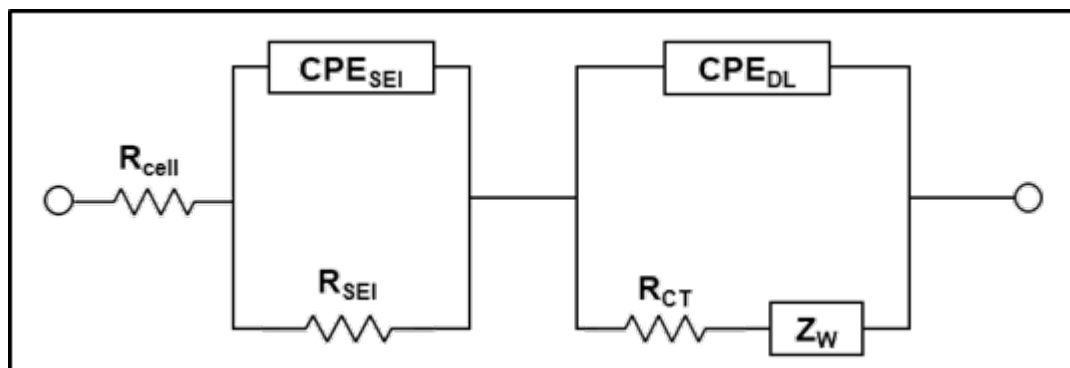


Figure C.5. Equivalent circuit utilized for fitting of electrochemical impedance spectra data. Equivalent circuit consists of a cell resistance, a constant phase element for SEI capacitance, a SEI resistance, a constant phase element for double layer capacitance, a charge-transfer resistance, and a Warburg diffusion element.

Table C.2.

Fitting parameters for Li-ion battery electrochemical impedance spectra measured at each temperature. All measurements were performed at 200 mV, for cells conditioned at C/10 for 10 cycles at 22°C.

Parameter	0°C	22°C	22°C	30°C	40°C
$R_{cell}$ ( $\Omega$ )	4.21E+00	3.03E+00	1.12E+00	9.29E-01	1.34E+00
$R_{SEI}$ ( $\Omega$ )	4.24E+02	1.32E+02	6.49E+01	3.53E+01	1.87E+01
$Q_{SEI}$ ( $S s^n$ )	5.97E-05	1.31E-04	1.07E-04	1.11E-04	1.04E-04
$n_{Q,SEI}$	8.74E-01	7.00E-01	7.00E-01	7.00E-01	7.00E-01
$R_{CT}$ ( $\Omega$ )	6.22E+01	1.84E+01	6.61E+00	4.61E+00	3.48E+00
$Q_{DL}$ ( $S s^n$ )	4.04E-03	4.38E-03	2.71E-03	2.26E-03	2.02E-03
$n_{Q,DL}$	1.00E+00	1.00E+00	1.00E+00	1.00E+00	1.00E+00
$\sigma_{Warburg}$ ( $\Omega s^{-1/2}$ )	2.18E+01	1.12E+01	1.32E+01	1.06E+01	8.25E+00

Table C.3.

Fitting parameters for K-ion battery electrochemical impedance spectra measured at each temperature. All measurements were performed at 500 mV, for cells conditioned at C/10 for 10 cycles at 22°C.

Parameter	0°C	22°C	22°C	30°C	40°C
$R_{cell}$ ( $\Omega$ )	1.11E+01	1.34E+01	1.28E+01	1.09E+01	3.15E+00
$R_{SEI}$ ( $\Omega$ )	2.38E+04	5.61E+03	1.91E+03	8.74E+02	2.48E+02
$Q_{SEI}$ ( $S s^n$ )	4.84E-05	4.93E-05	8.93E-05	1.06E-04	6.66E-05
$n_{Q,SEI}$	8.86E-01	9.29E-01	7.50E-01	7.26E-01	7.94E-01
$R_{CT}$ ( $\Omega$ )	4.30E+04	8.68E+03	2.24E+03	8.20E+02	4.96E+02
$Q_{DL}$ ( $S s^n$ )	4.76E-04	4.78E-04	7.10E-04	7.62E-04	6.47E-04
$n_{Q,DL}$	9.25E-01	7.50E-01	9.03E-01	9.86E-01	8.27E-01
$\sigma_{Warburg}$ ( $\Omega s^{-1/2}$ )	3.94E+03	1.04E+03	1.98E+02	1.38E+02	1.11E+02

Table C.4.

Fitting parameters for Li-ion battery electrochemical impedance spectra after three slow conditioning cycles ( $5 \text{ mA g}^{-1}$ ) at various temperatures. All electrochemical impedance spectra were measured at 200 mV (vs. Li/Li<sup>+</sup>) and 22°C, corresponding to the data in Figure C.7a

Parameter	0°C	22°C	22°C	30°C	40°C
$R_{cell} (\Omega)$	2.53E+00	4.89E+00	3.40E+00	5.80E+00	2.59E+00
$R_{SEI} (\Omega)$	4.41E+01	4.64E+01	6.46E+01	9.37E+01	1.22E+02
$Q_{SEI} (\text{S s}^n)$	6.30E-05	6.12E-05	3.72E-05	5.24E-05	7.15E-06
$n_{Q,SEI}$	7.35E-01	7.00E-01	7.31E-01	7.09E-01	7.48E-01
$R_{CT} (\Omega)$	2.00E+01	2.02E+01	5.17E+01	5.15E+01	6.44E+01
$Q_{DL} (\text{S s}^n)$	4.07E-03	4.19E-03	2.73E-03	4.08E-03	3.53E-03
$n_{Q,DL}$	7.03E-01	7.00E-01	7.40E-01	7.00E-01	7.43E-01
$\sigma_{Warburg} (\Omega \text{s}^{-1/2})$	1.15E+01	1.09E+01	1.38E+01	4.53E-02	1.49E+01

Table C.5.

Fitting parameters for K-ion battery electrochemical impedance spectra after three slow conditioning cycles ( $5 \text{ mA g}^{-1}$ ) at various temperatures. All electrochemical impedance spectra were measured at 500 mV (vs. K/K<sup>+</sup>) and 22°C, corresponding to the data in Figure C.7b

Parameter	0°C	22°C	22°C	30°C	40°C
$R_{cell} (\Omega)$	6.18E+00	5.51E+00	5.14E+00	3.59E+01	5.27E+00
$R_{SEI} (\Omega)$	1.05E+03	8.18E+02	8.21E+02	2.71E+03	4.28E+03
$Q_{SEI} (\text{S s}^n)$	2.34E-05	2.97E-05	2.77E-05	2.60E-05	2.00E-05
$n_{Q,SEI}$	9.47E-01	9.77E-01	9.89E-01	9.50E-01	8.40E-01
$R_{CT} (\Omega)$	3.67E+03	2.76E+03	3.49E+03	3.54E+03	1.07E+04
$Q_{DL} (\text{S s}^n)$	2.15E-04	3.78E-04	2.95E-04	2.95E-04	1.48E-04
$n_{Q,DL}$	6.72E-01	6.71E-01	6.40E-01	6.89E-01	6.95E-01
$\sigma_{Warburg} (\Omega \text{s}^{-1/2})$	9.83E+01	5.49E+01	8.83E+01	1.03E+03	2.24E+03

Table C.6.

Fitting parameters for Li-ion battery electrochemical impedance spectra after 100 cycles ( $50 \text{ mA g}^{-1}$ ) at various temperatures. All electrochemical impedance spectra were measured at 200 mV (vs. Li/Li<sup>+</sup>) and 22°C, corresponding to the data in Figure C.8a

Parameter	0°C	22°C	22°C	30°C	40°C
$R_{cell}$ ( $\Omega$ )	2.52E+00	2.34E+00	2.56E+00	2.98E+00	2.58E+00
$R_{SEI}$ ( $\Omega$ )	6.18E+00	4.88E+00	7.74E+00	6.63E+00	1.06E+01
$Q_{SEI}$ ( $S s^n$ )	1.62E-05	2.89E-05	1.59E-05	1.65E-04	4.63E-06
$n_{Q,SEI}$	7.50E-01	8.10E-01	7.63E-01	7.82E-01	7.76E-01
$R_{CT}$ ( $\Omega$ )	2.84E+01	3.56E+01	2.46E+01	2.24E+01	2.58E+01
$Q_{DL}$ ( $S s^n$ )	1.24E-04	1.55E-04	1.55E-04	2.46E-04	1.05E-04
$n_{Q,DL}$	7.50E-01	7.50E-01	7.50E-01	7.64E-01	7.50E-01
$\sigma_{Warburg}$ ( $\Omega s^{-1/2}$ )	7.93E+00	1.03E+01	1.03E+01	9.35E+00	8.78E+00

Table C.7.

Fitting parameters for K-ion battery electrochemical impedance spectra after 100 cycles ( $50 \text{ mA g}^{-1}$ ) at various temperatures. All electrochemical impedance spectra were measured at 500 mV (vs. K/K<sup>+</sup>) and 22°C, corresponding to the data in Figure C.8b

Parameter	0°C	22°C	22°C	30°C	40°C
$R_{cell}$ ( $\Omega$ )	5.38E+00	5.50E+00	1.26E+01	8.42E+00	9.64E+00
$R_{SEI}$ ( $\Omega$ )	1.11E+03	8.91E+02	2.12E+03	3.40E+03	5.79E+03
$Q_{SEI}$ ( $S s^n$ )	2.41E-05	4.34E-05	6.50E-04	7.67E-04	8.00E-05
$n_{Q,SEI}$	1.00E+00	8.91E-01	7.34E-01	7.11E-01	7.00E-01
$R_{CT}$ ( $\Omega$ )	2.87E+03	3.44E+03	1.27E+03	2.33E+03	3.04E+03
$Q_{DL}$ ( $S s^n$ )	1.74E-04	2.57E-04	4.52E-05	5.03E-05	2.51E-03
$n_{Q,DL}$	7.22E-01	7.50E-01	9.79E-01	9.56E-01	9.85E-01
$\sigma_{Warburg}$ ( $\Omega s^{-1/2}$ )	1.28E+02	9.46E+01	5.85E+01	2.13E+02	3.60E+01

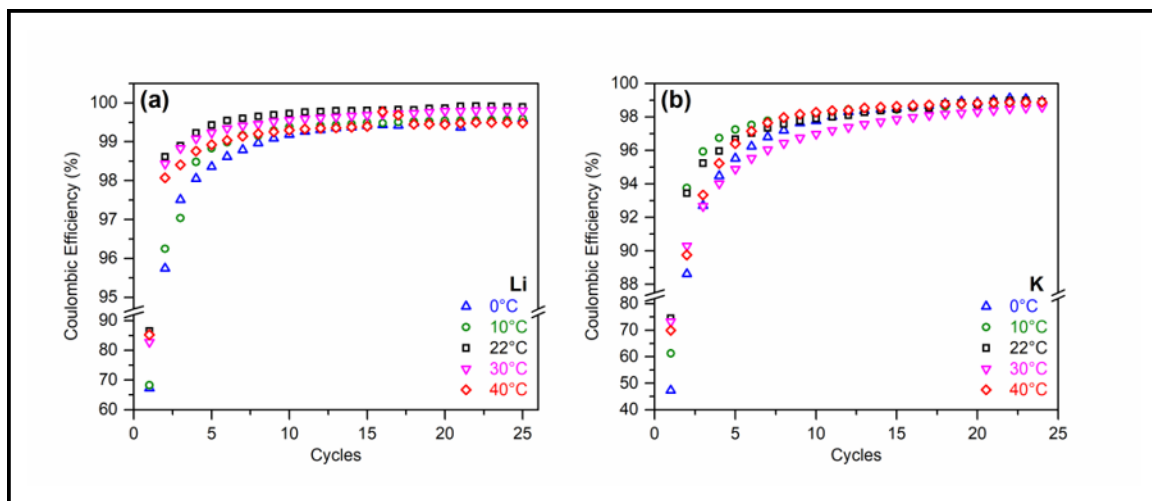


Figure C.6. Coulombic efficiencies for each operating temperature during initial cycles at  $50 \text{ mA g}^{-1}$ , corresponding to the data in Figure 5.3a-b. (a) Li. (b) K.

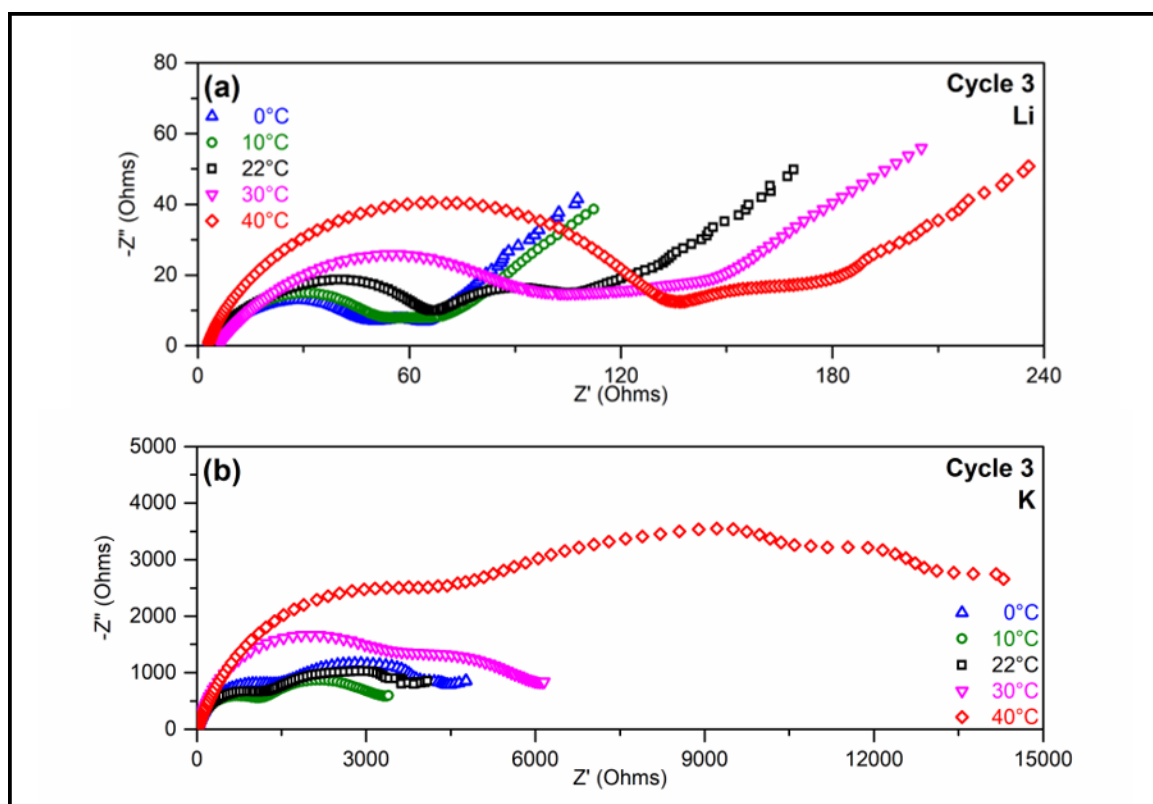


Figure C.7. Nyquist plots for electrochemical impedance spectra of cells conditioned with three formation cycles at 5 mA g<sup>-1</sup> at each corresponding temperature. All electrochemical impedance spectra were measured at 22°C and (a) 200 mV for Li, and (b) 500 mV for K.

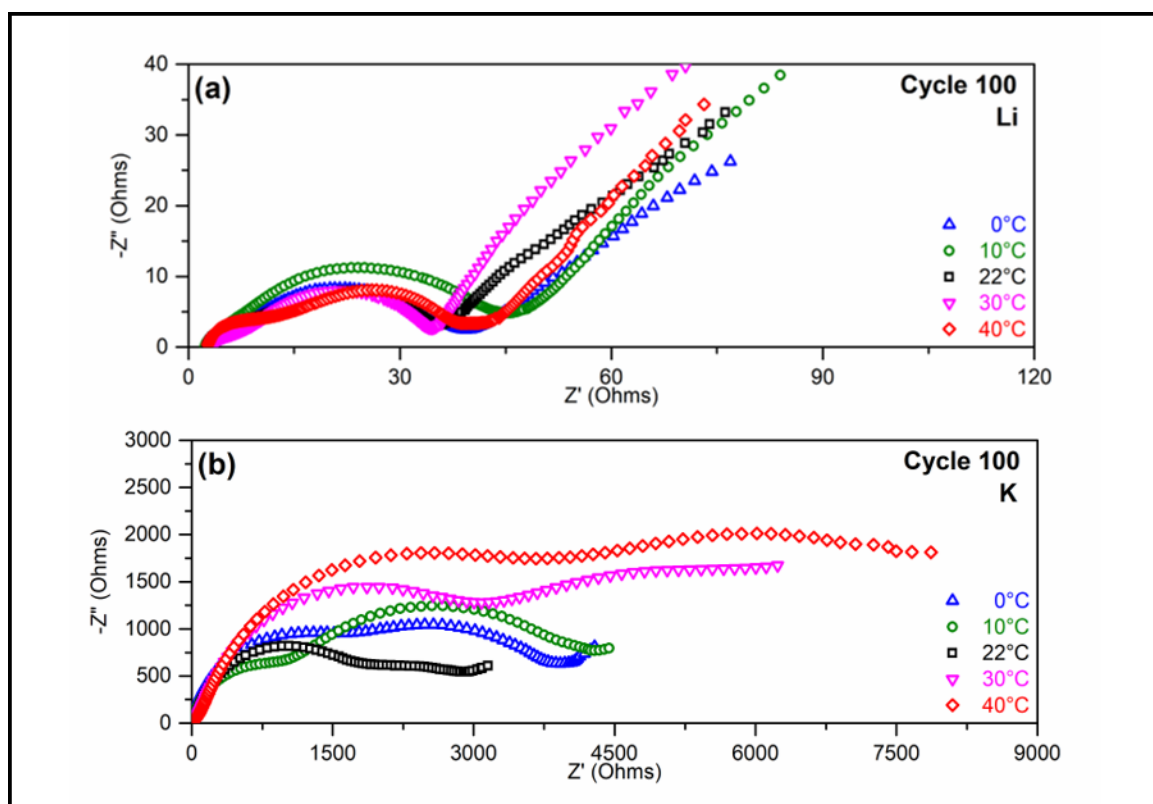


Figure C.8. Nyquist plots for electrochemical impedance spectra of cells after aging for 100 cycles at  $50 \text{ mA g}^{-1}$  at each corresponding temperature. All electrochemical impedance spectra were measured at  $22^\circ\text{C}$  and (a) 200 mV for Li, and (b) 500 mV for K.

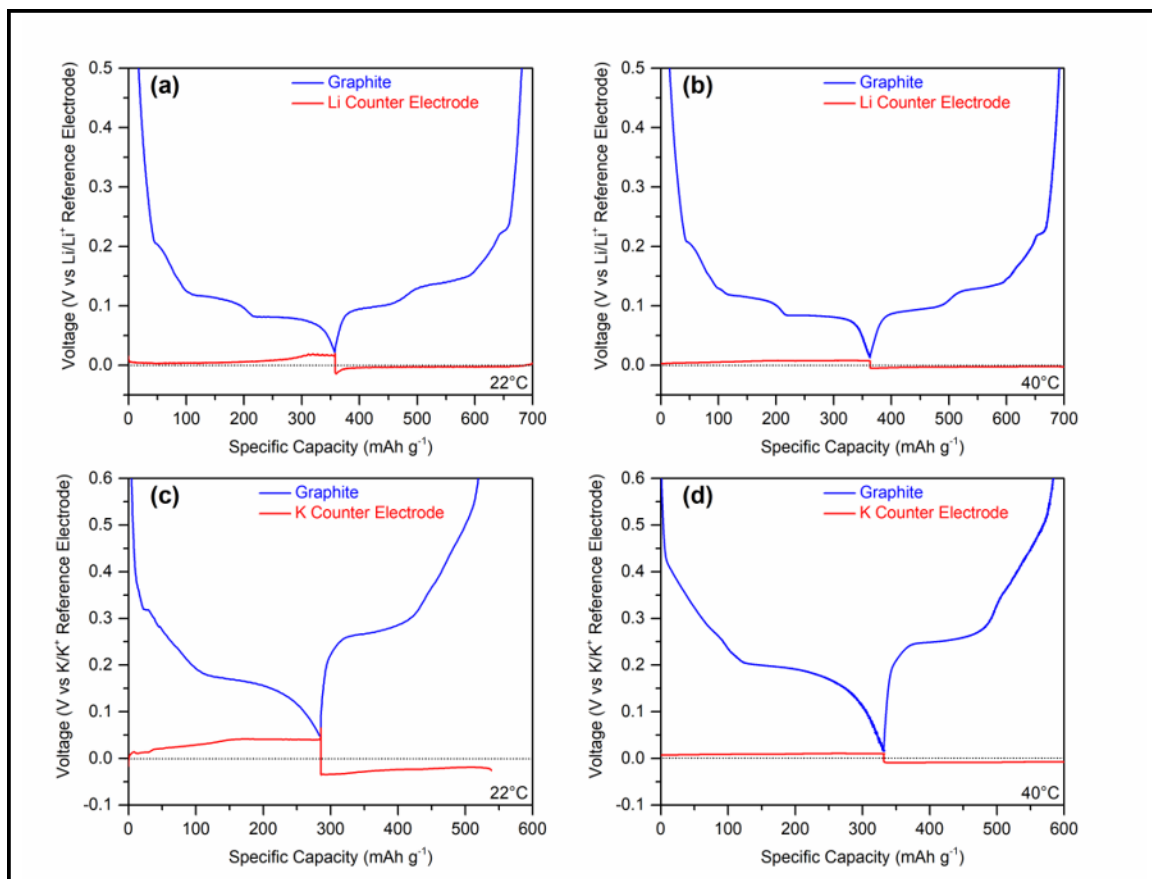


Figure C.9. Charge-discharge voltage profiles of 3-electrode cells at 20 mA g<sup>-1</sup> (after five conditioning cycles). (a) Li at 22°C. (b) Li at 40°C. (c) K at 22°C. (d) K at 40°C.

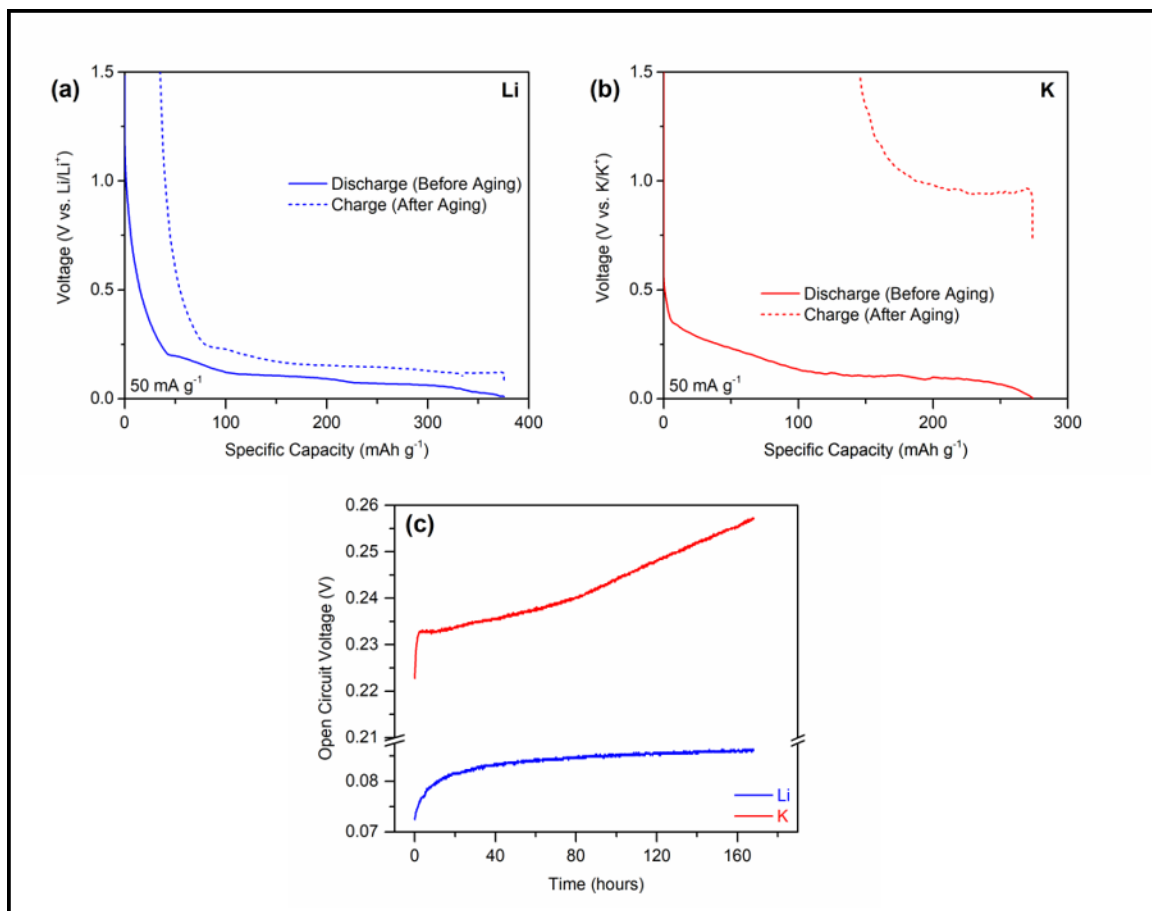


Figure C.10. Voltage profiles of cells before and after aging during cycle 6 of Figure 5.6a. (a) Li at 50 mA g<sup>-1</sup>. (b) K at 50 mA g<sup>-1</sup>. (c) Open circuit voltage profile of cells stored at 50°C for 7 days.

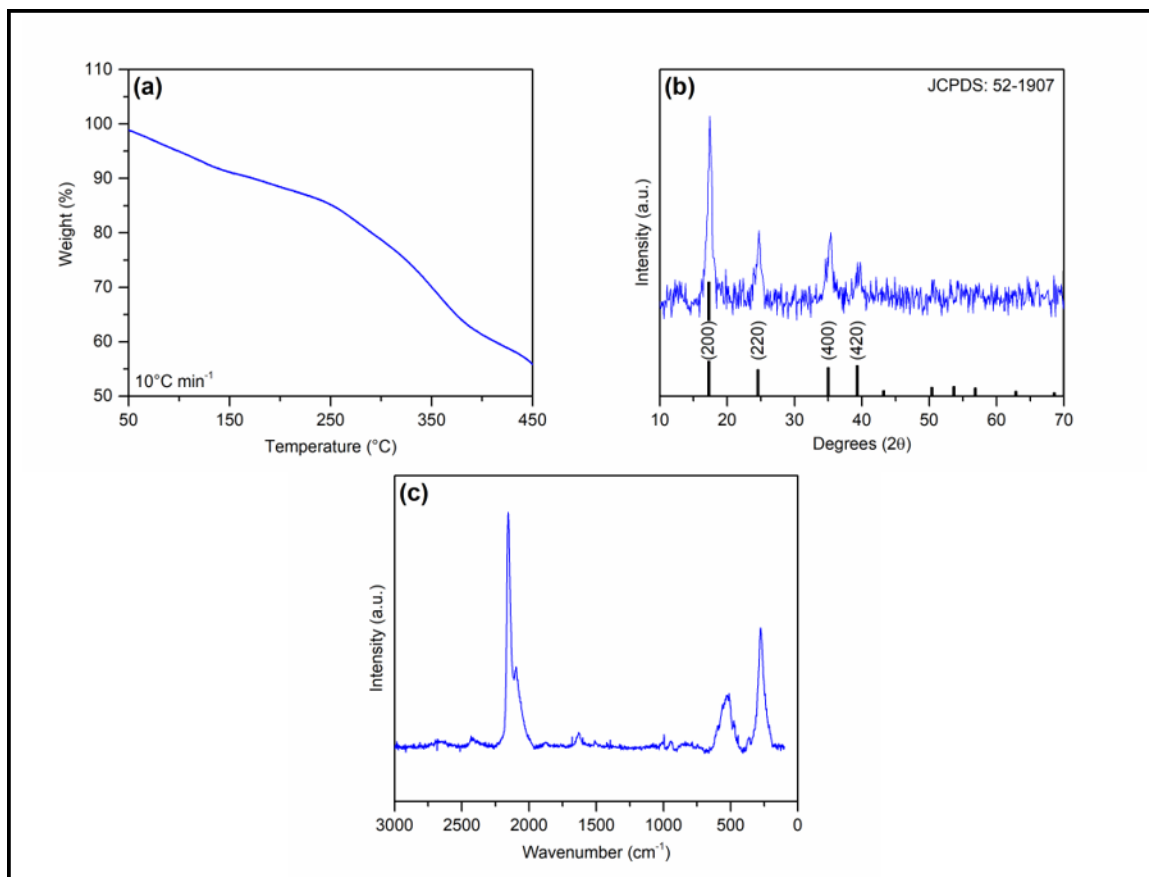


Figure C.11. Material characterization of synthesized Prussian blue cathode. (a) Thermogravimetric analysis conducted in argon atmosphere at 10°C min<sup>-1</sup> from 50 - 450°C. (b) X-ray diffraction pattern, with JCPDS 52-1907 reference card for Prussian blue Fe<sub>4</sub>[Fe(CN)<sub>6</sub>]<sub>3</sub>. (c) Raman spectrum.

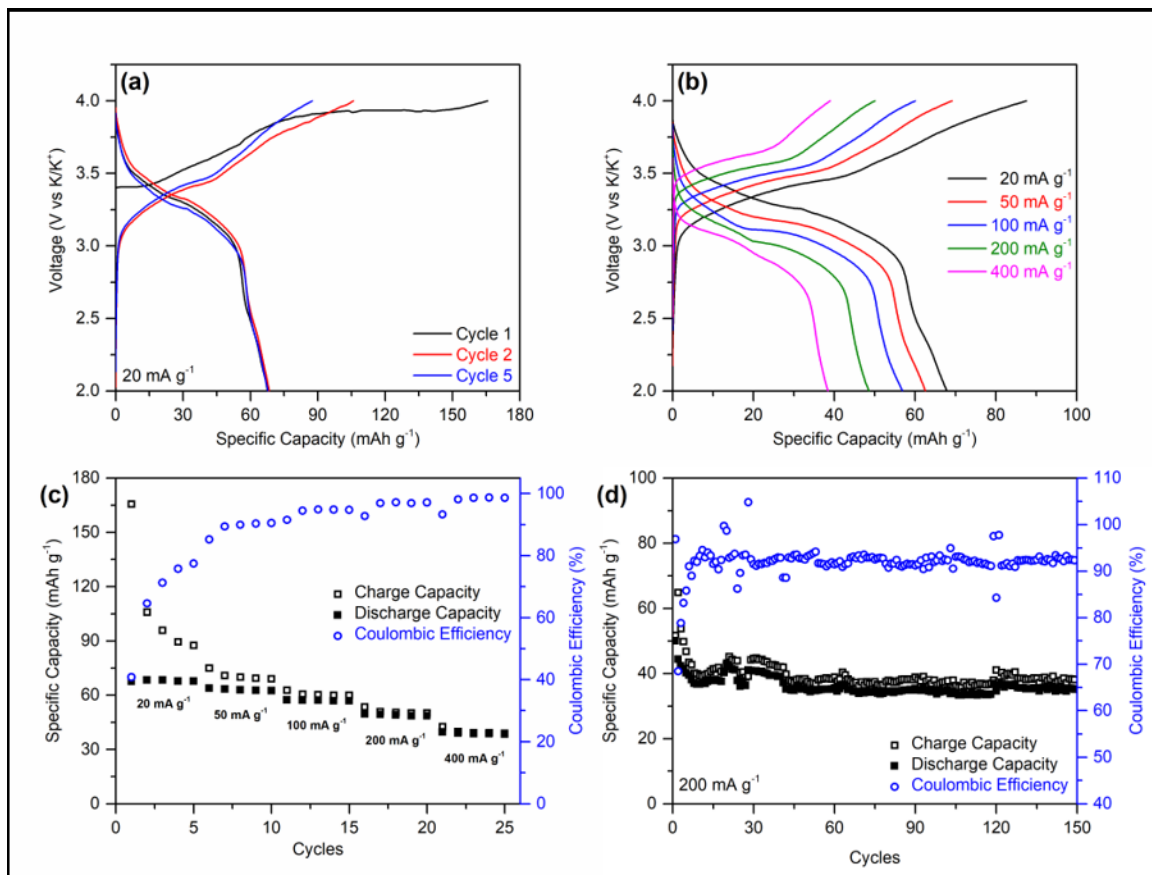


Figure C.12. Electrochemical analysis of Prussian blue cathode in half-cell configuration. (a) Charge-discharge voltage profile for cycle 1, 2, and 5 conducted at  $20 \text{ mA g}^{-1}$  from 2 - 4 V. (b) Charge-discharge voltage profile at various specific currents of 20 -  $400 \text{ mA g}^{-1}$ . (c) Rate study from 20 -  $400 \text{ mA g}^{-1}$ . (d) Long-term galvanostatic cycling conducted at  $200 \text{ mA g}^{-1}$ .

## D. CHAPTER 6 SUPPORTING INFORMATION

*Materials*

Synthetic graphite was purchased (MTI Corporation) and sieved to remove large particles (500 mesh,  $< 25 \mu\text{m}$ , Endecotts). Spherical carbon particles were prepared by an autogenic reaction as follows. In an argon-filled glovebox, 750 mg of mesitylene was tightly sealed in a 3 mL autoclave reaction vessel (stainless steel). The reactor was heated to  $700^\circ\text{C}$  with a ramping rate of  $30^\circ\text{C min}^{-1}$ . After holding the temperature at  $700^\circ\text{C}$  for 20 minutes, the reactor was cooled to room temperature over three hours. The obtained material was further pyrolyzed under argon at  $900^\circ\text{C}$  for two hours using ramp rates of  $5^\circ\text{C min}^{-1}$  to clean the sample and remove heteroatoms. To prepare the spiky carbon, bee pollen was carefully washed with DI water and sieved (500 mesh) to remove impurities. The pollen was then pyrolyzed under argon at  $900^\circ\text{C}$  for two hours to carbonize the material and remove heteroatoms.

*Electrode Preparation and Electrochemical Testing*

Electrodes were prepared by taking 80% wt. carbon, 10% wt. conductive additive (Timcal C65), and 10% wt. poly vinylidene difluoride (PVDF) polymer binder, using N-methyl pyrrolidone as a solvent to create a slurry. The slurry was cast on a copper current collector and dried at  $80^\circ\text{C}$  under vacuum overnight. 12 mm diameter electrodes were punched out, with average active material densities of  $3 \text{ mg cm}^{-2}$ . Coin-type 2032 half-cells were constructed in an argon glove box, utilizing lithium metal as the counter and a reference electrode. Celgard 2500 was utilized as a separator, while 1M  $\text{LiPF}_6$  in 1:1 (by volume) ethylene carbonate (EC): diethyl carbonate (DEC) was used as the electrolyte. Full cells were constructed with  $\text{LiCoO}_2$  as a cathode, with electrodes (A-C010) obtained from the U.S. Department of Energys CAMP (Cell Analysis, Modeling, and Prototyping) Facility, Argonne National Laboratory,

with average mass loadings of  $14.5 \text{ mg cm}^{-2}$ . Galvanostatic cycling was conducted with an Arbin cycler at  $22^\circ\text{C}$ , in a voltage range of 0.005 - 2.0 V (vs. Li/Li<sup>+</sup>), utilizing  $1\text{C} = 372 \text{ mA g}^{-1}$  (based off the theoretical capacity of graphite) to calculate the current densities. Potentiostatic electrochemical impedance spectroscopy (EIS) measurements were performed with 5 mV amplitude from 0.01 -  $10^6$  Hz using a Gamry-600+ instrument for cells conditioned to a voltage of 200 mV (vs. Li/Li<sup>+</sup>). Echem Analyst software was utilized for EIS spectra fitting.

It is known that cycling history affects the safety and thermal response of lithium ion batteries significantly. For example, harsh cycling conditions, such as elevated temperatures ( $>40^\circ\text{C}$ ) or fast charging rates, causes cell aging by kinetically enhancing side reactions, e.g. SEI layer growth, resulting in cell impedance rise, capacity decay, and irreversible loss of lithium and electrolyte. To test the significance of particle morphology with regards to this phenomena, each carbon anode was aged at 1C rate at  $50^\circ\text{C}$  for 100 cycles (Figure D.4). Notably, the spherical carbon material exhibits a lower average Coulombic efficiency ( $99.34\% \pm 0.28\%$ ), as compared to spiky carbon ( $99.73\% \pm 0.29\%$ ) and graphite ( $99.75\% \pm 0.17\%$ ), with appreciable capacity decay observed for all three materials.

#### *Thermal and Materials Characterization*

Differential scanning calorimetry (DSC) was performed with a TA Instruments Q20 unit, with a scan rate of  $5^\circ\text{C min}^{-1}$ . DSC samples were prepared by conditioning a coin cell (10 charge-discharge cycles at C/10 rate) to ensure complete SEI layer formation, and fully lithiating the sample by equilibrating the voltage to 0.01 V vs Li/Li<sup>+</sup>. Coin cells were then quickly disassembled in an argon glove box, where the electrode material was scraped off the Cu foil and sealed inside a hermetic aluminum pan with electrolyte, with the loading weight determined by a Mettler Toledo XS3DU microbalance. X-ray diffraction (XRD) was performed using a Rigaku SmartLab X-ray diffractometer via the Bragg-Brentano method and a Cu-K $\alpha$  X-ray source ( $\lambda = 0.15418 \text{ nm}$ ). Raman spectra were obtained with a Thermo Scientific DXR Raman microscope with a 633 nm laser. Nitrogen adsorption/desorption isotherms were

measured at 77 K with a Quantachrome Instruments NOVA 2200e. Scanning electron microscope (SEM) images were collected with a Hitachi S-4800 instrument. Elemental analysis was conducted using a CE-440 Elemental Analyzer from Exeter Analytical, Inc. A Quantachrome Instruments Autotap was used to measure tap density after 20,000 taps, with the volume measured for a weighed quantity of carbon placed in a graduated cylinder.

### *Interpreting DSC Trends*

In a DSC test setting, the sample temperature is linearly increased in time and the heat flow to and from the sample is measured. This heat flow provides an estimate of endothermic / exothermic transitions taking place in the sample. In the context of thermally activated side reactions in carbon-based electrode materials over the usual temperature range, the heat flow to DSC has the following expression:

$$q = -C \frac{dT}{dt} + H_s \frac{dx_s}{dt} + H_i \frac{dx_i}{dt} \quad (\text{D.1})$$

where  $q$  is heat flow to and from DSC in W/g and the experiment is carried out such that  $dT/dt$  is constant. The first term on the right refers to sensible heating and in general  $C = C(T)$ . The second term represents heat generated due to the reaction of metastable species in SEI with electrolyte, while the third term identifies reaction of intercalated lithium with electrolyte.  $dx/dts$  express reaction rates, while  $H_s$  are corresponding reaction enthalpies. Relevant expressions are:

$$\frac{dx_s}{dt} = -k_s \exp\left(-\frac{E_s}{k_b T}\right) x_s \quad (\text{D.2})$$

$$\frac{dx_i}{dt} = -k_i \exp\left(-\frac{E_i}{k_b T}\right) x_i \exp(-z/z_0) \quad (\text{D.3})$$

$$\frac{dz}{dt} = k_i \exp\left(-\frac{E_i}{k_b T}\right) x_i \exp(-z/z_0) \quad (\text{D.4})$$

Here  $x_s$  is dimensionless concentration of metastable species in the SEI,  $x_i$  is dimensionless intercalated Li concentration and  $z$  is dimensionless thickness of surface layer that forms as a result of reactions between intercalated Li and electrolyte ( $z_0$  is its initial thickness which is correlated to amount of chemical SEI formed after

cell fabrication and during formation cycling;  $k_b$  is Boltzmanns constant). From DSC testing, one has a temperature (T) and heat flow (q) information (i.e., time series). The set of equations (D.1) - (D.4) represent the DSC response of carbon-based electrode materials. This response is characterized by the materials heat capacity C, reaction enthalpies -  $H_s$  and  $H_i$ , reaction rate constants -  $k_s$  and  $k_i$ , activation energies -  $E_s$  and  $E_i$ , initial concentration of metastable species,  $x_s(t = 0)$ , initial concentration of intercalated Li,  $x_i(t = 0)$  and initial film thickness  $z_0$ . An inverse problem is posed that attempts to estimate the values of these properties such that the predicted response matches the measured one. Figure 6.6a pictorially shows this process. Values of the above-mentioned properties (i.e., reaction information) are varied such that the DSC response as predicted by equations (D.1) - (D.4) using these property values capture the observed response. In practice, these values are not varied manually but a multivariate optimization procedure is employed for a consistent interpretation.

#### *Electrochemical Dynamics*

Intercalation process in an active material particle is a combination of electrochemical reaction at the active surface and Li diffusion inside the particle. Mathematically this amounts to the following:

$$\frac{\partial C}{\partial t} = \nabla \cdot (D_s \nabla C) \quad (\text{D.5})$$

with boundary condition ( $\hat{n}$  is local surface normal):

$$-D_s \nabla C \cdot \hat{n} = \frac{i_{intercalation}}{F} \quad (\text{D.6})$$

Based on the particle geometry, the local normal can vary. Also, note that the gradient operation  $\nabla$  requires an appropriate three-dimensional representation. The total current applied to the particle is constrained as:

$$I_{app} = \int_S (i_{intercalation} + i_{side}) dS \quad (\text{D.7})$$

The relationship between applied current and particle capacity is:

$$I_{app} = C - rate \cdot Q_{particle} = C - rate \cdot \left( \frac{FC_s^{max} V_{particle}}{3600} \right) \quad (\text{D.8})$$

Intercalation flux is reversible and defined by Butler Volmer kinetics (Eqn. D.2). On the other hand, the side reaction flux is irreversible (Eqn. D.3). The resulting set of equations were solved in a finite volume fashion.

*Thermal Abuse Predictions*

Anode thermal abuse reaction information is derived from DSC measurements. A lithium cobalt oxide (LiCoO<sub>2</sub>) based cathode is used as a counter electrode and relevant properties are borrowed from literature. Similarly, the electrolyte thermal response is also described as in previous studies. With these, the following are the sources of heat generation during thermal runaway of a Li-ion full cell: *Reaction of metastable species in SEI with electrolyte:*

$$\frac{dx_s}{dt} = -k_s x_s \exp\left(-\frac{E_s}{k_b T}\right) \quad (\text{D.9})$$

*Reaction of intercalated lithium at anode with electrolyte:*

$$\frac{dx_i}{dt} = -k_i x_i \exp\left(-\frac{E_i}{k_b T}\right) \exp(-z/z_0) \quad (\text{D.10})$$

$$\frac{dz}{dt} = k_i x_i \exp\left(-\frac{E_i}{k_b T}\right) \exp(-z/z_0) \quad (\text{D.11})$$

*Reaction of intercalated lithium at cathode with electrolyte:*

$$\frac{dx_c}{dt} = k_c x_c (1 - x_c) \exp\left(-\frac{E_c}{k_b T}\right) \quad (\text{D.12})$$

*Electrolyte combustion:*

$$\frac{dx_e}{dt} = -k_e x_e \exp\left(-\frac{E_e}{k_b T}\right) \quad (\text{D.13})$$

These give rise to heat generation as:

$$Q_s = -m_a H_s \frac{dx_s}{dt} \quad (\text{D.14})$$

$$Q_i = -m_a H_i \frac{dx_i}{dt} \quad (\text{D.15})$$

$$Q_c = -m_c H_c \frac{dx_c}{dt} \quad (\text{D.16})$$

$$Q_e = -m_e H_e \frac{dx_e}{dt} \quad (\text{D.17})$$

where  $m_s$  represent corresponding anode, cathode and electrolyte masses in the cell. Cell temperature rise is related to each of the heat generations as well as thermal interactions with the ambient as:

$$mC_p \frac{dT}{dt} = Q_s + Q_i + Q_c + Q_e - hA(T - T_\infty) \quad (\text{D.18})$$

where  $(mC_p)$  is heat capacity of the cell and  $T_\infty$  is ambient temperature.

Table D.1.  
Material properties of carbon anodes

<b>Carbon Material</b>	<b>Surface Area (m<sup>2</sup> g<sup>-1</sup>)</b>	<b>Pore Volume (cc g<sup>-1</sup>)</b>	<b>Tap Density (g cc<sup>-1</sup>)</b>
<b>Graphite</b>	3.8	0.009	1.01
<b>Spherical Carbon</b>	1.5	0.002	0.86
<b>Spiky Carbon</b>	4.5	0.007	0.72

Table D.2.  
Elemental composition of carbon anodes (wt. %)

<b>Anode Material</b>	<b>Carbon</b>	<b>Hydrogen</b>	<b>Oxygen</b>	<b>Nitrogen</b>
<b>Graphite</b>	98.99 ± 0.61	0.55 ± 0.07	0.39 ± 0.71	0.06 ± 0.07
<b>Spherical Carbon</b>	96.63 ± 0.17	2.05 ± 0.05	1.27 ± 0.26	0.05 ± 0.02
<b>Spiky Carbon</b>	94.26 ± 0.27	0.98 ± 0.02	2.79 ± 0.46	1.97 ± 0.27

Table D.3.

Fitting parameters for electrochemical impedance spectroscopy modeling, conducted for carbon anodes before aging at 1C for 100 cycles at 50°C.

Parameter	Graphite	Spherical Carbon	Spiky Carbon
$R_{cell}$ ( $\Omega$ )	4.54E+00	5.32E+00	1.81E+00
$R_{SEI}$ ( $\Omega$ )	4.98E+00	4.46E+00	4.76E+00
$Q_{SEI}$ ( $S s^n$ )	1.91E-05	4.27E-05	4.16E-05
$n_{Q,SEI}$	8.04E-01	7.50E-01	8.01E-01
$R_{CT}$ ( $\Omega$ )	1.21E+01	2.53E+01	1.82E+01
$Q_{DL}$ ( $S s^n$ )	1.71E-04	8.43E-05	7.24E-05
$n_{Q,DL}$	8.32E-01	8.69E-01	9.05E-01
$\sigma_{Warburg}$ ( $\Omega s^{-1/2}$ )	4.81E+00	1.14E+01	7.02E+00

Table D.4.

Fitting parameters for electrochemical impedance spectroscopy modeling, conducted for carbon anodes after aging at 1C for 100 cycles at 50°C.

Parameter	Graphite	Spherical Carbon	Spiky Carbon
$R_{cell}$ ( $\Omega$ )	2.54E+00	1.60E+00	5.05E+00
$R_{SEI}$ ( $\Omega$ )	5.84E+00	7.32E+00	5.47E+00
$Q_{SEI}$ ( $S s^n$ )	2.94E-05	1.52E-01	2.60E-05
$n_{Q,SEI}$	7.99E-01	8.32E-01	8.00E-01
$R_{CT}$ ( $\Omega$ )	2.12E+02	3.03E+01	1.81E+01
$Q_{DL}$ ( $S s^n$ )	7.48E-05	4.88E-05	5.15E-05
$n_{Q,DL}$	8.82E-01	9.02E-01	9.01E-01
$\sigma_{Warburg}$ ( $\Omega s^{-1/2}$ )	6.52E+00	1.66E+01	8.44E+00

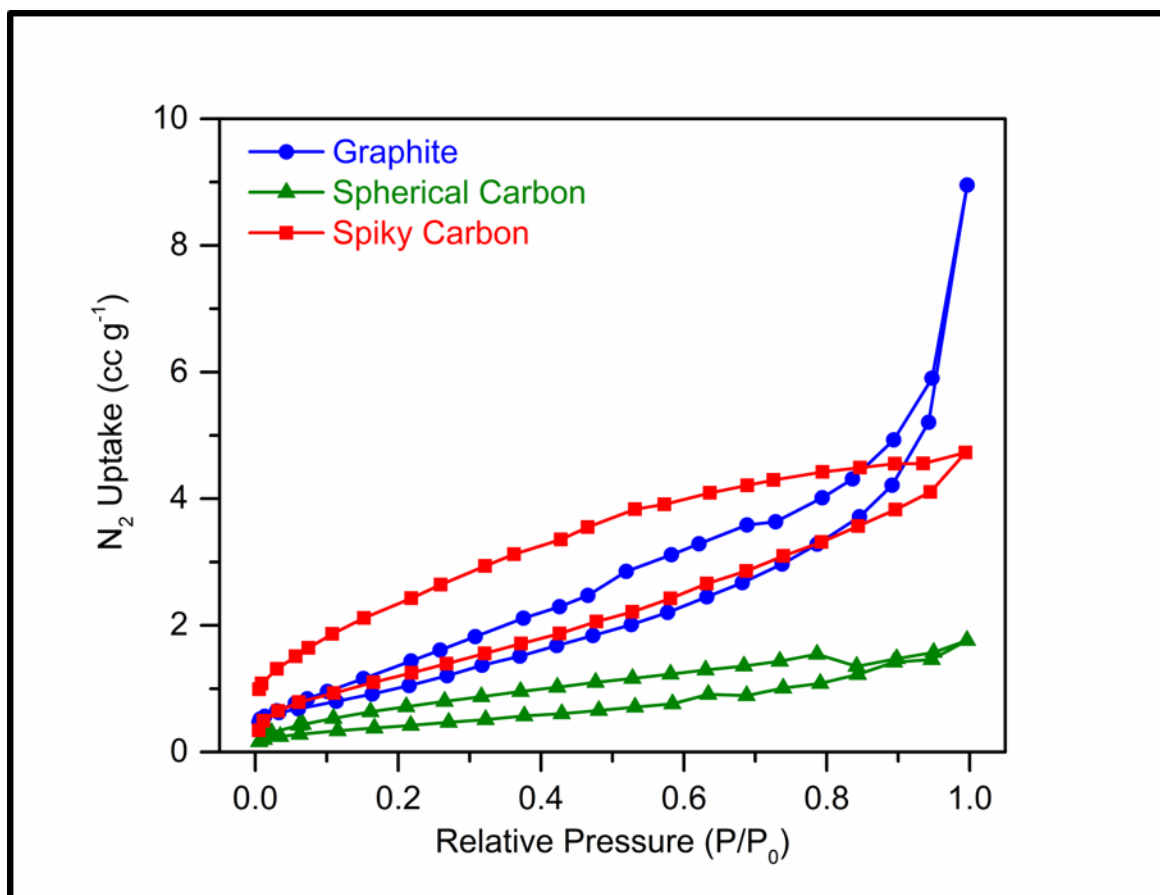


Figure D.1. Nitrogen adsorption/desorption isotherms obtained at 77 K for each carbon material.

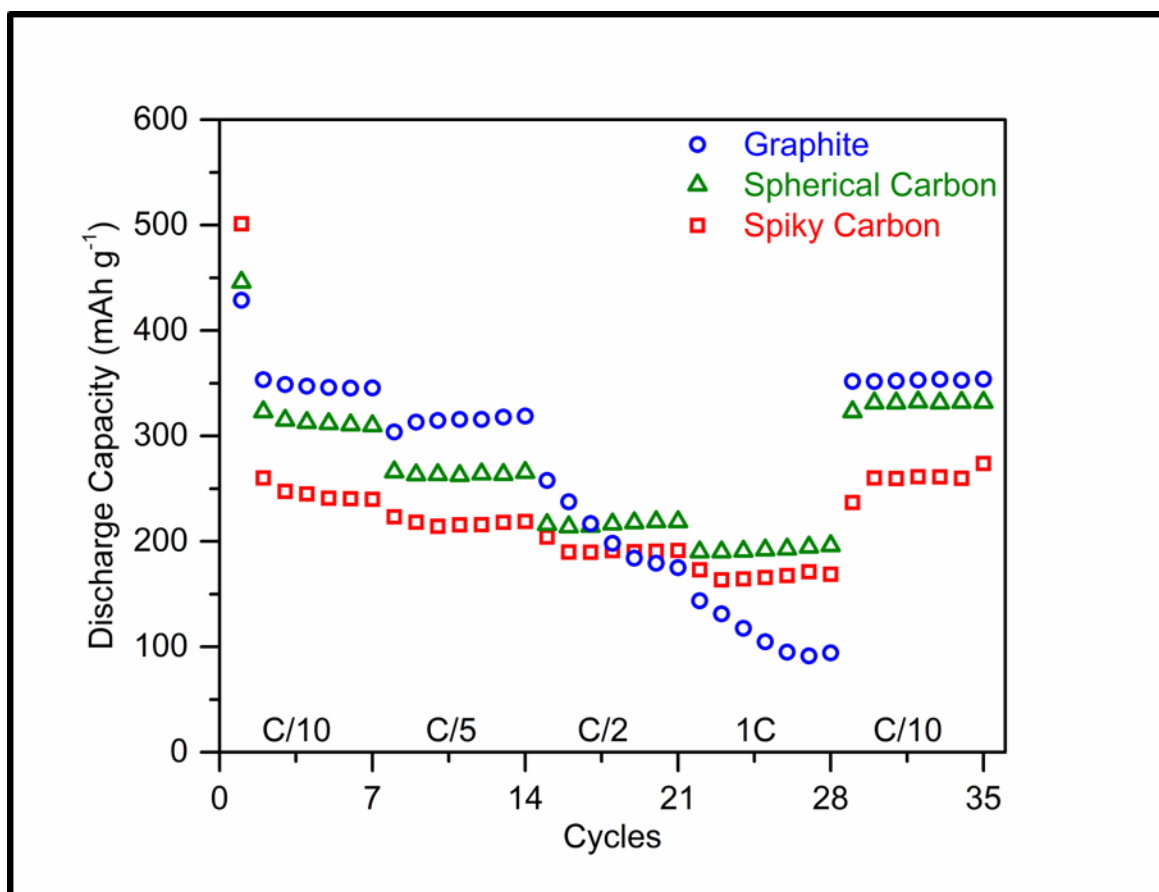


Figure D.2. Rate study of the three carbon materials, with 1C defined as 372 mA g<sup>-1</sup>.

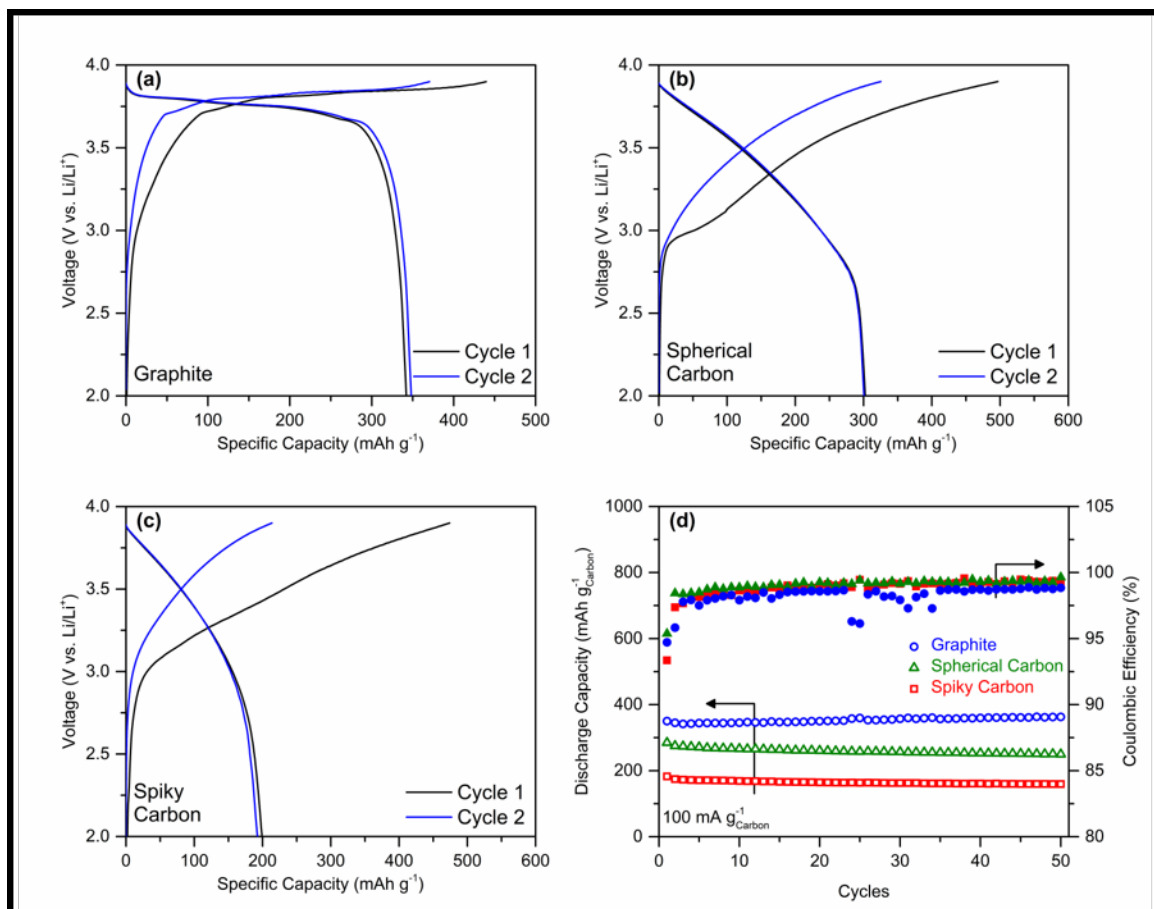


Figure D.3. Full cell data for tested carbon materials against a  $\text{LiCoO}_2$  cathode. First two cycle voltage profiles for (a) graphite, (b) spherical carbon, and (c) spiky carbon. Long-term cycling data with Coulombic efficiencies are shown in (d), using a current density of  $100 \text{ mA g}^{-1}$ , based on the weight of carbon.

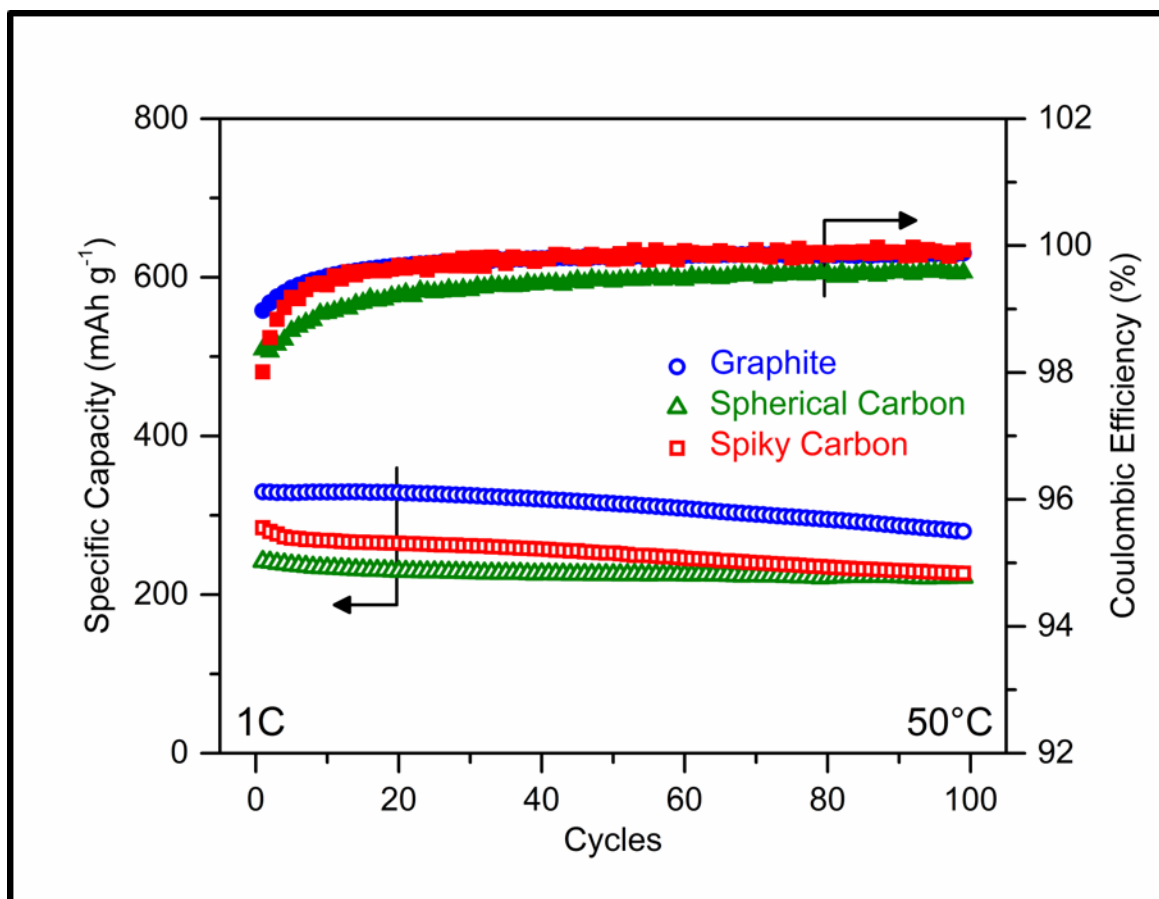


Figure D.4. Accelerated aging of carbon anodes with 1C rate conducted at 50°C for 100 cycles. EIS measurements were conducted before and after at 200 mV (vs. Li/Li<sup>+</sup>).

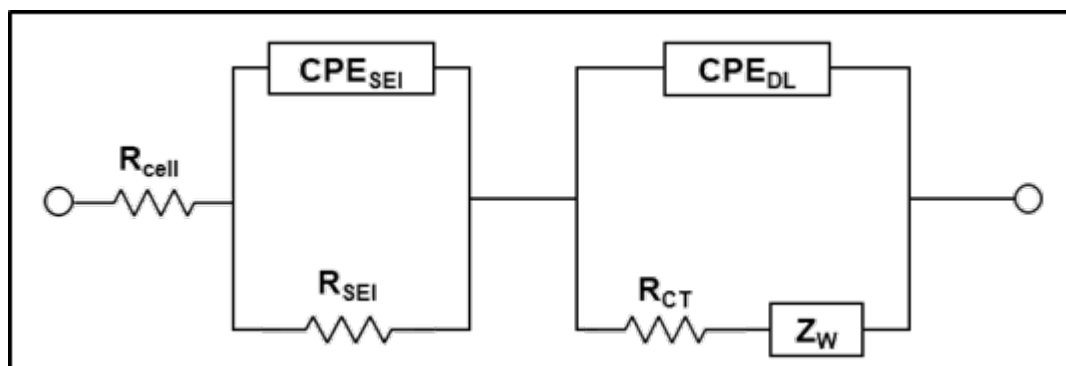


Figure D.5. Equivalent circuit utilized for electrochemical impedance spectra data fitting.

## E. CHAPTER 7 SUPPORTING INFORMATION

*Powders washing after HF etching*

After the reaction time elapsed, the powders were repeatedly washed with de-ionized (DI) water and centrifuged until the pH of the decanted liquid reached values higher than 4. Subsequently, the settled powders were filtered using a vacuum-assisted filtration device and allowed to dry at RT on the filtration device for at least 18 h.

*Electrodes preparation*

The slurry was mixed for 10 minutes in a Thinky mixer and tape-cast onto copper foil via a doctor-blade. The films were dried overnight in a vacuum oven at 80°C, and then 12 mm diameter electrodes were punched out with active material density of 1.75 mg cm<sup>-2</sup>. Stainless steel coin-type 2032 half-cells with potassium metal as the counter electrode were constructed in a high-purity glove box (99.998% Argon) with O<sub>2</sub> and H<sub>2</sub>O concentrations < 1 ppm for electrochemical testing. Whatman 934-AH glass microfiber was used as separator. The electrolyte was 0.8 M KPF<sub>6</sub> (Sigma-Aldrich 98%) in a 1:1 (by volume) of ethylene carbonate (EC, Sigma-Aldrich anhydrous 99%) and diethyl carbonate (DEC, Sigma-Aldrich anhydrous > 99%). All potentials mentioned in this study are vs. K/K<sup>+</sup> unless otherwise specified.

*Electrodes preparation*

The structure of the resultant MXene was confirmed using a Cu K-alpha X-ray diffractometer (Scintag X1, Scintag, Cupertino, CA, USA). The gas adsorption-desorption isotherms were obtained using a Quantachrome Autosorb-1 with nitrogen adsorbate. Nitrogen sorption analysis at 77 K was used for calculating the specific surface area (SSA) using the Brunauer-Emmet-Teller (BET) equation. The sample was outgassed under vacuum at 200°C for 48 h before the measurements. X-ray photoelectron spectroscopy (XPS) was performed utilizing a Kratos AXIS Ultra DLD Imaging X-ray

Photoelectron Spectrometer connected to an inert glovebox, to enable direct transfer of prepared samples for measurement. XPS measurements were performed on conditioned  $\text{Ti}_3\text{CNT}_z$  electrodes (pristine, 5 mV fully discharged, 3 V fully charged), after opened cells were washed with dimethyl carbonate and dried. Galvanostatic cycling was performed with an Arbin cyler at RT with a voltage range of 0.005 - 3.0 V and with current densities specified ( $10 \text{ mA g}^{-1}$  -  $500 \text{ mA g}^{-1}$ ). A Gamry Reference-600 electrochemical workstation was used to perform electrochemical impedance spectroscopy (EIS) in the frequency range of 0.01 Hz to  $10^6$  Hz. All the electrochemical measurements were carried out at room temperature.

To elucidate the contribution of carbon black for K-ion storage, we made an electrode from carbon black and PVDF (9:1 wt. ratio). The electrochemical results are shown in Fig E.5, where a reversible capacity of  $150 \text{ mAh g}^{-1}$  at  $28 \text{ mA g}^{-1}$  is achieved. The MXene electrodes have 15% wt. of carbon black, thus a small portion of the capacity are contributed by the carbon black. However, the peaks observed in the differential capacity plot (Fig. 7.1b) are not seen in the carbon black voltage profile meaning that an intercalation storage mechanism of K-ions in the MXene anodes is occurring.

Table E.1.

Atomic percentage estimated from X-ray photoelectron spectroscopy for all the elements on the surface of the  $\text{Ti}_3\text{CNT}_z$  electrodes before electrochemical cycling, after discharging to 5 mV, and recharging back to 3 V vs. K/K<sup>+</sup>.

Sample	C 1s	Cl 2p	F 1s	K 2p	N 1s	Na 1s	O 1s	P 2p	Ti 2p
Pristine	62.5	0.0	15.0	0.0	3.6	0.2	10.9	0.0	7.7
5 mV	23.2	0.6	17.4	24.4	0.0	0.2	31.8	2.3	0.0
3.0 V	18.4	0.7	21.8	23.9	0.5	1.5	29.6	18	1.7

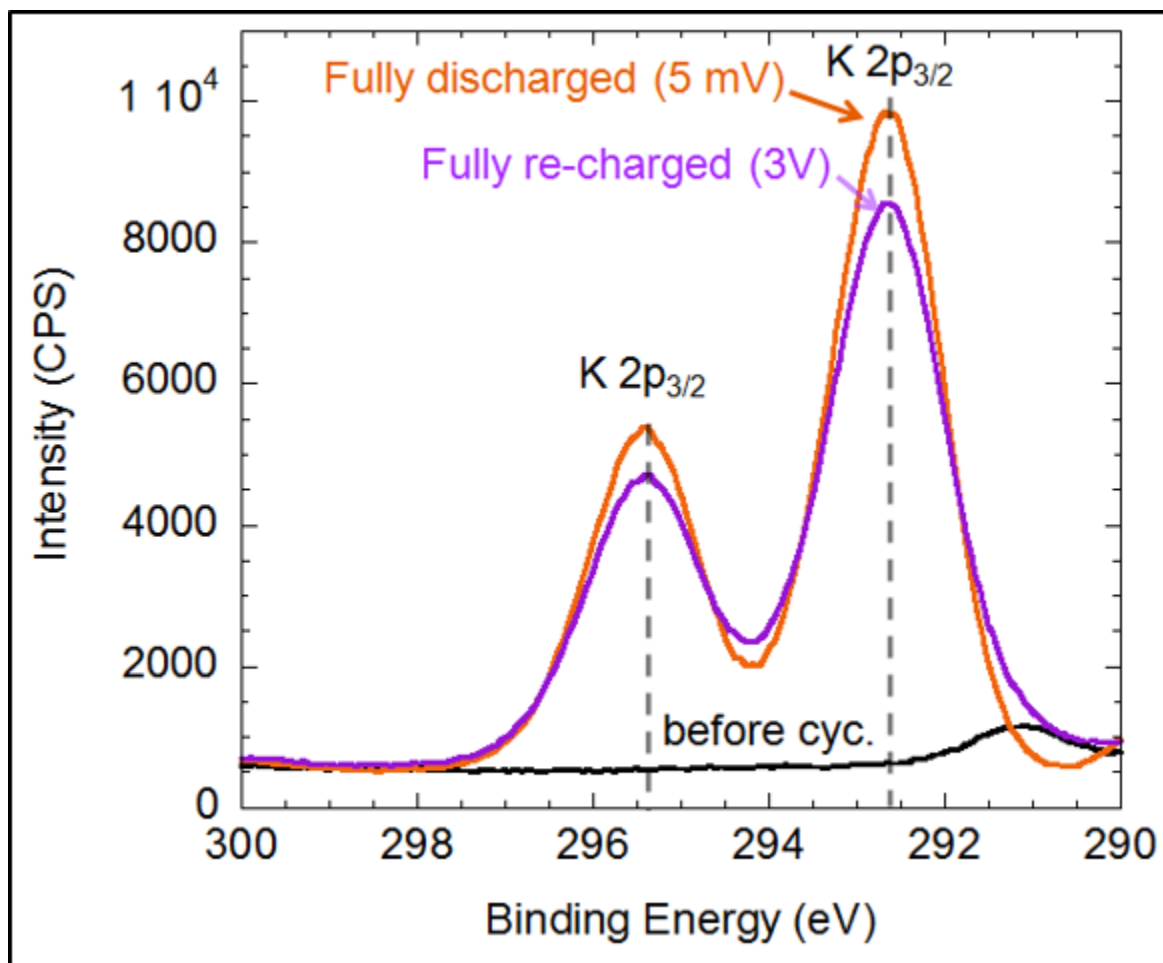


Figure E.1. K 2p X-ray photoelectron spectra for Ti<sub>3</sub>CNT<sub>z</sub> electrodes before cycling (black), after fully discharging down to 5 mV (orange), and after recharging back to 3V (purple).

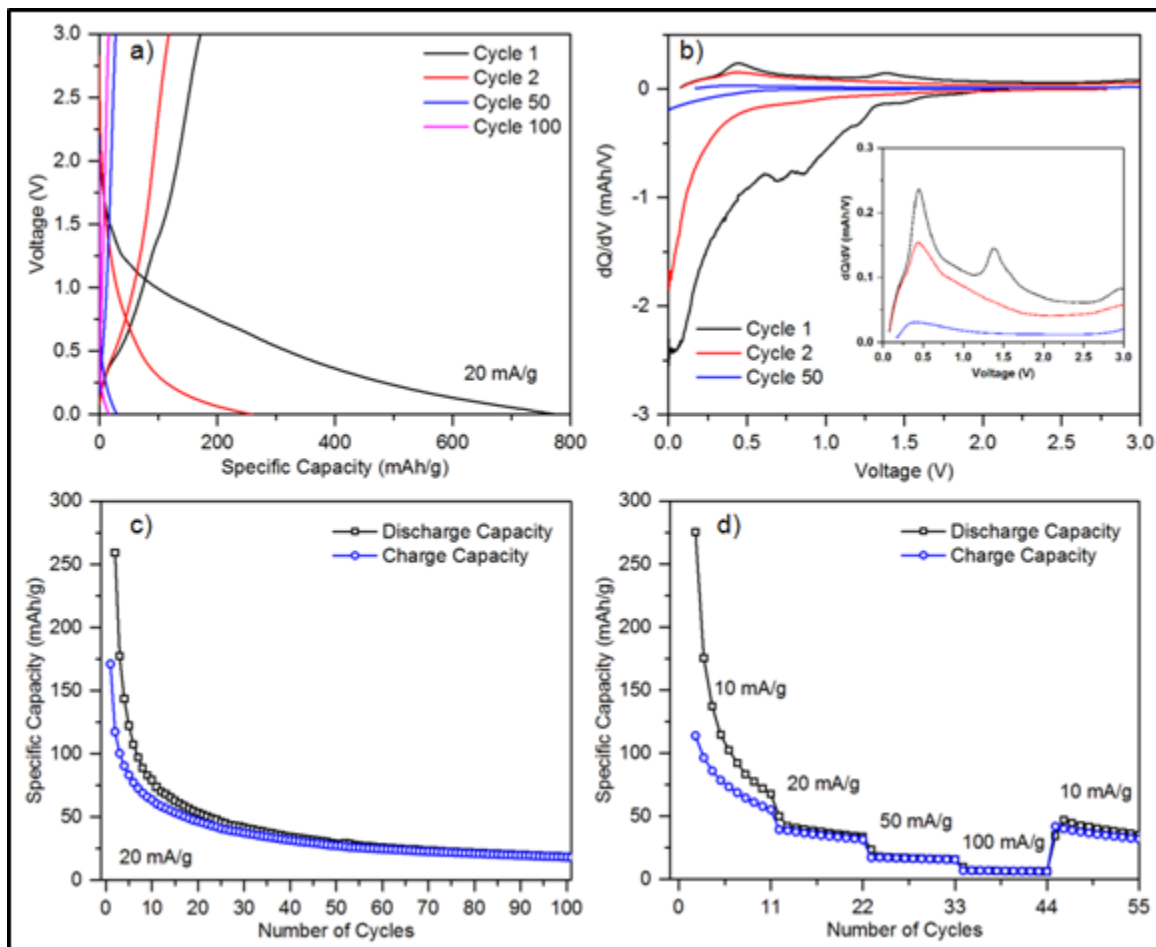


Figure E.2. The electrochemical performance of  $\text{Ti}_3\text{C}_2\text{T}_x$  electrode. (a) Galvanostatic voltage profile for cycle number 1, 2, 50 and 100 at 20 mA g<sup>-1</sup> between 5.0 mV and 3.0 V vs. K/K<sup>+</sup>. (b) The corresponding  $dQ/dV$  for the results presented in (a). The inset is a higher magnification for the potassiation part of the plot in (b). (c) Capacity vs. cycle number at 20 mA g<sup>-1</sup>. (d) Capacity vs. cycle number at rates of 10 - 100 mA g<sup>-1</sup>.

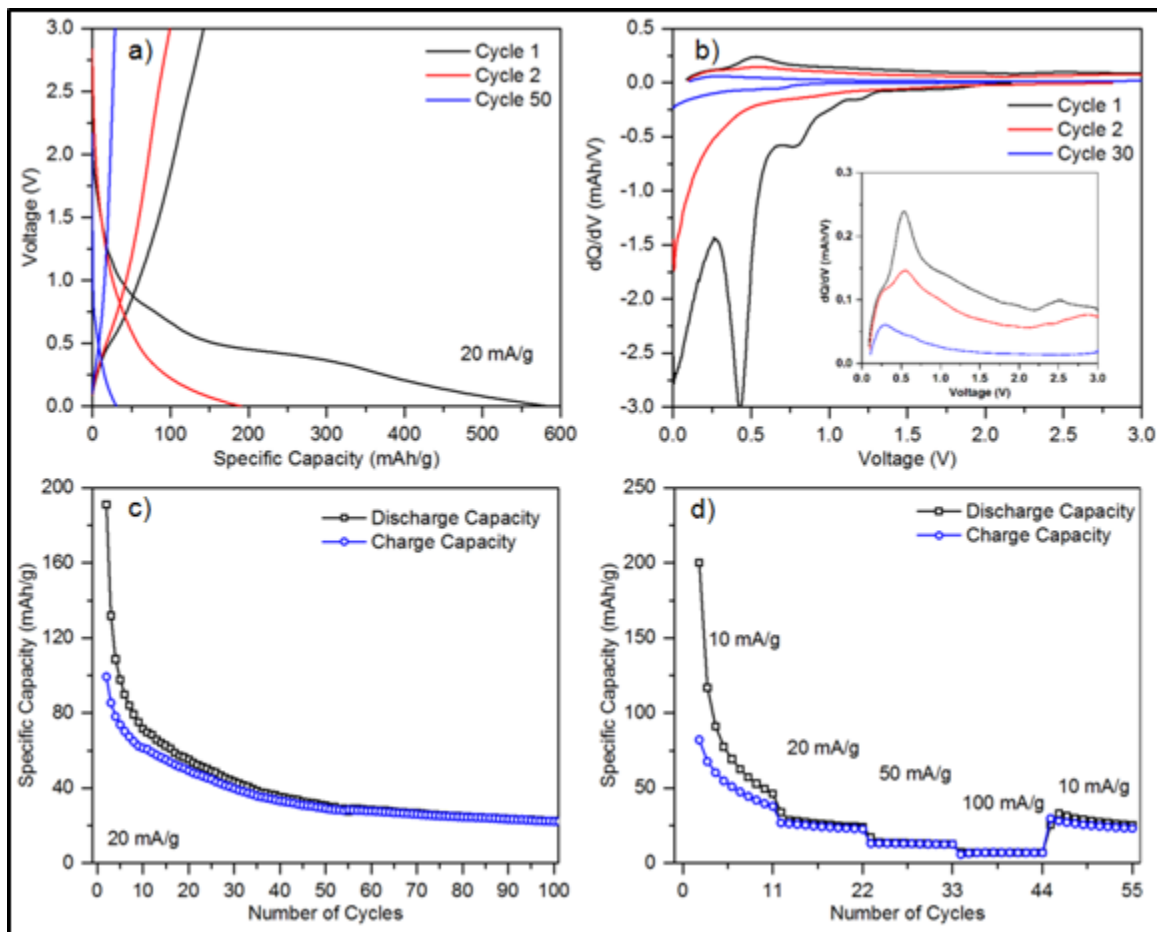


Figure E.3. The electrochemical performance of  $\text{Nb}_2\text{CT}_z$  electrode. (a) Galvanostatic voltage profile for cycle number 1, 2, 50 and 100 at 20 mA g<sup>-1</sup> between 5.0 mV and 3.0 V vs. K/K<sup>+</sup>. (b) The corresponding  $dQ/dV$  for the results presented in (a). The inset is a higher magnification for the potassiation part of the plot in (b). (c) Capacity vs. cycle number at 20 mA g<sup>-1</sup>. (d) Capacity vs. cycle number at rates of 10 - 100 mA g<sup>-1</sup>.

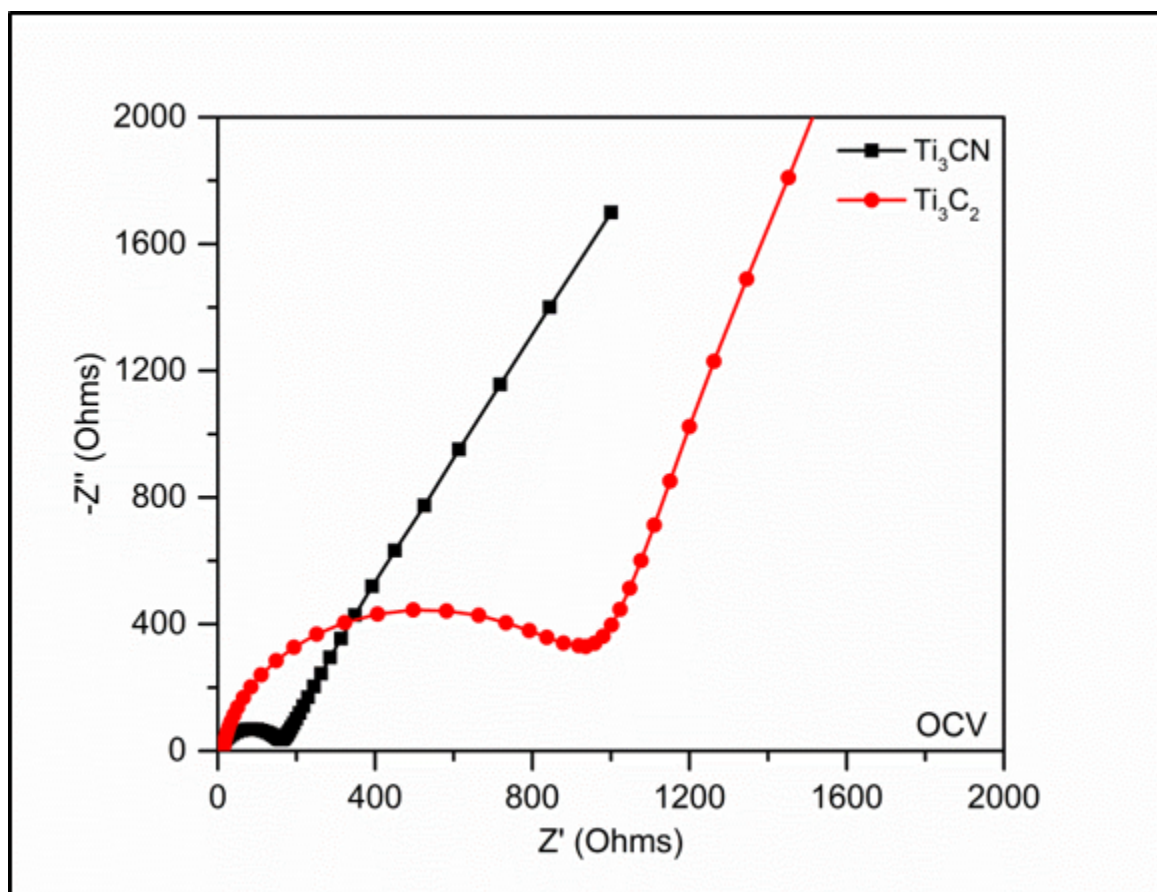


Figure E.4. Electrochemical impedance spectroscopy (EIS) Nyquist plot of  $Ti_3C_2T_x$  and  $Ti_3CNT_x$  at open circuit voltage.

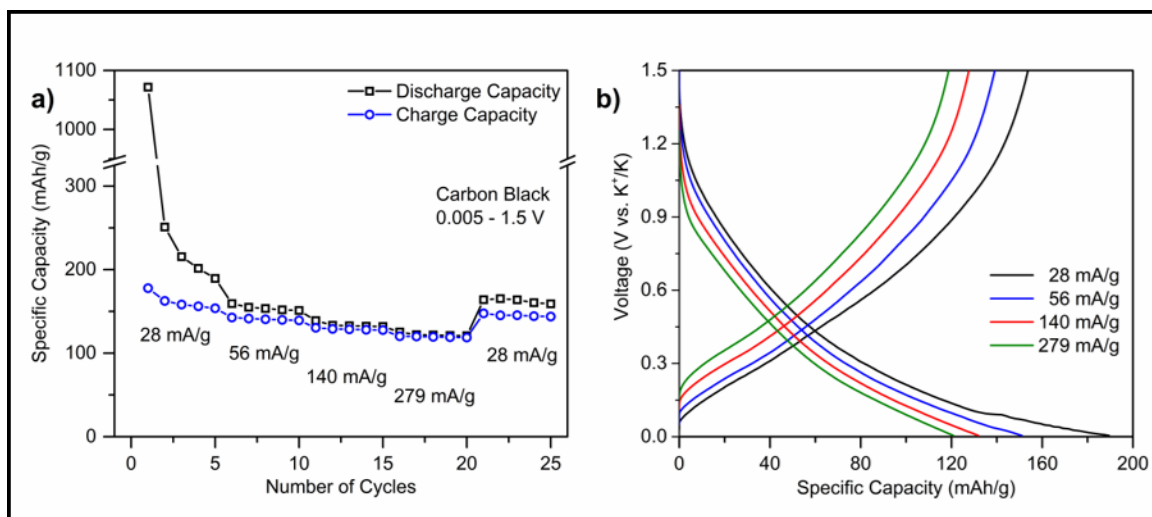


Figure E.5. The electrochemical performance of a carbon black electrode (90:10 carbon black to PVDF wt. ratio) in a KIB half cell. (a) Galvanostatic cycling at various current densities between 5 mV and 1.5 V. (b) Galvanostatic voltage profiles at various current densities.

VITA

## VITA

Ryan A. Adams received his Bachelors of Science in Chemical and Biomolecular Engineering with *Magna Cum Laude* honors from the University of California, Los Angeles in 2014. Adams began his research career in 2012 with a summer internship at the Scripps Research Institute, under the guidance of Dr. Kerri Mowen. There he determined the enzymatic activity and subcellular localization of a protein arginine methyltransferase using molecular cloning techniques. During the academic year, Adams continued his research endeavors in Professor Yi Tang's group, where he explored natural products by elucidating unknown biosynthesis pathways in aromatic polyketides. Adams completed another summer research internship in 2013, at the University of California, San Diego, in the research group of Professor Sadik Esener. Here, he engineered novel hollow silica nanoparticles properties via template synthesis for localized drug delivery in cancer treatment applications.

Adams subsequently enrolled at Purdue University in the Davidson School of Chemical Engineering in the Fall of 2014 under the mentorship of Professor Arvind Varma and Professor Vilas G. Pol. Between 2014 - 2019, Adams performed research in the field of energy storage, namely lithium-ion and potassium-ion batteries, developing new anode materials and investigating thermal runaway in batteries. His work has led to 12 publications and four oral presentations at the AIChE Annual Meeting (2016-2018). While at Purdue University, Adams has been highly involved with laboratory safety, serving as the ViPER group safety officer for three years and a member of the Chemical Engineering Departmental Safety Committee for two years. In 2019, Adams received a Doctorate of Philosophy in Chemical Engineering at Purdue University.

## PUBLICATIONS

Note: \* denotes equal contributions

1. Temperature Dependent Electrochemical Performance of Graphite Anodes for K-ion and Li-ion Batteries, **R. A. Adams**, A. Varma, and V. G. Pol, *Journal of Power Sources*, 410-411, 124-131 (2019).
2. One-step solution combustion synthesis of CuO/Cu<sub>2</sub>O/C anode for long cycle life Li-ion batteries, C. Xu, K. V. Manukyan, **R. A. Adams**, V. G. Pol, P. Chen, and A. Varma, *Carbon*, 142, 51-59 (2019).
3. Dynamic impact of LiCoO<sub>2</sub> electrodes for Li-ion battery aging evaluation, **R. A. Adams\***, B. Li\*, J. Kazmi, T. E. Adams, V. Tomar, and V. G. Pol, *Electrochimica Acta*, 292, 586-593 (2018).
4. "Investigation of LiCoO<sub>2</sub> Cathode Response to Dynamic Impact using Raman Imaging Based Analyses, B. Li\*, **R. A. Adams\***, J. Kazmi, A. Dhiman, T. E. Adams, V. G. Pol, V. Tomar, *Journal of The Minerals, Metals & Materials Society*, 1-7 (2018).
5. Mechanistic Elucidation of Thermal Runaway in Potassium-Ion Batteries, **R. A. Adams**, A. Varma and V. G. Pol, *Journal of Power Sources*, 375, 131-137 (2018).
6. "Li-ion storage in an amorphous, solid, spheroidal carbon anode produced by dry-autoclaving of coffee oil, K. Kim, **R. A. Adams**, P. J. Kim, A. Arora, E. Martinez, J. P. Youngblood, and V. G. Pol, *Carbon*, 133, 62-68 (2018).
7. High-stability tin/carbon battery electrodes produced using reduction expansion synthesis, T. L. Lee, **R. A. Adams**, C. Luhrs, A. Arora, V. G. Pol, C. Wu, J. Phillips, *Carbon*, 132, 411-419 (2018).

8. Binder-free N-and O-Rich Carbon Nanofiber Anodes for Long Cycle Life K-ion Batteries, **R. A. Adams**, J. Syu, Y. Zhao, C. Lo, A. Varma and V. G. Pol, *ACS Applied Materials & Interfaces*, 9, 17872-17881 (2017).
9. Electrochemical Performance of MXenes as K-ion Battery Anodes, M. Naguib\*, **R. A. Adams\***, Y. Zhao, D. Zemylanov, A. Varma, J. Nanda and V. G. Pol, *Chemical Communications*, 51, 1-4 (2017).
10. Sustainable Potassium-Ion Battery Anodes Derived from Waste-Tire Rubber, Y. Li, **R. A. Adams**, A. Arora, V. G. Pol, A. Levine, R. Lee, K. Akato, A. Naskar and M. Paranthaman, *Journal of The Electrochemical Society*, 164, A1234-A1238 (2017).
11. Tailored Solution Combustion Synthesis of High Performance  $\text{ZnCo}_2\text{O}_4$  Anode Material for Lithium-ion Batteries, **R. A. Adams**, V. G. Pol and A. Varma, *Industrial & Engineering Chemistry Research*, 56, 7173-7183 (2017).
12. Superior Lithium-Ion Storage at Room and Elevated Temperature in an Industrial Woodchip Derived Porous Carbon. **R. A. Adams**, A. Dysart, R. Esparza, S. Acua, S. Joshi, A. Cox, D. Mulqueen and V. G. Pol, *Industrial & Engineering Chemistry Research*, 55, 8706-8712 (2016).